INFORMATION TO USERS

This reproduction was made from a copy of a manuscript sent to us for publication and microfilming. While the most advanced technology has been used to photograph and reproduce this manuscript, the quality of the reproduction is heavily dependent upon the quality of the material submitted. Pages in any manuscript may have indistinct print. In all cases the best available copy has been filmed.

The following explanation of techniques is provided to help clarify notations which may appear on this reproduction.

1. Manuscripts may not always be complete. When it is not possible to obtain missing pages, a note appears to indicate this.

2. When copyrighted materials are removed from the manuscript, a note appears to indicate this.

3. Oversize materials (maps, drawings, and charts) are photographed by sectioning the original, beginning at the upper left hand corner and continuing from left to right in equal sections with small overlaps. Each oversize page is also filmed as one exposure and is available, for an additional charge, as a standard 35mm slide or in black and white paper format.*

4. Most photographs reproduce acceptably on positive microfilm or microfiche but lack clarity on xerographic copies made from the microfilm. For an additional charge, all photographs are available in black and white standard 35mm slide format.*

***For more information about black and white slides or enlarged paper reproductions, please contact the Dissertations Customer Services Department.**

Mazzone, Dominick Nicholas

AGGLOMERATION OF PARTICLES IN FLUIDIZED BEDS

City University of New York

PH.D. 1986

AGGLOMERATION OF PARTICLES IN FLUIDIZED BEDS

By

Dominick N. Mazzone

A dissertation submitted to the Graduate Faculty in Engineering in partial fulfillment of the requirements for the degree of Doctor of Philosophy, The City University of New York.

1986

This manuscript has been read and accepted for the Graduate Faculty in Engineering in satisfaction of the dissertation requirement for the degree of Doctor of Philosophy.

Oct 17, 1985
date

Chairman of Examining Committee

Oct 17, 1985
date

Executive Officer

Gabriel I. Tardos

Herbert Weinstein

David Rice

Leslie L. Isaacs

City University of New York

AGGLOMERATION OF PARTICLES IN FLUIDIZED BEDS

By

Dominick N. Mazzone

Adviser: Gabriel I. Tardos

ABSTRACT

An experimental and theoretical study of the agglomeration phenomenon which causes destabilization of certain low and high temperature fluidized beds was performed. A theoretical model was proposed to determine the conditions under which defluidization occurs in fluidized beds in which cohesion forces between granules arise due to the presence of sticky fluids and/or high temperatures. Bonding mechanisms between particles such as solid-liquid bridges, viscoelastic flattening and high temperature sintering were all considered. The model predicts breakup of aggregates by bubble motion and was compared to limiting fluidization-defluidization experiments performed by the author and others. An experimental method to measure surface softening of small particles heated to high temperatures was developed which consisted of using a dilatometer to measure the surface viscosity of the particles from rate of deformation data. Experimental methods to determine minimum sintering temperatures of a variety of granules were also presented. Lastly, experiments were performed to study the dynamic strength of two spheres coated with liquid moving away from one another. It was shown that the strength of the dynamic bridge was at least one order of magnitude greater than the corresponding strength of the static bridge between the two spheres.

To Connie and Christopher
the joys of my life

Acknowledgements

I would like to express my sincere thanks and appreciation to Professors Gabriel Tardos and Robert Pfeffer for their help and encouragement during the research.

I am also thankful to Professor Charles Maldarelli for his help, advice and friendship. Thanks go to Mr. Peter Compo for doing a lot of the work in Section 3.5 and for being a good friend.

Thanks are due Mr. Dov Firnberg, Mr. John Bodnaruk and Mr. Bill Hall for their help in constructing the experimental apparatii.

Many thanks to IFPRI (The International Fine Particle Research Institute) who helped fund the research from the onset of the Institute's existence and the start of my graduate studies.

Table of Contents

Table of Contents (Cont.)

List of Figures

List of Figures (Cont.)

List of Figures (Cont.)

List of Figures (Cont.)

List of Figures (Cont.)

List of Figures (Cont.)

List of Tables

NOMENCLATURE

a - compression distance (see Figure (3.11), cm

a_1 - radius of cylindrical plate, m

a_2 - constant defined in Eq. (3.23)

a^* - dimensionless viscosity term

A - Hamaker constant, J

A_1 - coefficient in Eq. (3.3), dimensionless

A_2 - constant in Eq. (3.8), dimensionless

b - radius of the bonding neck, m

b - sinter neck radius, cm

b_2 - constant defined in Eq. (3.23)

Bo - Bond number, defined in Eq. (4.1), dimensionless

c - constant in Eq. (3.5)

Ca - Capillary number, dimensionless

d_{ag} - diameter of agglomerate, m

d_b - diameter of bubble, m

d_B - diameter of the bed, m

D_p - particle diameter, m

D_s - sample diameter, m

E - Young's modulus

f_c - force due to liquid bridge, N

f - coefficient in Eq. (3.33), dimensionless

$f(Sa)$ - saturation dependent function defined in Eq. (3.6), dimensionless

f_1 - distance between granules, m

F_p - total compressive force between two particles, N

F_1, F_2 - dimensionless force (at points 1 and 2 in Figure 4.1)

F_{B1}, F_{B2} - buoyancy correction term in Eqs. (4.6) and (4.7), dimensionless

F_c^* - dimensionless capillary force

F_v - van der Waals attraction force, N

F_{vis} - force due to viscous effects, N

F_w - force due to lower falling sphere, N

g - acceleration due to gravity, m/s^2

Ga - Gallileo number (defined in Eq. (3.42))

G_v - maximum force acting on an object in a fluidized bed, N

h - height of a cylindrical plate (agglomerate), m

$h\omega$ - Lifshitz-van der Waals constant, J

H - interparticle bonding force, N

Ho - initial curvature ($\Delta P_o/2\gamma$), defined in Eq. (3.1), cm^{-1}

K - constant defined in Eq. (3.36)

K_1 - constant defined in Eq. (3.22), dimensionless

k_1, k_2 - coefficients in Eqs. (3.14) and (3.16)

k_3 - coefficient in Eqs. (3.19)

L - load on the sample, (g)

L_b - length of bridge, cm

L_b^* - dimensionless length of bridge

L_0 - bed height at rest, m

L_o - initial sample length, m

ΔL - sample contraction (dilatation), m

ℓ - height of the agglomerate above the distributor plate, m

ℓ_o - initial sample length ,cm

ℓ_1 - distance between two fixed points in the bed, m

$\Delta\ell$ - sample contraction (dilatation), cm

m - mass of a sphere

n_b - bubble frequency, s^{-1}

n - exponent in Eq. (3.36), dimensionless

ΔP_ℓ - pressure drop between two fixed points in the bed, Pa

q - pressure, Pa

q_{max} - maximum pressure acting on a cylindrical plate (agglomerate), Pa

R - sphere radius, cm

Re_{mf} - Reynolds number (defined in Eq. (3.43))

R_o - minimum radius of bridge at rupture, cm

Sa - saturation, dimensionless

S - dimensionless arc length

t - time, s

T - temperature, ^oC

T_1 - swelling temperature, ^oC

T_2 - sintering temperature of coal, ^oC

T_s - minimum sintering temperature, ^oC

U - dimensionless sphere profile

u_{mf} - minimum fluidization velocity, m/s

U_s - limiting velocity, m/s

$U_s - u_{mf}$ - excess velocity, m/s

v_s - velocity of particle separation, m/s

V_b - bridge volume, μL

V_b^* - dimensionless bridge volume

W - deflection of a plate

W_B - weight of solid in bed, kg

W_m - weight of moisture in bed, kg

X - dimensionless vertical coordinate, Eq. (4.1)

x_s - separation distance between two spheres, cm

Y - dimensionless horizontal coordinate, Eq. (4.1)

y_0 - neck radius at center of liquid bridge, cm

Z_0 - separation distance, nm

Greek Symbols

α - filling angle, degrees

β _ coefficient defined in Eq. (3.32), dimensionless

γ - surface tension, dyne/cm

γ_m - coating liquid surface tension, N/m

δ - friction angle, degrees

ϵ - porosity, dimensionless

η - fluid viscosity, poise

η_s - surface viscosity, poise

θ - contact angle, degrees

$\xi=x_s/R$ - dimensionless separation distance

μ - viscosity, poise

ν - Poisson ratio

ρ - fluid density, kg/m^3

ρ_g - gas density, kg/m^3

ρ_m - density of coating liquid, kg/m^3

ρ_s - density of solids in bed, kg/m^3

$\Delta\rho$ - density difference between fluid-fluid phase, (gm/cm^3)

Φ - angle between liquid-liquid profile and the horizontal, degrees

σ_o - strength of an agglomerate, N/m^2

σ_{OB} - strength of a wet agglomerate, dimensionless

σ_s - yield strength of the neck between granules, N/m^2

σ_y - yield strength of an agglomerate, N/m^2

τ - dimensionless time scale

ψ - function defined by Eq. (3.21), dimensionless

CHAPTER 1: EXECUTIVE SUMMARY

This work is concerned with the study of the agglomeration phenomenon which causes destabilization of certain low and high temperature fluidized beds. Specifically, if bed temperatures are high enough surface softening of the granules that comprise the bed can cause agglomeration or if a coating liquid is injected into the bed, agglomeration will occur. Given certain physical properties of the granules in a fluidized bed, one would like to be able to predict what minimum velocity is necessary to maintain stable fluidization.

A theoretical model is proposed in Section 3.2 to determine the conditions under which defluidization occurs in fluidized beds having cohesive forces arising between particles due to the presence of sticky fluids and/or high temperatures. These conditions define a set of operating parameters such as gas velocity, particle size, temperature or amount of sticky material in the bed which will ensure a stable fluidization without posing the danger of sudden or complete defluidization. Bonding mechanisms between particles such as solid-liquid bridges, viscoelastic flattening and high temperature sintering are considered. The theoretical model predicts breakup of agglomerates in the bed due to forces generated by bubble motion.

Section 3.3 deals with the experimental verification of the proposed theoretical model. The limiting fluidization-defluidization condition for fluidized beds of sticky particles has been studied experimentally in both low temperature beds in which defluidization occurs due to the presence of sticky fluids and in high temperature beds where agglomeration occurs due to sintering of the granules. The experimental results in this section as well as others taken from the literature are compared to predictions of the theoretical model developed in Section 3.2. For the injection of liquid material in the bed, the limiting velocity, U_s necessary to keep the bed fluidized, is seen to be dependent on the dimensionless amount of liquid added as well as measurable bed and fluid properties. For agglomeration due to

temperature effects, the theoretical model requires knowledge of two fundamental physical quantities, the surface viscosity, η_s, and the sinter neck yield strength, σ_s, both as functions of temperature. The yield strength can either be estimated using adhesion theory or calculated from experimental data as shown in Section 3.3.

An experimental method to measure the surface viscosity of small solid particles heated to high temperatures was devised and is presented in Section 3.4. A dilatometer which allows one to measure dilatations and contractions is used to measure surface deformations while the sample is heated at a certain rate and is simultaneously subjected to a compression force. From compression versus time data a surface viscosity is obtained.

It has been shown (Siegell, 1976 and Tardos et al., 1984) that the danger of agglomeration due to high temperature sintering occurs only after the temperature of the fluid bed is raised above a certain temperature characteristic of the particular material. Since the minimum sintering temperature is always less than the solid's melting point, an efficient method of measuring this temperature is very important for all fluidizable granules subjected to high temperatures. The danger of agglomeration during fluidization increases tremendously at temperatures higher than this so-called minimum sintering temperature and, therefore, special precautions must be taken to avoid defluidization under these conditions. Section 3.5 describes a set of experimental methods used to determine the minimum sintering temperature of a variety of materials. These methods include the use of a dilatometer in which the contraction-dilation versus temperature characteristics of a small sample is measured, a differential scanning calorimeter test and an Instron machine by which yield strengths are measured. It is clearly shown that for the majority of materials studied, the different methods give similar values for the minimum sintering temperature but that the dilatometer experiment is the simplest as well as the most reliable.

The observation that the proposed theoretical model underpredicted actual experimental data for the case of injection of a liquid coating into a fluidized bed, resulted in a careful examination of the strength of wet bonds in fluid beds. In the model developed in Section 3.2 only the static strength of liquid bridges (surface tension effects only) was considered. In a fluidized bed, where particles are in constant motion towards and away from one another at different velocities, it is expected that there should be some viscous effects that determine the strength of liquid bridges. An experimental program was carried out to study dynamic bridges and to compare them to the behavior of static bridges; the details are contained in Chapter 4.

While investigating static bridges (Section 4.2) it was found that under certain conditions the influence of gravity on the symmetry of the interfacial profile and the strength of the bridge can be quite significant. A rupture criterion was also proposed and compared very well with experimental data. Two types of dynamic bridge strength experiments were performed. One where a vertical sphere-liquid-sphere system had the bottom sphere falling due to gravity (Section 4.3.1) and another where the spheres separated at constant velocity by the use of a gas actuated piston (Section 4.3.2). A comparison of dynamic and static bridge strengths shows that the forces due to viscous dissipation are, on the average, at least one order of magnitude greater than the force due to surface tension (static bridge case).

Finally, conclusions and recommendations for future work are discussed in Chapter 5.

CHAPTER 2: INTRODUCTION

The formation of coarser granules from finely divided solids (powders) is generally termed agglomeration. This phenomenon may occur in a variety of different processes such as tumbling, fluidization, coagulation, spry drying, etc.. The agglomeration process may be induced by one or several causes such as pressure (external or resulting from interparticle impact), crystallization, melting and solidification (due to surface temperature variation), humidification and drying (due to liquid or moisture addition or removal), diffusion, etc. The process is very much dependent on the nature and especially on the size distribution of the agglomerating powder and the procedure which is used for agglomeration. Some agglomeration processes are deliberate and create more easily handled solids while others are detrimental and must therefore be eliminated. For example, agglomeration in fluidized beds can be a useful means to granulate fine material or to separate ash in fluidized bed combustors but can also result in the disturbing effect of defluidizing the bed at high gas humidity or high temperature.

Since the number of industrial processes in which agglomeration occurs is very large, research in the field is consequently very broad. The objective of the present study was confined to the agglomeration occurring in gas-solid fluidized bed systems. The basic understanding of the agglomeration process in this system is not restrictive in any sense and can include the characteristics of the agglomeration process in any other system.

The size of a solid particle moving around in a fluidized bed can decrease by attrition (erosion, or by any fragmenting effect), can be constant or may increase. Growth of fluidized particles can occur by one or both of the following mechanisms:

A. capture of relatively small size particles on the granule's surface, thereby resulting in slow, continuous enlargement without a pronounced alteration of shape.

B. clumping together of equal size particles thereby resulting in conglomerates with different shapes and much larger sizes than the individual particles.

When the fragmentation effect and the particle growth are in equilibrium, the size distribution in the fluidized bed remains constant. In a fluidized bed one or the other effect is predominant. An agglomerating fluidized bed is defined as one in which growth exceeds attrition. The process of particle size increase described above in A., is called granulation, growth by layering, snowballing, or coating and is generally a desired process while the formation of clumps or conglomerates described in B. is called agglomeration and is usually undesirable. Granules resulting by granulation have, generally speaking, different and more desirable physical and mechanical properties than agglomerates. These granules can be extracted from the bed leaving the smaller particles still fluidized while the formation of clumps and agglomerates causes a bed to defluidize if the process is carried too far.

Fluidized beds of fine particles are used extensively in the chemical industry due to such advantages as large contacting area between gas and solid, excellent heat transfer characteristics, simplicity of operation and low pressure drop. Stable operation of such systems is insured as long as the size of the fluidized particles can be controlled and maintained below a certain level. The presence of liquids (molten material) and/or high temperatures, in fluidized bed combusters, gasifiers and reactors can sometimes produce uncontrollable particle growth and subsequent loss of fluidization. It is important, therefore, to be able to predict that combination of gas velocity, particle size and temperature and/or quantity of agglomerating inducer (liquid) or molten substance which is safe for stable operation. Since the only source of particle energy in a fluidized bed comes from the fluidizing gas stream, a minimum gas velocity is necessary to keep particles in agitation for a given agglomerating process. The energy of the fluidizing gas can be imparted to the particles

through gas jets in or entering the bed or through the mechanism of bubble formation and rise. In fast and turbulent fluidized beds a combination of these effects are present.

The aim of the present research was to predict theoretically and to check experimentally the minimum gas velocity required to keep a bed of particles fluidized. Following this reasoning, it is necessary to be able to predict operating conditions which will prevent the loss of fluidization at points where potentially sticky particles are present or where fluids are fed into the fluidized bed. It is believed that the formation of bonds between particles due to liquid-solid bridges (at the contact point of wet particles), viscoelastic flattening (at the contact point of particles covered with a high viscosity fluid) and softening or sintering of the particles (in high temperature beds) is qualitatively similar and requires a certain energy when these same particles are to be separated. A relatively simple model based on these premises was developed and was successfully compared to experimental data; the theoretical approach to the prediction of fluidization velocities in an agglomerating bed was based on the theory of aggregate break-up due to forces generated in the bed by the motion of bubbles.

During the present work, an agglomerating fluidized bed was constructed and operated in the laboratory. A dilatometer was purchased, modified and interfaced to a minicomputer so that a physical characterization of the particles used in the fluidized bed experiments could be obtained. To study the strength of liquid bridges formed between particles coated with fluids an experimental apparatus was constructed and measurements were performed using fluids of varying viscosity and surface tension. The size of the particles used was also varied.

The results of the research may be of interest in a large number of specific applications since it focuses on the basic understanding of the agglomeration phenomenon.

CHAPTER 3: DESTABILIZATION OF FLUIDIZED BEDS DUE TO AGGLOMERATION

3.1 BACKGROUND AND LITERATURE REVIEW

The behavior of fluidized beds in which the size and/or the properties of the fluidized particles change during the process either due to high temperature or the addition of a solution or a coating to the bed, has not been extensively reported in the fluidization literature. Nevertheless, in many industrial applications, fluidized beds are operated under conditions of pressure and temperature which result in structural or chemical changes on the surface of the fluidized particles which can cause the formation of larger agglomerates from the initial feed. Furthermore, in fluidized bed processes such as coating, drying, etc., the formation of larger particles due to agglomeration can result in uneven, partial or total loss of fluidization. Defluidization may occur even though the bed is operated at gas velocities much higher than the minimum fluidization conditions of the initial feed.

Fluidized beds of fine solids are particularly susceptible to the formation of larger size agglomerates if the feed particles are potentially "sticky". Commercial fluidized beds tend to be operated with small size solids because, owing to their large specific surface area, they allow higher contacting rates; however, this very property creates problems once stickiness occurs. Therefore, a calculation of minimum fluidization conditions based on the initial feed particles in an agglomerating fluidized bed is not very meaningful whereas other "limiting conditions" on the fluidization velocity such as the bed temperature or the amount of sticky fluid added to the bed can become critical. These conditions depend on the initial particle size and size distribution, gas pressure, bed geometry, gas humidity or moisture content, particle surface composition, distributor geometry, and especially the mode of agglomerate formation in the bed. The effect of these conditions on the behavior of the bed

is not well understood and has received relatively little attention in the fluidization literature. The basic knowledge in the area is so limited that industry relies mostly on empiricism to avoid defluidization of beds containing sticky particles. Some of the solutions involve changing the operating conditions in the bed to avoid stickiness or adding inert materials to reduce the agglomeration tendency.

A review of fluidized beds operating under agglomerating conditions was presented by Gluckman et al. (1976), Tardos et al. (1980, 1981, 1982) and Siegell (1984). These reviews encompass commercial fluidized beds as well as experimental units and describe both beds where agglomeration was avoided by changing the operating conditions as well as beds where agglomeration was desired and stickiness was advantageously used in the process under consideration.

Iron ore reducing fluidized beds as described by Squires (1969), Tomasicchio (1967) and MacMullan and Johnson (1962) are only one example where a fine powder which is initially fluidized agglomerates and causes bed collapse to occur at temperatures as low as 370^{o}C, a value which is much lower than the melting temperature of the bed particles. Even at these low temperatures, bonds between particles occur due to solid state sintering (diffusion of solid matter toward the contact area between particles). Migration of solid material increases at higher temperatures and higher surface curvature, i.e., smaller particle size and, therefore, the tendency to form agglomerates also increases under these conditions. Increasing the gas velocity results in an increase in the temperature at which agglomeration occurs due to the fact that the contact time between particles is smaller than the time necessary for the formation of bonds strong enough to hold the particles together.

In a more novel approach, the reduction of iron ore was attempted (Langston and Stephens, 1960) in a bed of coarse iron particles at high gas velocities and high temperatures (700-870^{o} C). The feed, a fine iron-ore powder, is continuously introduced onto the coarse particles where the reactions occur and therefore

these particles grow continuously. The bed discharges coarse pure iron particles through an orifice near the distributor. This is the underlying principle governing the operation of "accreting" fluidized beds. Other examples of this type of fluidization are the Dorr-Oliver process to calcinate lime sludges and to roast Katanga ore and the Fuller cement process (Hovmand, 1978). A similar process of accreting fine ash particles in large solid agglomerates takes place in the ash agglomerating fluidized bed gasifiers and combustors described by Godel and Cosar (1967); Squires (1969), (1972); Yerushalmi et al. (1975) and Liss (1979).

Although pilot plant and full scale agglomerating fluidized beds have been operated with various degrees of success, an adequate theoretical and experimental basis for understanding the agglomeration process is still not available in the literature. Rumpf (1962, 1977) and his coworkers (Schubert, 1977; Rumpf et al. 1976) proposed theoretical models for particle-particle interactions for both high temperature sintering and low temperature viscous bonds, but these studies were not specifically applied to fluidized bed stability. Recently, Ormos and coworkers (Ormos and Pataki, 1979; Dencs and Ormos, 1978; Robinson and Waldie (1979) and Smith and Nienow (1981)), proposed models of agglomeration in low temperature "wet" fluidized beds but, the results were not expressed in a useful mathematical form. The work of Tsubaki and Jimbo (1978) and Kousaki et al. (1979) on dispersion of agglomerates in an air jet is also relevant, although it does not apply specifically to fluidized beds.

In order to study the behavior of agglomerating beds, Gluckman et al. (1976) and Siegell (1976) have conducted bench scale experiments at elevated temperatures in which the operating limits of beds of particles that tend to agglomerate by sintering have been investigated. Defluidization data for a number of solids including copper shot, glass beads, polymeric beads and coal ash were obtained. In a typical experiment, the bed was fluidized at a given velocity, and the temperature was then

increased until defluidization occurred. These investigators found that for a given solid (particle) there is a certain gas temperature below which the bed can always be fluidized at the minimum fluidization velocity, u_{mf}. Above this threshold temperature, the so-called minimum sintering temperature, T_s, stable fluidization requires correspondingly higher velocities. They also found that at temperatures above T_s the point of bed defluidization may be determined by observing the pressure drop through the bed. When the bed defluidizes the material clumps together on the gas distributor blocking the flow of the fluidizing air. Since the forces holding the individual particles together are small, compared to the pressure forces of the flowing gas, "rat holes" or "channels" are blown through the bed. The pressure drop through the bed with "rat holes" is substantially less than that of the original fluidized bed, so that bed defluidization is indicated by a sudden decrease in the pressure drop through the bed. It appears from the above results that the minimum sintering temperature, T_s, is an important characteristic of the bed particles. Gluckman et al. (1976) and Siegell (1984) suggested a method to measure this temperature using a dilatometer. This method was further developed and refined during the present work (Tardos et al. 1984).

A number of theoretical models of agglomerating fluidized beds have been proposed, using the method of population balance techniques as put forward by Sherwin et al. (1967) and Hulbert and Katz (1964), Levenspiel (1969) and Youngquist (1972). Using the concept of particle coalescence rather than growth by layering, Baker and Bergougnou (1974) also developed an agglomeration model. These and similar models by Harada (1972), Pulvermacher and Ruckenstein (1978) and Kapur (1978) are very useful to predict size distributions, feed and production rates once the predominant mechanisms for particle growth are known and the rate constants required in the model have been measured in pilot scale experiments. These models, however, do not allow for the prediction of limiting conditions below which fluidized beds of a given material become unstable and defluidization may occur.

3.2 THEORETICAL MODEL

In the present section a theoretical model is proposed for different fluidized bed and particle characteristics, which defines the limiting conditions beyond which it is not safe to operate the bed. These conditions define a set of operating parameters such as gas velocity, particle size, temperature and/or amount of sticky material in the bed which will ensure a stable fluidization without posing the danger of sudden or complete defluidization. The purpose of the theoretical model is to predict the limiting gas velocity, U_s, (above the minimum fluidization velocity of the initial feed, u_{mf}) which is necessary to break the largest agglomerate in the bed and thereby to keep a bed of sticky particles continuously fluidized at temperatures exceeding the minimum sintering temperature, T_s, and/or if the bed contains a sticky material such as a liquid binder. An advanced model of this type should assume that a fluidized bed can remain in stable fluidization, even though agglomerates form (the particles in the initial feed stick together), if the agglomerate size does not grow beyond certain limits, and as long as the dynamics of agglomerate formation and break-up are in equilibrium. This equilibrium is possible if the bonding forces which tend to keep the particles together are just balanced by forces resulting from the motion of the fluidizing gas in the bed.

In the present work, however, a more simplistic approach is taken in that it is assumed that under the extreme conditions of defluidization the largest agglomerate occupies almost the entire cross-section of the bed and the limiting velocity, U_s, is determined from the forces required to rupture this agglomerate. The advantage of such an approach is its relative simplicity and its applicability to relatively small size beds, while its main disadvantage is that in large beds it is possible and likely that defluidization will occur before the above mentioned limiting condition is achieved. It is therefore appropriate to use the results from this analysis as a limiting design criterion; the

predicted limiting velocity, U_s, should be considered as a lower bound for the fluidizing gas velocity.

Forces on agglomerates in a fluidized bed

The first step in developing the model is to assess the magnitude of forces acting on an agglomerate in a fluidized bed. Two types of forces were considered; hydrodynamic forces due to gas flow in the interstices and shear forces due to bubble motion in the bed. It was immediately apparent that hydrodynamic forces caused by the gas flow alone were much smaller than forces resulting from bubble motion and consequently, the first effect could be completely neglected when compared to the second.

It is a well known fact that the passage of bubbles in a fluidized bed near or around submerged objects creates an excess pressure on these objects. The forces resulting from this excess pressure are important in applications where heat exchange surfaces inside fluidized beds are required. Thus, the literature concerning the forces on slender axisymmetric bodies held in position within a fluidized bed is relatively abundant and has been summarized by Nguyen and Grace (1978) and Livshits et al. (1978).

If a large aggregate in a fluidized bed is viewed as an immersed body, it is easy to picture how forces due to bubble motion break up these aggregates. The only difference is that aggregates, unlike immersed objects such as heat exchange surfaces, are not held in position in the bed but will move around somewhat as bubbles pass through the bed. Unfortunately, the technical literature does not provide information on forces on immersed objects which are freely buoyant within the fluidized bed. It will be assumed therefore that the aggregate is kept in place in the bed and also that the aggregate's shape is a circular cylinder with diameter d_{ag} and height h (see Figure 3.1). The advantages of using this assumption are that the mechanics of the elastic-plastic circular laterally loaded plate (cylinder) are very well developed (Timoshenko and Godier, 1960; Hopkins and

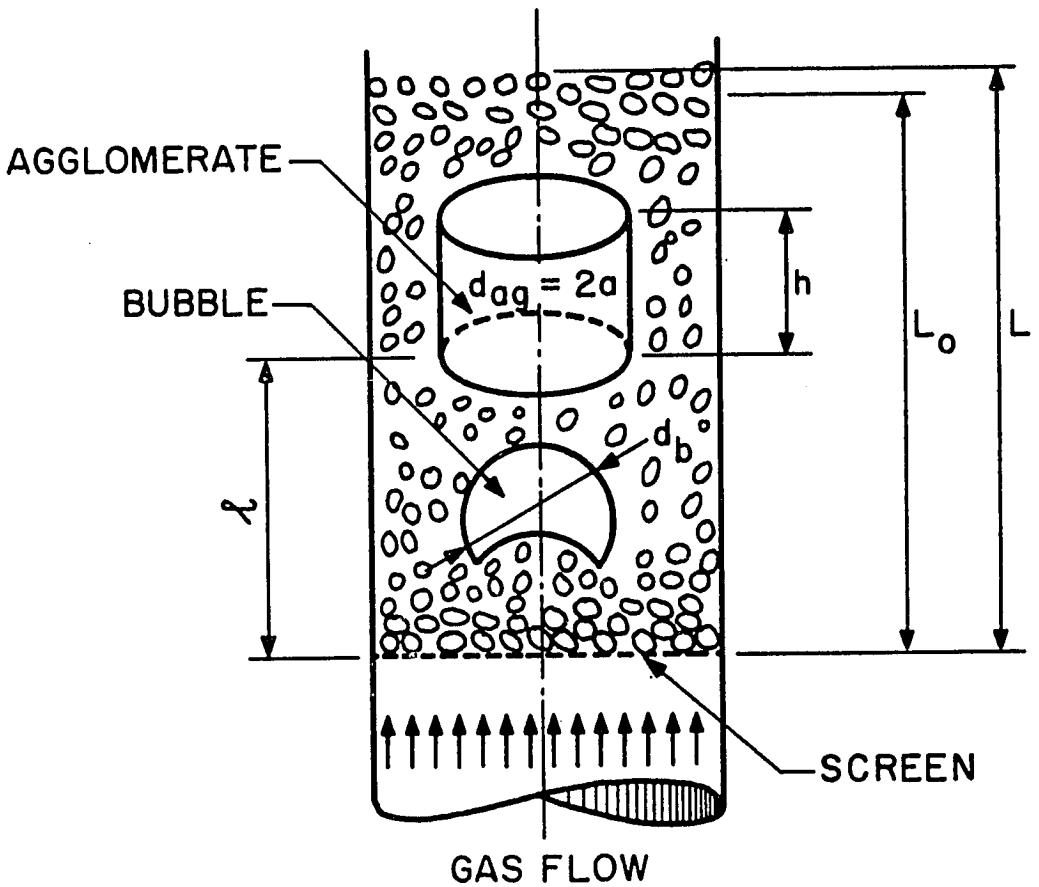

Figure 3.1. An aggregate situated in a fluidized bed.

Prager, 1953) and that the forces (pressures) on a cylinder in a fluidized bed have been extensively studied. The disadvantage of the model is that only an approximate solution is obtained, since the forces acting on a buoyant body are smaller than those on a fixed body and, furthermore, the shape of the aggregate is not necessarily cylindrical.

It is also well known that the vertical force on a submerged body fluctuates as a function of the position of the bubble. The maximum force that occurs was correlated with the dimensions of the axisymmetric body and the characteristics of the fluidized bed by Livshits et al. (1978) in the form

$$G_v = 0.1\rho_s d_{ag}^{1.5}\{1.9(d_B/L_0)^{1/2}[g(U_s-u_{mf})\ell]^{1/3}+U_s-u_{mf}\} \qquad (3.1)$$

where G_v is the maximum force, L_0 is the bed height at rest, d_B is the bed diameter, d_{ag} is the diameter of the agglomerate, ℓ is the height of the cylinder (aggregate) above the distributor plate and $(U_s - u_{mf})$ is the excess velocity above minimum fluidization. As seen from Eq. (3.1) the maximum force G_V, acting on an aggregate (cylinder) of fixed size, increases as the cylinder rises in the bed. If one assumes that the force G_V is uniformly distributed over the aggregate's (cylinder's) top or bottom surface the corresponding pressure can be obtained from

$$q = 4G_v/\pi d_{ag}^2 \qquad (3.2)$$

This pressure will cause failure of the aggregate (cylinder) if it exceeds the value (Timoshenko and Godier, 1960)

$$q_{max} = \sigma_y(2h/d_{ag})^2 A_1 \qquad (3.3)$$

where σ_y is the yield strength of the agglomerate (cylinder) and A_1 is a coefficient which depends on the boundary conditions and the yield criteria used and can be taken approximately as $A_1 = 2$ (Tardos et al., 1981, see Appendix D). Equating equations (3.2)

and (3.3), using the expression for the vertical force as given by Eq. (3.1), one obtains a relationship between the excess velocity, $U_s - u_{mf}$, and the yield strength of the aggregate (cylinder), σ_y.

Agglomerate strength calculations

The second step in developing the model is to compute the strength of an agglomerate σ_0, which is defined (Rumpf, 1977) to be the maximum tensile stress, at zero shear under which the agglomerate will deform indefinitely. This definition is consistent with assuming that the agglomerate is an elastic-plastic body with a yield strength, σ_y, equal to σ_0.

Rumpf (1977) and Schubert (1977) computed the strength of a wet agglomerate, σ_{OB}, in which bonding forces are produced by the presence of a liquid, from the following equation:

$$\sigma_{OB} = [(1-\epsilon)\gamma_m/(\epsilon D_p)] \cdot F_B^*(\epsilon, Sa, \theta, x_s/D_p) \qquad (3.4)$$

where D_p is the initial particle size, γ_m is the liquid surface tension, ϵ is the porosity, θ is the wetting angle, x_s is the distance between the granules and F_B^* is a complicated function of many variables. At high saturation (Sa = 1) the function F_B^* can be taken approximately as

$$F_B^* = c \cos \theta \qquad (3.5)$$

where c is a constant between 6 and 8. Using experimental and theoretical data by Capes (1980), Adorjan (1977), Pietsch et al. (1969) and Newitt and Conway-Jones (1958), Eqs. (3.4) and (3.5) can be rewritten in the form

$$\sigma_{OB} = f(Sa) \frac{1-\epsilon}{\epsilon}(\gamma_m/D_p) \qquad (3.6)$$

for $0.35 < \epsilon < 0.5$, $\theta < 15^o$ and $x_s/D_p < 10^{-2}$, where f(Sa) is a function of the saturation value Sa, given by

$$Sa = \frac{1-\epsilon}{\epsilon} \frac{\rho_s}{\rho_m} \frac{W_m}{W_B} \tag{3.7}$$

In Eq. (3.7), ρ_s and ρ_m are the density of the solid and of the liquid, respectively, W_m is the total weight of liquid (coating) added to the bed, and W_B is the weight of the solid particles. For relatively small values of the saturation, Sa (Sa $\leq$ 0.2), the function f(Sa) can be assumed to be linear so that (Tardos et al., 1981)

$$\sigma_{OB} = A_2 \left(\frac{1-\epsilon}{\epsilon}\right)^2 \frac{\rho_s}{\rho_m} \frac{W_m}{W_B} \frac{\gamma_m}{D_p} \tag{3.8}$$

where A_2 is a constant found by a linear regression of available experimental data to be $A_2 = 10.2$.

The strength of a sintered agglomerate can be computed from Rumpf's (1977) equation

$$\sigma_{OS} = \frac{1-\epsilon}{\epsilon} (H/D_p^2) \tag{3.9}$$

where H is the interparticle bonding force. This force depends mainly on the contact area between the granules. If it is assumed that the radius of the contact area b is small as compared to the granule diameter, D_p, it can be shown (Rumpf et al., 1976) that the radius b for a sintered bond is given by

$$\left(\frac{b}{D_p}\right)^2 = \left[\frac{4}{5} \frac{\gamma_s}{D_p} + \frac{2}{5\pi} \frac{F_v+F_p}{D_p^2}\right] (t/\eta_s) \tag{3.10}$$

where γ_s is the material's surface tension, t is the time of contact during which compression occurs and η_s is the "viscosity" of the granule's surface. The forces F_v and F_p are the van der Waals attraction and the total pressure on the granule during compression, respectively. Assuming that the bonding force H can be computed from the equation

$$H = \pi b^2 \sigma_s \tag{3.11}$$

where σ_s is the yield strength of the neck between the particles (granules) and that the compression resulting from the action of the surface tension γ_s and the van der Waals force F_v is small compared to the action of the pressure force F_p (Rumpf, 1977), Eq. (3.9) can be written as

$$\sigma_{OS} = \frac{2}{5} \frac{1-\epsilon}{\epsilon} (F_p t \sigma_s / \eta_s D_p^2) \tag{3.12}$$

This equation gives the strength of the sintered aggregate as a function of the surface viscosity η_s of the particle and the time t, of compression.

The important feature of Eqs. (3.10) and (3.12) is the fact that the radius of the flattened surface of the granule, b, increases with time and is a function of the viscosity, η_s, of the material. This quantity is clearly temperature dependent and therefore the strength of a sintered neck, σ_{OS} is also strongly temperature dependent. A proper value for the yield strength σ_s is difficult to pinpoint since it depends on the nature of contact between particles. For very strong sinter necks, it can be assumed that the strength of the neck is identical to the strength of the granular material itself. Some experimental evidence supporting this assumption was given by Siegell (1976) and by Rumpf (1977) who showed that when sintered aggregates are broken the necks do not break, but rather the failure zone enters the particle to a certain depth. However, for other agglomerates the yield strength σ_s may be much weaker and in the limit where only flattening has occurred, it then may be taken as the van der Waals attraction between the two surfaces.

Prediction of limiting gas velocities for agglomerating fluidized beds

The criteria of rupture given in Eqs. (3.2) and (3.3) can now be easily applied to both situations, that of wet and that of

sintering beds using Eqs. (3.8) and (3.12) which give the agglomerate strength, σ_0, and Eqs. (3.1) and (3.2) which give the pressure. The basic assumption made here is that the aggregate failure will occur at the point where the maximum stress will equal the aggregate strength, σ_0. A more advanced theory, but which will not be attempted here, should also contain considerations regarding the non-homogeneity of the aggregate and the fact that aggregates can fail at lower stresses than σ_0 due to crack formation and by forces applied on impact.

Simple algebraic manipulations of Eqs., (3.1), (3.2), (3.3) and (3.8), after taking the size of the aggregate as

$$h = d_{ag} \tag{3.13}$$

and assuming the worst case in which the agglomerate is situated on the distributor plate (ℓ=0), yield the expression for the excess velocity, $U_s - u_{mf}$.

$$U_s - u_{mf} = \frac{\pi A_2}{2k_1} \left(\frac{1-\epsilon}{\epsilon}\right)^2 \frac{\gamma_m}{W_B d_B} \left(\frac{d_{ag}}{g}\right)^{1/2} \frac{W_m}{\rho_m D_p} \tag{3.14}$$

Here $k_1 = 0.1 d_B / g^{1/2}$ is a constant and g is the acceleration of gravity. Eq. (3.14) can be put into dimensionless form by using the minimum fluidization velocity of the initial particles u_{mf}. given by Kunii and Levenspiel (1969) as

$$u_{mf} = \left\{ \frac{\phi D_p}{1.75} \frac{\rho_s}{\rho_g} g\epsilon^3 \right\}^{1/2} \tag{3.15}$$

where ϕ is the shape factor and ρ_g is the gas density. From Eqs. (3.14) and (3.15) one obtains

$$\frac{U_s - u_{mf}}{u_{mf}} = k_2 \frac{(1-\epsilon)^2}{\epsilon^{7/2}} \frac{\gamma_m}{W_B g} \left\{ \frac{\rho_g d_{ag} d_B}{\rho_s} \right\}^{1/2} \left[\frac{W_m}{\rho_m (D_p^3 d_B^3 \phi)^{1/2}} \right] \tag{3.16}$$

where $k_2 = 6.75\pi / k_1$ and is a numerical constant.

In calculating the limiting velocity, U_s, one may take the maximum size of the agglomerate before total defluidization occurs to be approximately the bed diameter, $d_{ag} \simeq d_B$. Thus, Eq. (3.16) gives the limiting velocity U_s for a wet bed as a function of the dimensionless amount of liquid added to the bed (quantity in brackets) and a dimensionless constant which incorporates bed and fluid properties.

In order to obtain the limiting velocity, U_s, for the case of the sintered agglomerate, one has to combine Eqs. (3.1), (3.2), (3.3) and (3.12). Before doing so, however, one must observe the specific way agglomerates are formed and determine the compression time, t, and the pressure force, F_p, in Eq. (3.12). Aggregates will form in the fluidized bed during the time elapsed between two consecutive bubbles which pass through the same region in the bed. In this region the particles are compressed under their own weight and, therefore, a conservative approximation of the pressure force, F_p, which causes sinter bonds to form is the weight of the aggregate itself (see Figure 3.1). The pressure force is then given by:

$$F_p = \pi d_{ag}^2 h(1-\epsilon)\rho_s g/4 \qquad (3.17)$$

The time of compression, t, is assumed to be the time between two consecutive bubbles which pass near the same point. This time can be estimated from the bubble frequency, n, to be (Kunii and Levenspiel, 1969)

$$t = \frac{1}{n_b} = \frac{d_b}{1.5(U_s - u_{mf})} \qquad (3.18)$$

Combining Eqs. (3.12), (3.17) and (3.18), using the rupture criteria given in Eq. (3.3) and the expression for the pressure in Eqs. (3.1) and (3.2) (for $\ell=0$), and Eq. (3.15), the dimensionless excess velocity $(U_s - u_{mf})/u_{mf}$ becomes

$$\frac{U_s - u_{mf}}{u_{mf}} = k_3 \frac{1-\epsilon}{\epsilon^2} \frac{d_{ag}^{7/4} d_b^{1/2}}{d_B^{1/2} D_p^{3/2}} \left\{ \frac{\rho g \sigma_s}{\phi \rho_s \eta_s g^{1/2}} \right\}^{1/2} \qquad (3.19)$$

where k_3 is a numerical coefficient and d_b is the bubble diameter. As in Eq. (3.16) the maximum size of the agglomerate d_{ag} has to be assumed in order to calculate the limiting velocity, U_s, and can be taken in the extreme case to be $d_{ag} = d_B$. As seen in Eq. (3.19) the limiting velocity U_s depends on both bed and particle characteristics as well as on the physical properties of the neck between granules such as its strength σ_s and the granule's surface viscosity η_s; all these quantities are temperature dependent.

The importance of the equations presented above lies in their ability to illustrate the important experimental parameters which have to be known for a given situation in order to be able to predict the limiting velocity, U_s. These parameters are the surface tension, γ_m, of the wetting fluid in a bed containing a sticky liquid or a coating, the yield strength σ_s, and the viscosity η_s in a high temperature bed where sintering and/or surface deformation are causing particle stickiness. Once these quantities are known one can show, for example, that the minimum sintering temperature T_s is the temperature at which the expression in braces in Eq. (3.19) increases rapidly. At temperatures higher than T_s the variation of the limiting velocity, U_s, as a function of temperature can be determined using Eq. (3.19).

In order to put the theoretical model in proper perspective, the main assumptions which were made are summarized below:

a. The aggregate has a cylindrical shape with a diameter equal to its height

b. The maximum pressure, q_{max}, arising from bubble motion is evenly distributed on one side of the aggregate, so that the yield condition can be written as

$$q_{max} \leq 4\sigma_0 A_1 \qquad (3.20)$$

where A_1 is a function which depends, in a complex way, on the assumed loading (see Appendix D). In our calculations A_1 was assumed to be the average value, A_1=2

c. The aggregate strength varies linearly with moisture content, Sa, over the range from zero to Sa=0.20
d. The wetting angle of the fluid to the solid particles is very small ($\theta < 15^{o}$)
e. The aggregate is situated in close proximity to the distributor plate
f. The size of the aggregate is taken equal to the diameter of the bed ($d_{ag} = d_B$), this being the extreme situation when the bed is completely defluidized
g. Bonds between granules are formed due to sintering under the contact pressure force F_p which was taken to be equal to the weight of the aggregate
h. The contact time between sintering granules is taken to be the inverse of the bubble frequency
i. The effect of surface tension and of the van der Waals force on the neck size was neglected
j. Breaking of aggregates occurs at points where the stresses resulting from bubble motion exceed the agglomerate strength, σ_0

3.3 EXPERIMENTAL VERIFICATION

Introduction and background

Section 3.1 of this thesis has presented a review of theoretical and some experimental studies of agglomerating fluidized beds where aggregation of particles is caused by interparticle cohesion. In this section a review of some of the more recent experimental studies in the field as well as some experimental results obtained by the author are presented together with a comparison of these findings with the theoretical model.

Basu (1982) and Basu and Sarka (1983) studied agglomeration of coal-ash in an externally heated fluidized bed. Liquid

petroleum gas was burned in a fluidized bed of ash particles between 0.7-1.4 mm in diameter. The fluidizing gas was reduced slowly until defluidization occurred. The experiments were repeated at temperatures below and above the minimum sintering temperature of the ash granules in a manner similar to the experiments performed by Siegell (1976). The minimum sintering temperature was determined in a separate experiment using a dilatometer as was proposed earlier by Gluckman et al. (1976). The experimental defluidization data were correlated by Basu (1982) by an expression of the form:

$$\frac{U_s}{u_{mf}} - 1 = \frac{\psi(T, L_0, D_p)}{(1-\epsilon)(\rho_s - \rho_g)} \tag{3.21}$$

where U_s is the limiting gas velocity which keeps the bed fluidized at the temperature T, u_{mf} is the minimum fluidization velocity without agglomeration at temperature T, L_0 is the bed height, D_p is the particle diameter, ϵ is the bed porosity and ρ_s and ρ_g are the solid and gas density, respectively. The function ψ was written in the form:

$$\psi = K_1(T-T_s)f_1(D_p)f_2(L_0) \tag{3.22}$$

where T_s is the minimum sintering temperature. The constant K_1 was determined from the experiments as the slope of the experimental fluidization velocity vs. temperature, but the functions $f_1(D_p)$ and $f_1(L_0)$ were not calculated.

A more complete review of defluidization data at high temperatures was presented by Liss et al. (1983). These authors, using experimental data by Siegell (1976) which appeared recently in the open literature in Siegell (1984), proposed an expression to compute the limiting gas velocity at high temperatures which, for small particle sizes, i.e., low Reynolds numbers, is given by

$$\frac{U_s}{u_{mf}} - 1 = a_2\left(\frac{T-T_s}{T_s}\right)^{b_2} \tag{3.23}$$

where a_2 and b_2 are constants determined from experiments and T_s is the minimum sintering temperature. Values for a_2 and b_2 were determined by curve-fitting, as shown in Figure 3.2.

The drawback of the above equations proposed to compute the limiting velocity, U_s, is that the function ψ, in equations (3.21) and (3.22) and the constants a_2 and b_2 in equation (3.23) must be determined from fluidization experiments. In Section 3.2, a theoretical relationship for the excess gas velocity, $U_s - u_{mf}$, in a sintering fluidized bed was developed in the form:

$$\frac{U_s - u_{mf}}{u_{mf}} = 3.3 \frac{1-\epsilon}{\epsilon^2} \frac{d_B^{5/4} d_b^{1/2}}{D_p^{3/2}} \left\{ \frac{\rho_g \sigma_s}{\phi \rho_s g^{1/2} \eta_s} \right\}^{1/2} \qquad (3.24)$$

where, in addition to the notations already used, d_B is the bed diameter, d_b is the bubble size, σ_s is the yield strength of the sinter neck and η_s is the granule surface viscosity. One has to note here that, unlike Eqs. (3.21-3.23), Eq. (3.24) was determined from purely theoretical considerations and that the R.H.S. of Eq. (3.24) does not depend on the temperature difference $(T - T_s)/T_s$ as in Eq. (3.23), but rather depends on two physical properties, the neck yield strength σ_s and the surface viscosity η_s which are both temperature dependent. In fact, for a solid particle which does not deform appreciably (below the sintering temperature T_s), the viscosity, η_s, approaches infinity and the limiting velocity becomes $U_s = u_{mf}$. At higher temperatures, the viscosity η_s decreases and the particles stick together forming agglomerates. Thus, the definition of the minimum sintering temperature T_s, as that temperature at which the fluidized granule surface viscosity suddenly decreases becomes clear.

The advantage of the theoretical expression Eq. (3.24), over the empirical equations, Eqs. (3.21-3.23), is that the limiting velocity U_s can be determined directly, once the granule properties σ_s and η_s are known or are measured in separate non-fluidized experiments. A comparison of the results obtained by Basu (1982) and Liss et al. (1983) and by the present author is

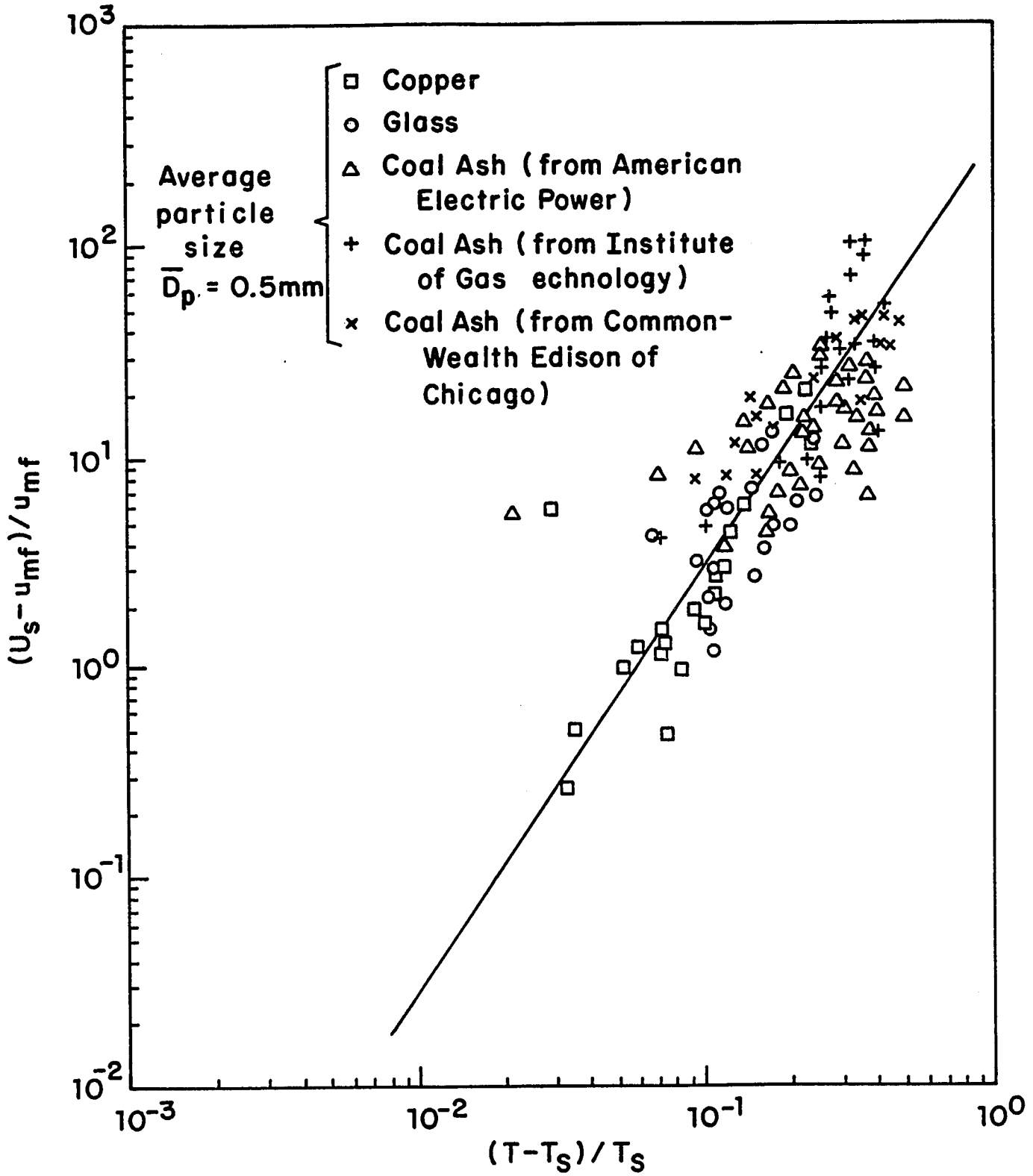

Figure 3.2. Dimensionless excess velocity vs. dimensionless temperature (after Liss et al (1983)).

given below for both low temperature beds as well as high temperature agglomeration.

Apparatus and procedure

A schematic representation of the experimental apparatus is shown in Figure 3.3. Fluidizing air from either one of two Roots positive displacement rotary pumps is passed through an Adams Poro-Stone centrifugal air filter which eliminates oil and water from the air stream. The compressed air stream is then sent through a regulator and the total flow rate is measured by a rotameter. Air temperature and pressure are measured at the rotameter exit to correct for air density changes. From this point the air stream can be passed either through heater (1) or through heater (2), or both. Heater (1) is a Chromalox 30 KW circulation heater, which can heat 2.5 m^3/min of air to a maximum of 750°C. Heater (2) is a 9 KW packed bed unit designed to heat air up to 250°C. The air stream exiting the heaters is split and enters a mixing chamber 20 cm in diameter at two opposite side openings. Consequently, the flow enters a 15 cm diameter calming section in which the gas pressure and temperature are measured. The pressure is measured by a Validyne DP15 pressure transducer and the reading is displayed on a four channel HP Voltmeter and printed. Gas temperatures are measured by two K-type thermocouples, one of which is connected to the HP Voltmeter and its reading is printed. The other thermocouple is connected to a temperature controller, which regulates the heaters and ensures a set air temperature at the entrance of the fluidized bed. The air then passes through the distributor plate and enters the bed.

The bed consists of a 15 centimeter diameter "measuring" section in which an exposed junction thermocouple measures the bed temperature which is then displayed on the HP Voltmeter and printed. Above this section a 15 cm diameter, 60 cm long Pyrex glass tube is mounted which allows for visual observation of the bed. The bed is also equipped with a spray nozzle of the Bete 40° full cone type which is retractable. Spray solution stored

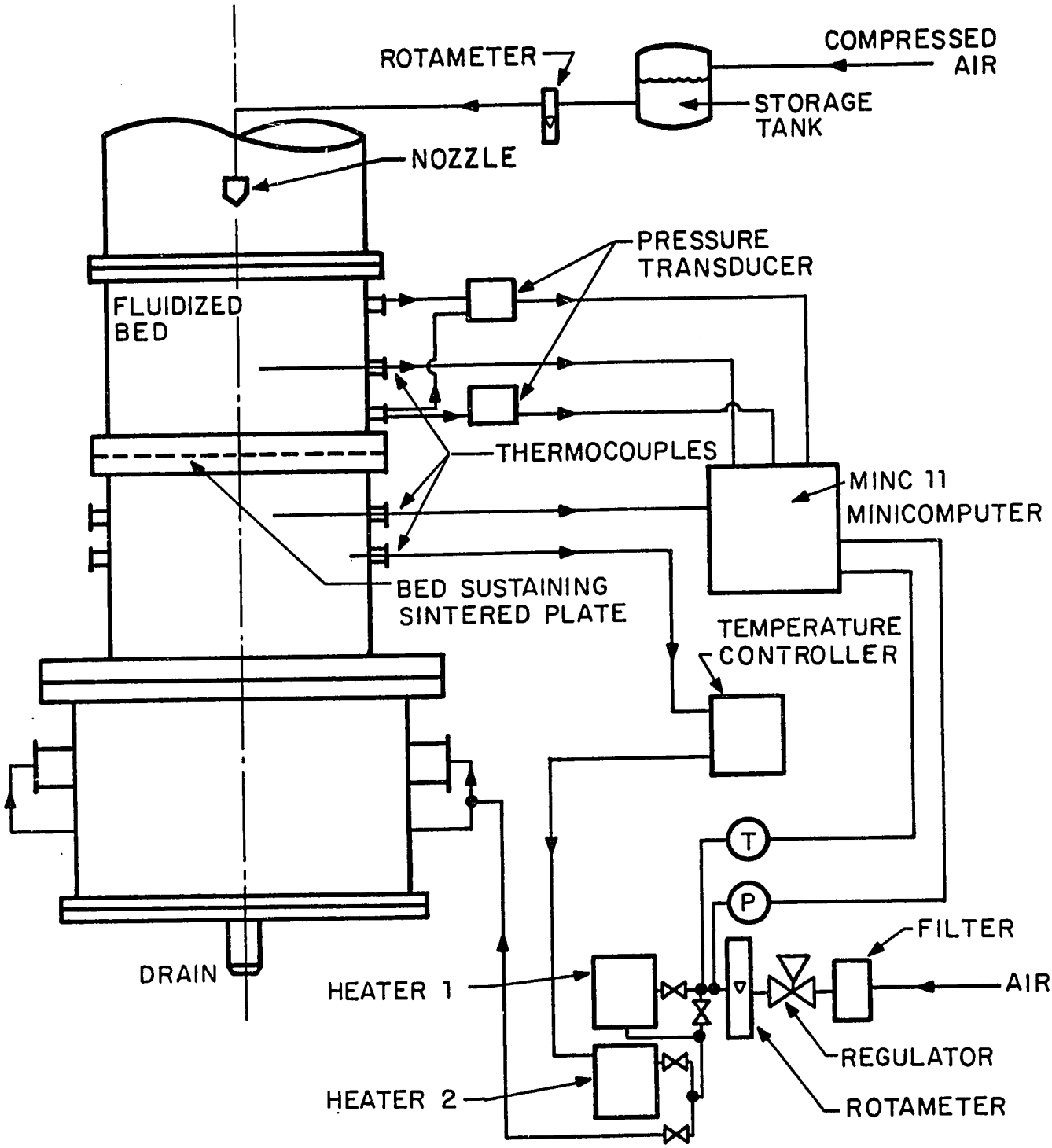

Figure 3.3. Schematic of experimental apparatus to study defluidization phenomena in fluidized beds.

in a steel tank is metered and is injected through the nozzle with compressed air. The sprayer is able to inject up to 90 cm^3/min of spray with an air pressure of up to 300 Kpa.

An additional test section was designed and built to replace the transparent tube. This section, made of stainless steel, 15 cm in diameter and 25 cm long, is mounted directly above the distributor plate and is equipped with a Validyne DP15 pressure transducer to measure the pressure drop, ΔP_ℓ, between two fixed points in the bed, situated at a given distance ℓ_1 apart. The value, ΔP_ℓ, can be used to calculate the average porosity of the bed at any gas velocity since

$$\epsilon = 1 - \frac{\Delta P_\ell}{g(\rho_s - \rho_g)\ell_1} \tag{3.25}$$

where ρ_s is the density of the solid particle, ρ_g is the density of the fluidizing gas, and g is the acceleration due to gravity. The test section is also equipped with ceramic heating elements which are regulated to keep the bed wall temperature equal to the gas temperature and thus minimize horizontal temperature gradients in the bed.

All temperature, pressure and flow rate readings are also recorded and displayed on a Digital Equipment Minc II data acquisition system so that defluidization data are readily obtained directly from the computer. The program that performed the actual data collection is FBED and is listed in Appendix A.3.

During a typical low temperature (liquid coating) experiment the total amount of fluid sprayed by the nozzle onto the bed is metered and pressure drop data at a given gas velocity is recorded until defluidization occurs. Defluidization is observed when the pressure drop through the bed decreases suddenly because particles are no longer sustained by the gas stream. When the data were compared with the theoretical predictions, it was assumed that the coating (high viscosity fluid) was evenly distributed in the bed. The premise for this assumption was met by adding the sticky coating over a long period of time to insure

that a thorough mixing of the particles occurred during the experiment.

A typical high temperature (sintering) experiment is performed as follows: the air flow is started to fluidize a bed of particles at approximately 2.5 to 3 times the minimum fluidization velocity. The temperature controller is set to the desired air temperature to be maintained throughout the run, and the heaters are energized. The system is allowed to reach thermal equilibrium for about 30 minutes. The experiment is then started by decreasing the gas velocity in equal increments. The rotameter reading along with the pressure and temperature at the rotameter are recorded. The temperature and pressure of the gas under the distributor plate as well as the temperature and pressure in the bed itself are all displayed and printed. The gas velocity is decreased in set increments repeatedly until the bed defluidizes. The gas velocity is further decreased in the fixed bed state so that six to eight data points can be recorded. The velocity is then increased in set increments so that the bed is refluidized. Pressure drop through the bed versus gas velocity data at a preset gas (bed) temperature are automatically recorded and stored in the computer.

Low temperature (coating) experiment

Some typical results using a coating material (Ace plastic coating #3100, Ace Glass, Vineland, New Jersey) with a surface tension of $\gamma_m = 0.039$ N/m were obtained using TCC (thermal cracking catalyst) beads in the size range from 2-14 mesh. The material properties of the particles and the gas were: $\rho_s = 1400$ kg/m^3, $\rho_g = 1.2$ Kg/m^3, $\rho_m = 1200$ kg/m^3, $d_B = .0762$m, $W_B = 0.4$ Kg and $\epsilon = 0.4$. Using these properties the experimental data could be correlated as seen in Figure 3.4 by the expression

$$\frac{U_s - u_{mf}}{u_{mf}} = 0.098 \left\{ \frac{W_m}{\rho_m D_p^{3/2} d_B^{3/2} \phi^{1/2}} \right\} \qquad (3.26)$$

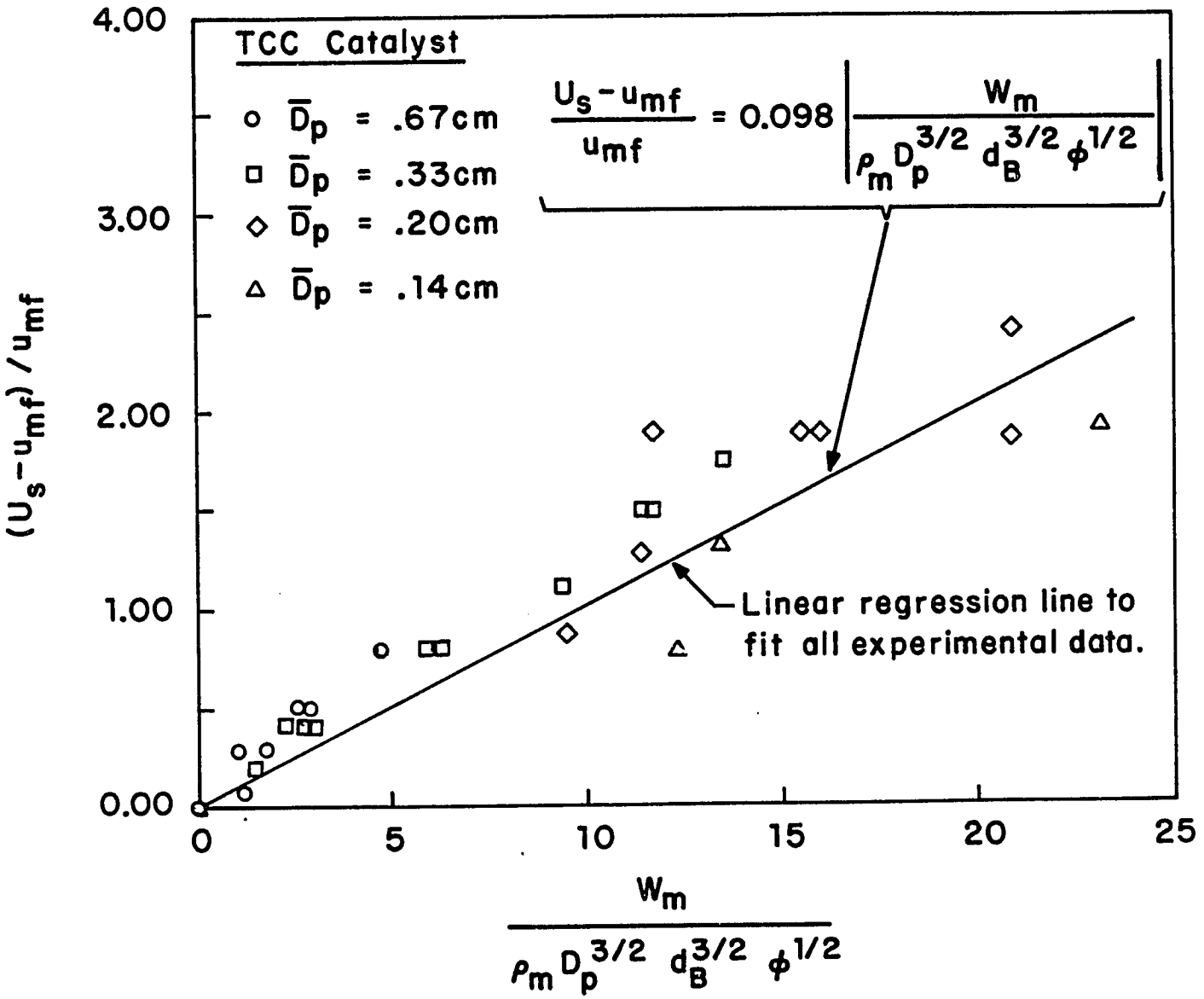

Figure 3.4. Dimensionless excess velocity vs. dimensionless liquid content of the bed.

whereas the theoretical result (Eq. (3.21), in Section 3.2 of this thesis), assuming that the critical agglomerate size $d_{ag} = d_B$, yields a coefficient (quantity outside the brackets) of 0.040. Taking into account the large number of assumptions made in order to obtain the theoretical results, the fit of the experimental data is quite good. The main reason why the theory underpredicts the value of the gas velocity U_s is that the aggregate strength is in fact larger than that initially assumed which takes into account only surface tension. In reality, the force separating the particles in the agglomerate has to overcome not only the pressure due to the surface tension but also the viscous flow of the material around the contact point. This effect was not taken into account in the theoretical considerations but is further investigated in Chapter 4.

Defluidization experiments at high temperatures

The sintering experiments were performed using two sizes of polyethylene particles of diameter $D_p = 0.32$ cm and $D_p = 0.07$ cm. The minimum fluidization velocity, u_{mf}, at room temperature was determined from the intersection of two linear least-squares fitted lines corresponding to the pressure drop in the fixed bed and the fluidized bed region, respectively (see Appendix C). The experiment was repeated at moderate temperatures between 25°C and 90°C to see if there was any agglomeration effects at temperatures below the observed minimum sintering temperature, T_s. It was noted that the adhesive forces between particles at these temperatures are not strong enough to have an effect on the minimum fluidization velocity and the fluidized bed can be operated with no concern for the possibility of defluidization. Experiments at higher temperatures were performed to obtain the minimum fluidization velocity under conditions where agglomeration would occur. In these experiments, the bed was kept in the fluidized state at a given temperature T, while the gas velocity was reduced to the point of the limiting velocity, U_s, and only brought below this value for a short time in order to get an

accurate value of U_s. Table 3.1 shows the dimensionless excess velocity $(U_s - u_{mf})/u_{mf}$ versus temperature for the two sizes of particles used in the experiments, above the minimum sintering temperature of the material.

The two fundamental physical properties required for predicting defluidization velocities as determined by Eq. (3.24) are the surface viscosity, η_s and the yield strength, σ_s. Surface viscosity measurements were performed as described in Section 3.4, while the yield strength of the sinter neck was estimated using adhesion theory which assumes that van der Waals forces are the dominant (short-range) attractive forces within particle-particle bonds once they are formed. This assumption is correct for weak particle-particle bonds.

The strength of a particle-particle bond is given by (Krupp, 1967) as

$$\sigma_s = \frac{\hbar\omega}{8\pi^2 Z_0^3} \tag{3.27}$$

where $\hbar\omega$ is the Lifshitz-van der Waals constant, which depends on the material and Z_0 is the separation distance of the granules. Values of the Hamaker constant, A, for different materials which is related to the Lifshitz constant by the relation:

$$A = \frac{3}{4\pi}\hbar\omega \tag{3.28}$$

can be found in Visser (1972). The value for polyethylene is given as $A = 1.0 \times 10^{-19}$ Joules (0.624eV). The only quantity undetermined in the calculation of σ_s using Eq. (3.27) is the separation distance, Z_0. This was left as a free parameter in the comparison of the experimental data with the theoretical model.

Figure 3.5 shows the comparison between experimentally determined defluidization velocities as compared to the theoretical model (using Eq. (3.24)) versus temperature. These results are for the polyethylene granules of average size equal to .07cm

Table 3.1. Dimensionless excess velocity as a function of average bed temperature for two sizes of polyethylene particles.

Temperature (°C)	$\frac{U_s - u_{mf}}{u_{mf}}$ (D_p = 0.07cm)	$\frac{U_s - u_{mf}}{u_{mf}}$ (D_p = 0.32cm)
108	---	0.18
110	1.61	---
111	---	0.20
115	2.14	0.32
120	4.30	0.50

Note: Minimum sintering temperature $T_s \cong 106°C$.

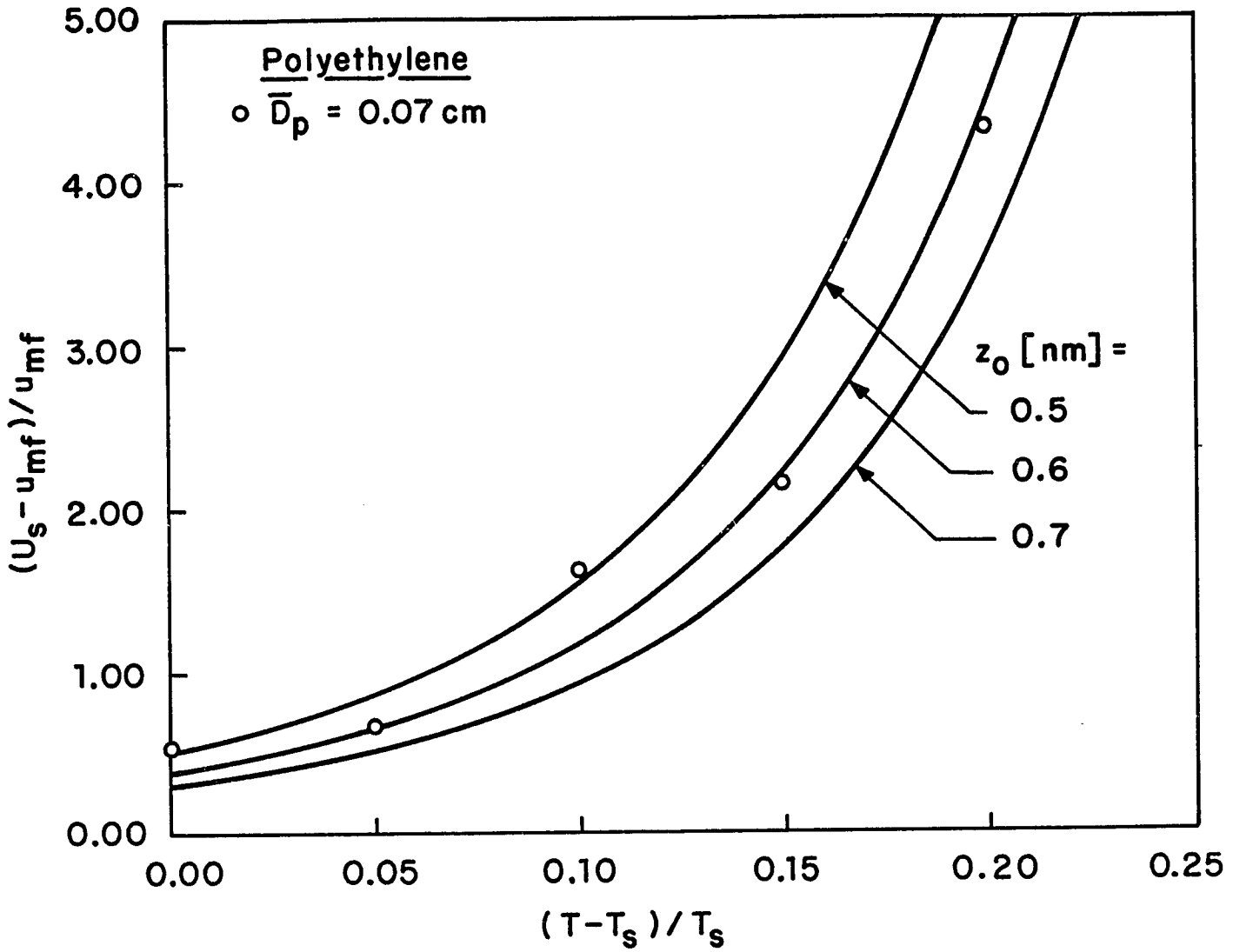

Figure 3.5. Dimensionless excess fluidization velocity vs. dimensionless temperature for a bed of polyethylene particles.

and for a bubble diameter d_b taken equal to one quarter of the bed diameter. The choice of Z_0 plays an important role in determining the fit between experiment and theory, and as seen from Figure 3.5 an average value of Z_0 equal to 0.6nm yields a good fit of the dimensionless excess velocity $(U_s-u_{mf})/u_{mf}$ versus temperature as compared to the experimental data. Figure 3.6 presents defluidization velocities versus temperature for both samples of polyethylene using a separation distance of 0.6nm. From Figure 3.6, one can clearly see that, using the same separation distance, the model is able to predict defluidization velocities for both relatively small granules as well as larger granules. It is important to observe that the value found for the separation distance Z_0=0.6nm is very close to the widely accepted value of Z_0=0.4nm (Rumpf, 1977), thus attesting to the soundness of the proposed model.

Additional defluidization experiments were performed with two different sizes of polypropylene granules of diameter, D_p = 0.2 cm and D_p = 0.32 cm, respectively (see Appendix C). To eliminate the use of the van der Waals force for estimating the agglomerate strength, which is a somewhat arbitrary choice and which only holds for very weak agglomerates, experiments were performed on the polypropylene agglomerates formed in the fluidized bed. The measurements were performed by a group at Chuo University in Japan (Sekiguchi and Tohata, 1982) using the following procedure. A weighed agglomerate is mounted on the head of a needle shaped sample holder, which is connected to a microbalance. The microbalance is kept in equilibrium while a stream of hot air is passed around the agglomerate at steadily increasing velocities until the agglomerate fails. From these experiments the critical drag force, σ_{OS}, at which agglomerate breakup occurs is obtained. Table 3.2 shows the critical drag force as a function of air stream temperature. The yield strength of the agglomerate σ_s can be obtained by using the equation:

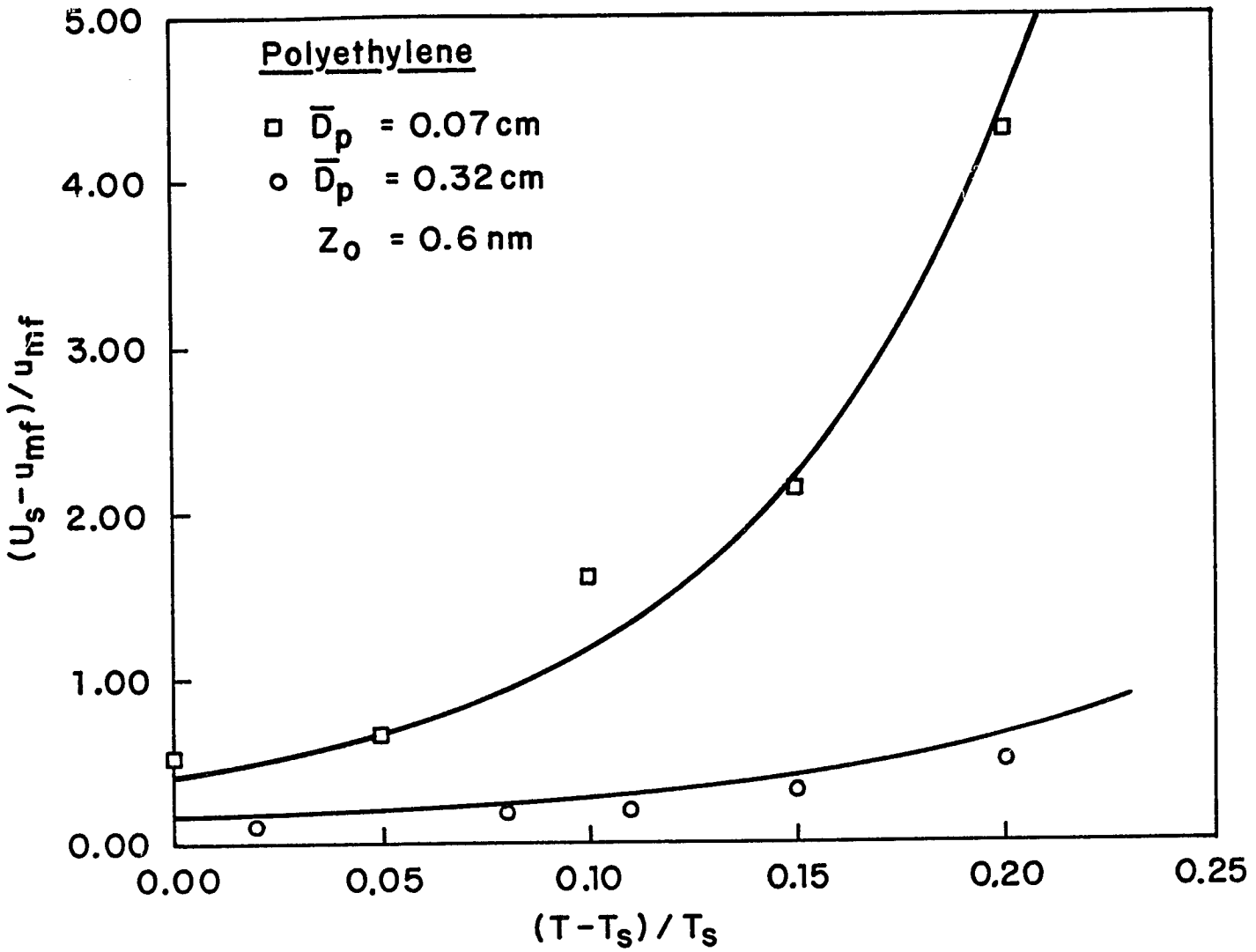

Figure 3.6. Dimensionless excess fluidization velocity vs. dimensionless temperature for polyethylene.

Table 3.2. Effect of temperature on the breakage strength of agglomerates in streams of hot air.

Run No.	Air Velocity (m/s)	Weight (Kg)x10^3	Temperature (^oC)	Critical Drag Force, σ_{OS} (Kg/m^2)
A-1	6.82	0.941	165	0.641
A-2	8.99	0.779	160	1.075
A-3	9.68	0.820	161	0.979
A-4	10.46	0.877	160	1.075
A-5	11.16	0.486	156	1.494
A-6	11.97	1.181	149	2.404
A-7	5.31	1.120	167	0.510
B-1	6.82	0.860	156	1.002
B-2	8.99	0.760	155	1.102
B-3	9.68	0.977	152	1.425
B-4	10.46	0.659	146	2.219
B-5	11.16	1.099	148	1.935
B-6	10.46	1.159	153	1.313

A. Agglomerate polypropylene particles produced at 164^oC.

B. Agglomerate polypropylene particles produced at 160^oC.

$$\sigma_s = \frac{\epsilon}{1-\epsilon} \frac{1}{\pi} \left(\frac{D_p}{b}\right)^2 \sigma_{OS} \qquad (3.29)$$

and values so calculated were used in the model instead of using the van der Waals estimation for the strength of the polypropylene agglomerates. Figure 3.7 shows the comparison between experiment and theory, for a slugging bed ($d_b = d_B$) and a neck radius, b, taken as 3.5 percent of the average particle diameter. This value gave the best agreement with the experimental data.

Comparison with other experimental data

Figure 3.8 shows a comparison of the theoretical and experimental data from all of the works discussed above. The dimensionless excess velocity $(U_s-u_{mf})/u_{mf}$ is plotted here as a function of the temperature difference $(T-T_s)/T_s$. As seen in the figure the dependency of U_s-u_{mf} with temperature is similar in all cases but appears to depend on, at least, one more parameter. Inspecting Eq. (3.24) the most likely additional parameter is the granule size, D_p. In Figure 3.9, the same data were replotted against the quantity $[T - T_s)/T_s]\cdot(D_p/d_B)^{-3/2}$ and as seen the fit between the different data is much better, especially at the higher temperatures. At low temperatures one cannot expect an empirical relationship of the form given by Eq. (3.23) to be valid whereas the computed curves based on Eq. (3.24) appear to show the correct trend.

3.4 MEASUREMENT OF SURFACE VISCOSITIES USING A DILATOMETER

Procedure and apparatus

Heating a packed bed of small solid particles (granules) to high temperatures is sometimes accompanied by surface softening and subsequent deformation. Assuming that the softened material on the surface behaves as a Newtonian fluid, a so-called surface

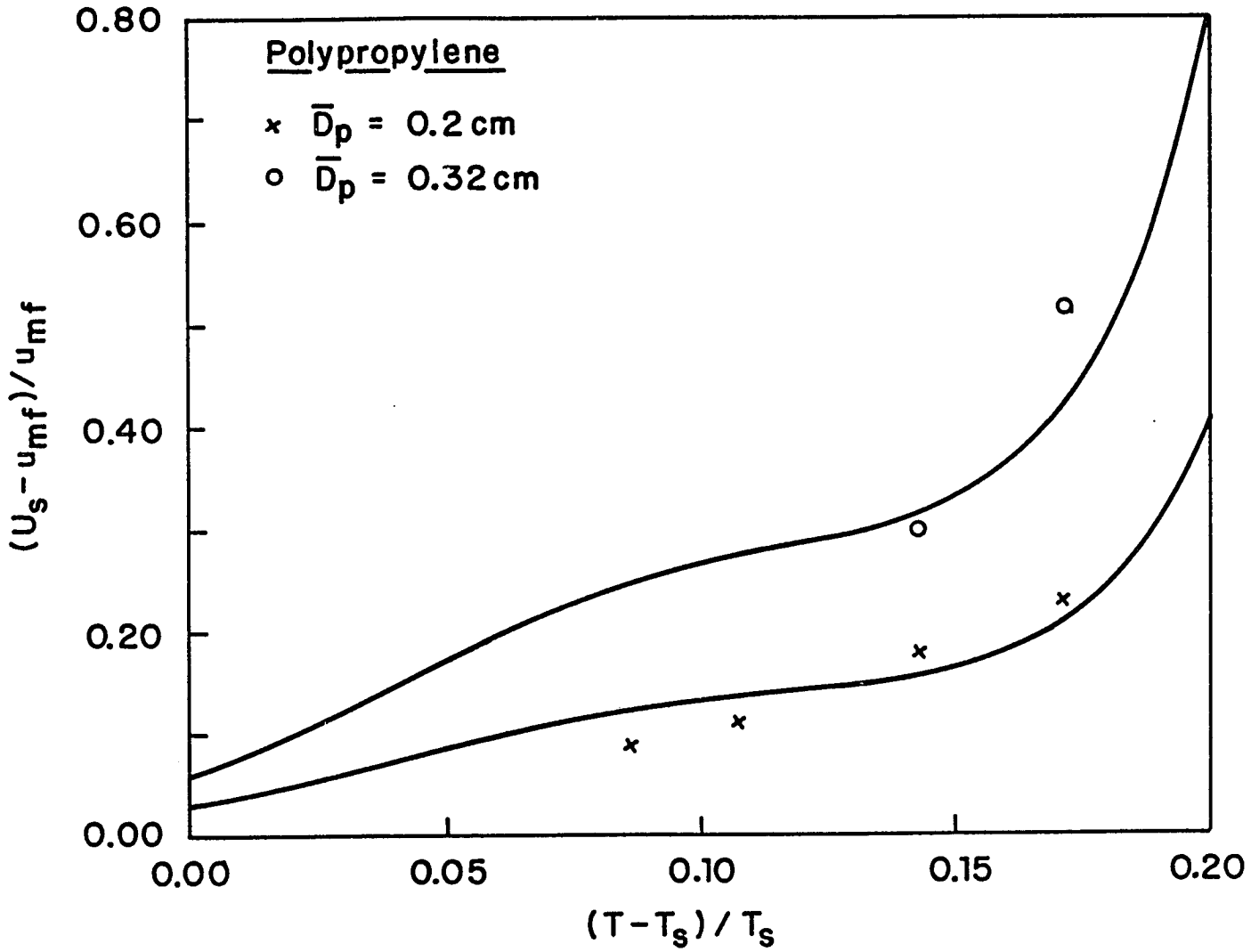

Figure 3.7 Dimensionless excess fluidization velocity vs. dimensionless temperature for polypropylene.

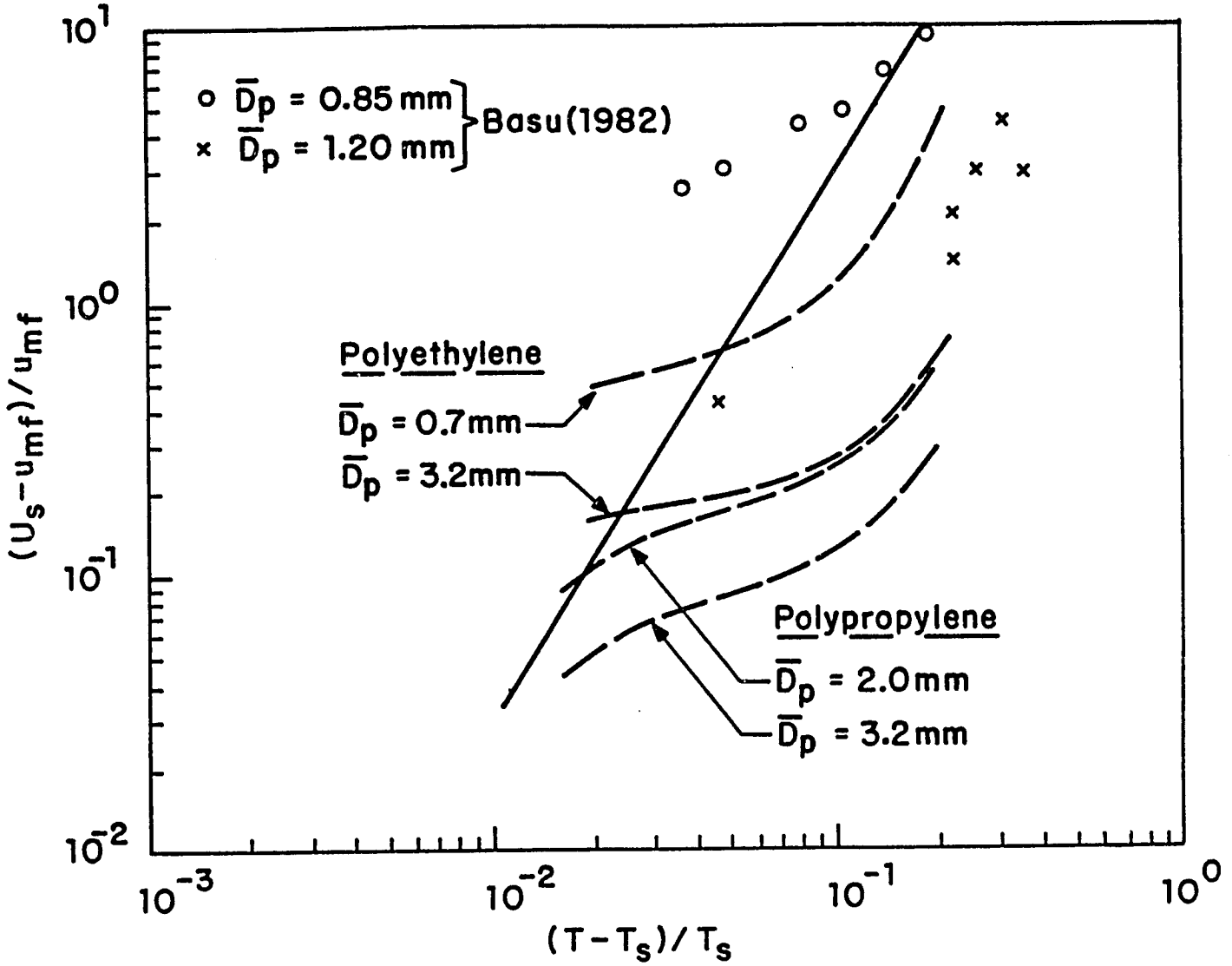

Figure 3.8. Comparison of theoretical and experimental results.

——— Correlation of Liss et al. (1983) of data by Siegell (1976)

— — — PRESENT WORK

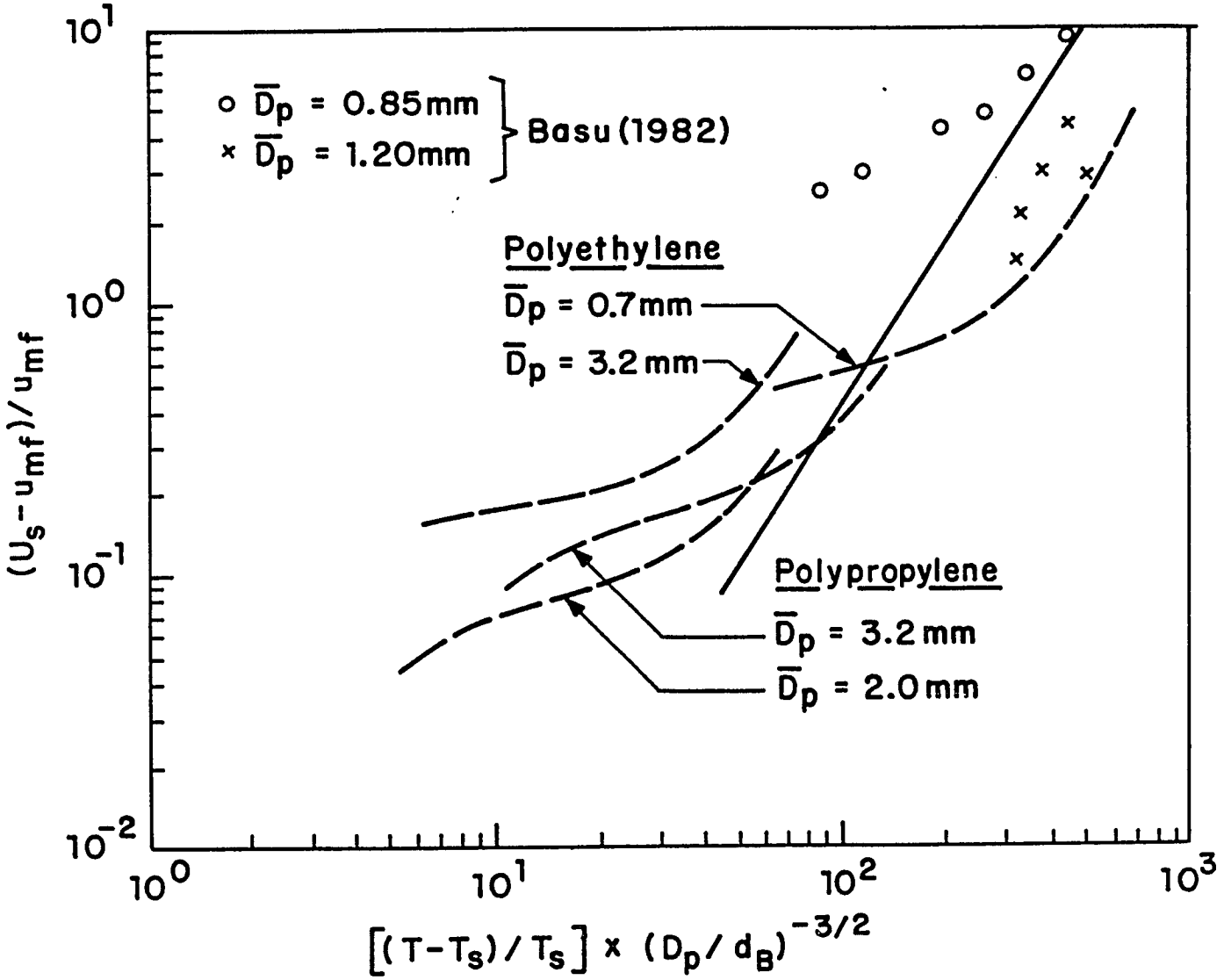

Figure 3.9. Comparison of experimental data and theoretical calculations using a modified temperature scale.

——— Correlation of Liss et al. (1983) of data by Siegell (1976)

– – – PRESENT WORK

viscosity can be defined and, postulating a mode of surface deformation under a given shear field, the surface viscosity, η_s, can be measured. The measuring procedure for the viscosity is based on the compaction (contraction) of a porous rod made of the granules in question while it is subjected to a compression load and heated at a certain rate.

A porous rod made out of individual granules behaves differently while heated than a similar compact rod of the same material. The porous rod will initially dilate as the temperature increases, but will subsequently contract due to the viscous flow and/or sintering which occurs at the intergranular contact points. This behavior is due to the softening, flattening and/or flow of the granule's surface at the point where compacting forces are concentrated. This property of porous materials was used earlier by Gluckman et al. (1976) and Siegell (1976) to measure sintering temperatures of copper shot and fly ash particles.

In order to perform the measurements, a Theta Industries-Econo I dilatometer (Theta Industries, Inc., Port Washington, N.Y. 11050) is used. This instrument enables one to measure the deformation (magnification up to 10^5) and the deformation rate of a material sample compressed by a certain load (up to 0.5 kg). The material sample, which can be of maximum diameter of 2 cm and length of up to 5 cm can be heated or cooled at any rate up to $15^{\circ}C$/min in a quartz glass holder situated in an electric heater capable of heating the probe up to $1200^{\circ}C$.

The instrument can be used to measure elongations (or contractions) of the sample while the temperature is increased, decreased, or held constant. It can also be used to measure elongation and deformation rates of the sample while under a constant load at constant temperature. The sample holder is constructed in such a way that granular material of particle size down to about 0.05 mm in diameter can be poured into it and, by using a quartz piston, one can measure elongations of the porous material. There is also a special holder made out of a quartz tube of 4 mm in diameter with a spherical quartz sphere as a

piston to measure the deformation of a chain of large particles, between 1 mm to 3 mm (see Figure 3.10). The instrument can be operated in a horizontal as well as in a vertical position. This arrangement enables one to apply any force on the particles by an appropriate arrangement of weights in the apparatus. The temperature in the furnace is electronically controlled, while the temperature of the probe is measured directly with a thermocouple dipped into the sample holder. The dilatometer was connected to a MINC 11 minicomputer so that contraction versus time data could be stored and displayed in graphical format. The computer program used was CONTIM and is listed in Appendix A.3. In order to diminish the effect of radial temperature gradients in the sample holder, and because of the low conductivity of the materials used, the rate of temperature increase is held low (usually below 5^{o}C/min). This imposes a restriction on the rate at which dilatometer data can be obtained.

Theoretical considerations

For the case of coarse particles which can be arranged in a linear (chain-like) manner in the dilatometer, simple geometric considerations (see Figure 3.11) yield a unique relationship between the contraction of the sample $\Delta\ell/\ell_0$ and the radius of the flattened contact points, b:

$$\Delta\ell/\ell_0 = 2a/D_p = 1 - \{1 - (2b/D_p)^2\}^{1/2} \qquad (3.30)$$

where D_p is the granule diameter and a is the distance over which flattening has occurred. For the case of small particles arranged randomly within the sample, a similar simple relationship exists:

$$\Delta\ell/\ell_0 = (2/3\beta)[1 - \{1 - (2b/D_p)^2\}^{1/2}] \qquad (3.31)$$

where β is the so-called layer spacing (Dullien, 1979) and is given as a function of the porosity, ϵ, of the sample as:

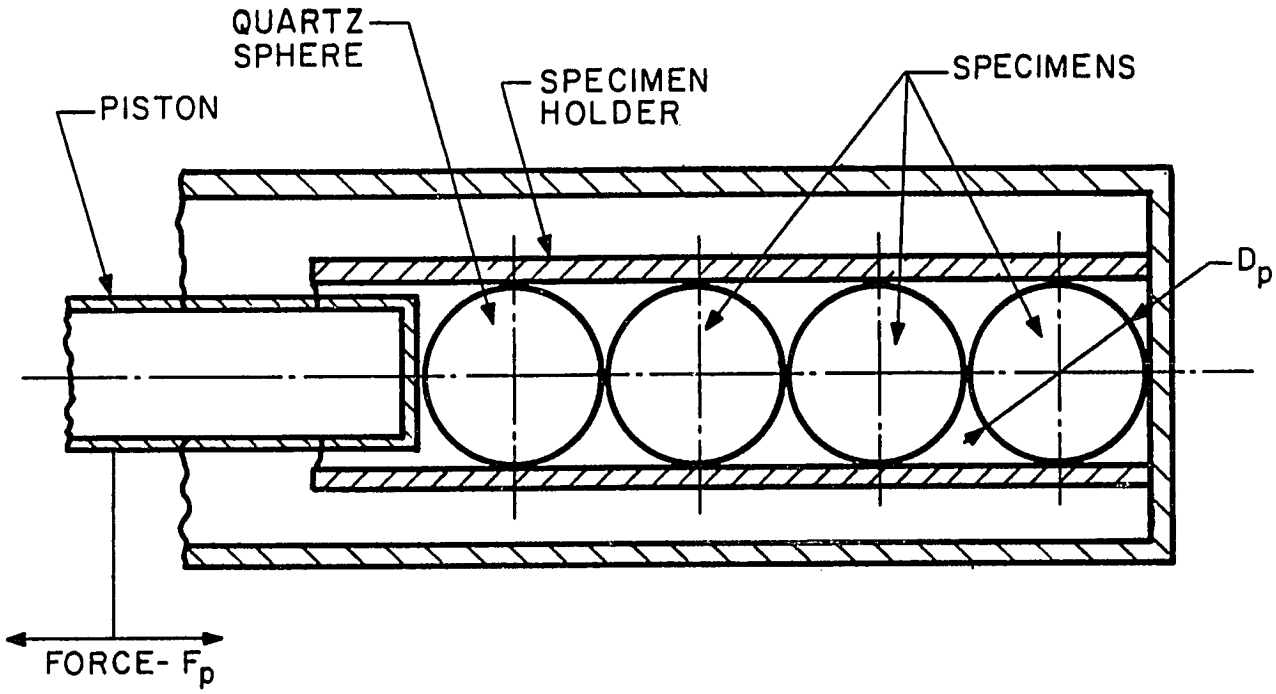

Figure 3.10. Schematic of Large Size Particle Holder.

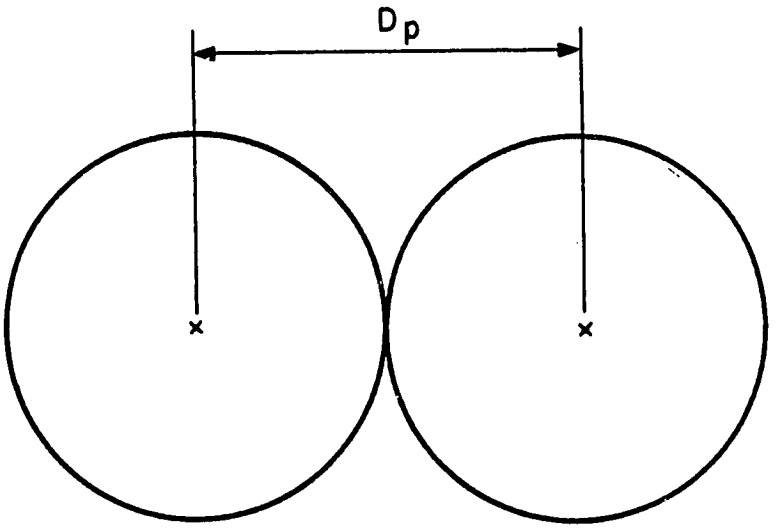

BEFORE COMPACTION

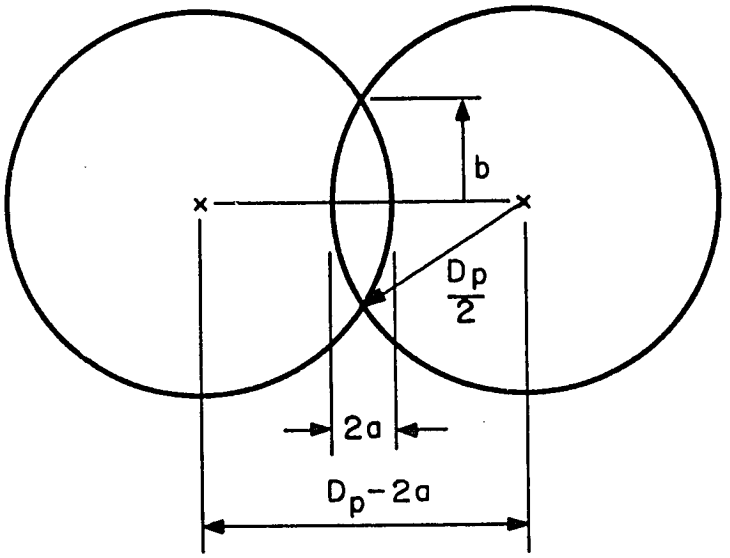

AFTER COMPACTION

Figure 3.11. Compaction of a Chain-Like Aggregate.

$$\beta = \sqrt{2/3}\,[\pi/3\sqrt{2}(1 - \epsilon)]^{1/3} \qquad (3.32)$$

Usually the contraction (dilation) of the sample $\Delta\ell$ is small as compared to its initial length ℓ_0 and therefore Equations (3.30) and (3.31) can be simplified accordingly to read:

$$b/D_p \cong [f\Delta\ell/2\ell_0]^{1/2} \qquad (3.33)$$

where the coefficient $f = 1$ for large size particles if they are situated on top of each other in a linear arrangement, and $f = 3\beta/2$ for a random arrangement of small particles forming a porous mass; Equation (3.33) enables one to obtain (approximately) the size b (or its growth rate) of the sinter (flattened) neck between two particles from a simple reading of the dilatometer.

The relationship between the size of the neck b and the surface viscosity η_s, was shown by Rumpf (1977) to be:

$$(b/D_p)^2 = [4\gamma_s/5D_p + 2(F_v + F_p)/5\pi D_p^2](t/\eta_s) \qquad (3.34)$$

if sintering and the action of surface tension γ, is taken into account, whereas it is given by:

$$(b/D_p)^3 = [3(F_v + F_p)/32D_p^2]\ (t/\eta_s) \qquad (3.35)$$

if viscoelastic flattening is the governing mechanism of shrinkage. In Equations (3.34) and (3.35), F_v is the van der Waals force and t is the time of contact during which the interparticle compression force F_p is applied (see Figure 3.10). Neglecting the compression produced on the particles by the surface tension and also the van der Waals force, F_v with respect to the force F_p, the general relationship between the size of the sinter neck b, the compression force F_p, the time t and the viscosity η, becomes:

$$b/D_p = [KF_p t/D_p^2\eta_s]^n \qquad (3.36)$$

where K is a numerical constant. Inserting Equation (3.33) into Equation (3.36) and taking the derivative with respect to t^n one obtains:

$$\partial(f\Delta\ell/2\ell_0)^{0.5}/\partial(t^n) = [K\ F_p/\eta_s D_p^2]^n \qquad (3.37)$$

Solving for the viscosity η_s one obtains from the above equation:

$$\eta_s = KF_p D_p^{-2}/[\partial(f\Delta\ell/2\ell_0)^{0.5}/\partial(t^n)]^{1/n} \qquad (3.38)$$

If the coefficient n takes the value 0.5, then Equation (3.38) reduces to:

$$\eta_s = KF_p D_p^{-2}/[\partial(f\Delta\ell/2\ell_0)/\partial t] \qquad (3.39)$$

where the denominator is simply the slope of the deformation versus time and the constant $K = 2/5\pi$.

The procedure to measure surface viscosity from the dilatometer data (measured values of $\Delta\ell$ versus time) suggests itself from Equations (3.36) and (3.38). A porous sample of initial length ℓ_0 and granule size D_p is heated at a certain rate and compressed by a known force F_p while the contraction $\Delta\ell$ is measured as a function of time t. On a log plot the deformation $\Delta\ell$ versus time t will yield the coefficient n as the slope of the obtained curve (line). Then the slope of the deformation $\Delta\ell$ versus time raised to the power n yields the surface viscosity η_s, through Equation (3.38). The coefficient n is expected to take values between 1/3 to 1/2 based on Equations (3.34) and (3.35). The assumption in applying Equations (3.34), (3.35) and (3.38) is that the size of the neck b is small as compared to the size of the particles D_p and, therefore, it is important that the coefficient n be determined from $\Delta\ell$ versus t measurements at small times. The dependence of the surface viscosity η_s, on the temperature T is thus obtained through two parameters, the interparticle compression force F_p and the particle size D_p, or

rather their ratio F_p/D_p^2 and the rate of deformation (contraction) versus time.

For the special case when the sample in the dilatometer is a finely divided powder, i.e., the granule size of the material under testing is much smaller than the diameter of the sample holder, D_s, the interparticle compression force, F_p, is no longer equal to the load on the sample as depicted in Figure 3.10. In this case the values of the force F_p to be used in Equation (3.38) or (3.39) can be computed using the relation (Rumpf, 1977):

$$F_p = 4\epsilon D_p^2 L/\pi(1 - \epsilon)D_s^2 \qquad (3.40)$$

where L is the load on the sample.

Results and discussion

Actual elongation data $(f\Delta\ell/2\ell)^{1/2}$ versus time of deformation, for polyethylene granules of $D_p = 0.07$ cm at a temperature of $T = 116^oC$ as obtained from the dilatometer, are given in Figure 3.12 on a log plot. The experiments were performed by applying different loads, L, to the sample at values between 10 to 30g. As seen, the results are approximately straight lines of slopes varying between 0.42 and 0.50 as expected. At high values of the compression force there is a slight change in the slope at large times (above 150 s) due to excessive increase of the contact zone, b, between particles. Figure 3.13 shows the slopes of deformation versus time for different loads, L, on the sample at the same temperature of $T = 116^oC$. From these slopes the viscosity η_s, was computed using Equations (3.39) and (3.40).

The same procedure, as outlined above, was used at several different temperatures to obtain viscosity, η_s, versus temperature data in the range between $T = 90^oC$ up to the melting point of the material, T_m, for polyethylene and polypropylene granules and the results are presented in Figure 3.14. As seen, both materials have a very high viscosity (around 10^{11} Pa·s) at low

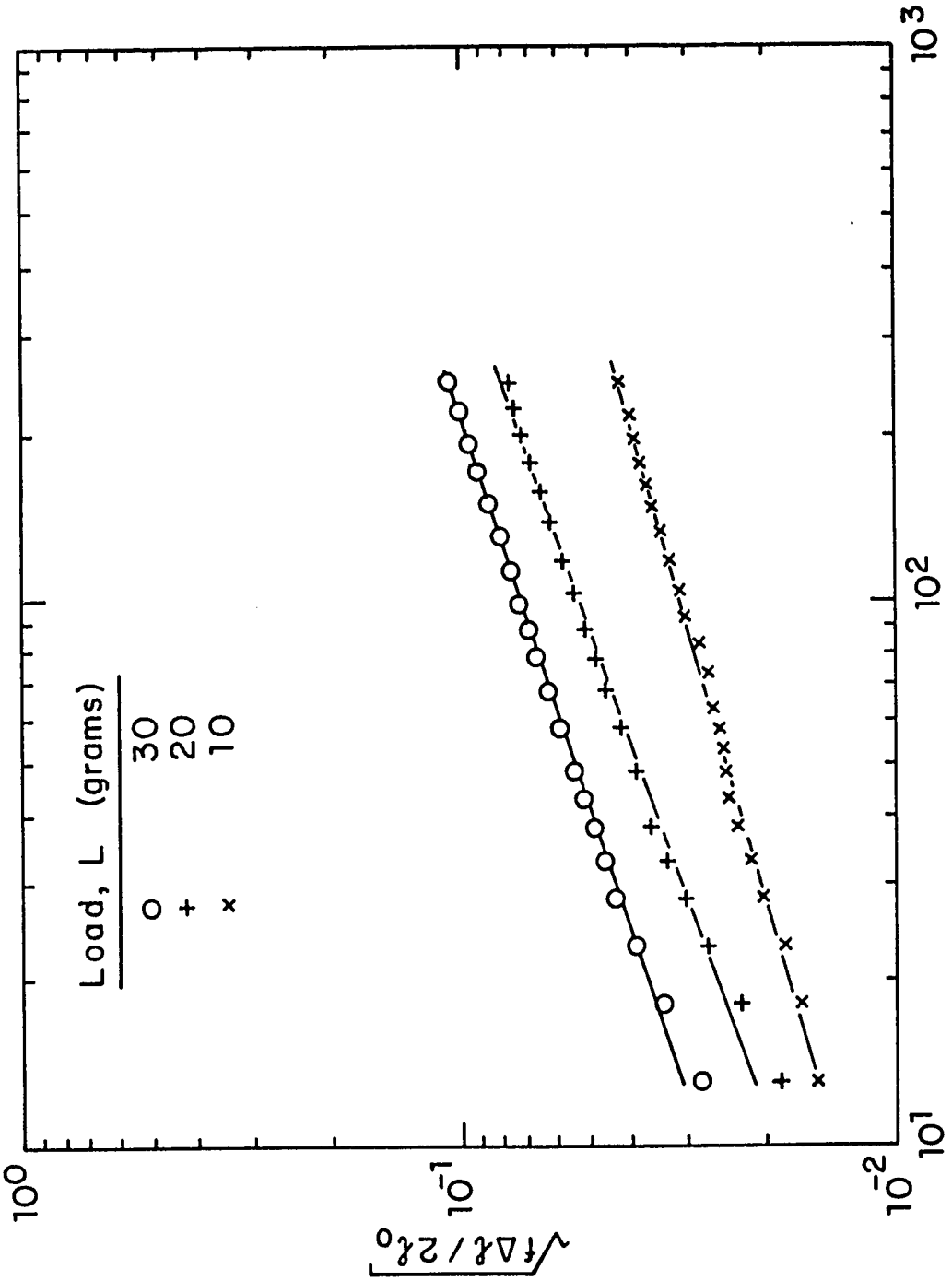

Figure 3.12. Contraction raised to the one-half power vs. time for polyethylene at a temperature of 116°C (D_p = 0.07 cm. f = 1.314) with L as a parameter.

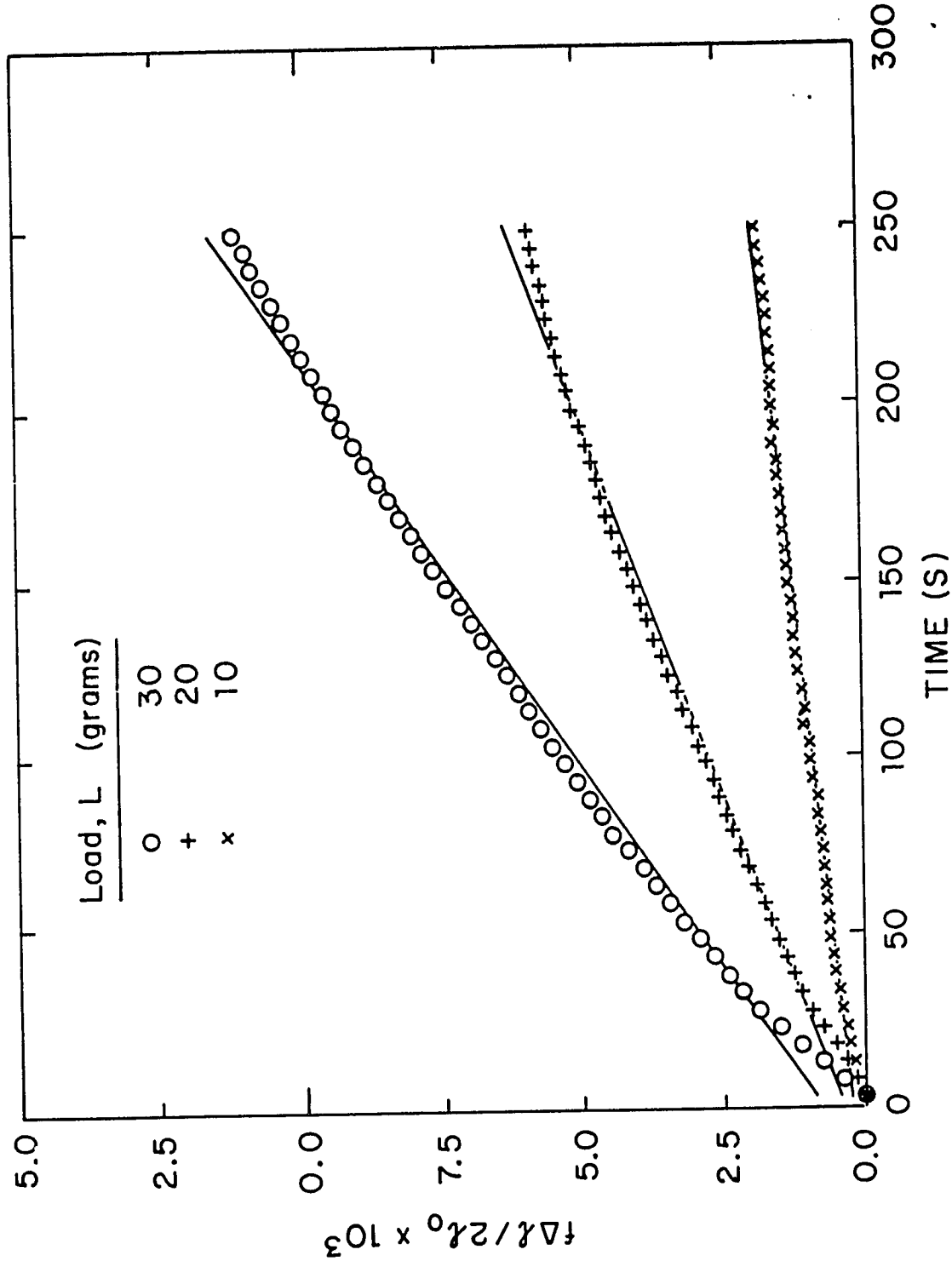

Figure 3.13. Contraction vs. time for polyethylene at a temperature of 116°C (D_p = 0.07 cm, f = 1.314) with L as a parameter.

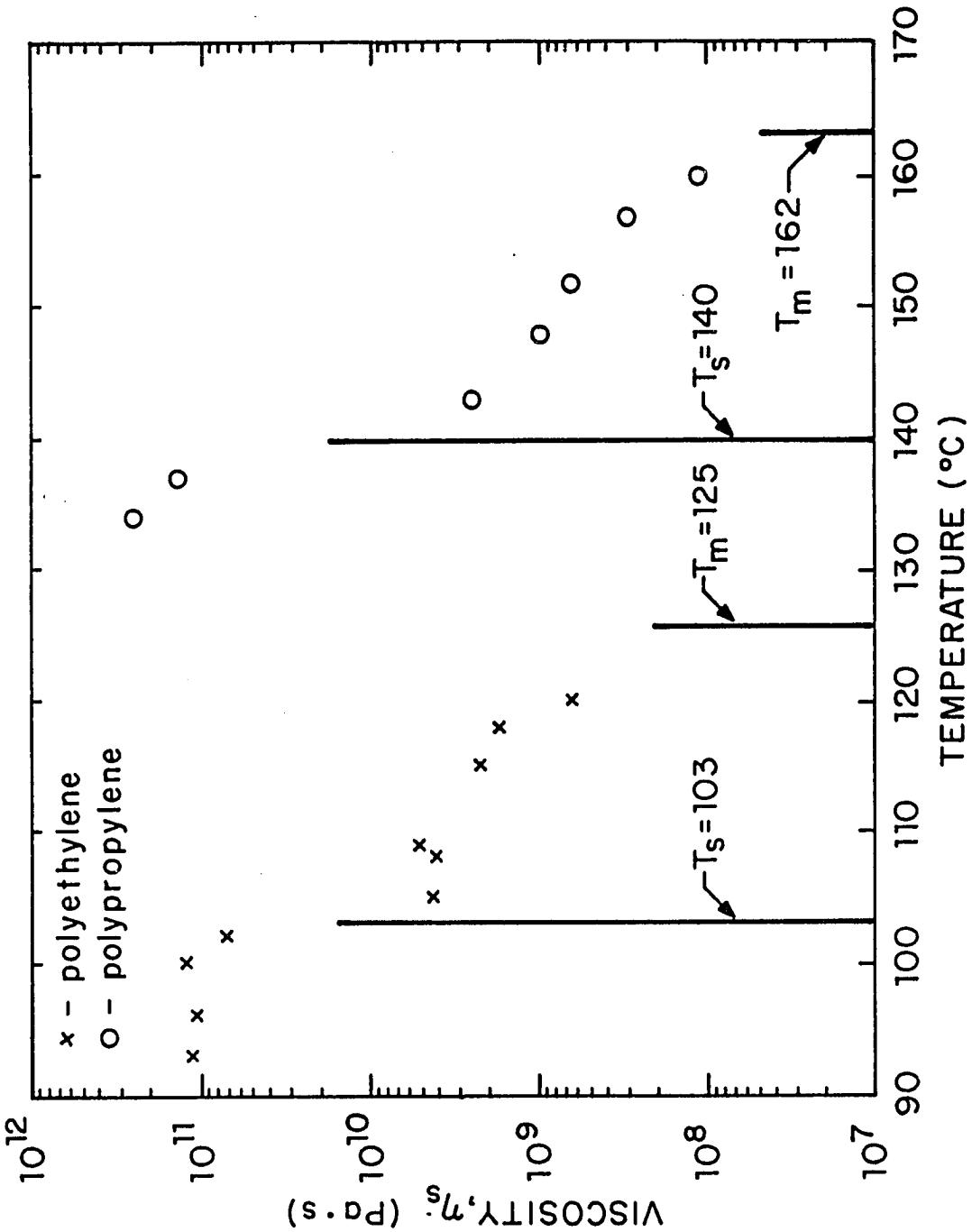

FIGURE 3.14 VISCOSITY VS. TEMPERATURE FOR TWO TYPES OF POLYMERS.

temperatures and this value does not change significantly as the temperature is increased from room temperature. At a given temperature, characteristic of each material, the viscosity drops sharply, about two orders of magnitude, indicating a surface softening: this is the so-called minimum sintering temperature T_s, and is the point where surface stickiness first appears. There is a subsequent gradual decrease in viscosity (see Figure 3.14) as the temperature is further increased and a last sharp drop as the melting temperature T_m is reached. Thus, the importance of having surface viscosity data versus temperature is evident since the minimum sintering temperature can be determined at the point where a sharp drop in viscosity occurs. Furthermore, the deformation (flow) of the particle surface above this temperature while under a certain load can also be predicted. This behavior is important when these same particles are being fluidized or compressed at high temperatures.

Additional surface viscosity measurements were performed on coal and glass particles (powders). A typical example of surface viscosity versus temperature for small glass beads (D_p = 0.07 cm) is presented in Figure 3.15. The glass behaves somewhat differently than the polymers in that the viscosity decreases continually as the temperature is increased. The relative sharp drop around 560°C indicates the minimum sintering temperature of the glass.

3.5 MINIMUM SINTERING TEMPERATURES OF FLUIDIZABLE PARTICLES

Introduction

When fluidization of small particles takes place at high temperatures, the softening and/or partial melting of the solid's surface often requires higher gas velocities to keep the bed in the fluidized state. This behavior is due to the fact that energy imparted to the particles by the fluidizing gas has to overcome not only the weight of the bed but also particle-particle interaction forces due to surface stickiness. These

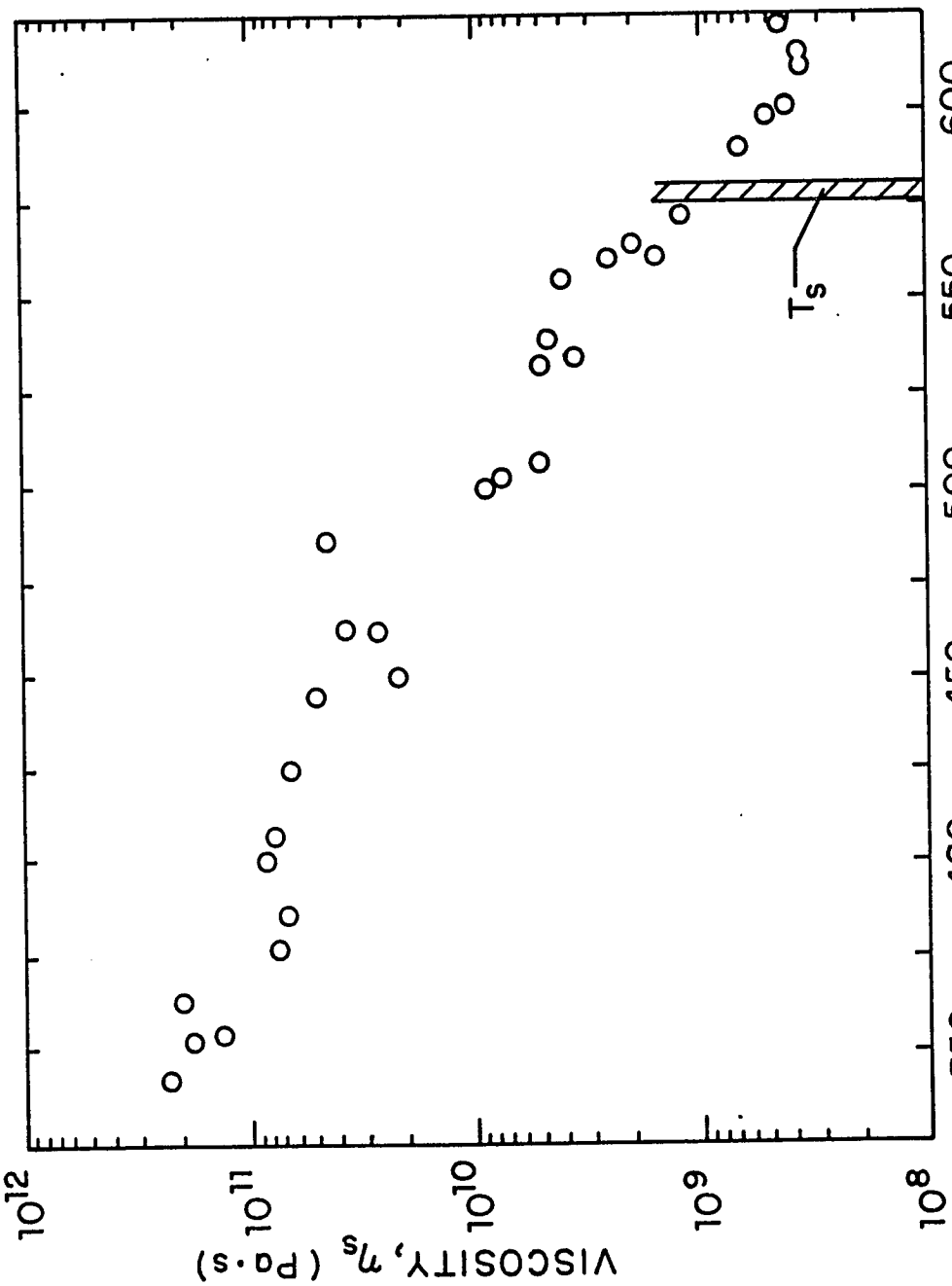

Figure 3.15. Surface viscosity vs. temperature for glass particles.

interaction forces which are cohesive in nature become significant above a certain temperature level. The existence of this characteristic temperature level was clearly demonstrated by recent research in high temperature fluidization (Gluckman et al (1975), Siegell (1976), Tardos et al. (1984), Basu (1982), Basu and Sarkà (1983) and Liss et al. (1983)), where it was shown that above the so-called minimum sintering temperature, T_s, fluidization of a given granular material (powder) is accompanied by agglomeration. This temperature is determined at the point where a large drop in granule surface viscosity occurs (Tardos et al., 1984) as was demonstrated in the previous section and is consistent with the observation that at or above this temperature, stickiness and surface deformation of the granules becomes apparent.

The purpose of the work presented in this section was to develop a comprehensive method to measure the minimum sintering temperature for different materials. An obvious way to determine this temperature is to perform fluidization-defluidization experiments in a pilot fluidized bed using the granules in question and to correlate the minimum fluidization velocity as a function of temperature. At the point where permanent agglomerates form and/or the minimum fluidization velocity no longer corresponds to the values calculated from the well known relation (Kunii and Levenspiel, 1969):

$$Ga = 150(1 - \epsilon_{mf}) \frac{Re_{mf}}{\phi^2 \epsilon_{mf}^3} + \frac{1.75}{\phi \epsilon_{mf}^3} Re_{mf}^2 \qquad (3.41)$$

the minimum sintering temperature is obtained. The following notations were used in Eq. (3.41): ϵ_{mf}, is the void fraction of minimum fluidization, ϕ is the shape factor and the Gallileo and Reynolds numbers were defined as:

$$Ga = \rho_g(\rho_s - \rho_g)D_p^3 g/\mu \qquad (3.42)$$

$$Re_{mf} = \rho_g u_{mf} D_p/\mu \qquad (3.43)$$

The drawback of the procedure described above is that it requires the use of a well instrumented pilot fluidized and, in addition, a large number of time consuming tests at different temperatures have to be performed.

During the present work, other simpler and more direct methods to measure minimum sintering temperatures are presented which do not require a fluidization-defluidization experiment to be performed on the granules. Some of the methods are based on the fact that at the point of sintering the granule's solid surface deforms and a surface viscosity can be defined and/or a contraction can be measured. Others are based on a thermal analysis (heat absorption versus temperature) and still others are based on mechanical strength testing. The development of such methods is important since a knowledge of the minimum sintering temperature enables one to properly design a fluidized bed which operates at high temperatures; special precautions to avoid agglomeration are only necessary if the bed temperature exceeds the minimum sintering temperature.

Polymers

The method to determine surface viscosity of granular material at different temperatures using a dilatometer is described in detail in the previous section. Typical results for surface viscosity versus temperature for polyethylene and polypropylene particles of different sizes are given in Figure 3.14. It is evident that at a certain temperature (T_s = 105°C for polyethylene and T_s = 142°C for polypropylene) there is a drastic reduction in viscosity. The viscosity of 10^{11} Pa•s can be regarded as "infinitely" high corresponding to a "solid" while viscosities of the order of 10^8-10^9 Pa•s are characteristic of a very viscous fluid. More important (see Figure 3.14) is the apparent sharp drop in viscosity of about two orders of magnitude at a given temperature, which indicate a softening of the surface. Since the measurement of surface viscosity is rather involved and time consuming (Tardos et al., 1984) a more direct

method for measuring the minimum sintering temperature was devised: a contraction-dilation versus temperature curve for a porous rod composed of the granular material in question and compressed by a certain load was recorded using a dilatometer. The dilatometer was interfaced to a MINC 11 minicomputer so that data could be stored and displayed graphically (the computer program used was CONTEM and is listed in Appendix A.3). Similar curves for copper shot and coal ash were obtained earlier by Siegell (1976) but this was not followed by a thorough analysis of the results.

The general shape of the dilation-contraction curves was the same for all materials studied (see Figure 3.16A). As the temperature is raised from ambient the sample exhibits thermal expansion; the thermal expansion can be determined using this initial part of the test. At some higher temperature the sample no longer increases in size and a plateau is reached where the sample remains at a constant length. Here, the effects of surface deformation (contraction) balances the effects of thermal expansion. At a slightly higher temperature the sample begins to contract rapidly due to a greatly increased rate of surface deformation (sintering) at the intergranular contact points. The temperature at which the sample starts to shrink (contraction predominates over thermal expansion) is considered to be the minimum sintering temperature, T_s.

Elongation vs. temperature was measured for polypropylene particles (average particle diameter D_p = 0.32 cm) under a compression load L, on the sample of 38g. Two methods of heating were used; in the first run (Figure 3.16A) a $1^{o}C$/min temperature increase was maintained up to the softening temperature which was found to be $141.7^{o}C$. The second sample was heated at $5^{o}C$/min from 25 to $100^{o}C$ and then at $1^{o}C$/min from $100^{o}C$ on (Figure 3.16B); the measured softening temperature was $141.5^{o}C$ showing the reproducibility of the results.

Additional elongation vs. temperature experiments were performed with polyethylene particles (D_p = 0.32 cm) at a heating rate of $2^{o}C$/min under two different loads, L (see Figure 3.17).

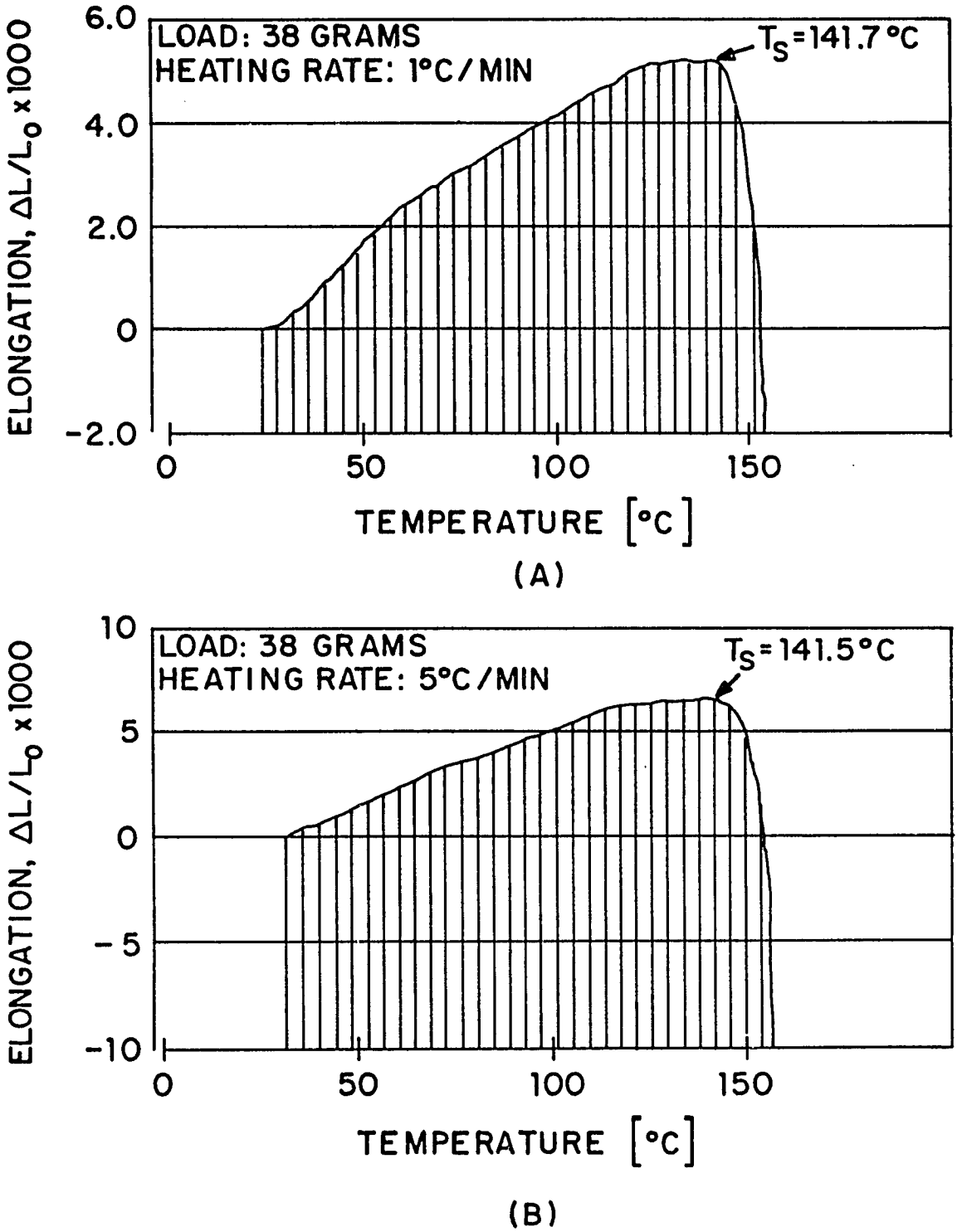

Figure 3.16. Minimum Sintering Temperature for Polypropylene Particles.

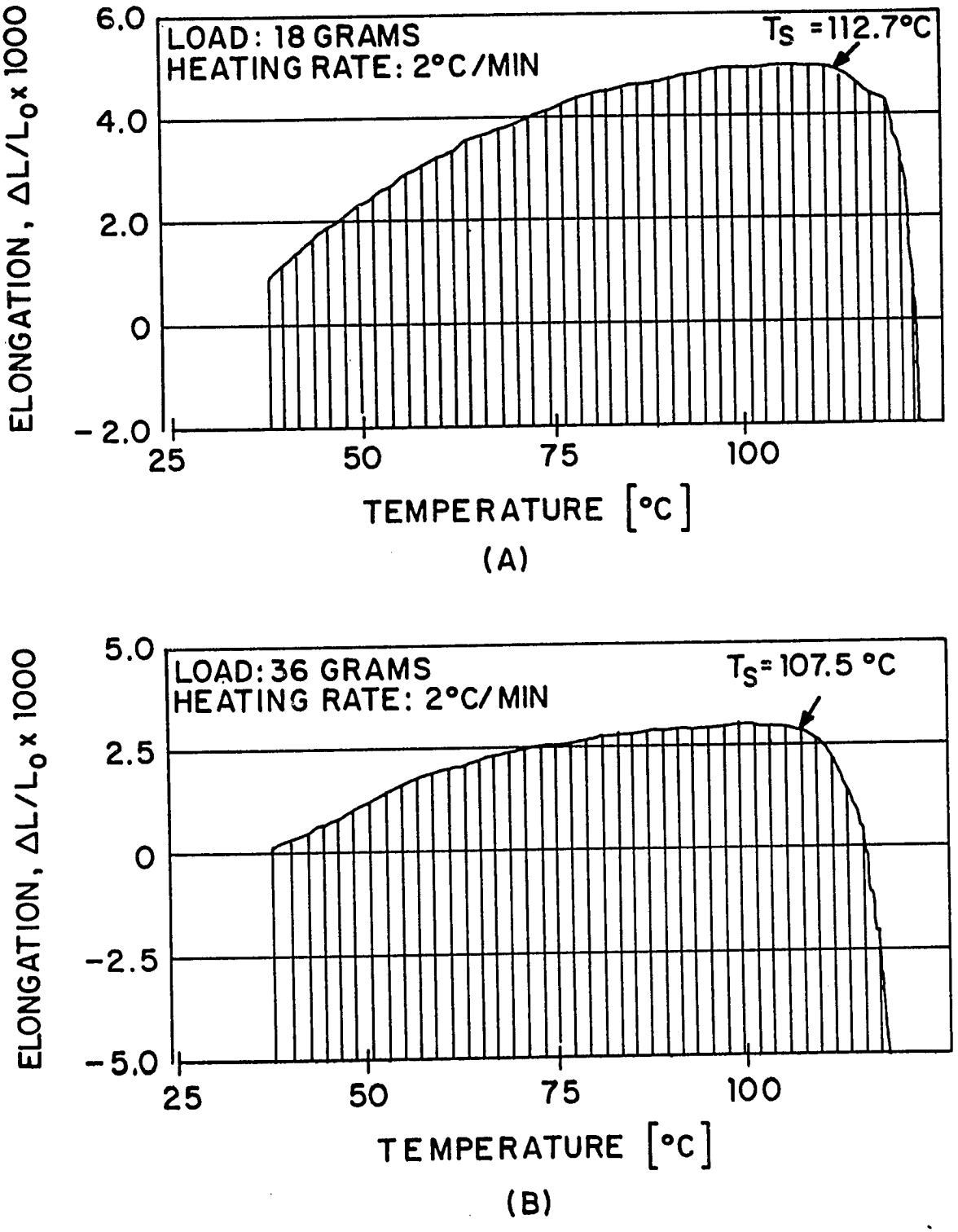

Figure 3.17. Minimum Sintering Temperature for Polyethylene Particles.

At a load L = 18g the softening temperature was found to be 112.7°C (Figure 3.17A) while at a load of L = 36g (doubling the intergranular pressure) the minimum sintering temperature was found to be somewhat lower, T_s = 107°C (Figure 3.17B). Both sintering temperatures for the two polymers are close to those determined from viscosity measurements (see Figure 3.14).

To further confirm that the minimum sintering temperature T_s is a well defined property of the material, a set of yield strength tests were performed on the same polypropylene particles by Sekiguchi and Tohata (1982) using the instrument schematically shown in Figure 3.18. This instrument is capable of measuring interparticle forces at any given temperature on chains of (agglomerated) particles. The results of the test indicate that the material does not behave as a solid (does not exhibit tensile strength) at temperatures close to and above the minimum sintering temperature, T_s. It is appropriate therefore to determine this temperature either from viscosity measurements or from contraction versus temperature data.

Additional experiments using the dilatometer were performed on polyester, a high melting temperature polymer. A typical elongation-contraction diagram is shown in Figure 3.19A. The polymer shows a drastic contraction at around 120°C and another contraction between 252 and 260°C. One would assume that sintering occurs at the first contraction of 120°C but this is not the case; a second reheating of the initial granules shows only a contraction at around 257°C, as seen in Figure 3.19B, demonstrating that 120°C is only a point of crystalline rearrangement but not a point of surface softening (sintering).

Glass

Dilatometer and surface viscosity experiments were performed on glass samples in order to determine sintering characteristics of this material. Figure 3.15 shows surface viscosities versus temperature for a glass powder in the size range from 20 to 30 mesh over the temperature range of 325 to 625°C. As seen in the

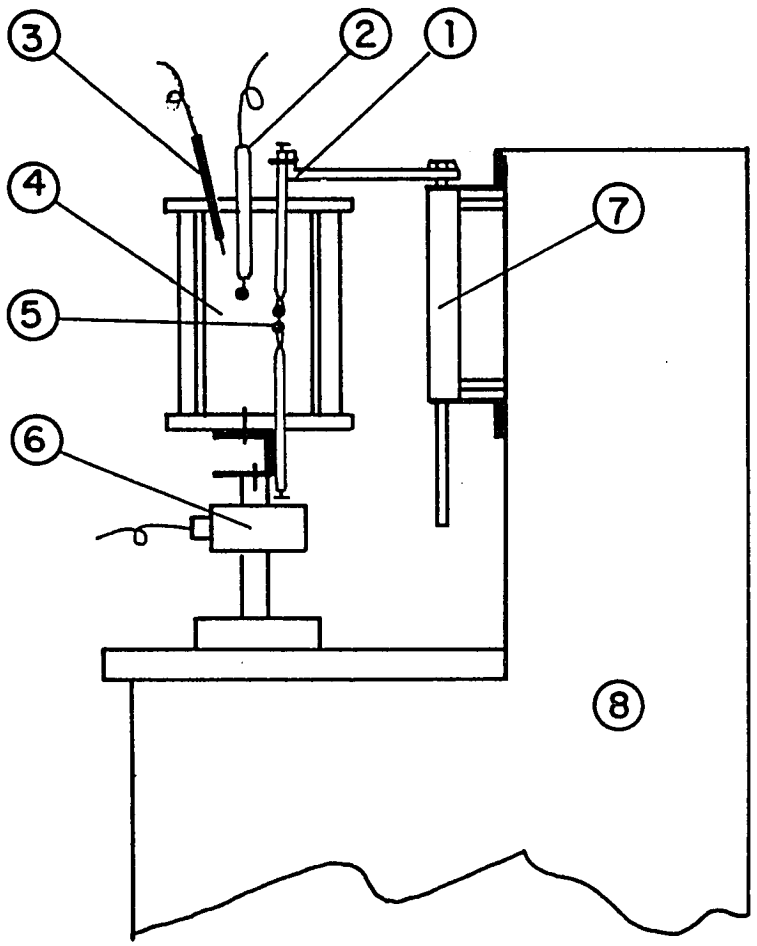

1. TEST PIECE HOLDER
2. THERMOCOUPLE
3. THERMOMETER
4. HEATING BOX.
5. POLYPROPYLENE PARTICLES
6. LOAD CELL
7. OIL HYDRAULIC CYLINDER
8. OIL HYDRAULIC SYSTEM

Figure 3.18. Schematic diagram of Interparticle Force Testing Equipment.

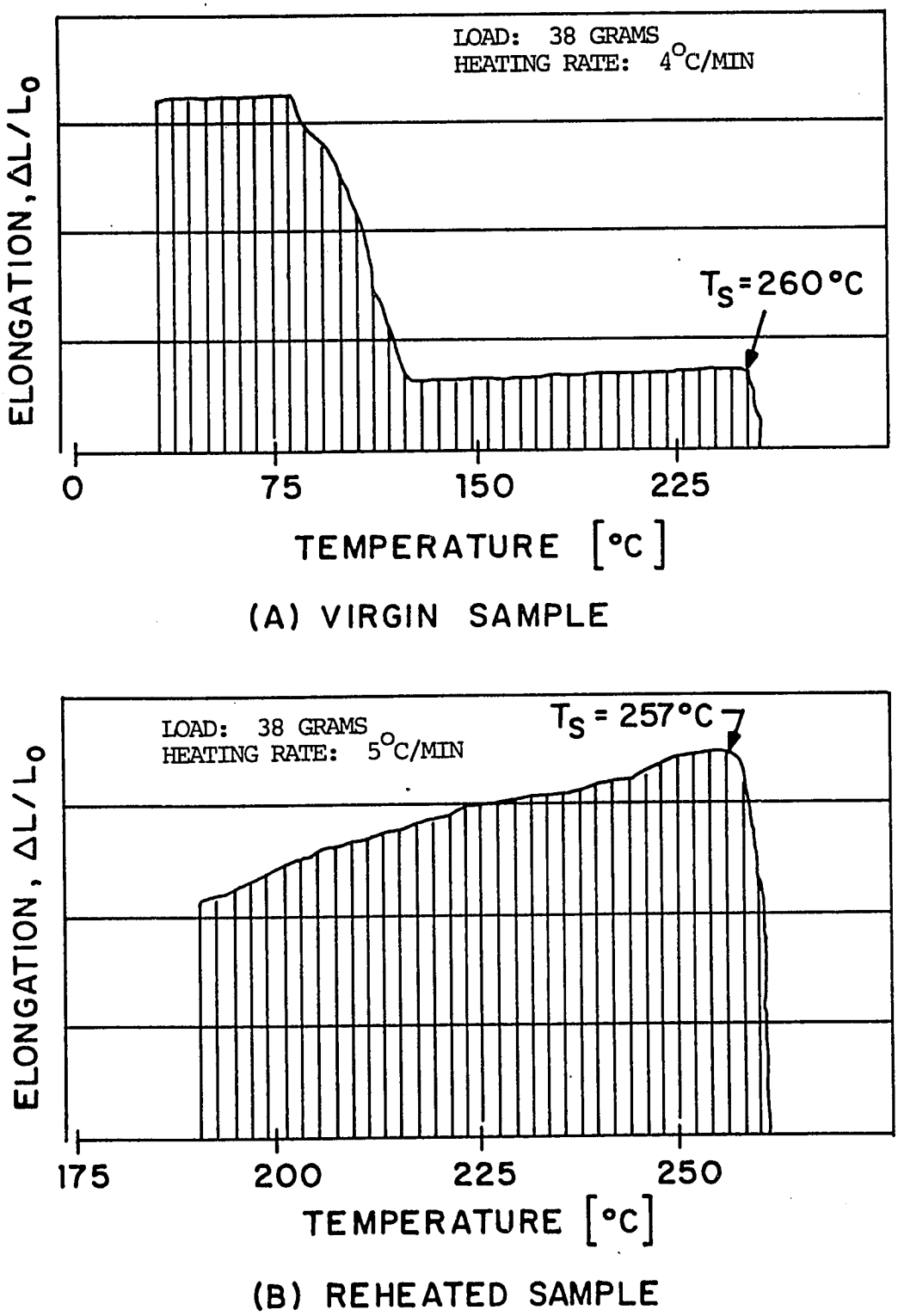

Figure 3.19. Elongation-Contraction vs. Temperature for Polyester Particles.

figure the viscosity decreases three orders of magnitude over a 300°C temperature range but there is no sudden change in the viscosity clearly visible from the data. It is, therefore, difficult to determine sintering temperatures from this test.

Dilation-contraction measurements versus temperature for the same material are presented in Figure 3.20. It is clear from this figure that dilation is counter-balanced by contraction at around 420°C and that sintering occurs at 577°C where the rate of contraction versus temperature is very high and where the minimum sintering temperature, T_s, is defined.

A series of experiments were performed to study the influence of the applied load on the sample, of the intergranular compression force, F_p, and of the particle size on the minimum sintering temperature. The intergranular compression force F_p which is the actual surface force between two contacting granules in the sample is related to the total load, L, on the sample through the well-known Rumpf equation given in the last section (Rumpf, 1977):

$$F_p = 4\epsilon D_p^2 L/\pi(1-\epsilon)D_s^2 \qquad (3.40)$$

For large granules where the diameter of the particles is close to the diameter of the sample ($D_p = D_s$) the above equation is not applicable since, in this case, the force L is readily applied to a chain of large granules and, therefore, one can take the interparticle compression F_p to be $F_p = L$ (Tardos et al. (1984)). The experiments were performed using different sizes of glass particles from 50 to 400μm combined with different loads, L, between 20 and 220 g so as to obtain constant intergranular compressions F_p as computed through Eq. (3.40). The results, minimum sintering temperature vs. particle size for two values of the force F_p are given in Figure 3.21A. As seen, the influence of particle size is not very pronounced although the sintering temperature seems to increase somewhat with particle size at constant compression F_p. The complimentary result of variation of sintering temperature T_s vs. the intergranular force F_p (see

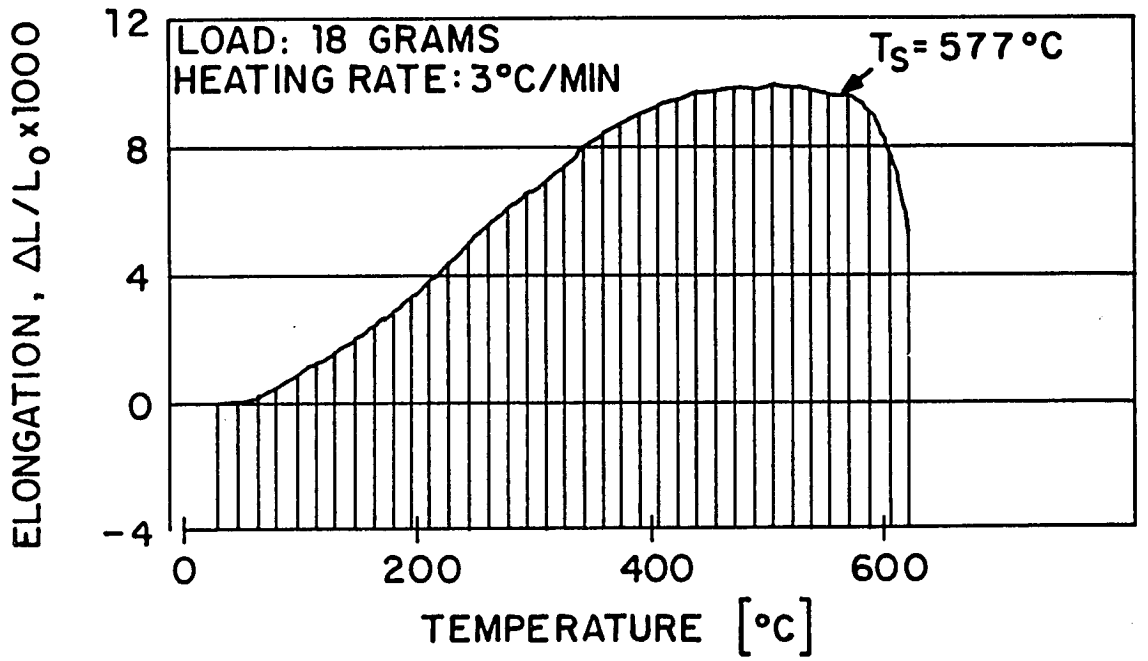

Figure 3.20. ELONGATION vs TEMPERATURE FOR GLASS PARTICLES (D_p = 195μ)

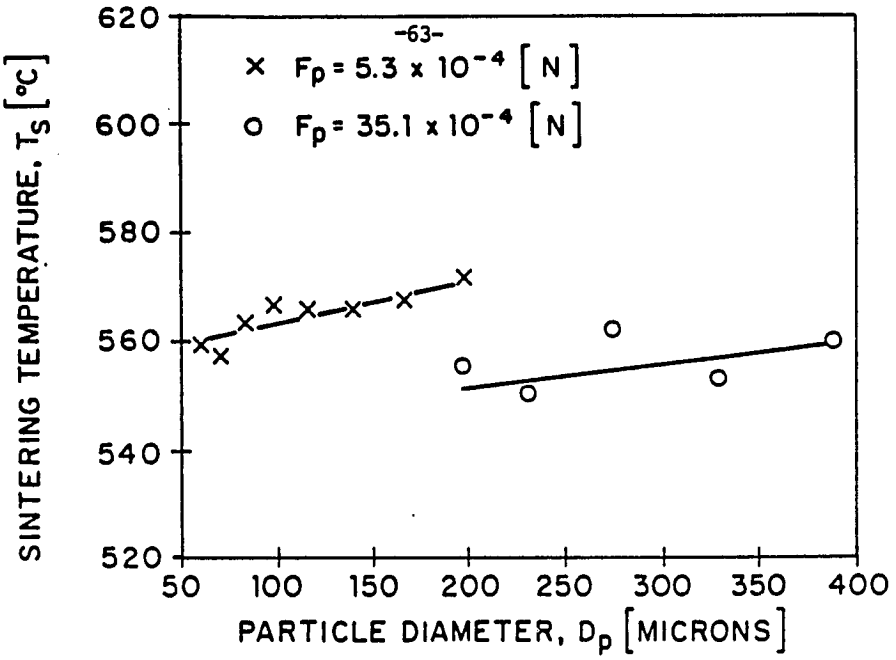

Figure 3.21A. SINTERING TEMPERATURE, T_S vs PARTICLE DIAMETER, D_p FOR GLASS PARTICLES AT CONSTANT INTERGRANULAR FORCE, F_p

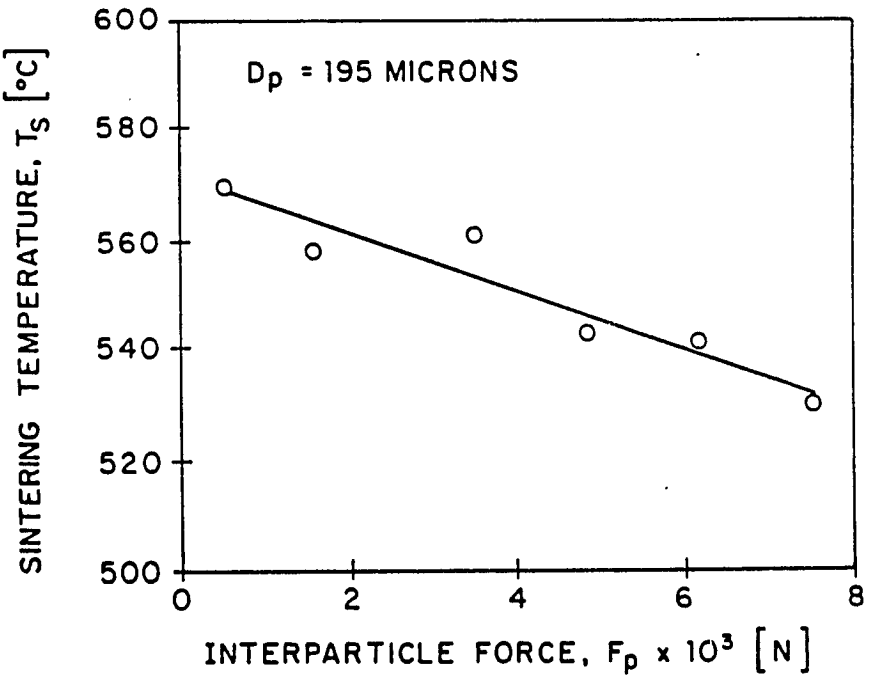

Figure 3.21B SINTERING TEMPERATURE vs INTERPARTICLE FORCE FOR GLASS BEADS

Figure 3.21B) is also not significant if one takes into account the fact that the force was varied over more than one order of magnitude. These findings are somewhat different from the earlier results by Siegell (1976) where a strong dependence on particle size was evident but where the experiments were conducted under constant load, L, rather than under constant force F_p. It is clear that experiments performed with constant load and varying particle size in the same sample holder will yield different results, since in the sample with smaller particles there are more contact points per unit surface area and consequently lower forces between particles as compared to a sample with larger particles. In order to compensate for larger forces between contact points in a sample of large particles, one has to increase the load on a sample made of smaller particles according to Eq. (3.40), and therefore a better way to compare experimental results obtained on small and large particles is to use tests performed with a constant intergranular force F_p, as shown in Figures 3.21A and 3.21B.

Coal

A series of dilatometer tests were performed on two different coal samples to determine the sintering characteristics of this material. Figure 3.22 shows dilatation-contraction versus temperature for an Elkhorn-Pike coking coal at two different loads, L. As seen, the dilatation of the material is not significant up to the temperature, T_1, around 410°C, where swelling occurs. This process is followed by a rapid contraction at a temperature, T_2, around 450°C. As the load on the sample increases (see Figure 3.22B), the swelling becomes less evident and the contraction (sintering) occurs at a lower temperature. The same trend is shown in Figure 3.23 where both the swelling temperature T_1 as well as the sintering temperature T_2 are given as a function of the load applied on the sample. The experiments represented in Figures 3.22 and 3.23 were performed in nitrogen

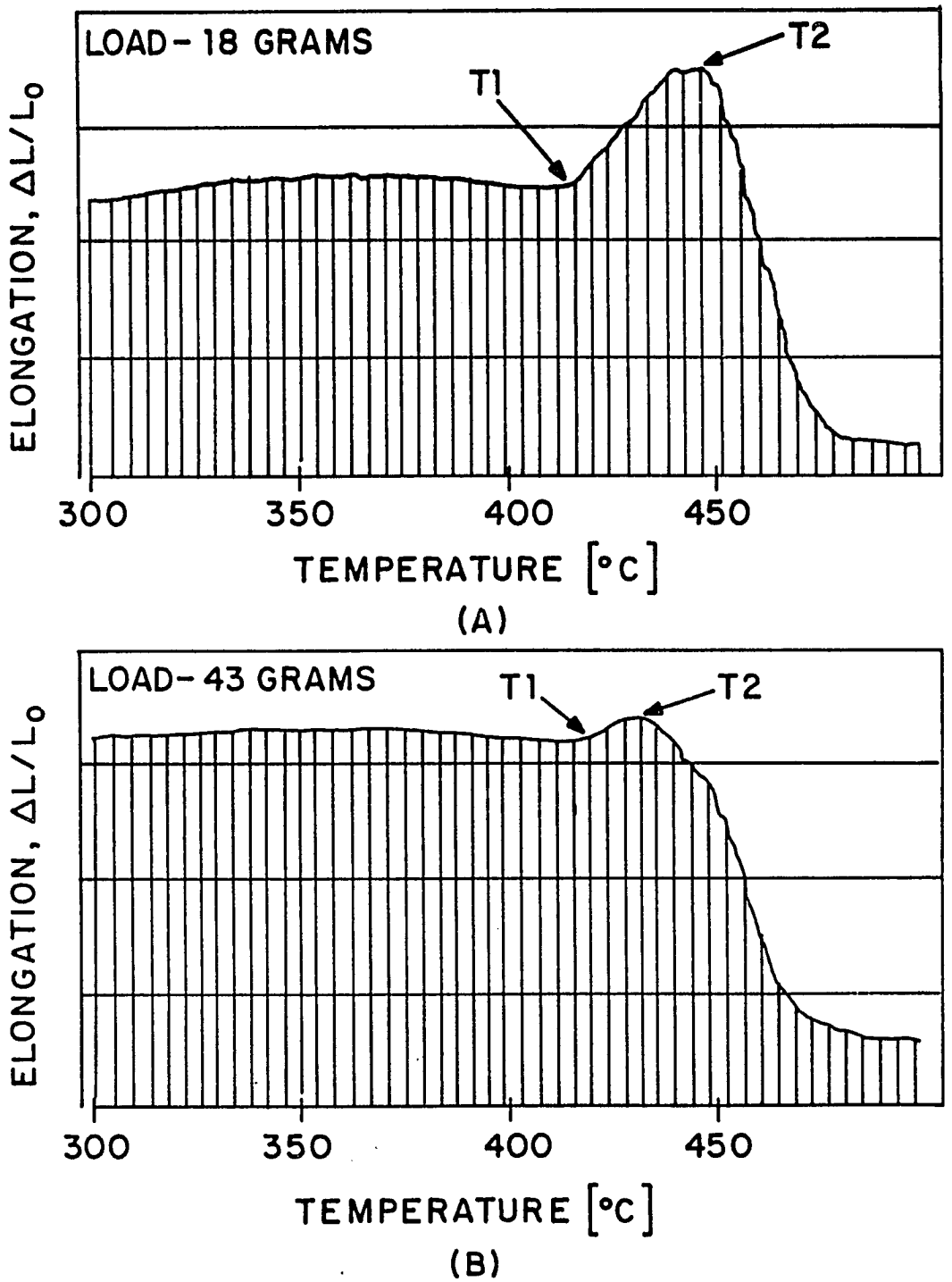

Figure 3.22. ELONGATION vs TEMPERATURE FOR ELKHORN-PIKE COAL IN NITROGEN GAS WITH 10°C/MIN HEATING RATE

T1 - SWELLING TEMPERATURE
T2 - SINTERING TEMPERATURE

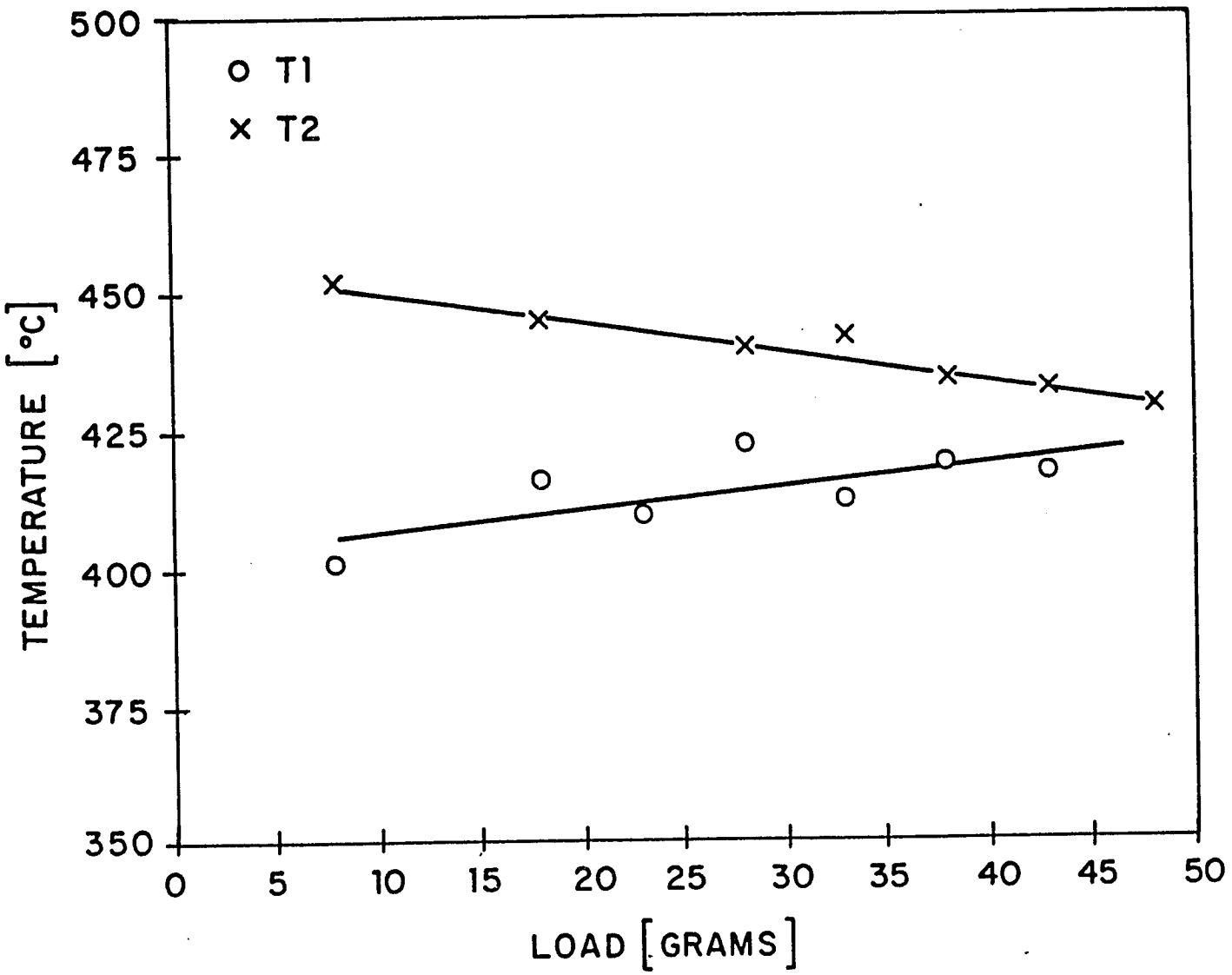

Figure 3.23. Swelling and Sintering Temperatures vs. Load for Elkhorn-Pike Coal in Nitrogen Gas with 10°C/min. Heating Rate.

to prevent burning of the sample. Figure 3.24 shows the dependence of the two temperatures, T_1 and T_2, on the heating rate. As seen, the dependence is very slight; both temperatures increase somewhat as the heating rate is increased from $1^{\circ}C$/min to about $15^{\circ}C$/min (upper limit of the instrument). To confirm the existence of the two characteristic temperatures, T_1 and T_2, a Differential Scanning Calorimeter (DSC) test using a DSC DuPont 1090 microcomputer based thermal analysis system was performed, and the results are shown in Figure 3.25; the two transition temperatures are clearly seen. This test indicates that swelling and contractions are accompanied by heat absorption and/or heat release.

For comparison with the above results obtained on a coking coal, a dilatometer test was performed on a standard Illinois No. 6 coal taken from the Penn State coal bank. The results are presented in Figure 3.26 as elongation versus temperature. As seen, the coal does not show swelling but does sinter at around $T_s = 380^{\circ}C$. The experiment was performed with a load of 18 g at a heating rate of $10^{\circ}C$/min in a nitrogen atmosphere.

As a conclusion, one can state that using dilatometer and DSC tests, one can determine sintering temperatures of different coals and can compare them to a standard sample; cokeability can then be determined with respect to a few standard coals. One can criticize here the criteria for agglomeration proposed recently by Lau (1981) which considers agglomeration in a coal combustor to be signaled by the swelling of the coal. As was shown in this study, swelling only occurs if the applied load (pressure) on the sample is low, while if the pressure is high, sintering occurs immediately without previous swelling. Other types of coal such as Illinois No. 6 do not swell at all before sintering.

Inorganic salts

An extended study of sintering of crystalline materials (salts) was undertaken to elucidate the behavior of these materials at high temperatures. In Table 3.3, data for the

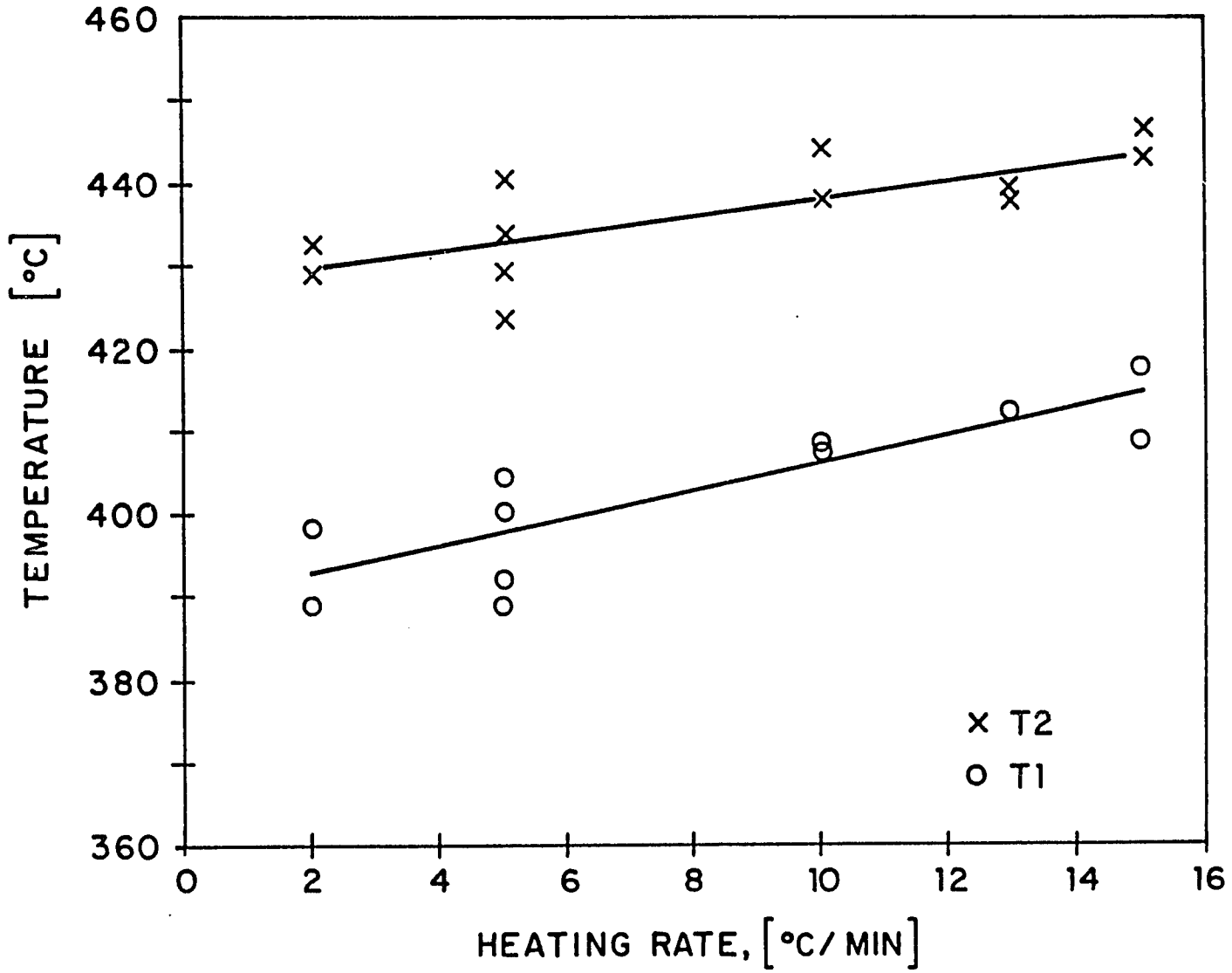

Figure 3.24. Swelling and Sintering Temperatures vs. Heating Rate for Elkhorn-Pike Coal in Nitrogen Gas with an 18 Gram Load.

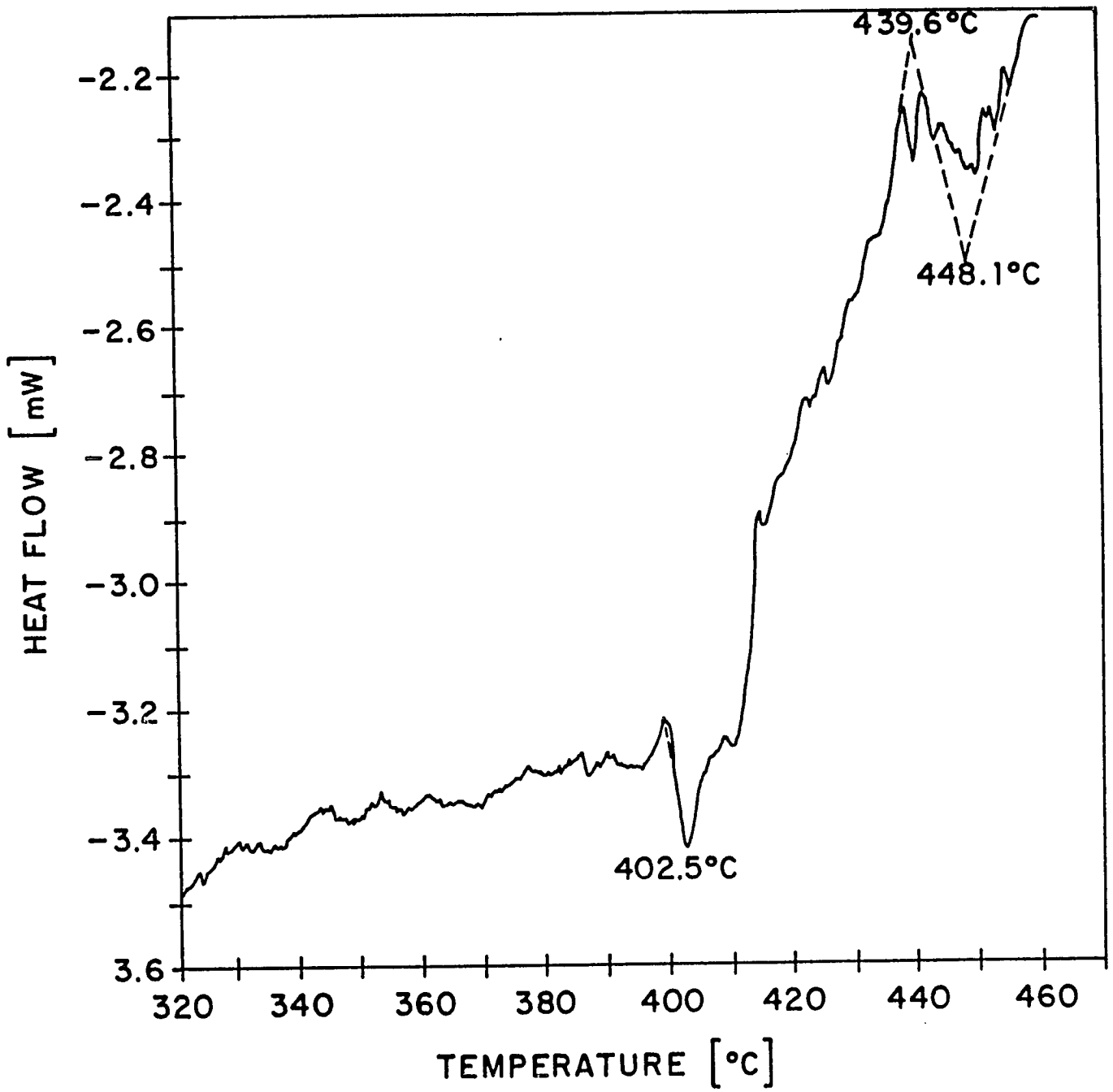

Figure 3.25. Elkhorn-Pike Coal in Nitrogen Gas at Atmospheric Pressure; Coking Endotherm and Sintering Temperature.

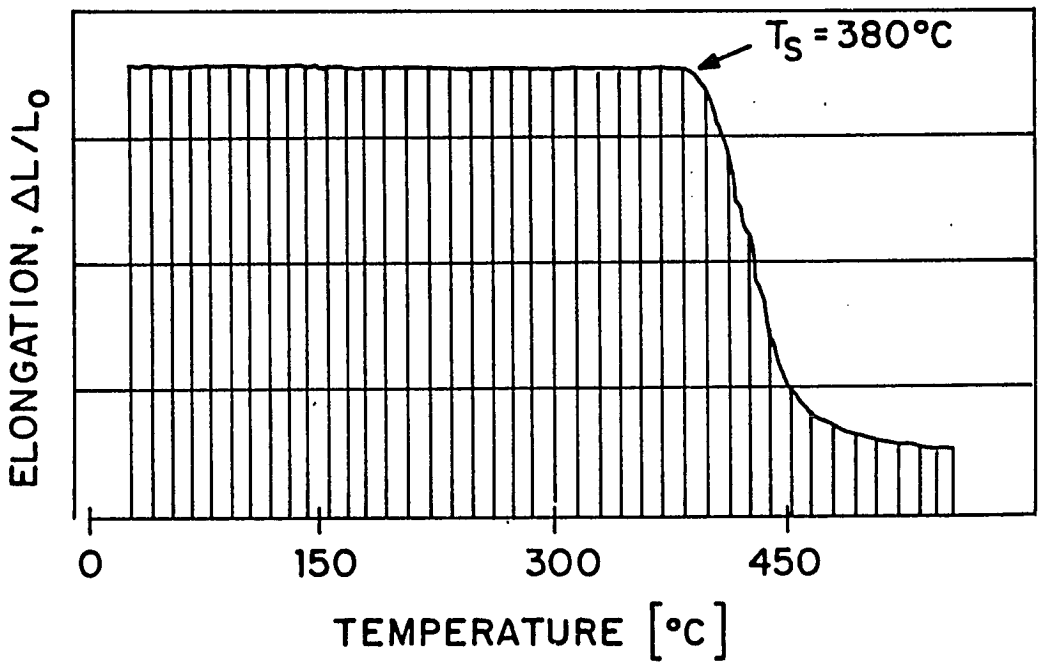

Figure 3.26. Elongation vs. Temperature for Illinois No. 6 Coal with a Load of 18 Grams and a Heating Rate of 10°C/min. in a Nitrogen Atmosphere.

series of experiments performed in the dilatometer using aluminum sulfate ($Al_2SO_4 \cdot 14H_2O$) is presented. The virgin sample could not be used in the dilatometer because the release of surface water dissolved the sample and formed a solution.

The sample, dried at 100°C, expanded greatly at 120°C and formed an agglomerate. It is believed that this agglomeration was caused by the release of intercrystalline water from the material and was not due to sintering. A sample was dried up to 230°C in the fluidized bed (drying of the sample in an oven is not feasible because agglomeration occurs due to water release) to eliminate crystalline water and subsequently heated in the dilatometer to temperatures approaching the decomposition point (see Figure 3.27). A large contraction was observed at 340°C but this was not accompanied by any agglomeration (Table 3.3, run no. 3). A similar experiment, using the pretreated sample of run no. 3, was performed to see whether the contraction is due to the elimination of additional bound water or to some other cause. The absence of the contraction at 340°C in the reheated sample (run no. 5) suggests that the contraction may be due to a crystalline compaction or the eliminaton of water. A sample was then dried up to 420°C to eliminate all possible water at 340°C (run no. 6) and then compressed in the dilatometer. The result suggests that the contraction at 340°C is not due to water elimination but to a crystalline rearrangement not accompanied by sintering. In fact, no sintering of the dried sample was observed up to the decomposition temperature and the elongation vs. temperature for the sample dried to 420°C was similar to the one shown in Figure 3.27. The above result, as confusing as they may seem at first glance, indicate that crystalline material may behave differently than amorphous granules because of water release and crystalline rearrangement not accompanied by sintering. The results also reveal that dilatometer data must be interpreted with great caution. Large contractions may indicate sintering, but actual agglomerate formation must confirm these findings.

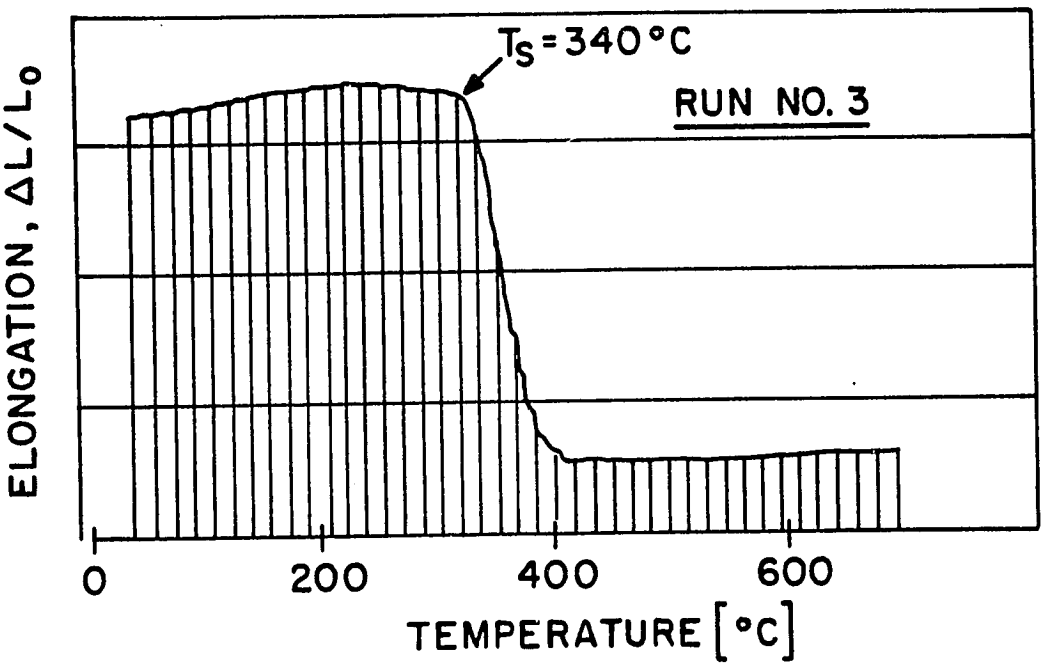

Figure 3.27. ELONGATION-CONTRACTION vs TEMPERATURE FOR ALUMINUM-SULFATE PARTICLES

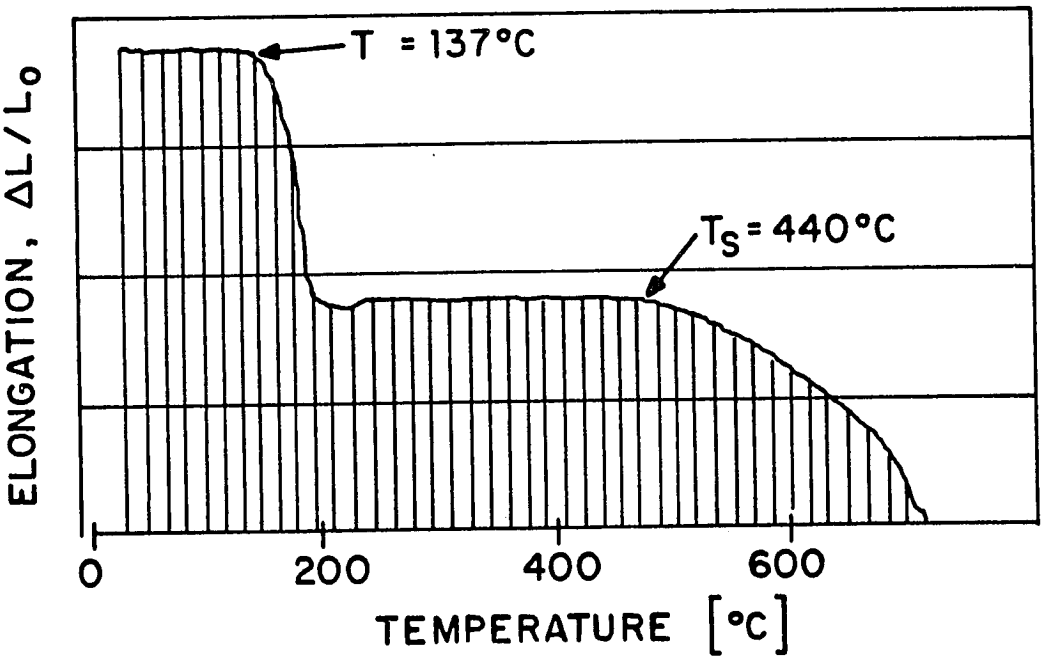

Figure 3.28. ELONGATION-CONTRACTION vs TEMPERATURE FOR CALCIUM-CHLORIDE PARTICLES

Table 3.3. Experiments with Aluminum Sulfate [$Al_2(SO_4)_3 \cdot 14H_2O$]

RUN #	PRETREATMENT OF SAMPLE	PROCEDURE	RESULTS
1	Pure hydrated crystal	10°C/min heat rate 33g load	At 110°C large amounts of water from the sample produced a solution
2	Sample preheated to 100°C in fluid bed	10°C/min heat rate 33g load	At 120°C, sample expanded greatly and hardened into a a solid cylinder.
3	Sample preheated to 230°C in fluid bed	10°C/min heat rate 33g load	Expansion at 120°C is eliminated. Large contraction present at 340°C (NO AGGLOMERATION)
4	Sample from Run #3	Cooled sample to 200°C then reheated under the same conditions as run #3	Contraction at 340°C completely eliminated. Change of slope at 600°C (NO AGGLOMERATION)
5	Same as Run #4	Sample from run #4 removed, shaken and quickly returned to the dilatometer and run under the same conditions as run #4	Same results as in run #4. Change of slope at 610°C is more clear (NO AGGLOMERATION)
6	Sample dried in fluid bed to 230°C, then heated in an oven to 430°C	Heat rate: 0 → 300°C 25°C/min 300 → 700°C 10°C/min 33g load	Contraction at 340°C, and also change in slope at 600°C seen very clearly
7	Sample dried in fluid bed to 230°C	10°C/min heat rate 58 gram load (smaller sample holder and smaller size particles used)	The change in load, diameter of the holder and particle size did not change the results from run #3 (NO AGGLOMERATION)

In Figure 3.28 results of a dilatometer experiment performed on calcium chloride ($CaCl_2 \cdot 2H_2O$), dried initially at 120°C in the fluidized bed, are shown. Elongation vs. temperature measurements were obtained with a heating rate of 10°C/min and a load of 18 g. The first contraction at 132°C is due to the anhydrous salt being formed. The second, at 440°C, is due to surface softening and the filling up of voids created by the water removed and is accompanied by the formation of a strong agglomerate.

The example of two crystalline materials demonstrates the very complex way these substances behave while heated to high temperatures. Release of crystalline water complicates the picture of dilation and contraction, especially if the rearrangement of the molecules after the water is eliminated is accompanied by a bulk volume change. Some volume changes are accompanied by sintering of the surface (calcium chloride) while others are not (aluminum sulfate). A careful examination of the sample obtained in the dilatometer after the dilation-contraction test reveals whether agglomeration has in fact occurred.

CHAPTER 4: A STUDY OF LIQUID BRIDGES BETWEEN STATIONARY AND MOVING PARTICLES

4.1 BACKGROUND

As shown in Section 3.3 a theoretical model has been developed to compute minimum gas velocities which keep a bed of particles to which a (sticky) fluid or a solution is added, in stable fluidization. The model underpredicted the experimental results by roughly a factor of two. To obtain better agreement between theory and experiment a more detailed study of a wet agglomerate was undertaken.

The interparticle force used in the model was derived from the action of surface tension (Eq. (3.4)) and only takes into account the static strength of the bond, that is, the strength under extremely slow deformation. This static strength can be obtained from the theory of capillarity between granular material. The Laplace-Young equation which describes the equilibrium of an interface can be solved to determine the interfacial profile as well as the force due to the liquid bridge. The static strength of the bond is important insofar as it can be compared to the strength under dynamic conditions i.e. where the particles are moving with respect to each other.

While investigating static bridges it was found that under certain conditions the influence of gravity on the symmetry of the interfacial profile of the liquid bridge is quite significant. A thorough investigation was performed along with the construction of an experimental apparatus to study this effect and the results are described in Section 4.2.

In a fluidized bed where particles move about under dynamic conditions, the strength of liquid bonds should be different from the strength due to surface tension only because one also has to take into account viscous flow of liquid material in the bridge. A set of experiments was performed with fluids of various viscosities and bridge volumes to verify this hypothesis and Section 4.3 contains these results together with a comparison with the static strength under the same physical conditions.

4.2 THE EFFECT OF GRAVITY ON THE SHAPE AND STRENGTH OF A LIQUID BRIDGE BETWEEN TWO STATIONARY SPHERES

Introduction

The study of a liquid bridging a gap between two solid surfaces has been the subject of numerous investigations in recent years. Specifically, researchers have been concerned with the geometry of the surface, the shape of the liquid profile, the volume of the liquid bridge and the attraction force between the two solid bodies created by the bridge.

A detailed chronological summary of most of the previous work on the subject has been compiled by Mehrotta and Sastry (1980). Recently, work has centered on the stability of these liquid-solid systems. Erle et al. (1971) used a variational approach to derive, from a first variation, the Laplace-Young equation and to solve for the shape, as well as for the force of cohesion, of a fluid bridge between two spheres when gravity is neglected. Their results showed what has been demonstrated elsewhere (Fortes, 1982, Boucher et al., 1982) that, in certain cases, there are two distinct solutions to the Laplace-Young equation while under some special conditions no solutions are possible. From the comparison of experimental results to their model, Erle et al. (1971) made a conjecture as to which of the two distinct solutions, when such solutions exist, was stable; no mathematical condition for stability was given. Coriell et al. (1976) studied the shape and stability limit of a liquid zone between two coaxial circular plates which included the effect of gravity. These authors performed a first variation to obtain the Laplace-Young equation and then a second variation to obtain a condition of stability for a given profile. They showed that if the second variation is positive, the energy is a minimum and the profile is stable. De Bisschop and Rigole (1982) proposed that the physically realizable profile, for a bridge between two spheres without the effect of gravity, is the one that minimizes the free energy of the three phase system. For two possible solutions having equal bridge volume the solution that gives the minimum surface area will be the stable one. These authors also

showed that the region in which the two distinct solutions become equal is the demarcation between a stable liquid profile and the rupture of the bridge. The equivalent problem for the case where gravity forces are considered was not solved by these authors. De Bisschop and Rigole (1982) pointed out, however, that at large bridge volumes and large particle size the effect of gravity can no longer be neglected.

There has been some disagreement in the literature as to the expression for the capillary force acting within the liquid bridge. Force measurements performed by Wolfram and Pinter (1979) (two flat plates slowly separated) using a liquid bridge immersed in a second insoluble liquid, compared favorably with the force expressions that took bouyancy of the plates and of the liquid bridge into account. These authors showed that when the bouyancy term was neglected by using the classical force expression due to Fisher (1926), the agreement between theory and experiment was poor. Hotta et al. (1974), reviewed several methods for the computation of the force of a liquid bridge and also determined, by comparison with experiments, a similar expression as obtained by Wolfram and Pinter (1979).

In this section, the force and the rupture criteria of a liquid bridge between two spheres in a gravitational field is considered; this problem, as pointed out above, has not yet been completely solved. The Laplace-Young equation is solved numerically including the effect of gravity. The shape, the force and the separation distance of a liquid bridge of given volume between two spheres is determined and compared to experimental data of the author as well as to experimental data of Mason and Clark (1965) and De Bisschop and Rigole (1982). Theoretical and experimental results for the maximum stable separation distance (rupture point) for a sphere-liquid-sphere system having a given volume are reported and compared to experimental data and to another proposed rupture criteria.

Theoretical considerations

The analysis of a fluid-fluid interface at rest is described by the equation of Laplace and Young, which relates the difference in hydrostatic pressure to the local mean curvature and the surface tension of the interface. In the case of a gravitational field the pressure variation as a function of height above a reference plane has to be considered in accordance with Pascal's law. The equation can also be derived by using the calculus of variations and minimizing the free energy of the system and then solving the resulting Euler equation. For the system shown in Figure 4.1, the dimensionless equation of equilibrium has the form (Orr et al., 1975):

$$2HoR - BoX = \frac{d^2X/dY^2}{[1+(dX/dY)^2]^{3/2}} + \frac{dX/dY}{Y[1+(dX/dY)^2]} \qquad (4.1)$$

where the coordinates X and Y are made dimensionless with respect to the sphere radius, R, $Bo=\Delta\rho gR^2/\gamma$ is the Bond number, $Ho=\Delta Po/2\gamma$ is the curvature and ΔPo is the pressure difference across the fluid-fluid interface at X=0, $\Delta\rho$ is the density difference and γ is the interfacial tension between the two phases. The influence of the gravity force is taken into account in Eq. (4.1) by the Bond number. Many researchers neglect the influence of gravity or more generally the existence of the term including the Bond number in Eq. (4.1) and compare the predictions of the model to experiments performed by either using small diameter spheres or immiscible fluids of nearly equal density. Since X is of order one, the second term on the left hand side of Eq. (4.1) can be neglected when $Bo/2HoR \ll 1$. This condition is usually satisfied for the case of small particles and small liquid volumes.

Equation (4.1) was rearranged to allow for easier numerical solution to obtain the following set of first order differential equations (see Appendix E):

$$d\Phi/dS = (2HoR - BoX) - (\sin\Phi)/Y \qquad (4.2)$$

$$dY/dS = \cos\Phi \qquad (4.3)$$

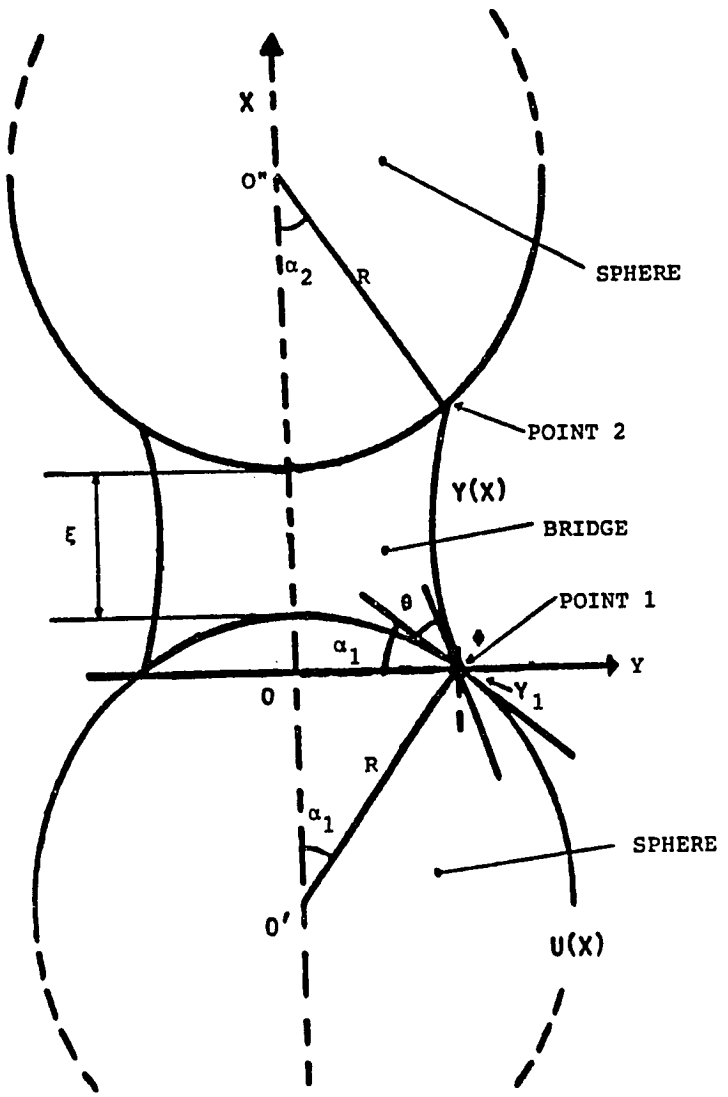

Figure 4.1. Coordinate system and notation used in the model of the static bridge.

$$dX/dS = \sin \Phi \tag{4.4}$$

where S=s/R is the dimensionless arc length of the liquid profile from the point $(Y_1,0)$ to the point (Y,X) (see Figure 4.1) and Φ is the angle between the profile and the horizontal (Boucher and Evans, 1975). A solution of the above equations is obtained by using a Runge-Kutta type scheme. The volume of the liquid bridge is determined by subsequently integrating the meridional profile about the X axis:

$$V_b^* = \pi \int_0^{X_2} (Y^2-U^2)dX \tag{4.5}$$

where the bridge volume is made dimensionless with respect to the cube of the radius, and U is the dimensionless profile of the two sphere sectors that are wetted by the liquid bridge (see Figure 4.1).

The balance of forces at the upper boundary between the liquid and the solid sphere gives the net external dimensionless force applied on the sphere which is necessary to maintain the configuration in equilibrium:

$$F_2 = f_c/\pi R\gamma = 2Y_2 \sin \Phi_2 - 2\, Y_2^2 HoR + BoY_2^2 X_2 - F_{B2} \tag{4.6}$$

$$F_{B2} = \frac{Bo}{3} (1 - \cos \alpha_2)^2 \{3-(1-\cos \alpha_2)\}$$

where the force F_{B2} is due to the effect of the variation in the pressure distribution along the sphere under the horizontal plane through point 2 (see Figure 4.1). This term only arises when gravity is considered since the Bond number Bo=0 otherwise. The force on the bottom sphere at point 1 (see Figure 4.1) is similarly given by (see Appendix E for derivation):

$$F_1 = 2Y_1 \sin\Phi_1 - 2Y_1^2 HoR + F_{B1} \tag{4.7}$$

$$F_{B1} = \frac{Bo}{3} (1 - \cos \alpha_1)^2 \{3-(1-\cos \alpha_1)\}$$

It is easily seen from Figure 4.1 that for given values of the angles α_1 and α_2 the minimum distance physically possible between the two spheres from the points X=0 to X=X_2 is:

$$X_{min} = 2 - (\cos \alpha_1 + \cos \alpha_2) \tag{4.8}$$

The difference in forces between the top and bottom spheres which is equal to the weight of the bridge is related to the volume of the bridge by the following dimensionless relationship:

$$V_b^* = \pi (F_2 - F_1)/Bo \tag{4.9}$$

This relation gives a second independent method of calculating the liquid volume for the cases when gravity is taken into account (Bo≠0). It should be noted here that the method of calculation of the liquid profile is the same if the bridge is between two flat plates instead of two spheres, the differences being that the calculation of the volume using Eq. (4.5) would have U equal to zero and the forces F_{B1}=F_{B2}=0 since there is no variation in pressure along a flat plate at a given constant elevation.

Equations (4.2-4.4) are the governing set of differential equations to be solved for the determination of the liquid profile. The solution of the three equations proceeds as follows: starting at the lower surface, a meridian curve has an initial value $\Phi_1 = 180^\circ - (\theta + \alpha_1)$, for a chosen filling angle α_1 (or alternatively at a certain value of Y_1, which determines the filling angle since $Y_1 = \sin \alpha_1$). For given values of the parameters Y_1, Ho and Φ_1, the integration of Eqs. (4.2-4.4) is performed numerically (see Apendix A for program listing) with the arc length as the independent variable. The integration marches along the arc length until the angle Φ approaches the appropriate filling angle α_2, corresponding to a sphere with a given radius R and contact angle θ. Specifically the numerical scheme checks the following relation to determine when the solid surface has been reached

$$Y = \sin (\Phi - \theta) \tag{4.10}$$

The above procedure gives the shape of the fluid-fluid interface.

Often, one is primarily concerned with the force of attraction exerted by the liquid bridge on the two spheres as a function of bridge volume and of separation distance between the spheres. As can be observed from the above method of solution and from Eqs. (4.6) and (4.7), no direct method of obtaining the force of the bridge by either specifying the liquid volume or the separation distance of the spheres is possible. This is due to the fact that the volume and separation distance are determined only after the profile is obtained. What is usually done is that a matrix of possible initial curvature values Ho and filling angles α_1 is used to obtain dimensionless separation distances, $\xi=x_s/R$, and total bridge volumes V_b^*. By means of interpolation, a grid of solution subsets can be determined whose elements all have the same volume and another subset whose elements all have the same separation distance. This was done for the gravity free case by Erle et al., (1971). The method is not very efficient however, since much interpolation is necessary and for the case where gravity is important a different matrix of values would need to be developed for each specific Bond number, Bo.

In order to overcome this difficulty and obtain a solution for any value of the Bond number, two computer programs were developed during the present work (see Appendix A.1). The first program calculates the volume of the liquid bridge as a function of the filling angle for two spheres that are a specified separation distance ,ξ, apart. It uses a Newton-Raphson trial and error scheme to determine what value of the parameter Ho is required for a given initial filling angle α_1, in order for the spheres to be a given ,ξ, distance apart. This is equivalent to specifying that the separation distance X_2, as determined from the integration of Eqs. (4.2-4.4), be just equal to the minimum distance possible for that configuration which is determined by Eq. (4.8) plus the actual separation distance ,ξ, between the two spheres. In this way, by varying the filling angle from $\alpha=\alpha_{min}$ to $\alpha=\alpha_{max}$ the strength of the bridge can be determined as a function of liquid volume. An example of such a calculation

along with a comparison of interpolated results given by Schubert (1977) for zero Bond number and zero separation distance is shown in Figure 4.2. The good agreement of the results indicates the soundness of the above numerical scheme.

The second computer program (see Appendix A.1) determines, again by using a Newton-Raphson trial and error method, the value of the parameter Ho necessary for a given filling angle α_1, with the volume V_b^* as a constraint (listing of both computer programs is contained in Appendix A.1). As was shown by Tardos et al. (1983), increasing separation corresponds to decreasing filling angles α_1 as the volume remains constant. The program therefore gives a fast method of determining the force of cohesion (strength) caused by the liquid bridge as a function of separation distance (diminishing contact angle) with a constant liquid bridge volume.

The comparison of the numerical method for the computation of the force and rupture distance to the often used circle approximation (Fisher, 1926, Mason et al., 1968) for the determination of the shape of the meridian curve of an axially symmetrical liquid bridge was also attempted. The motivation for assuming a circular profile lies in the fact that the computation of the force, volume and separation distance of a circular shaped bridge is greatly simplified, even though this profile does not have a surface of constant mean curvature as dictated by eq. (4.1). Figure 4.3 shows a comparison of the force vs. bridge volume with the separation distance as a parameter for the two methods of solution. It is seen that when the spheres just touch (ξ=0) there is only a slight discrepancy between the two solutions, but as the separation distance increases to 5 and then 10% (ξ=.05 and .1) of the sphere radius, respectively, the circle approximation significantly underestimates the force as obtained from the numerical solution of the Laplace-Young equation. It is clearly seen that only for the specific cases of small liquid volumes and touching spheres is the circle approximation a good estimate for the strength of a liquid bridge.

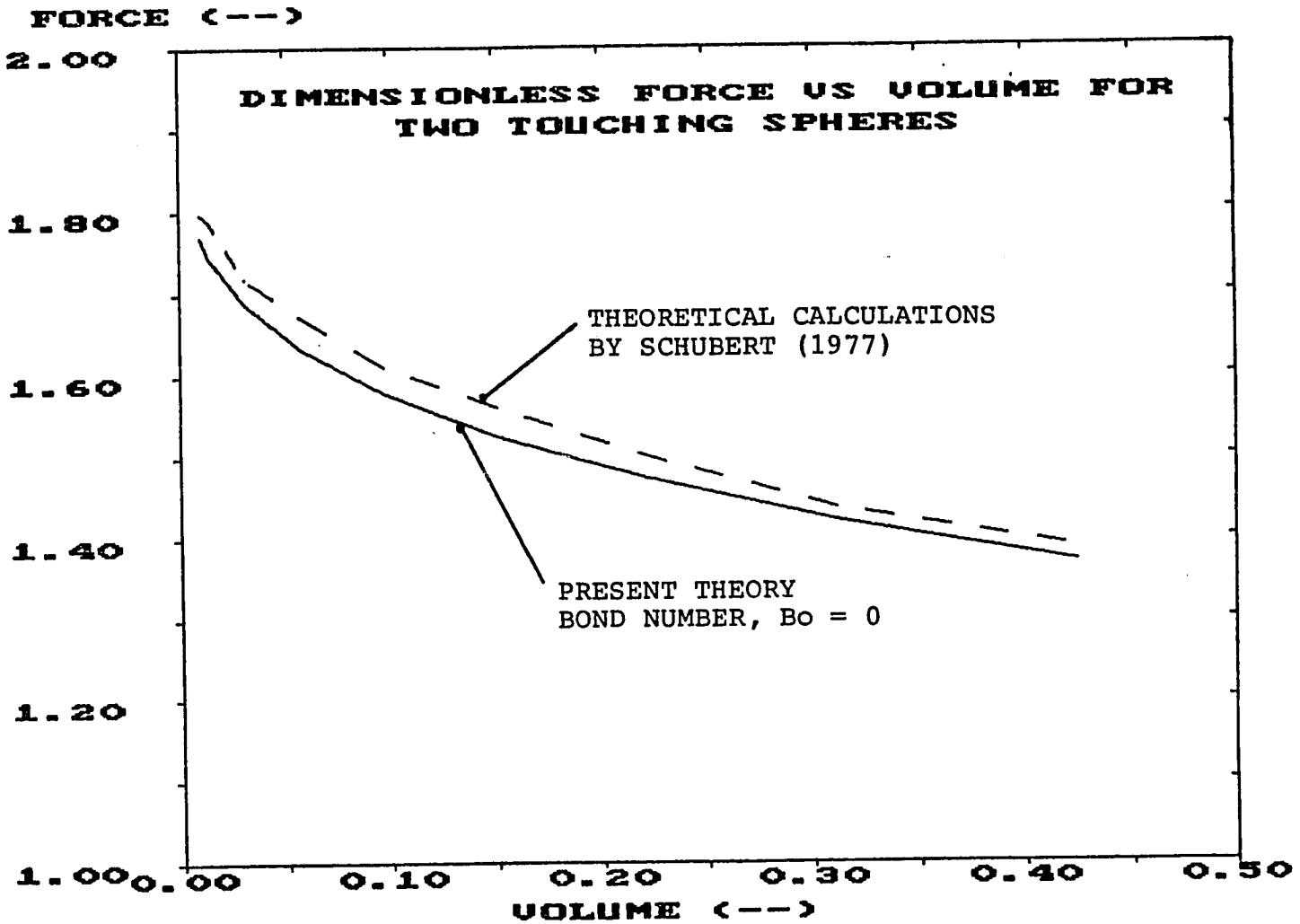

Figure 4.2. Dimensionless force vs dimensionless volume for two touching spheres. Comparison of present theory with calculations by Schubert (1977).

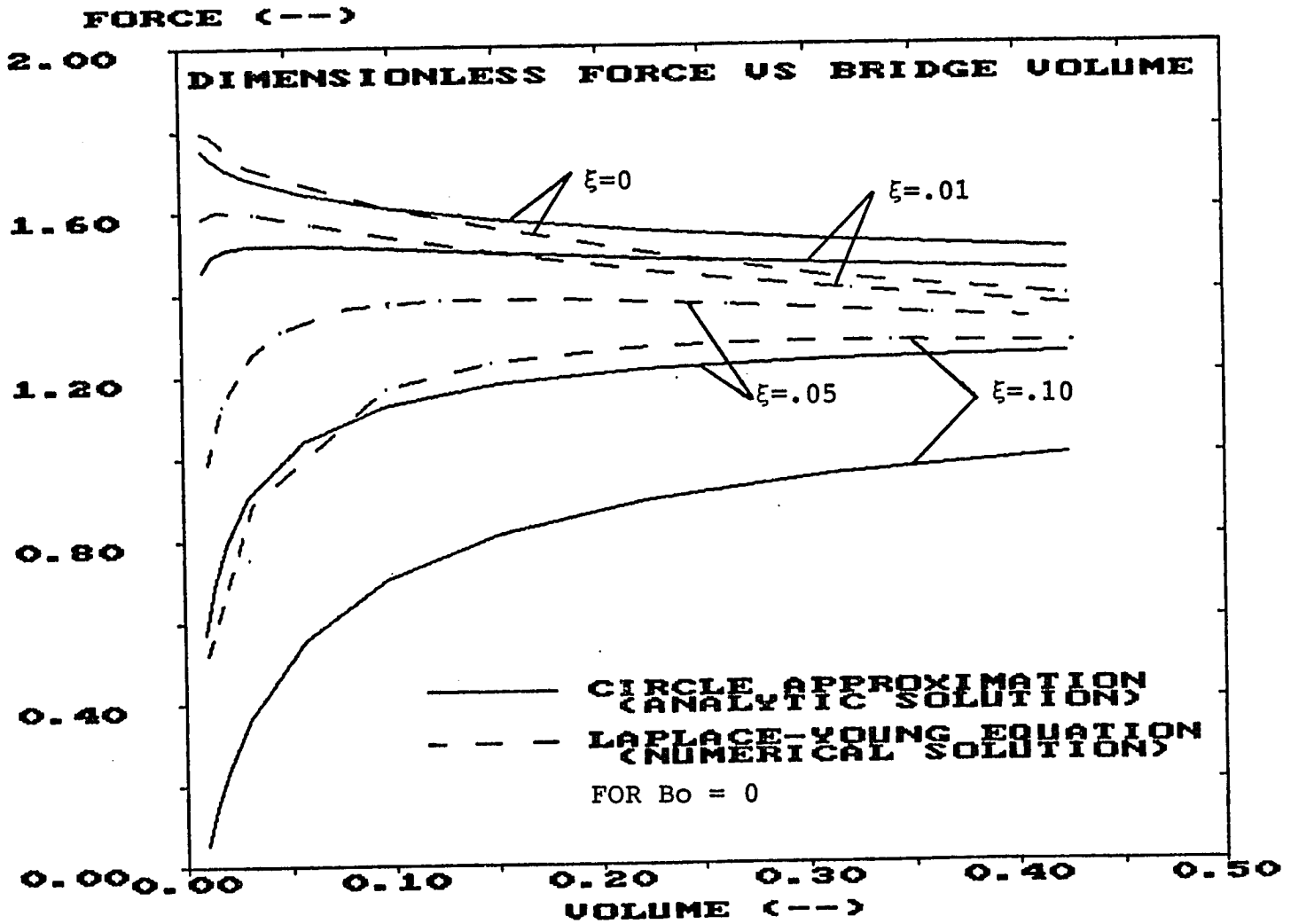

Figure 4.3. Dimensionless force vs bridge volume for Bo = 0.

Apparatus and experimental procedure

In order to study the stability, shape and force of cohesion (strength) of liquid bridges, an experimental set-up was constructed. A photograph of the experimental apparatus is shown in Figure 4.4A and a schematic representation is shown in Figure 4.4B. The apparatus consisted of a Nikon 6C projection microscope modified to allow for the projection, onto the viewing screen, of the profile of the liquid bridge. The Nikon 6C was rotated 90^{o} and mounted so that it rested in the horizontal position. The stage of the microscope has two verniers and a focusing wheel that allows complete three dimensional freedom of movement; a special mount was constructed to fit onto the grooves of the stage so that a moving support holding the upper sphere could be fixed to the mount. A second identical sphere was vertically aligned to the upper sphere by means of another three dimensional positioner which consists of a modified microscope stage with a two dimensional moving platform resting on it. The force of the bridge was determined by hanging the upper sphere from a stainless steel arm connected to two strain gauges that made up half a Wheatstone bridge circuit. The bridge was completed and the signal amplified by the use of a Validyne CD19 carrier demodulator which could give up to 1mV/V sensitivity. The output of the strain gauge was calibrated before every experiment by using several one milligram weights which were added directly onto a tiny plastic platform glued to the arm holding the top sphere. The output of the Validyne CD19 carrier demodulator was connected to an IBM/XT microcomputer equipped with a Data Translation 2805 interface board that could resolve a voltage signal to as low as 2.5 micro-Volts. The computer program that collected the data was STRAIN and is listed in Appendix A.3.

A typical experiment proceeded as follows: a certain amount of liquid of given volume was attached to the top sphere by the use of a micro-liter syringe; the bottom sphere was brought into contact with the top sphere and then slowly separated in set

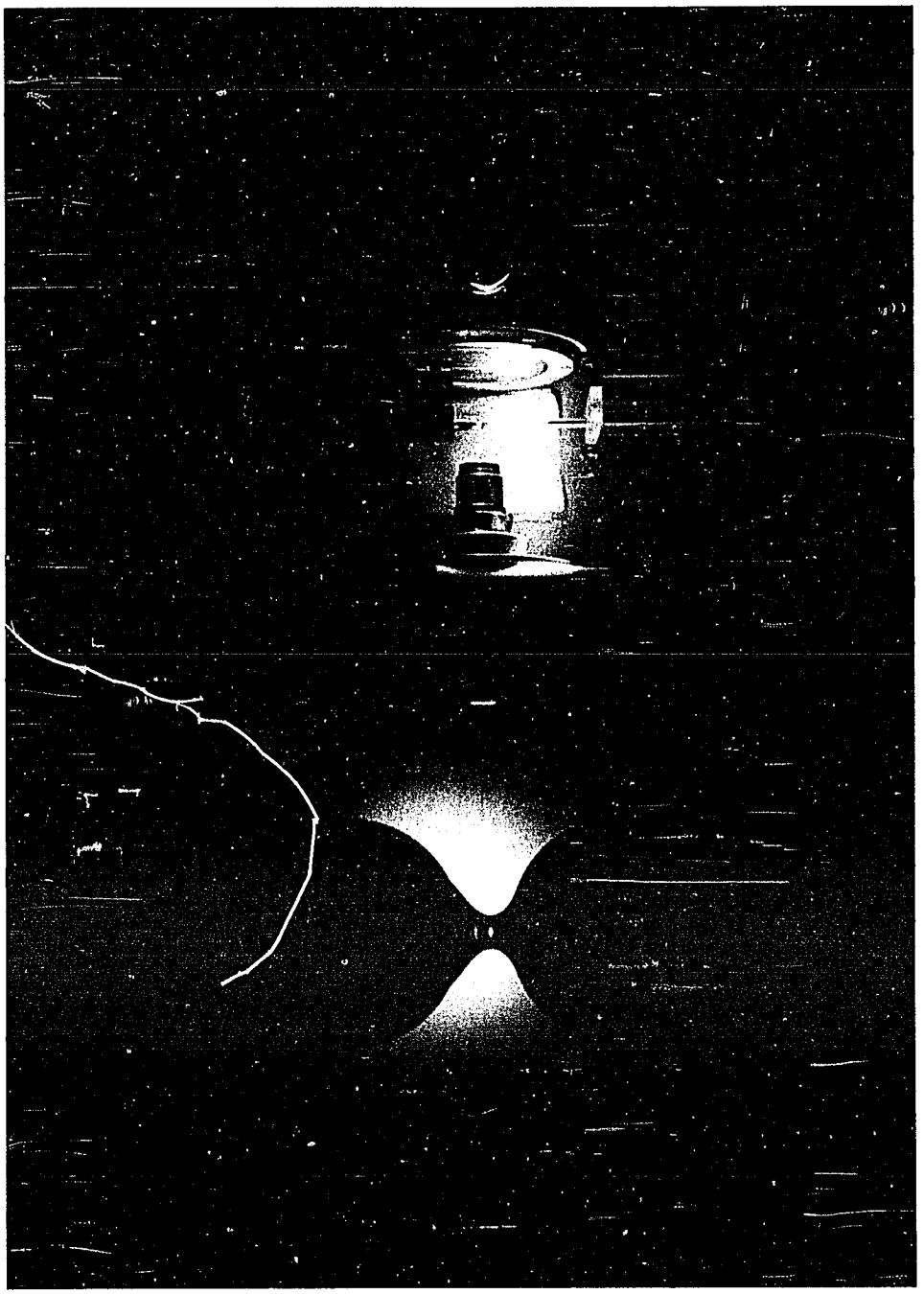

Figure 4.4A. Photograph of the static bridge strength experiment.

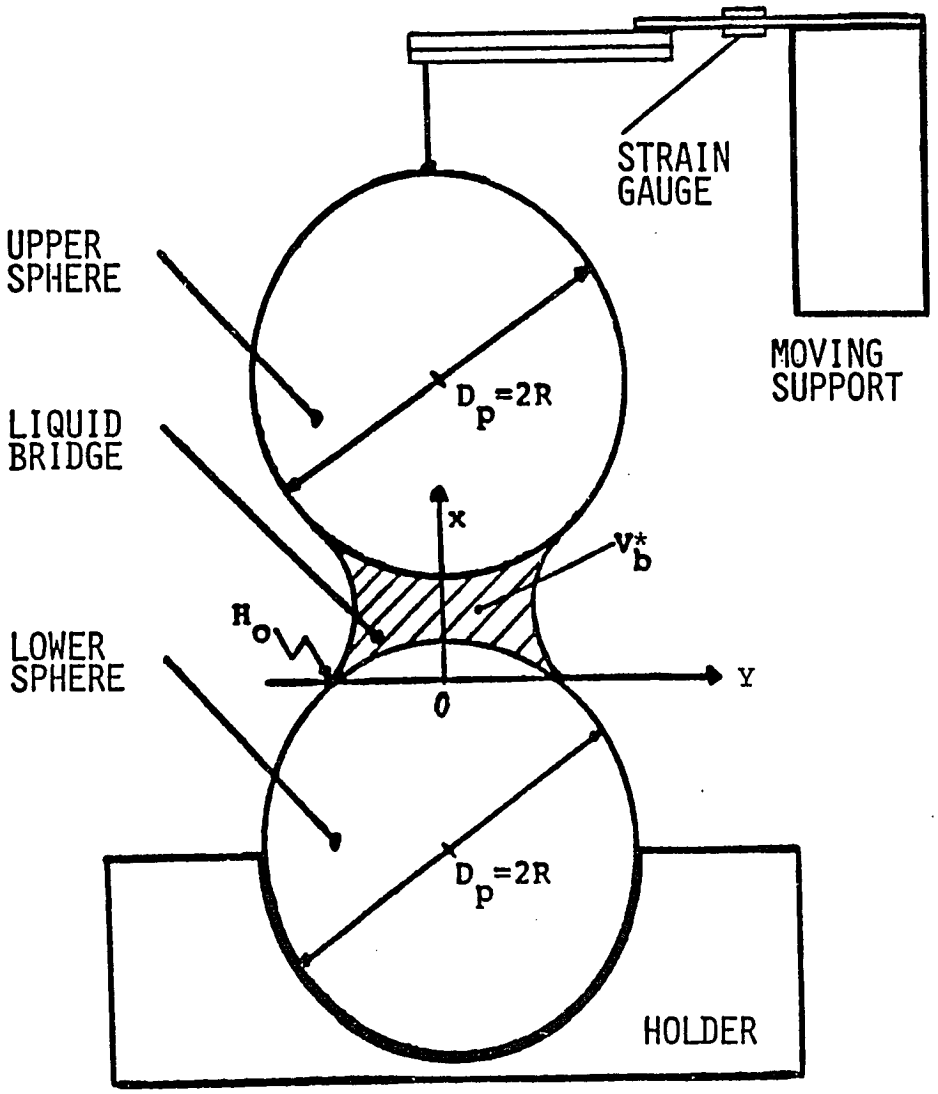

Figure 4.4B Schematical representation of the experimental apparatus to study liquid bridges between two spheres.

increments of increasing separation until the bridge eventually ruptured. The force at each given separation distance was determined by integrating, over a 5 second period, 512 points collected by the computer. The separation distance was obtained from the projection microscope screen and also entered into the computer. The computer used the least squares fit of force vs voltage from the calibration data and then plotted force vs separation distance curves for each set of experiments (see Appendix B for sample calibration results).

Comparison of present theory to experimental data

A set of experiments was performed according to the procedure described above using dibutylphtalate (DBT) as liquid bridge material and two stainless steel spheres as particles. Table 4.1 contains the physical characteristics of the system studied.

Figure 4.5 contains dimensionless force, $F=f_c/\pi R\gamma$ vs dimensionless separation distance $\xi=x_s/R$ for the DBT system together with a set of theoretical calculations. As seen the agreement between calculated and measured values is quite good. There is a maximum value of the force at a small but nonzero separation distance. This is a characteristic experimental phenomenon also observed by Mason and Clark (1965) and Hotta et al. (1974) and is not explained by the solution of the Laplace-Young equation which predicts the maximum force at zero separation distance or when the two spheres just touch. As seen from Figure 4.5, the strength of the bridge continuously decreases as the spheres are separated until a certain minimum value is reached after which the bridge suddenly ruptures.

Figure 4.6 depicts a family of curves of measured force vs separation distance with the bridge volume as a parameter. As seen, the variation in the value of the force for different bridge volumes follows the same general trend: the largest force is obtained at a very small separation distance of about 5% of the sphere radius after which the force decreases as the separation distance increases. Larger bridge volumes yield larger

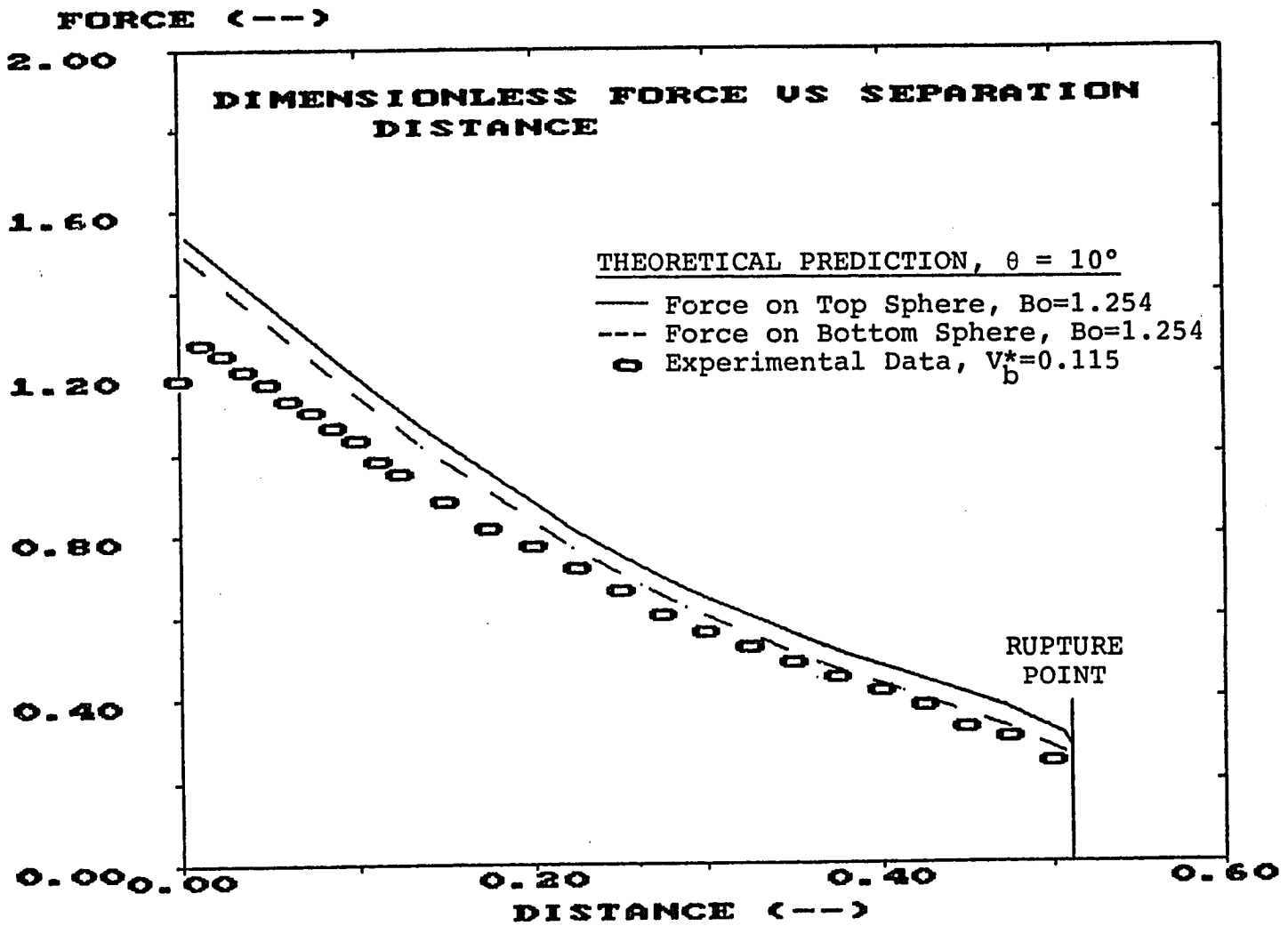

Figure 4.5. Dimensionless force vs separation distance. Comparison of theoretical model to experimental data.

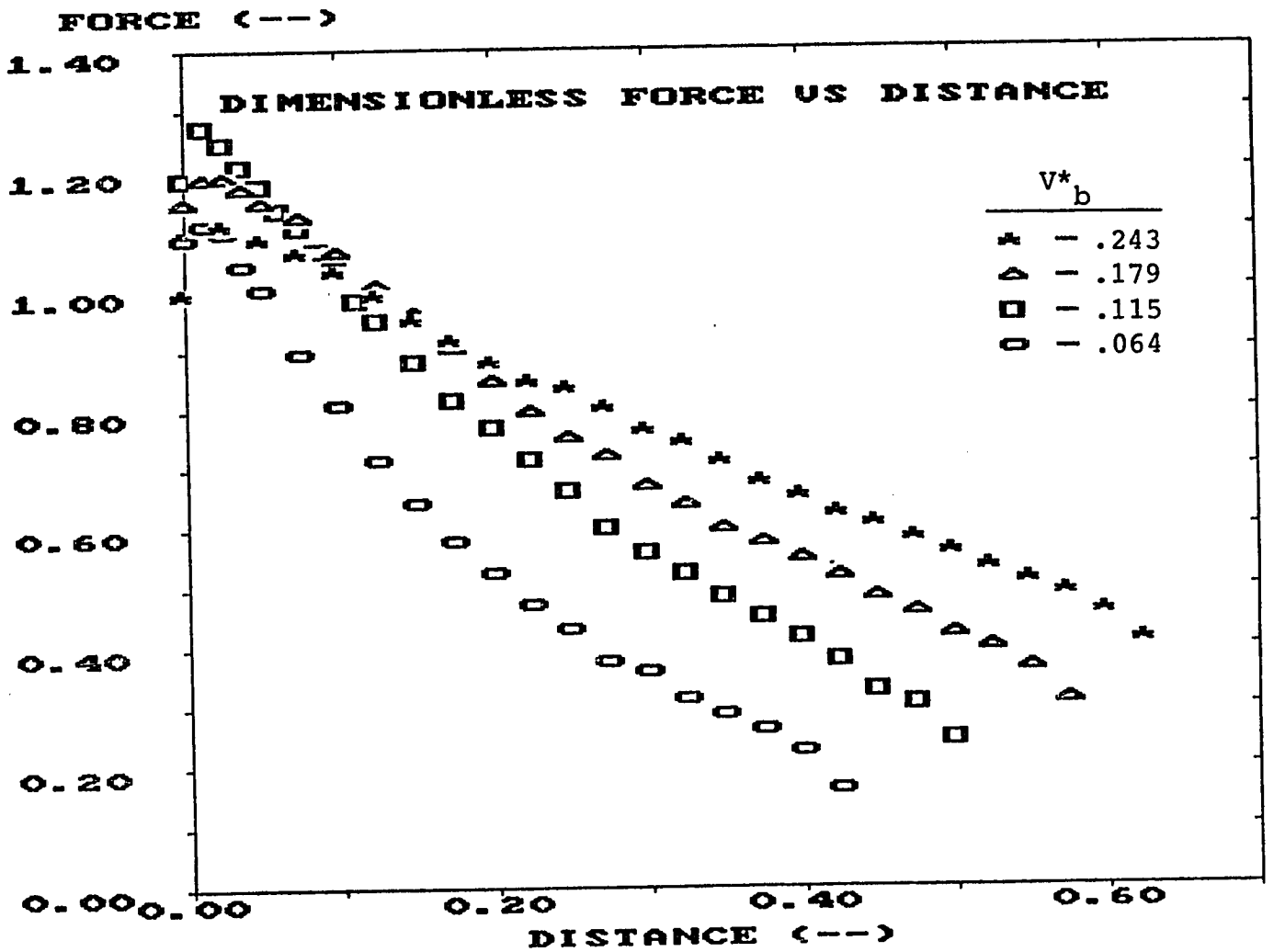

Figure 4.6. Force vs separation distance for several bridge volumes.

forces and rupture of the bridge occurs at larger separation distances. Similar findings were reported by Mason and Clark (1965).

Figure 4.7 shows the variation of the dimensionless force as a function of the dimensionless bridge volume with separation distance as a parameter. The figure contains experimental values taken from Figure 4.6 as well as theoretical predictions using the numerical integration scheme and the system properties contained in Table 4.1. It is seen that theoretical and experimental results at distances, ξ=.3 and ξ=.4 agree quite well.

Some experimental data by Mason and Clark (1965) was also compared to the present theory. These authors performed experiments on relatively large spheres (R = 1.5cm) using a fluid-fluid system consisting of two immiscible fluids one of which comprised the liquid bridge. The gravitational effects on the interfacial profile were eliminated by using two fluids of equal density, hence Bo=0 since $\Delta\rho$=0. These authors used a similar method as was employed during the present work in that two spheres having a fixed volume of liquid between them were allowed to slowly separate until the bridge ruptured. Force vs separation distance and the distance of rupture were recorded; the experimental values are given in Figure 4.8. When similar curves of force vs separation distance were generated theoretically by the present authors using the rupture criteria proposed by De Bisschop and Rigole (1982), the calculated rupture distances were always 45-55% smaller than those determined experimentally (see Figure 4.9). It is therefore believed that De Bisschop and Rigole's criteria for rupture is not entirely accurate and therefore an improved criteria is proposed below.

De Bisschop and Rigole state that, as separation of the spheres for a given constant volume occurs, the filling angle continuously decreases until a point is reached where no solution of the Laplace-Young equation is possible for a given minimum filling angle α_{min}. They considered this to be the rupture point of the bridge. It was actually observed during the experiments

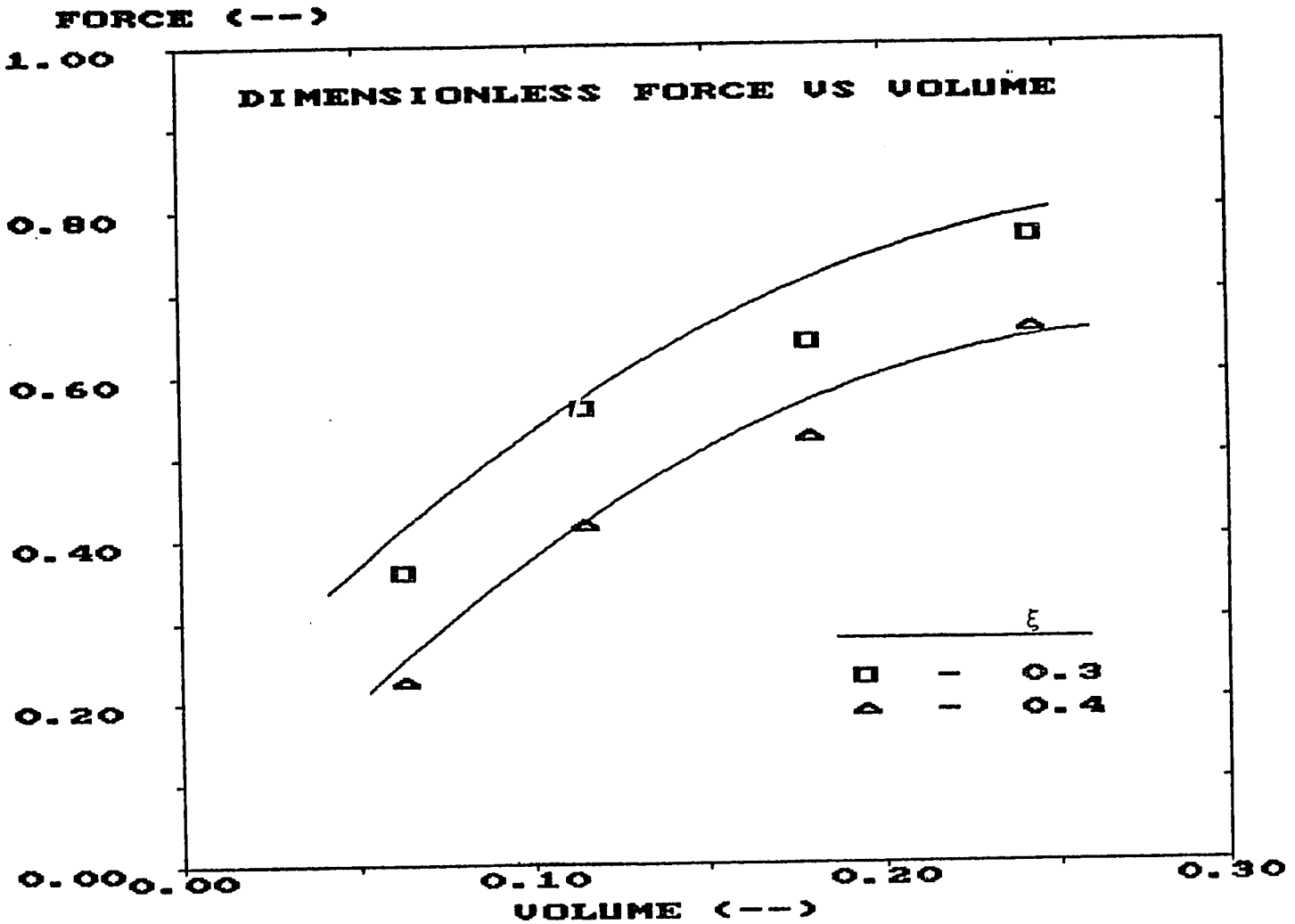

Figure 4.7. Dimensionless force vs dimensionless volume. Comparison of experimental results with present theory (contact angle, $\theta = 10°$).

Table 4.1. Physical Characteristics of liquid bridge material

Bridge Material	Dibutylphtalate (DBT)
Volume (V_b)	0.5, 0.9, 1.4, 1.9 μL
Viscosity (μ)	0.14 Poise
Density (ρ)	1.023 gm/cm^3
Surface Tension (γ)	32.24 dyne/cm
Bond Number (Bo)	1.25×10^{-4}
Contact Angle (θ)	0°
Radius of spheres (R)	0.1985 cm

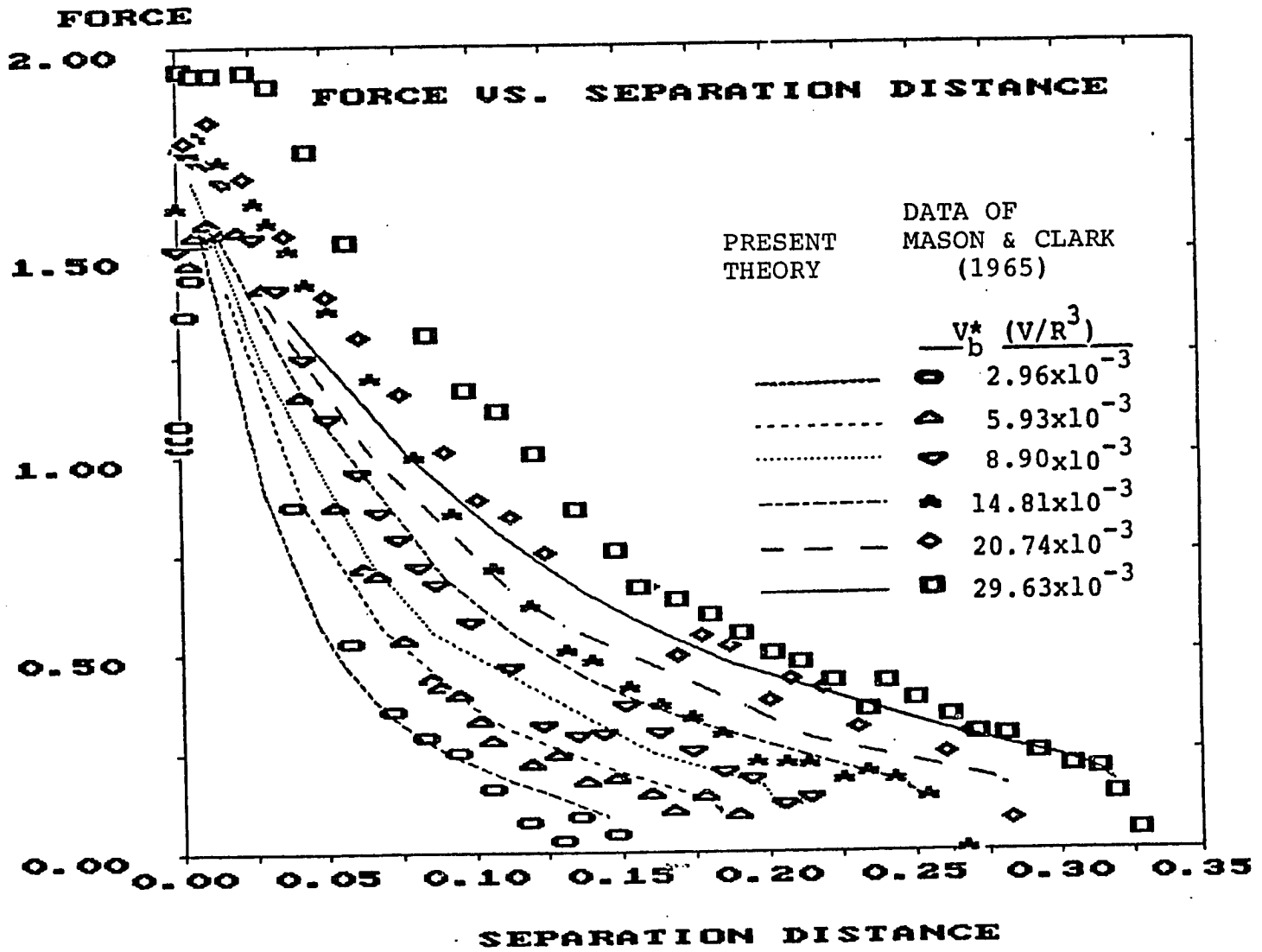

Figure 4.8. Comparison of present theory with experimental data by Mason and Clark (1965). The various lines represent present theory.

that indeed a minimum filling angle is reached when the spheres are separated but after this point stable bridges with increasing separation distance were still possible. These configurations are those where the fluid spreads out onto the two spheres, or in other words, at these distances increasing filling angles occur. Thus a revised theoretical rupture criteria can be summarized as follows. Two spheres that are just touching with a certain given liquid volume determine a certain filling angle α and an initial curvature Ho (Ho is usually negative for this case). As the filling angle decreases the separation distance increases. A minimum filling angle is reached with a determined value of the parameter Ho and then the filling angle needs to be increased to yield new solutions that correspond to larger separation distances, smaller forces, and larger values of the parameter, Ho. A point is reached where, as the filling angle is further increased, the separation distance no longer increases; this is the maximum value of the separation of the bridge for that given volume and rupture will occur at any larger distance.

The above modified criteria were used to compare Mason and Clark's data with our generated numerical solution and the results are given in Figure 4.8. As seen, the theoretical values underestimate the experimentally determined force at small separation distances for all volumes studied. This discrepancy between theory and experiment was also observed by Erle et al. (1971) who questioned the accuracy of Mason and Clark's data at small separation distances. Their model did not fit Mason and Clark's data either but did fit other available data of Cross and Picknett (1963).

The rupture distances as measured by Mason and Clark's experiments are plotted as a function of the liquid bridge volume and the results are given in Figure 4.9 together with numerically determined rupture distances determined by using the present rupture criterion. As seen, the fit between theory and experiment is very good, especially when one takes into account the possible errors in the measurement of the volume of the bridge

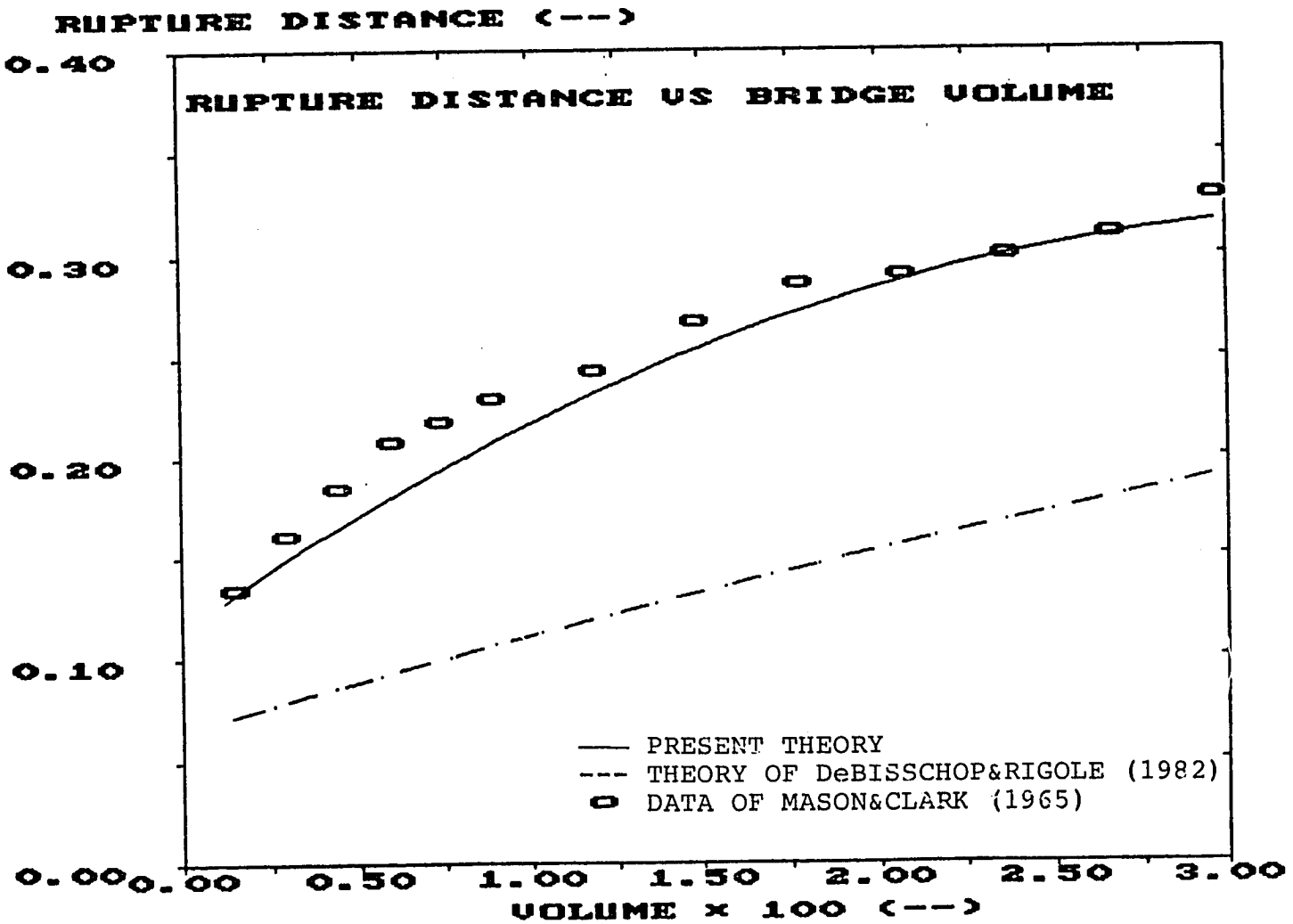

Figure 4.9. Dimensionless rupture distance vs dimensionless volume. Comparison of present theory to data by Mason and Clark (1965) and theory of DeBisschop and Rigole (1982).

and the separation distance in the experiments by Mason and Clark (1965).

De Bisschop and Rigole (1982) gave two experimental force vs separation distance values using a dibutlyphtalate (DBT) liquid in air system, spheres of radius R=0.1585cm and a dimensionless volume of V_b^*=.5154. Their data along with the computed values of the force using the present theory when gravity is neglected ($Bo=\Delta\rho gR^2/\gamma$ =0) and when gravity is included (Bo=0.754) is shown in Figure 4.10. When gravity is included, two values of the force are obtained; one is the force exerted on the top sphere (Eq. (4.6)) and the other on the lower sphere (Eq. (4.7)), both due to the liquid bridge. The difference between the two forces is seen to be a constant and is related to the liquid volume by Eq. (4.9) and is in fact the dimensionless weight of the bridge. The middle curve in Figure 4.10 is the theoretical force vs separation distance calculated when gravity is neglected and then only one value for the force is obtained for each separation distance since the forces on the top and bottom spheres are equal. As seen in Figure 4.10, the experimental data agree better with the force exerted on the lower sphere when gravity is taken into account (minimum value of the force) than the force when gravity is completely neglected.

The effect of gravity on the behavior of the liquid bridge

The same dibutylpthalate-sphere system (see Table 4.1) was used to record rupture distance as a function of liquid bridge volume and to compare it to calculated values when gravity effects become important. Figure 4.11 shows the results of experiments performed by the author and the comparison between the case when gravity is neglected (Bo=0) and when gravity is taken into account (Bo=1.254). At low liquid volumes the gravitational effect on the rupture distance is small, but as the volume increases, the difference becomes significant. Experimental results agree closely with the theoretical rupture distances that take the effect of gravity into account. It is

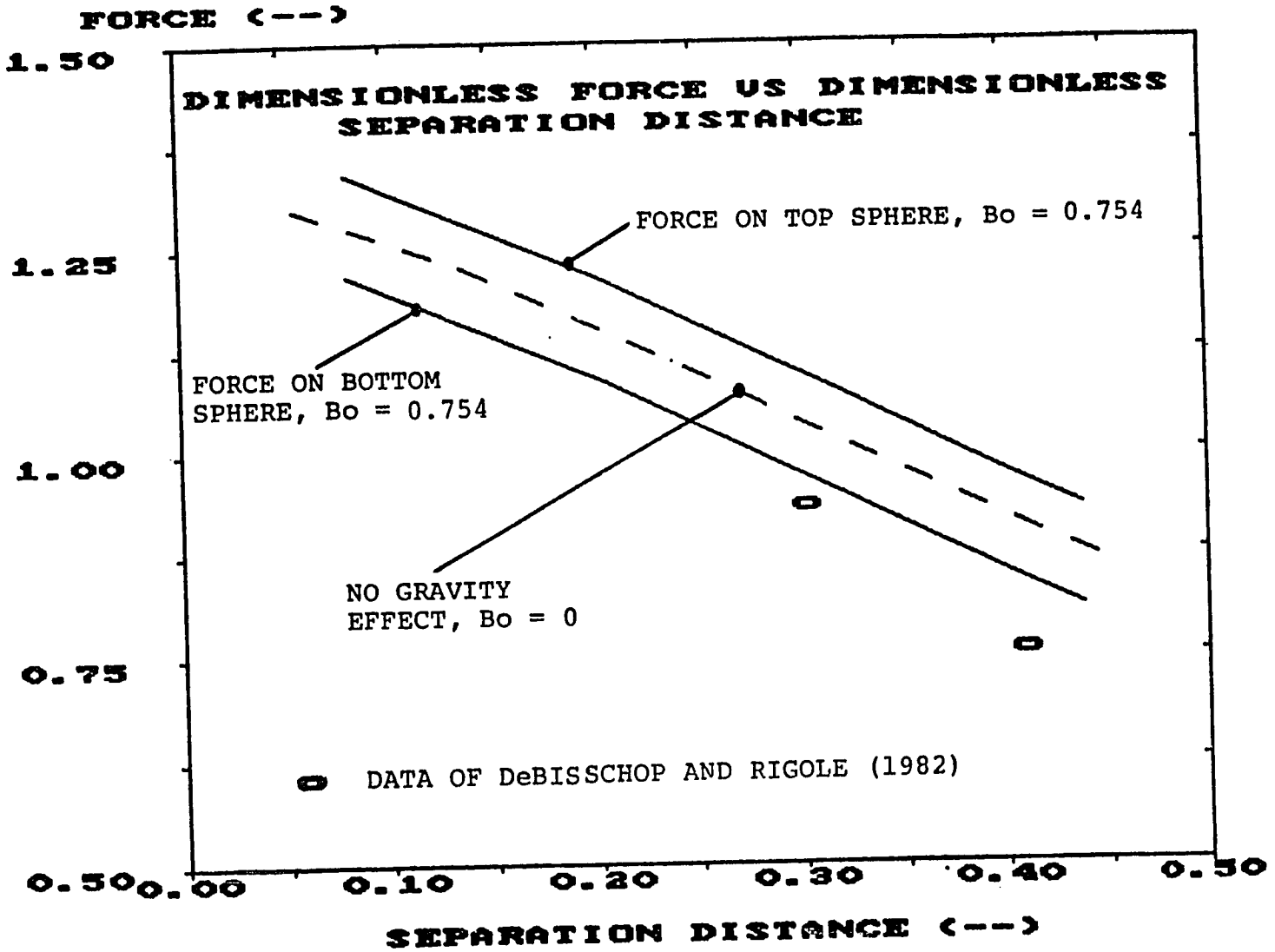

Figure 4.10. Dimensionless force vs dimensionless separation distance. Comparison of present theory with data of DeBisschop and Rigole (1982).

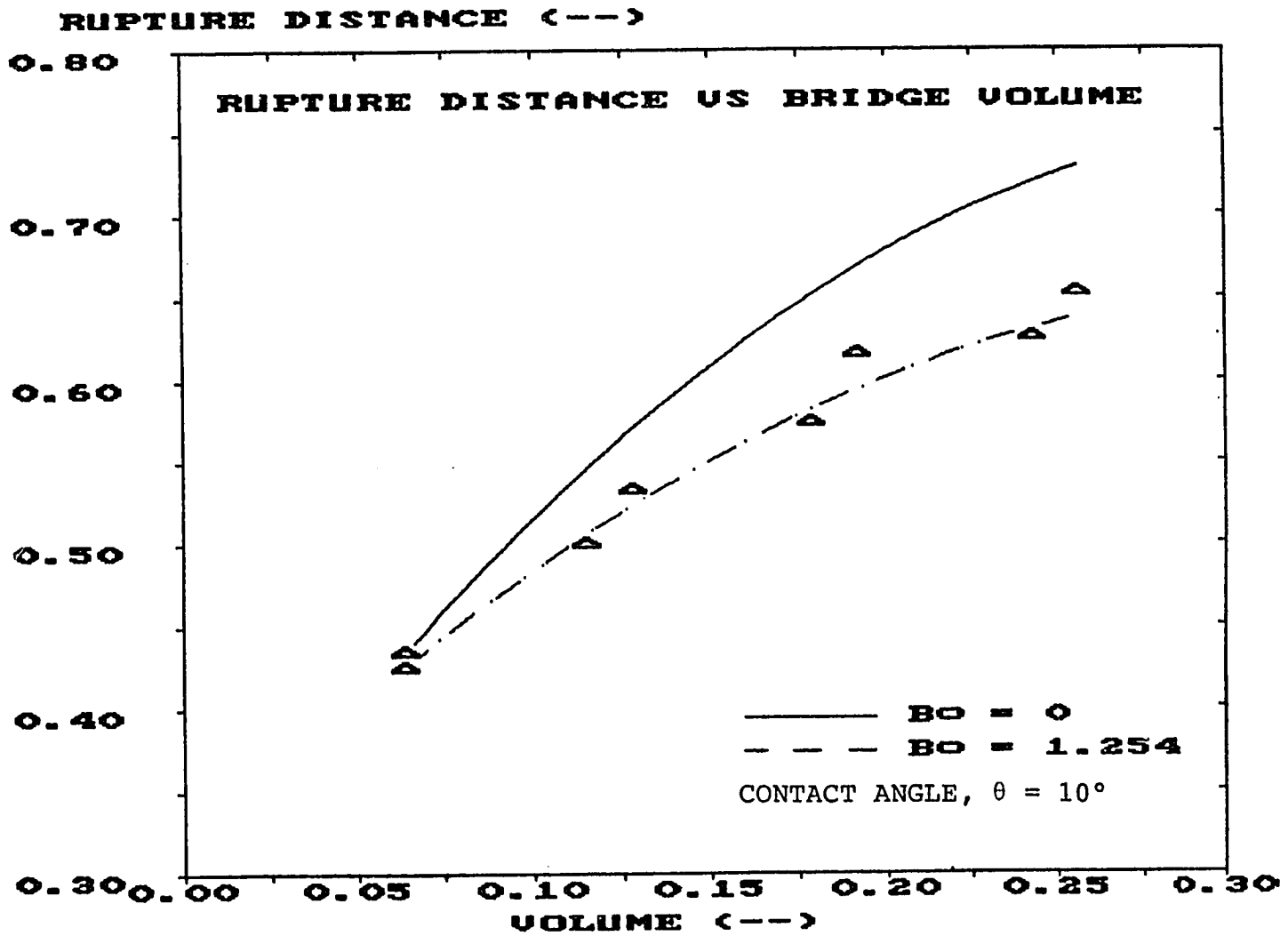

Figure 4.11. Dimensionless rupture distance vs dimensionless bridge volume. Comparison of present experimental data with theoretical model. The influence of gravity on the rupture distance of a static bridge.

seen that as the volume increases the rupture distance becomes strongly dependent on the magnitude of the bond number, Bo.

Even more significant is the difference in the actual profile of the bridge if gravity is taken into account as the particles separate. Figure 4.12 shows profiles for a constant liquid volume (V_b^*=0.1280) and constant separation distance (ξ=.501) when gravity is neglected (Bo=0) and when gravity is taken into account (Bo=1.254). It is clearly seen that gravity acts to distort the profile and render it asymmetric.

The comparison between an actual bridge profile and a calculated one is shown in Figure 4.13. The agreement is seen to be excellent. It is clear from these results why gravity tends to lower the strength of the bridge and make it rupture earlier. For larger values of the Bond number i.e. larger spheres, denser fluids or fluids of lower surface tension, the difference in shape between the gravity free case and the case when gravity is taken into account is even more pronounced. Gravitational effects become even more noticeable when the spheres are far apart (see Figure 4.12); this was also found in the experiments by De Bisschop and Rigole (1982).

4.3 THE BEHAVIOR OF A LIQUID BRIDGE BETWEEN TWO MOVING SPHERES

4.3.1 SPHERES SEPARATING DUE TO GRAVITY

Introduction

During the earlier part of this research, (Section 3.3) it was seen that the theory developed for the minimum gas velocity necessary to maintain stable fluidization in a fluidized bed into which a liquid coating is injected underestimated actual experimental data. The main reason why the theory underpredicted the value of the gas velocity, U_s, is that the aggregate strength is, in fact, larger than that initially assumed (see Section 3.3) which took into account only the liquid surface tension. In reality, the force separating the particles in the agglomerate must also overcome the resistance due to flow of the material

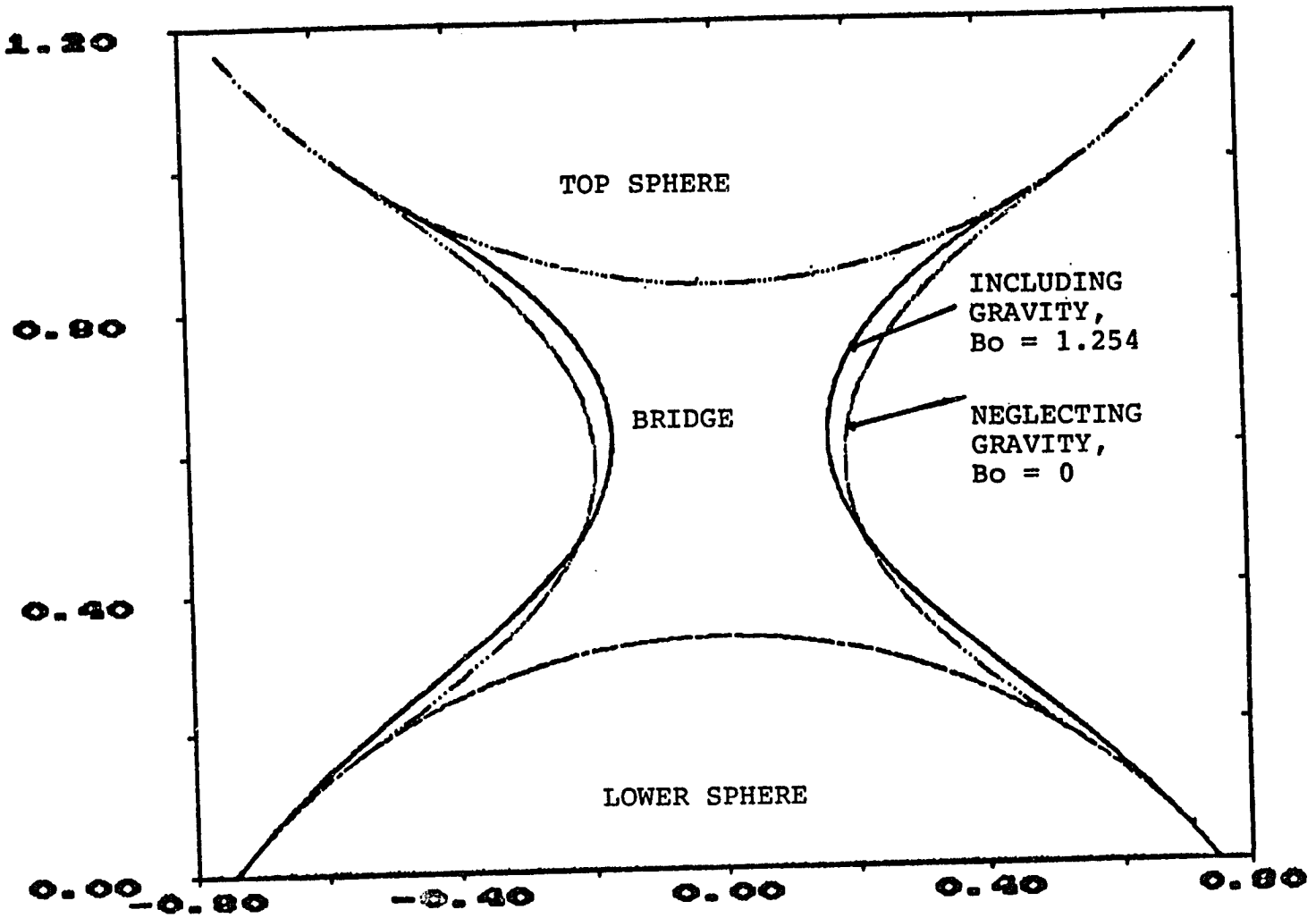

Figure 4.12. The influence of gravity (weight of the bridge) on the shape of the equilibrium profile.

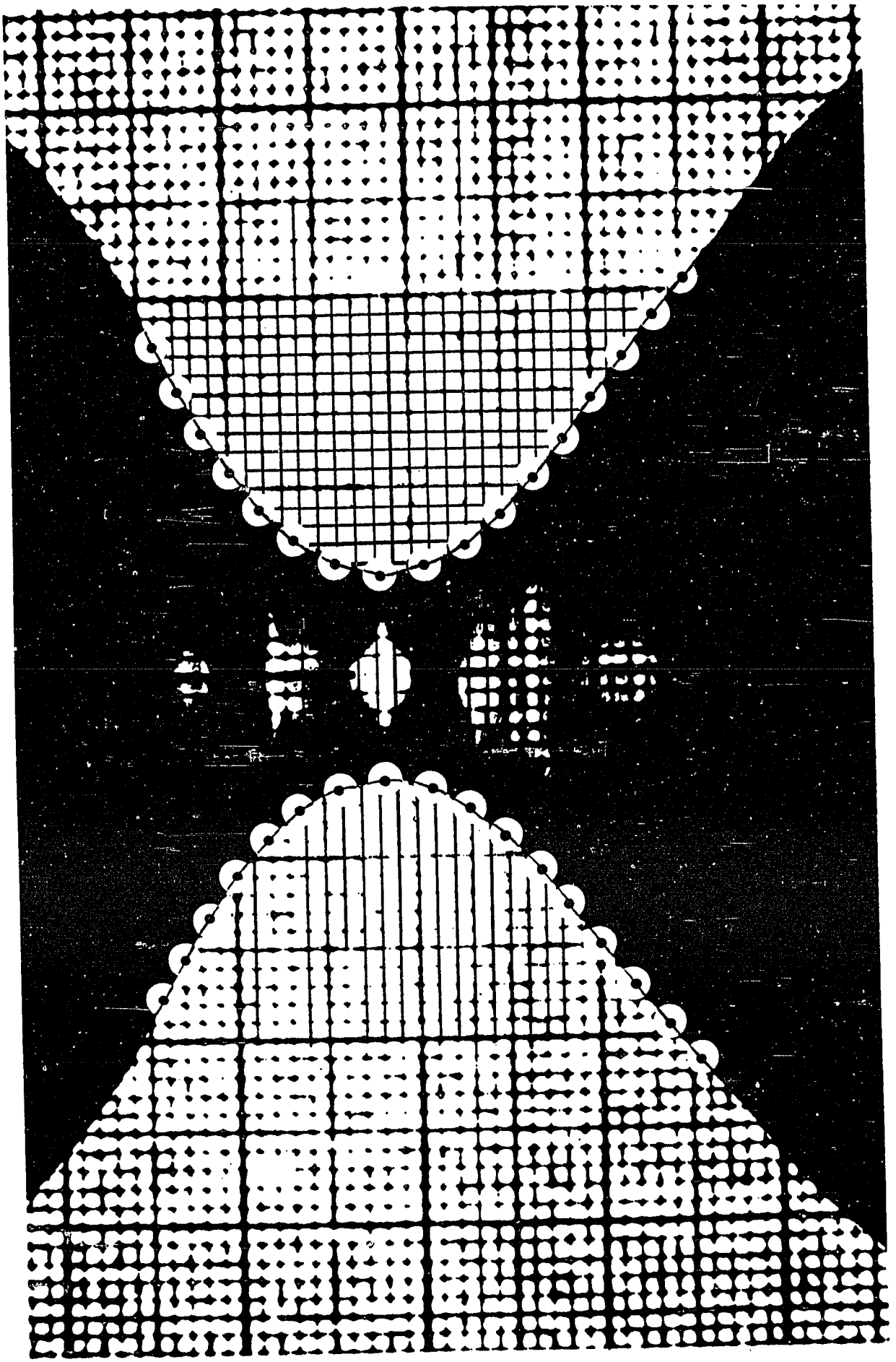

Figure 4.13. Comparison of calculated and observed liquid bridge profile. ($V_b^* = 0.115$, $\xi = 0.500$, $\theta = 10°$)

around the contact point; this was not taken into account in the simplified theory.

A simplified model of the strengthening of a liquid bridge between two moving particles has been developed that takes into account the acceleration of the moving particles and the pressure gradient across the liquid-gas interface; an outline of this theoretical approach is presented below.

Theoretical model

A force balance on a moving sphere-liquid system as presented schematically in Figure 4.14, consists of the viscous force of the liquid bridge resisting separation F_{vis}, the force produced by the fluid-fluid interface f_c and the weight of the lower freely falling sphere, F_w. The force balance obtained is thus:

$$m \frac{d^2x_s}{dt^2} = \Sigma F = F_{vis} + f_c + F_w \qquad (4.11)$$

where t is the time, x_s is the separation distance between the spheres and m is the mass of the falling sphere. The force produced by the fluid-fluid interface is given by:

$$f_c = 2\pi y_o \gamma + \Delta P \pi y_o^2 \qquad (4.12)$$

where y_o is the neck radius (see Figure 4.14), γ is the surface tension and ΔP is the pressure difference across the fluid-fluid interface. There is an inherent simplification embodied in Eq. (4.12), in that it is assumed that the force f_c can be computed from the knowledge of the neck size y_o just as if the bridge were quasi-static at each separation distance. This assumption is not necessarily valid for a fast moving bridge. The weight of the lower sphere is simply:

$$F_w = mg \qquad (4.13)$$

BRIDGE DEFORMATION DUE TO PARTICLE MOTION

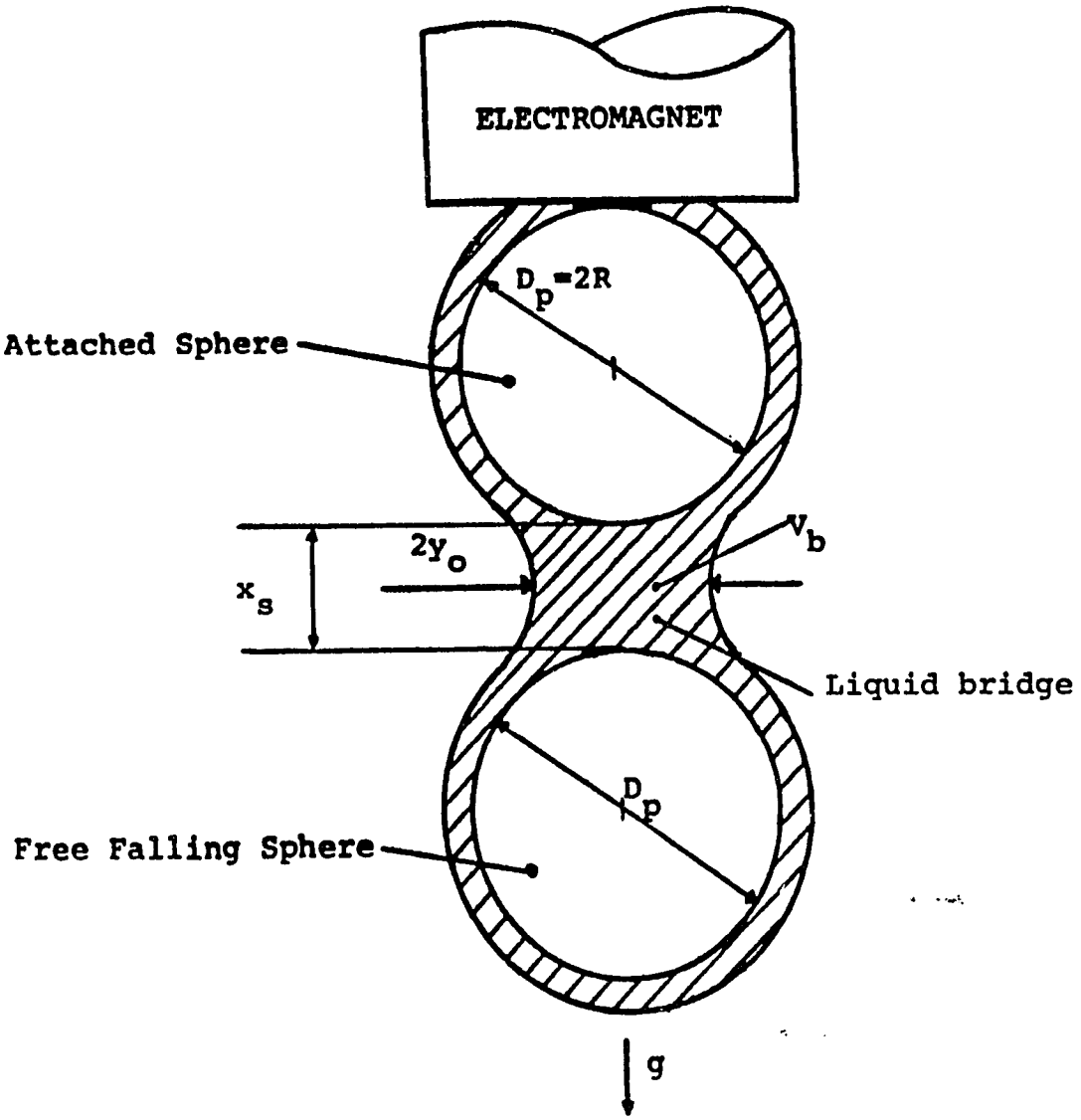

Figure 4.14. Schematic representation of a moving bridge.

The expression for the viscous force can be written in the form:

$$F_{vis} = 6\pi\mu R\lambda_1\left(\frac{x_s}{R}\right)\frac{dx_s}{dt} \qquad (4.14)$$

where μ is the viscosity of the fluid and R is the sphere radius and the function $\lambda_1(x_s/R)$ can take various forms. For small separation distances between two spheres in a infinite fluid, the viscous function λ_1 can be taken as (Weinbaum and Caro, 1976):

$$\lambda_1\left(\frac{x_s}{R}\right) = \left\{1 + \frac{2R}{x_s}\right\} \qquad (4.15A)$$

For small separation distances the classical theory of flow between parallel plates solution using the lubrication simplification (Stefan, 1874) was modified by Adams and Perchard (1984) for flow between two spheres and the viscous function is given as:

$$\lambda_1\left(\frac{x_s}{R}\right) = \left\{\frac{R}{2x_s}\right\} \qquad (4.15B)$$

The Weinbaum and Caro expression is simply an addition of the stokes relation (first term on the right hand side of Eq. (4.15A)) to a viscous resistive term at small separation distances (second term on right hand side of Eq. (4.15A)). At small separation distances the Adams and Perchard (1984) relation is seen to give a viscous force of exactly one-quarter magnitude to that of the Weinbaum and Caro expression.

Another variation of the expression used to compute the viscous force, is to employ the Stokes relation but to integrate the force only along the wetted surface of the spheres and not along the entire sphere surface. Performing such a calculation (Jen and Tsao, 1980) the following result was obtained:

$$\lambda_1\left(\frac{x_s}{R}\right) = \left\{\frac{1}{2} - \frac{1}{2}\cos\alpha\right\} \qquad (4.15C)$$

where α is the filling angle of the liquid bridge. This expression for the viscous force does not have a functional dependence on the separation distance. None of the three expressions for the viscous force Eqs. (4.15A-4.15C) is strictly appropriate to calculate the strength of the bridge since the basic assumption underlying all three equations is that the particles move in an infinite fluid. Clearly this is not the case here (see Figure 4.14) even in the specific situation presented in the figure where both particles (spheres) have a surrounding liquid layer. Combining Eqs. (4.11), (4.12), (4.13) and (4.14) yields:

$$m \frac{d^2x_s}{dt^2} = mg - 6\pi\mu R \lambda_1\left(\frac{x_s}{R}\right) \frac{dx_s}{dt} - 2\pi y_o \gamma - \Delta P \pi y_o^2 \qquad (4.16)$$

Using dimensionless distance and time in Eq. (4.16), defined as:

$$\xi = \frac{x_s}{R} \quad ; \quad \tau = t\,(g/R)^{1/2}$$

and that the mass of the lower sphere is $m=\rho_s V_s = \rho_s 4\pi R^3/3$, the following dimensionless form of Eq. (4.16) is obtained:

$$\left(1 - \frac{d^2\xi}{d\tau^2}\right) = \frac{1}{a^*}\left\{ \lambda_1(\xi) \frac{d\xi}{d\tau} + \frac{F_c^*}{Ca} \right\} \qquad (4.17)$$

where:

$$a^* = \frac{2\rho_s (R^3 g)^{1/2}}{9\mu} \quad \text{and} \quad Ca = \frac{6\mu\,(Rg)^{1/2}}{\gamma}$$

Ca is the so-called Capillary number which relates the effects of viscous to surface tension forces, a^*, is a dimensionless viscosity term, and $F_c^*=f_c/\pi R\gamma$ is the dimensionless strength of the bridge due to surface tension and pressure drop, which is a function of bridge volume V_b^* and separation distance, $F_c^*=f(V_b^*,\xi)$. In equation (4.17) the resistance to gravitational acceleration (left hand side of the equation) is equated to forces due to viscous dissipation, surface tension and pressure,

which tend to keep the particles together. The relative magnitude of the terms on the right hand side of the equation are directly related to the Capillary number, Ca and the dimensionless viscosity term, a^*. Large values of the parameter Ca correspond to liquids of high viscosity, so that the first term on the right hand side predominates as compared to the second term (surface tension). Moreover, the acceleration term on the left hand side of Eq. (4.17), $d^2\xi/d\tau^2$, will grow steadily as the lower sphere falls from a constant value at τ=0 to a final value of one; at this value there is no resistance to motion due to the presence of the liquid bridge and the right hand side of Eq. (4.17) becomes equal to zero. It should be noted that, at this point the integrity of the bridge may still be intact (bridge not ruptured yet) but there is no noticeable attractive force due to the liquid bridge.

In order to solve the differential equation (4.17) initial conditions for the system must be specified:

$$\xi = \xi_o \qquad \text{at } \tau = 0 \tag{4.18}$$

$$\frac{d\xi}{d\tau} = 0 \qquad \text{at } \tau = 0 \tag{4.19}$$

It is sometimes possible to impose rupture conditions while solving equation (4.17) and thereby compute the distance and the resistance of the bridge at that point. One possible way to specify such a condition is to assume that the bridge deforms as a jet where the Plateau or the Rayleigh instability condition applies:

$$L_b > 2\pi R_o \tag{4.20A}$$

or in dimensionless form (see Figure 4.15)

$$L_b^* > (4\pi V_b^*)^{1/3} \tag{4.20B}$$

Breakage occurs due to instability of the elongated bridge.

Rupture condition according to Plateau and Rayleigh:

$$L > 2\pi R_o$$

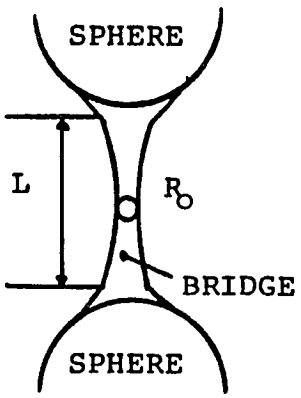

where L and R_o are related to the initial volume of the bridge.

$$L^* > (4\pi V_b^*)^{1/3}$$

Figure 4.15. Rupture condition for a moving bridge.

where L_b is the length of the bridge, R_o is the radius at rupture, V_b is the bridge volume which excludes the liquid material which sticks to the spheres and $L_b^* = L_b/R$ and $V_b^* = V_b/R^3$. Equation (4.17) was solved using a fourth order Runge-Kutta method (computer listing is given in Appendix A.2); integration starts by applying the initial conditions and ends when the rupture condition is satisfied. The trajectory of the falling particle is thereby obtained.

Experimental

In order to verify the model of dynamic separation of two particles and to compare the strength of the moving liquid bridge to the static case, a set of experiments was performed, using the experimental apparatus shown schematically in Figure 4.16. A small steel sphere of high magnetic permeability and low retentivity was permanently attached to an electromagnet and a liquid of known viscosity and surface tension was adhered to the sphere. A second identical sphere was then placed below the first sphere with the aid of a 3-dimensional positioner. With the electromagnet power on, the lower sphere was attached and held fixed below the top sphere. The entire setup was mounted in the viewing field of a Nikon 6C projection microscope which was rotated 90^o to allow for the vertical displacement of the lower sphere. The alignment of the lower sphere could be performed accurately with the aid of the Nikon microscope. The microscope has a "surface" and "shadow" illumination mode; the shadow mode allows one to see the sphere-liquid-sphere system on the projection screen. The surface mode was used to send a high intensity light source from behind the sphere-liquid-sphere system directly into the lens of a high speed camera positioned in the line of vision (see Figure 4.16). This was required because high intensity light was needed for the high camera frame-rates used during the experiment. The high speed camera used was a HYCAM model K20S4E which is capable of frame rates of 50-10,000 frames/sec. The camera has an "Event Synchronization" feature which is simply a follower arm that

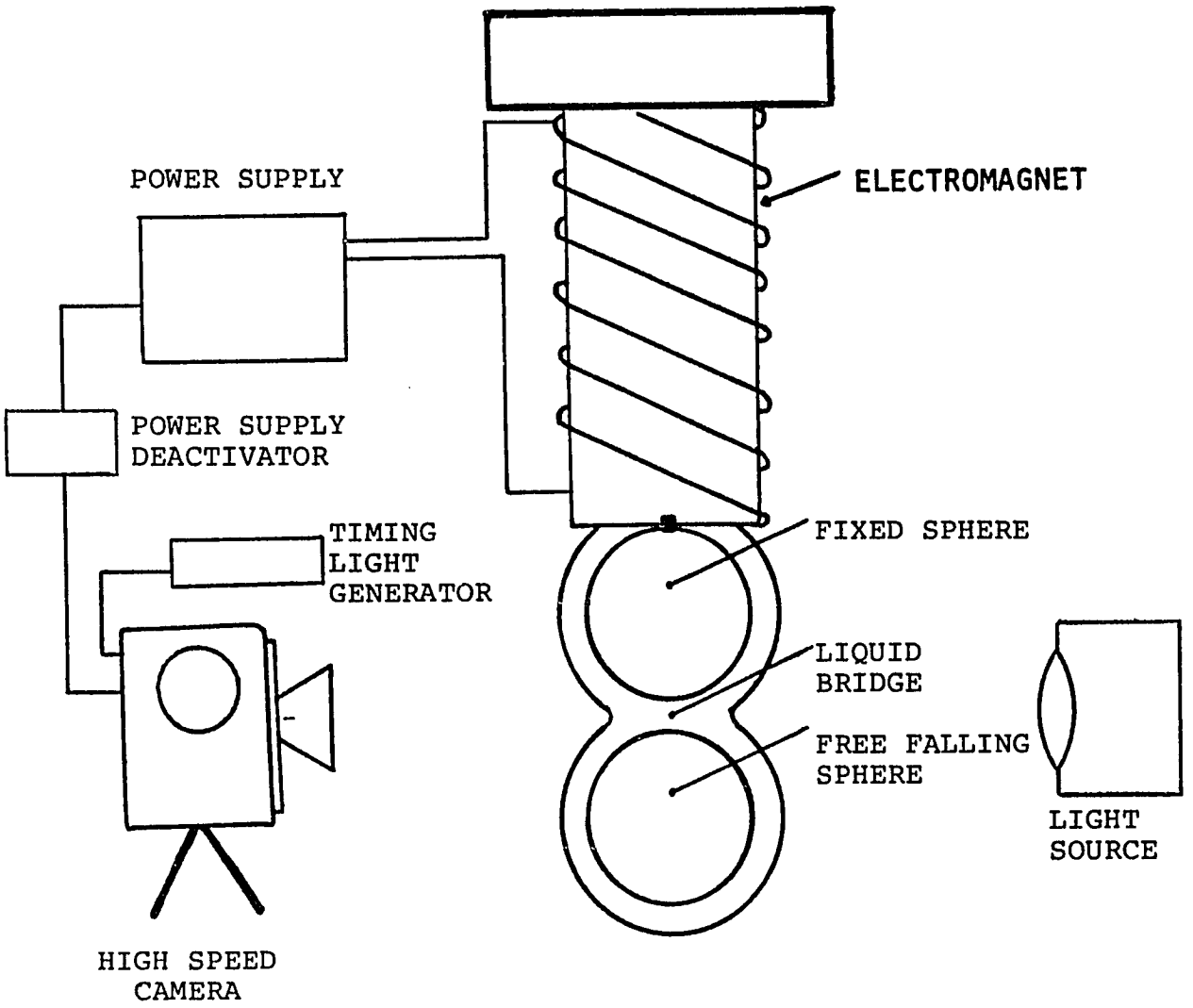

Figure 4.16. Schematic representation of the set-up to study dynamic strengthening of a liquid bridge.

rests against the film spool; when the arm reaches a predetermined position (footage of film taken-up), the event switch actuates, opening the event circuit which deactivates the power to the electromagnet that holds the lower sphere. In addition, since the film accelerates before it reaches a steady state speed, a timing light generator was used to pulse a light beam onto the outer edge of the film every 1/1,000th of a second. By using the event synchronizer and the timing light generator accurate time measurements were obtained.

A typical experiment was carried out as follows: the camera start switch was flipped on and the electromagnet power was energized. The event synchronizer would then deactivate the power to the electromagnet after a certain footage of film had been used (for example, 25 feet of a 100 feet roll) to ensure steady speed of the film. The camera would record the fall of the lower sphere and the movement (flow) of the bridge. The lower sphere, having a known mass, fell with a time varying acceleration which tended to be less than gravitational acceleration due to the presence (resistance) of the liquid bridge.

The shape of the interface, the time and distance of breakage, the acceleration as a function of time, as well as, the force due to the liquid bridge were determined from the analysis of the movie film. The separation distance and time for each experiment were determined using frame by frame measurement of the distances between the spheres. The time of each frame was determined by the timing light on the edge of the film frame. Experiments were performed with fluids of varying liquid volume, viscosity and surface tension so that the variation due to each parameter could be obtained.

A typical set of experimental data as obtained by frame by frame analysis is shown in Figure 4.17. The figure contains a plot of separation distance vs time for a liquid bridge of 0.5μL in volume using an Immersion oil of viscosity, μ =12.5 Poise and surface tension, γ=31.5 dyne/cm. As seen, there is a time-lag before the bottom sphere started to noticeably separate. A fourth order least square fit of the experimental data was

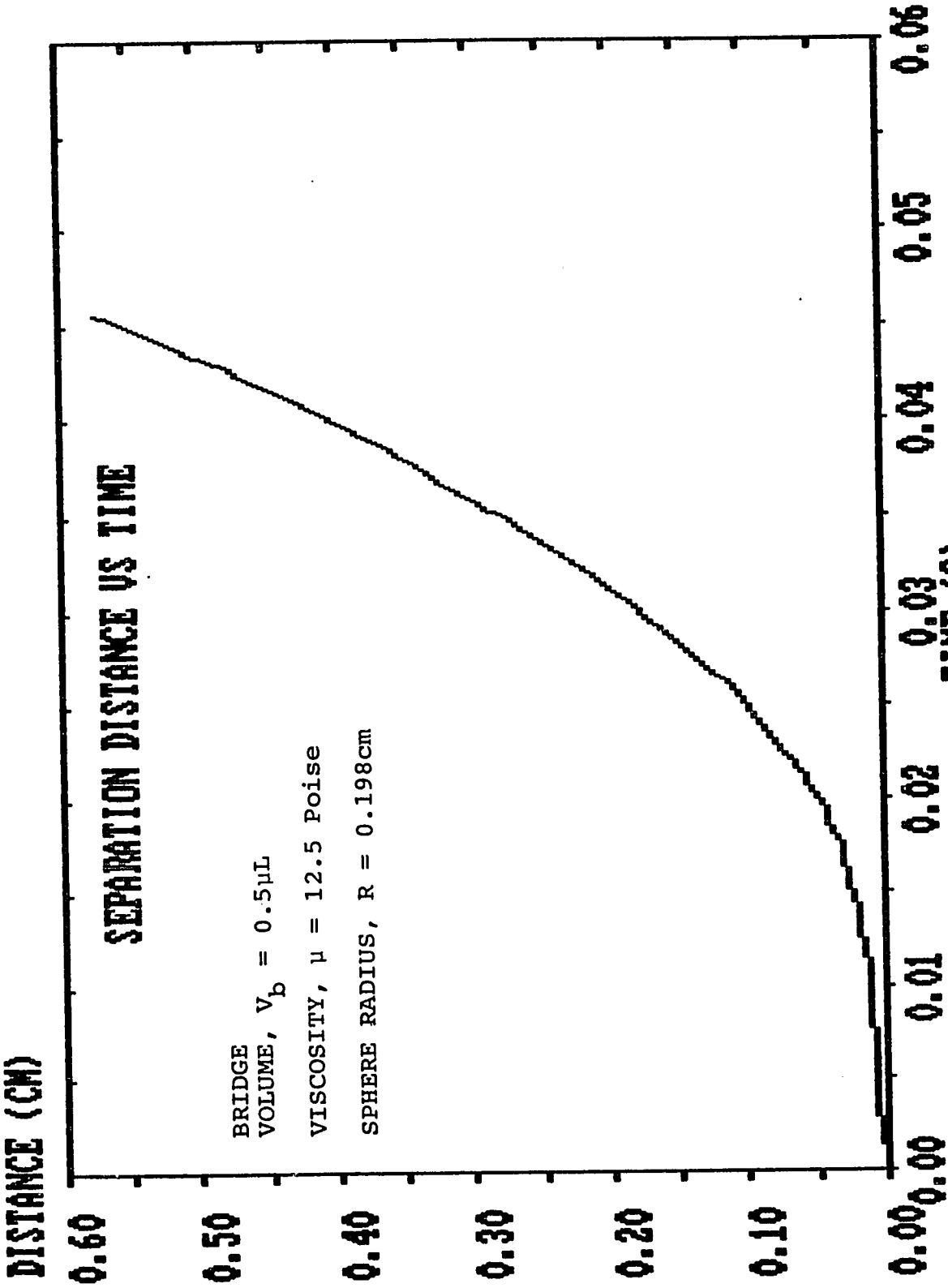

Figure 4.17. Separation distance vs time for an immersion oil liquid bridge. Experimental result obtained from frame-by-frame analysis.

performed; the resulting polynomial is differentiated twice to obtain the acceleration of the falling sphere as a function of time. Figure 4.18A is a plot of acceleration versus time of fall. As seen in the figure the acceleration does not reach a plateau at an acceleration of 980cm/s^2 as it should. This discrepancy is attributed both to the error in measurement and to the taking of second derivatives from "measured" data. To remedy this, a plateau was forced onto the data by setting all points greater than 980 cm/s^2 equal to 980 cm/s^2; Figure 4.18B contains the result of this modification. In order to obtain the strength of the bridge from the above data the ordinate of Figure 4.18B is subtracted from the gravitational acceleration g and then multiplied by the weight of the lower sphere. The procedure to calculate the retardation force exerted on the lower sphere due to the liquid bridge is simply seen to be the sum of terms on the left hand side of the Eq. (4.17). Some results using this procedure are shown in Figure 4.19 for the Immersion oil-sphere system. From the original data (see Figure 4.17), the time is also related to its appropriate separation distance and thus the retardation of the bottom sphere as a function of distance is obtained. In the figure, the force was made dimensionless by $F_c^* = f_c/\pi\gamma R$ and the distance by $\xi = x_s/R$. The above method was used for all dynamic separation experiments performed and the results are given in the next section.

Results and discussion

Trajectory and strength measurements as described above were performed with a variety of fluids with different viscosities and surface tensions. First a dibutylphtalate (DBT) liquid (static experiments were performed as described in section 4.2) with a relatively low viscosity of μ = 0.14 Poise and a surface tension of γ = 32.2 dyne/cm was used. The measured trajectory and rupture distance were compared to the values calculated using the solution given by Eq. (4.17) with initial conditions, Eqs. (4.18-4.19) and the rupture condition, Eq. (4.20). Since there was no

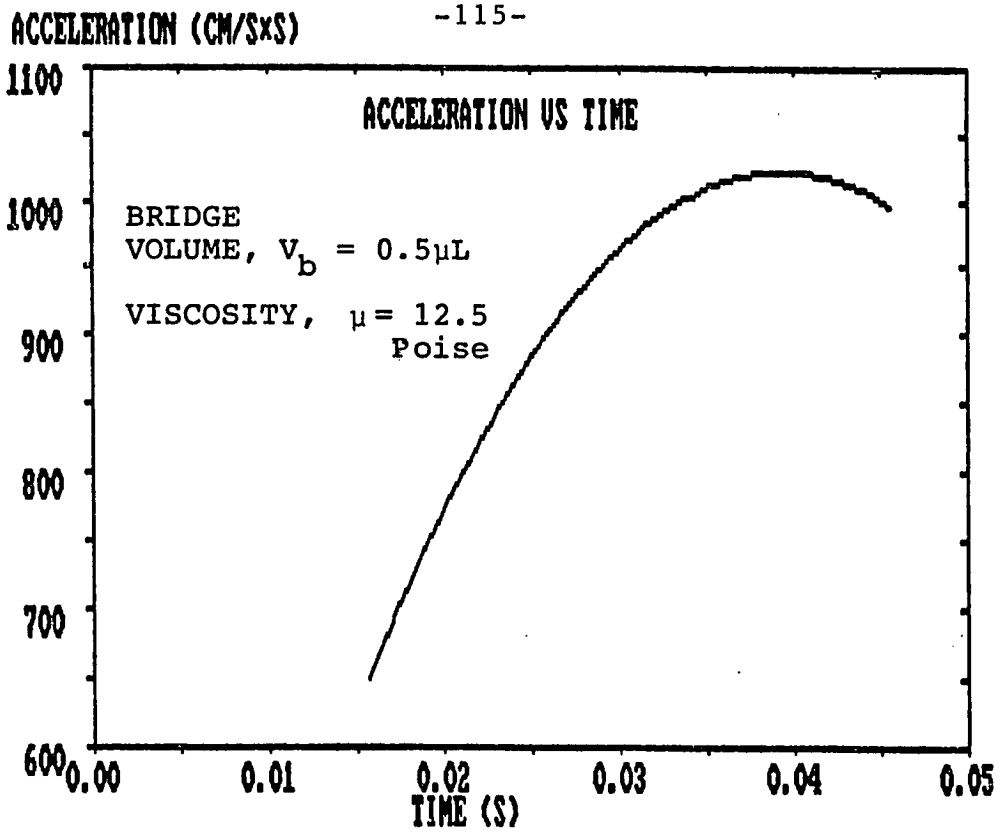

(A)

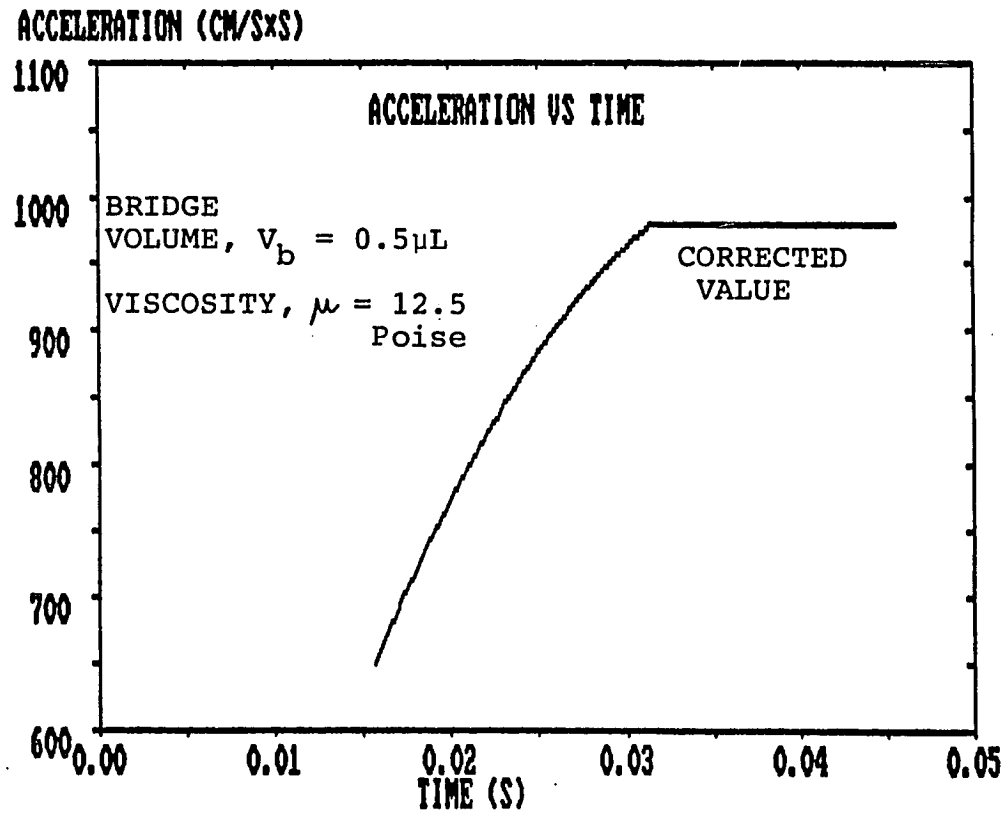

(B)

Figure 4.18. Acceleration vs time for an immersion oil liquid bridge.

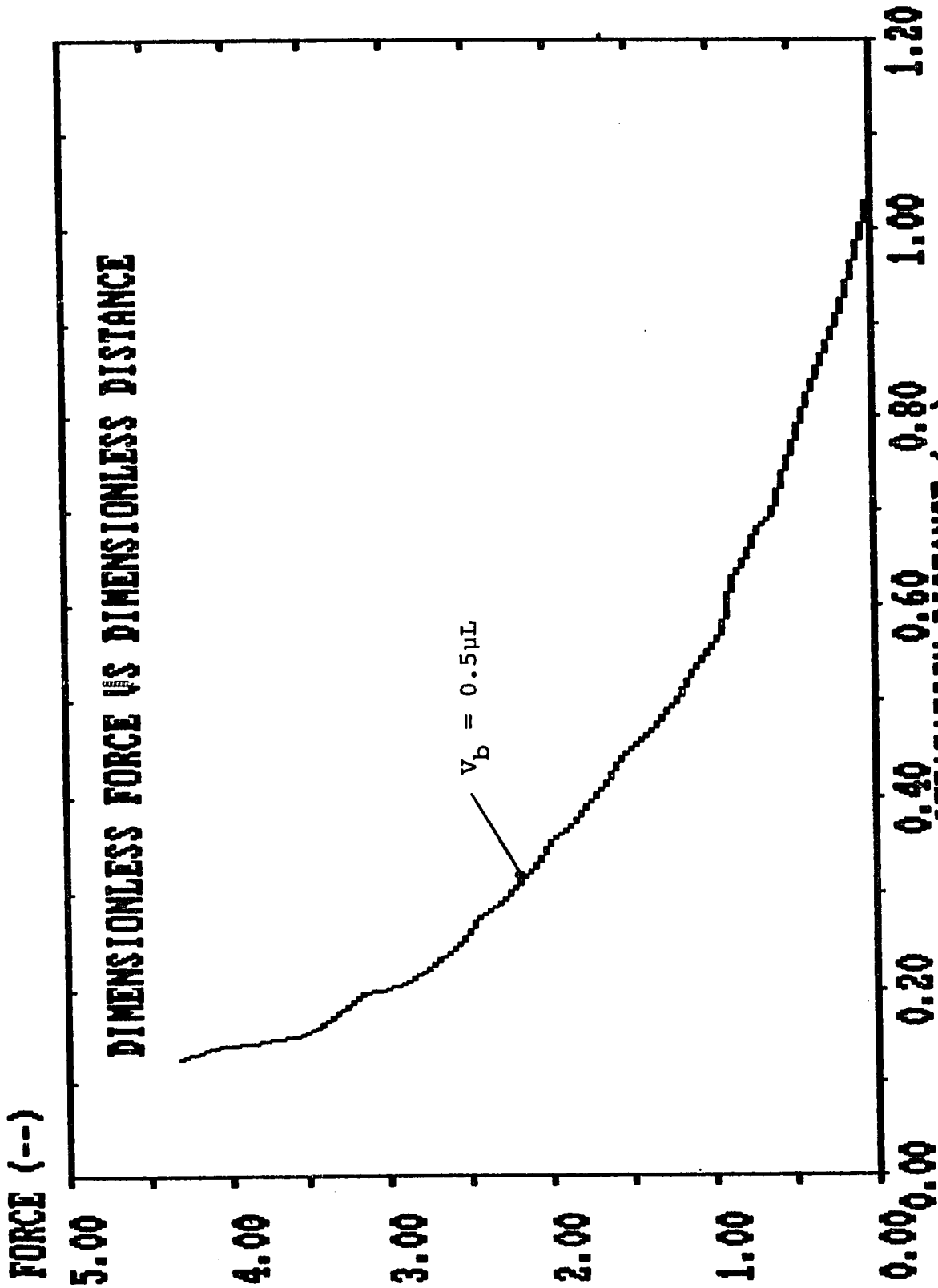

Figure 4.19. Dimensionless force vs dimensionless separation distance for an immersion oil liquid bridge.

direct way of measuring the force due to the fluid-fluid interface, F_c^* was taken as the corresponding force from the static experiments Eq. (4.7), $F_c^*=f(V_b^*,\xi)$. Also since Eq. (4.17) becomes unbounded when the two spheres just touch ($\xi=0$), when equations (4.15A) or (4.16B) are used for the viscous force, the initial separation distance $\xi=\xi_o$ was left as a free parameter.

Figure 4.20 shows the comparison of the theory with experimental data for the DBT system with $V_b^*=0.1152$, Ca=.368, $a^*=31.2$ and the volume of the cylindrical liquid rod which is subject to rupture (see Figure 4.15) taken as 60% of the total bridge volume. The data is given as dimensionless distance $\xi=x_s/R$ vs dimensionless time $\tau=t(g/R)^{1/2}$ and uses the viscous force expression due to Weinbaum and Caro (1976) (Eq. (4.15A)). The general form of the numerically generated curves are similar to the experimental data and when the initial separation distance is taken as $\xi_s=0.050$ the model fits the data well. For this particular fluid-sphere system the viscous effects on the overall strength of the liquid bridge were not very strong so that the Weinbaum and Caro expression for the viscous force gave good agreement with experimental results.

Dimensionless separation distance vs dimensionless time for a 1.0μL and μ=12.5 poise Immersion oil-sphere system is shown in Figure 4.21. On the same figure, the theoretically calculated results using the solution of Eq. (4.17) with F_{vis} given by each of the three previous expressions for the viscous force is shown (ξ_s=.09, the actual experimental value at which separation distance started to noticibly change with time). It is seen that the prediction using the first two expressions for the viscous force term, $\lambda_1(\xi)$, gives poor results when compared to the experimental data. The reason for this discrepancy is, as pointed out earlier, that the viscous resistive term, F_{vis} (see Eqs. (4.15A) and (4.15B)) is strictly valid only when the spheres are totally immersed in the fluid. Since the fluid is of relatively high viscosity the viscous term in Eq. (4.17) predominates, therefore the Weinbaum and Caro and Adams and Perchard relations both overpredict the viscous force at small separation distances.

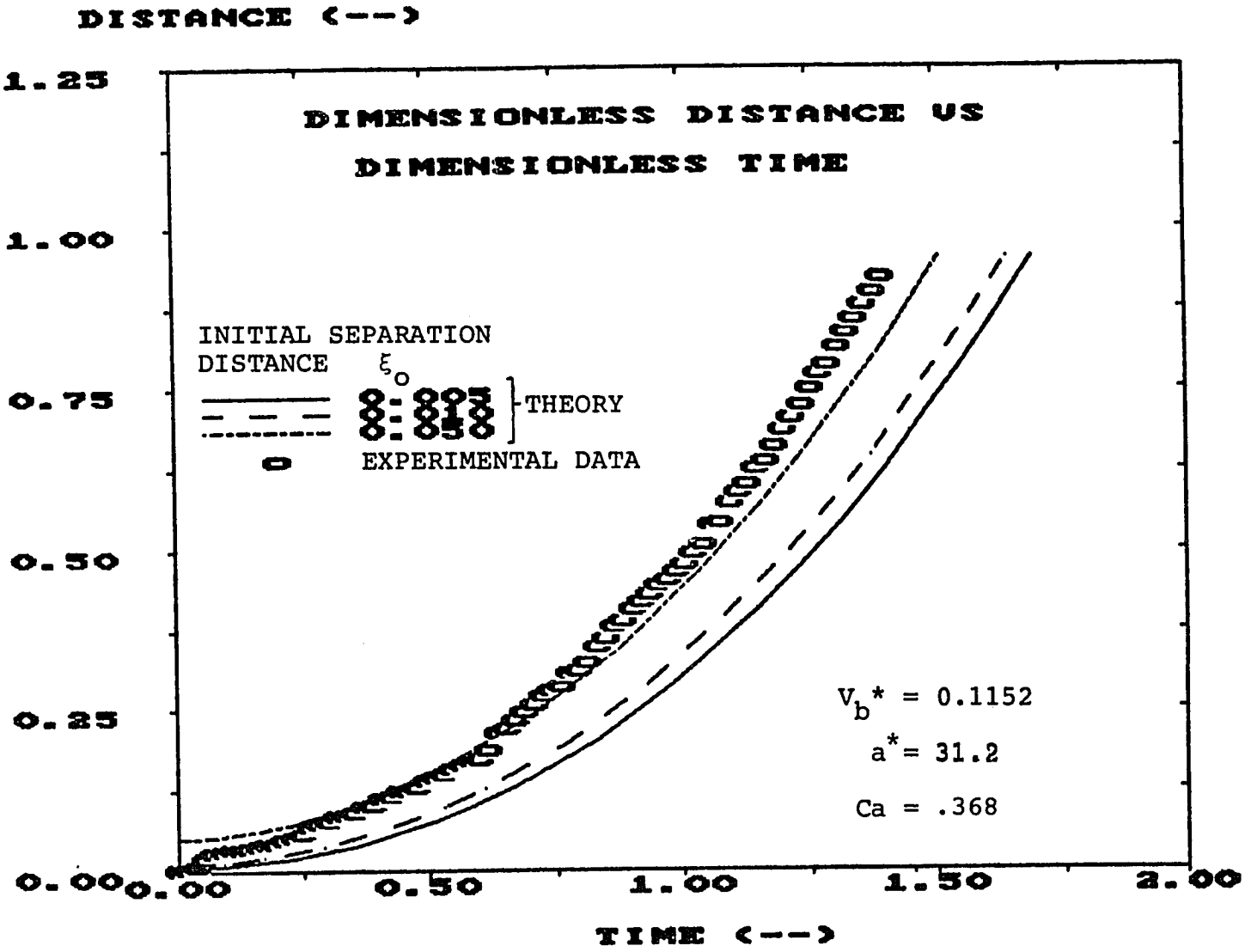

Figure 4.20. Dimensionless separation distance vs dimensionless time for a dibutylphtalate (DBT) liquid bridge. Comparison with theoretical results.

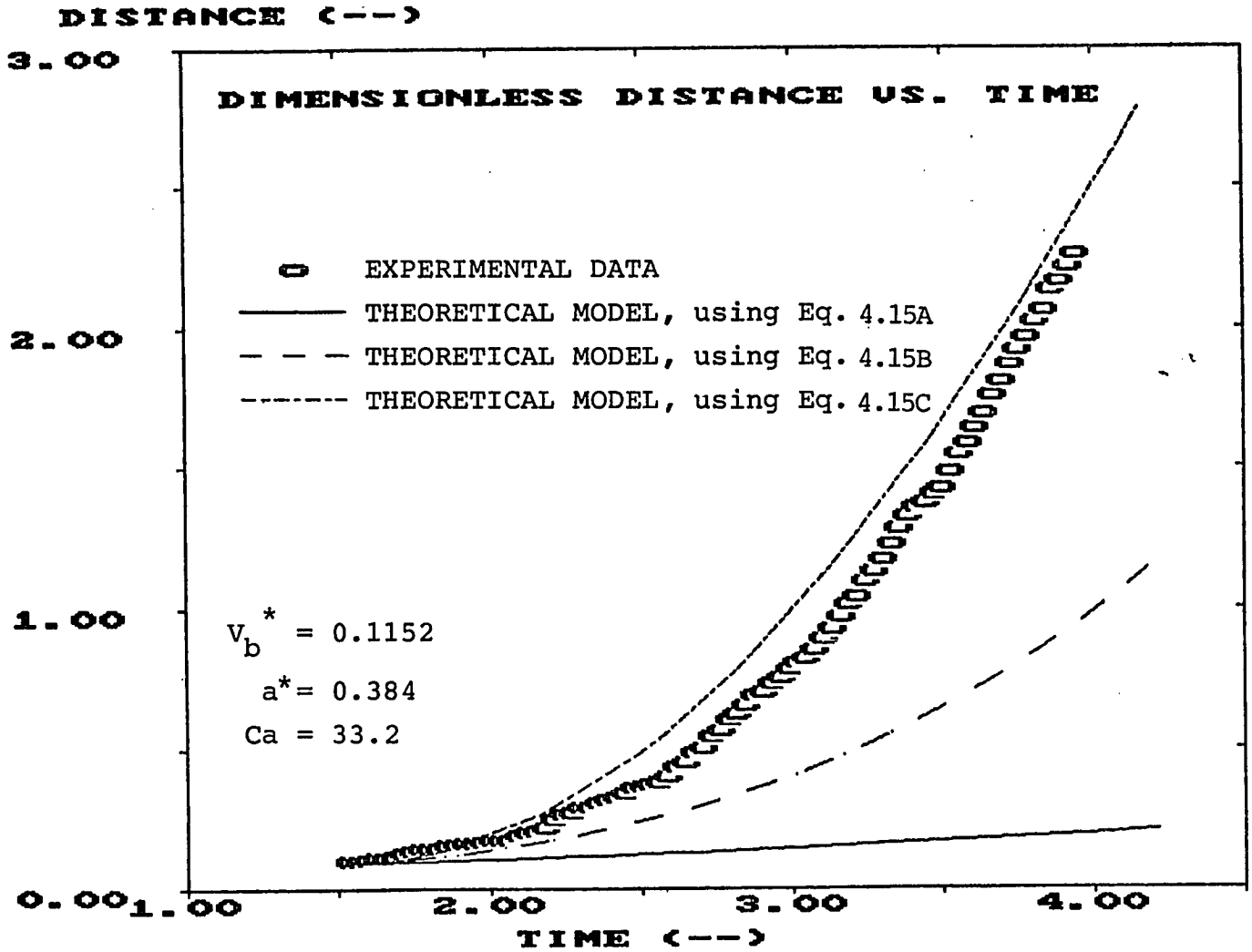

Figure 4.21. Dimensionless separation distance vs dimensionless time for an immersion oil liquid bridge. Comparison with theoretical results.

The overprediction of the viscous force in the model causes the strength of the bridge to be much larger than it actually is and thus, the spheres separate according to the model at a much slower rate than in reality. The last expression used for the viscous force which integrates the force along the wetted surface of the sphere up to the filling angle, α, (see Eq. (4.15C)) compared best to experimental data. For this experiment the filling angle which actually changes slightly as the spheres separate was taken to be the maximum value which is when the spheres are just touching.

Finally the separation vs. time for the very viscous 125 poise Dow Corning Silicone fluid of $V_b = 1\mu L$ was compared to the model using the Stokes expression for the viscous force (Eq. (4.15C)) with various values of the filling angle as a parameter; this comparison is shown in Figure 4.22 (once again Eqs. (4.15A) and (4.15B) greatly overestimate the actual viscous force). As seen, the best fit of the model to the experimental data occurs when the filling angle is not the maximum but some intermediate value between the maximum (spheres just touching) and the minimum (rupture of the bridge).

Further experiments were performed to study the influence of the fluid viscosity and the bridge volume on the strength of the bridge. Figure 4.23 shows a log-log plot of force vs separation distance of the Immersion oil system for two liquid volumes of $1.0\mu L$ and $0.5\mu L$. For small separation distances the larger liquid volume, $V_b = 1.0\mu L$, results in a greater retarding force at a given separation distance as compared to the bridge with the smaller volume, $V_b = 0.5\mu L$, but, as the separation distance increases the force decays very quickly and at a certain point becomes less than the force due to the smaller volume bridge. At larger separation distances there is no significant viscous retardation effect due to the presence of the liquid and, in fact, the greater liquid volume acts to separate the lower sphere more quickly because of the increased mass of the liquid-sphere system. Figure 4.23 also shows the corresponding strength of the

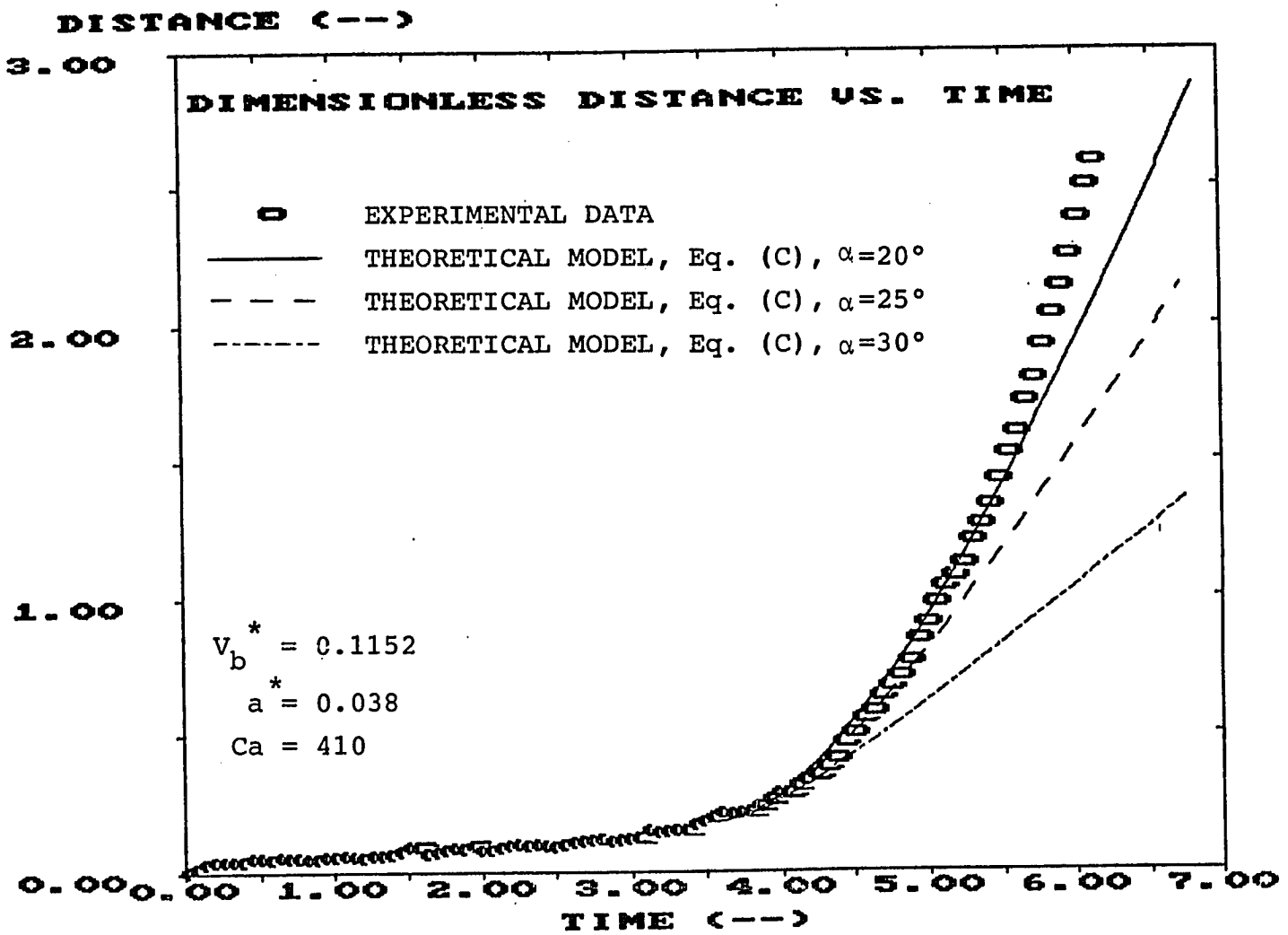

Figure 4.22. Dimensionless separation distance vs dimensionless time for a 125 poise liquid bridge.

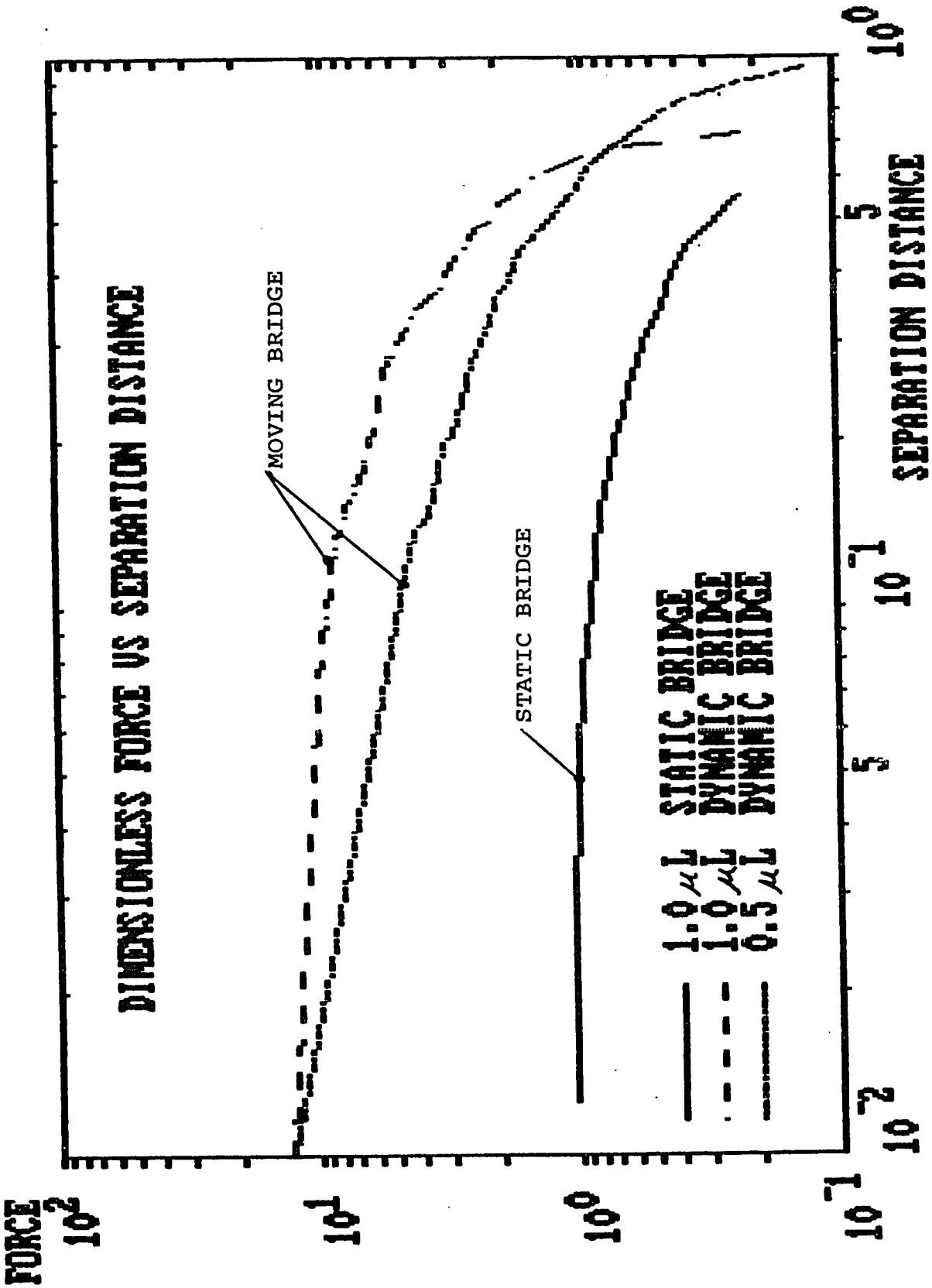

Figure 4.23. Dimensionless force vs dimensionless separation distance for an immersion oil liquid bridge. The influence of liquid volume on the strength of the bridge.

liquid bridge for the case where the spheres are slowly separating as determined from a static experiment performed on a similar system with a liquid volume of 1μL (see Section 4.2). For a wide range of distances the dynamic strength is about an order of magnitude larger than the corresponding force given by the static experiments. Moreover, the rupture distances for the dynamic experiments were 2-3 times larger than those for the static case. At the point where the strength becomes close to zero (see Figure 4.23) the bridge may still be intact. Indeed, when the acceleration of the falling sphere system reaches 980cm/s^2, it doesn't matter whether the integrity of the bridge is maintained or not because there is no attractive force between the spheres at that point.

Figure 4.24 contains a log-log plot of the dimensionless force vs separation distance for the entire range of fluids studied with viscosities ranging from 0.14 Poise to 300 Poise. It is seen that as the viscosity increases from the lowest to the largest value, the corresponding strength of the bridge at a given separation distance increases. For each curve there is an initial region where the force varies linearly with the separation distance. Above a certain separation distance, which varies for different viscosity fluids, the force decreases at a very high rate until it eventually drops to zero as the falling sphere reaches gravitational acceleration. It should be noted that for the case of the 300 Poise fluid the downward trend was not observed as with the other fluids studied. In this case the lower sphere accelerated so slowly that it did not reach gravitational acceleration until it was out of the field of view of the movie camera and therefore only the initial linear portion of the force vs distance was obtained.

4.3.2 SPHERES SEPARATING AT FIXED VELOCITY

As described in the previous Section (4.3.1) the method of measuring the resistance of the dynamic bridge was accomplished

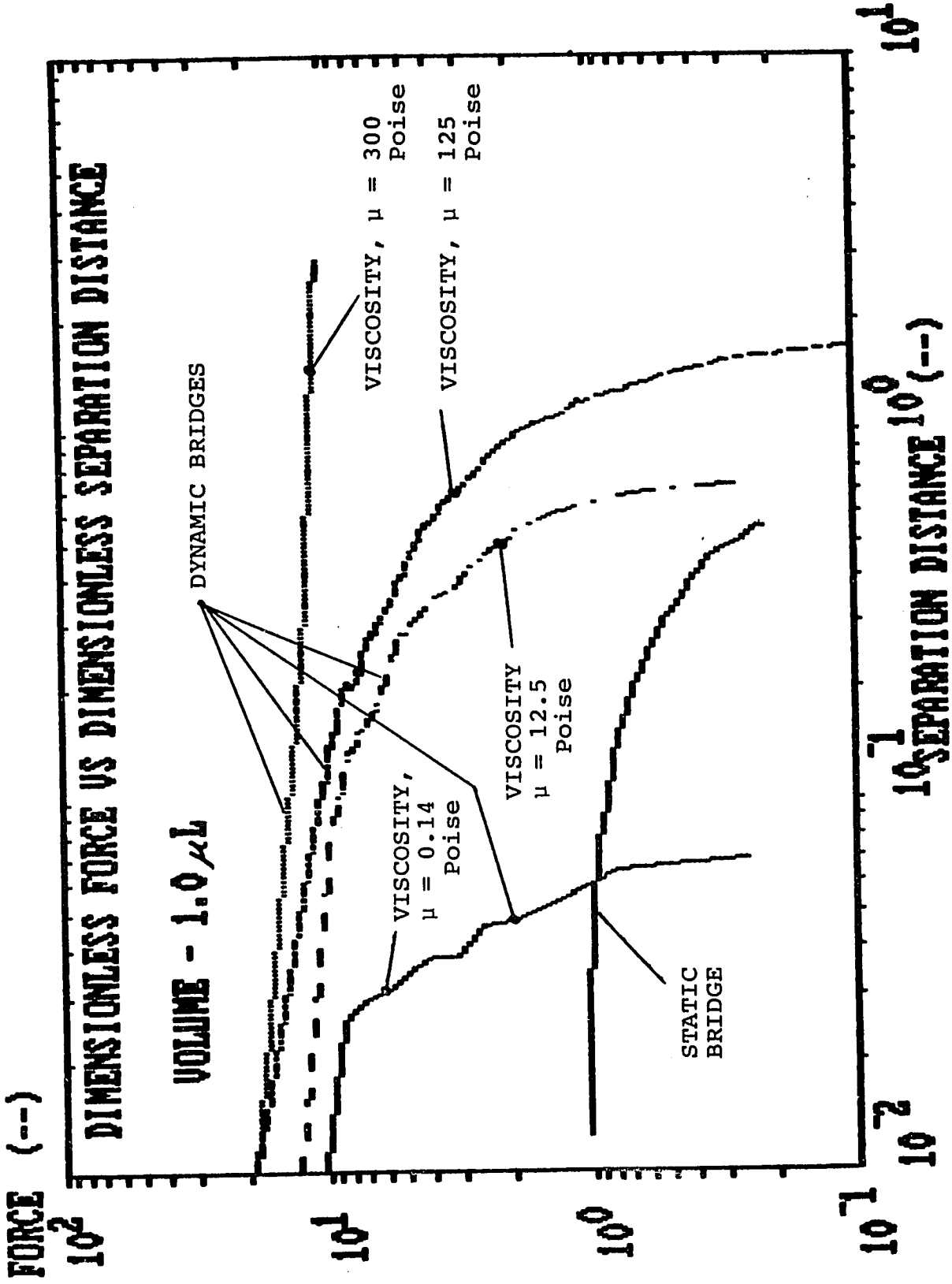

Figure 4.24. Dimensionless force vs dimensionless separation distance for various viscosity liquid bridges.

by using frame by frame analysis of a high speed movie film. The inherent problems in this method were that each experiment involved the exposure of a 100 foot roll of film of which, roughly, 5 feet contained the experimental run. The film then had to be developed and tediously analyzed frame by frame.

In order to measure the force directly, to be able to vary the separation velocity of the two spheres and to perform experiments faster and more accurately, the experimental setup described in Section 4.3.1 was modified. Figure 4.25A contains a photograph and Figure 4.25B shows a schematic representation of the new experimental apparatus. The bottom sphere, instead of falling due to gravity, is connected to a dual motion gas actuated piston (Bimba, model 011-DP). The piston rod is capable of moving in an inward or outward stroke depending on the direction of the high pressure gas flowing through the piston cylinder. Two pressure lines go from the piston cylinder to a four way solenoid valve (Asco Red Hat, model 8345E1) which subsequently is connected to a nitrogen gas supply tank. The four way solenoid valve acts to reverse the nitrogen flow through the piston and as a result the piston rod retracts separating the bottom sphere from the top sphere at a given rate. Each of the two pressure lines from the piston to the solenoid valve has a micro valve (Hoke, model 1315M4B) connected to it so that by adjusting the valve the flow rate through the piston would change and the rate of piston separation (sphere separation) could be controlled.

The displacement of the bottom sphere is measured by the use of a Linear Variable Differential Transformer (LVDT, Sangamo model AE12) whose body is held fixed while its core is connected to the retracting piston rod and thus moves with the bottom sphere. The LVDT was connected to a Validyne CD19 high sensitivity carrier-demodulator. The top sphere is mounted onto two strain gauges which form half a Wheatstone bridge circuit. The bridge is completed and the signal amplified using another Validyne CD19 carrier-demodulator which could give up to 1mV/V sensitivity. Since the entire separation process occurs on the

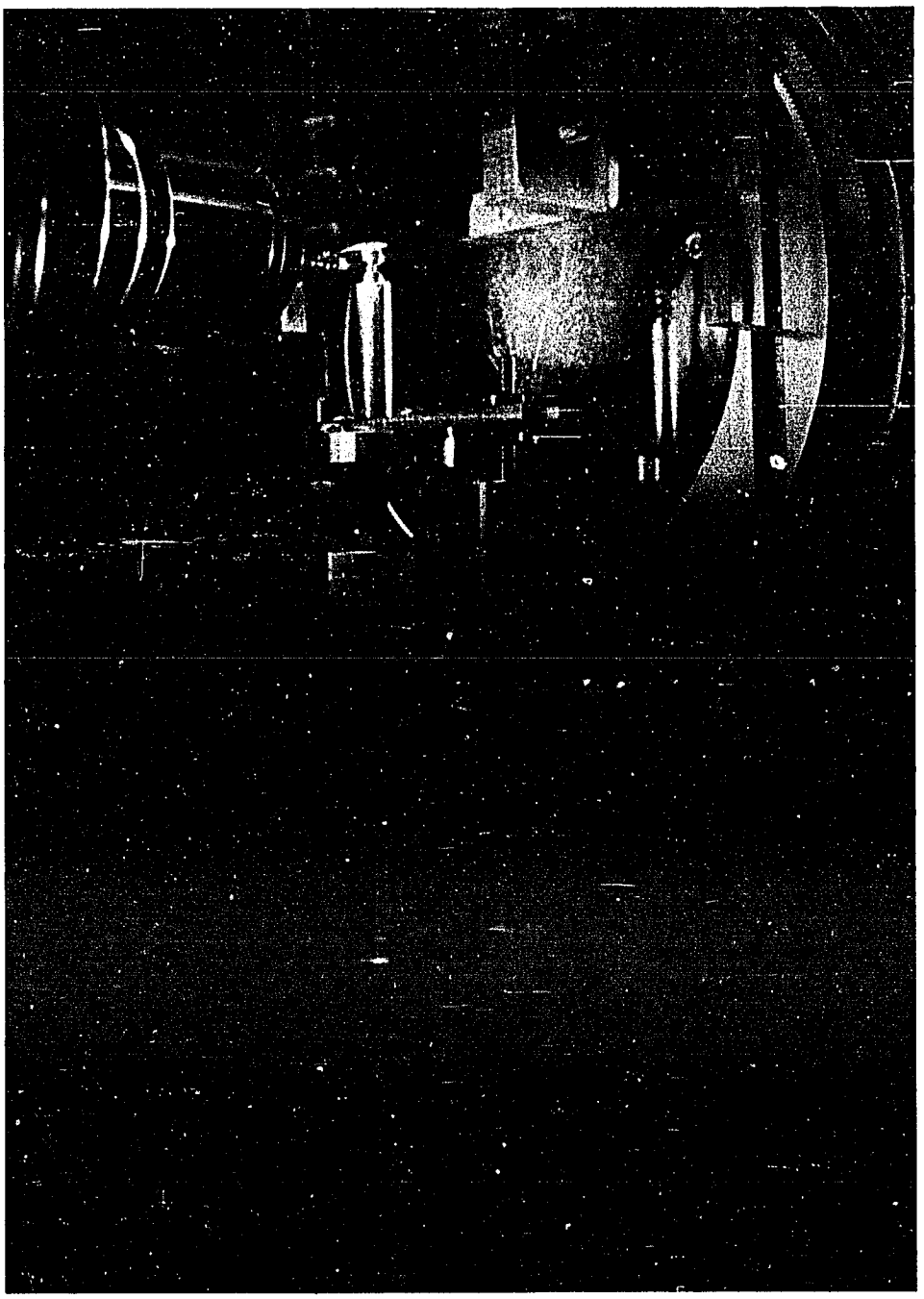

Figure 4.25A. Photograph of the sphere separation at a fixed velocity experiment.

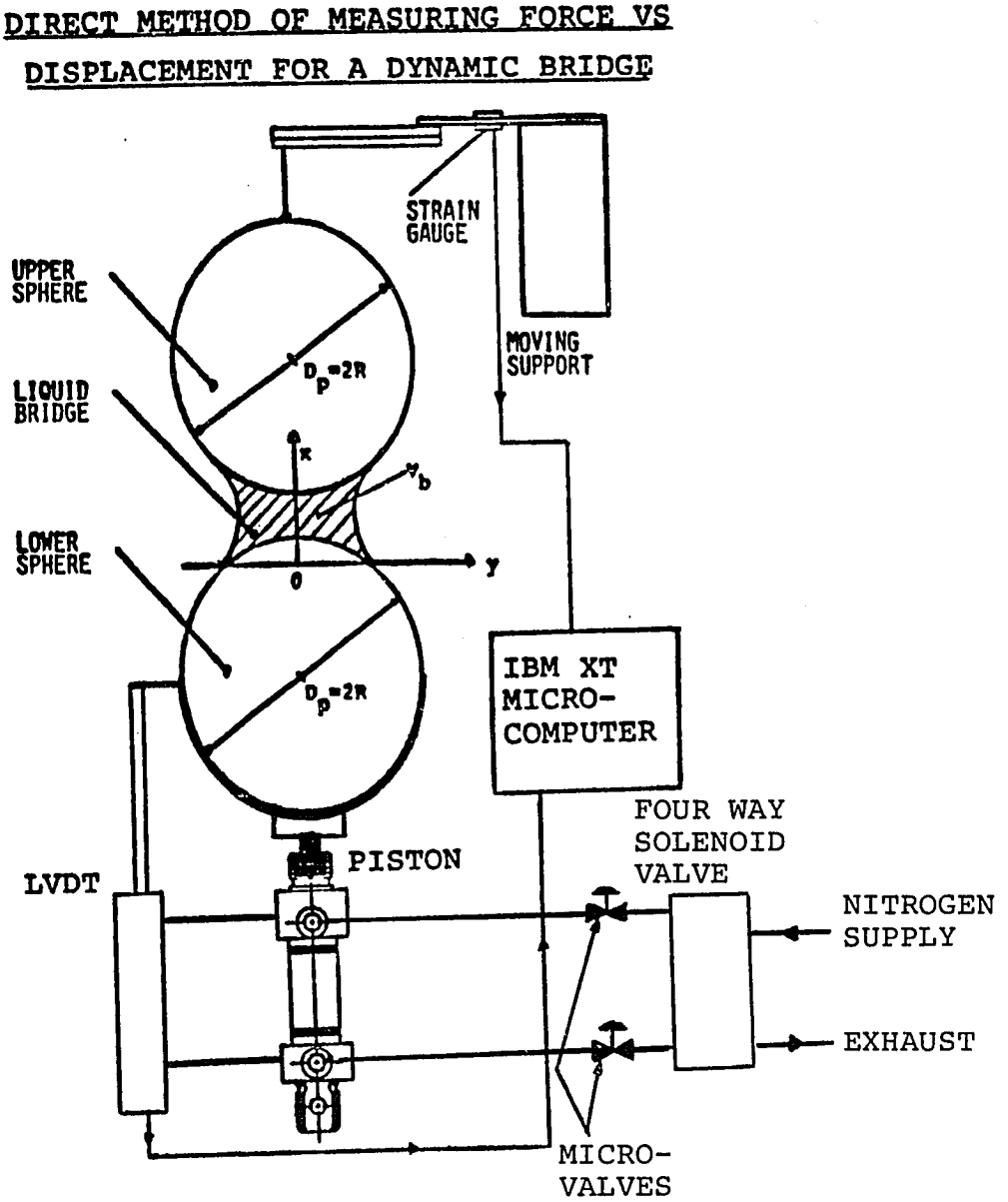

Figure 4.25B Schematic of Direct Method of Measuring Force vs. Displacement for a Dynamic Bridge.

order of one-half a second, an IBM XT microcomputer was used to record the displacement and the force versus time data. The IBM-XT microcomputer was equipped with a Data Translation 2805 Interface board that allowed sampling rates up to 6,000 samples per second (Appendix A.3 contains the computer program PISTON which was used for the collection of data in these experiments). The strain gauge and the LVDT were calibrated as described in Appendix B. With these recorded signals, force versus separation distance was obtained.

A typical experiment proceeded as follows: the piston is held at its maximum stroke by high pressure nitrogen from a gas cylinder supply. The sphere-liquid-sphere system is adjusted so that the spheres are perfectly aligned and just touching. The computer, with a Digital Out signal activates a relay (CRYDOM, model TD1210 solid state relay) which in turn energizes the four way solenoid valve thereby switching the flow of gas through the piston causing the piston rod to retract (bottom sphere separates). The computer records the strain guage and LVDT signal at a given sampling rate and stores it in a file for later data manipulation. In this way, displacement of the sphere versus time, as well as force versus time were obtained.

Experiments were performed using Dow Corning Silicone Newtonian fluids of varying viscosity and also one type of binder material. The velocity was obtained by taking the first derivation of the displacement versus time data. A set of experiments using spheres of radius R = 0.1985cm, bridge volume V_B= 1μL, separation velocity v_s= 22 cm/s and three different viscosities of 10, 5 and 2 poise is shown in Figure 4.26. The force was made dimensionless with respect to the maximum static force of the liquid bridge obtained from static bridge strength experiments (see Section 4.2). The displacement was made dimensionless with respect to the sphere radius, R. It is seen that the strength of the dynamic bridge is proportional to the viscosity of the fluid. From the figure it is seen that the force reaches a maximum not at zero separation but at a certain small distance apart because the piston accelerates slightly when it first moves and thus the

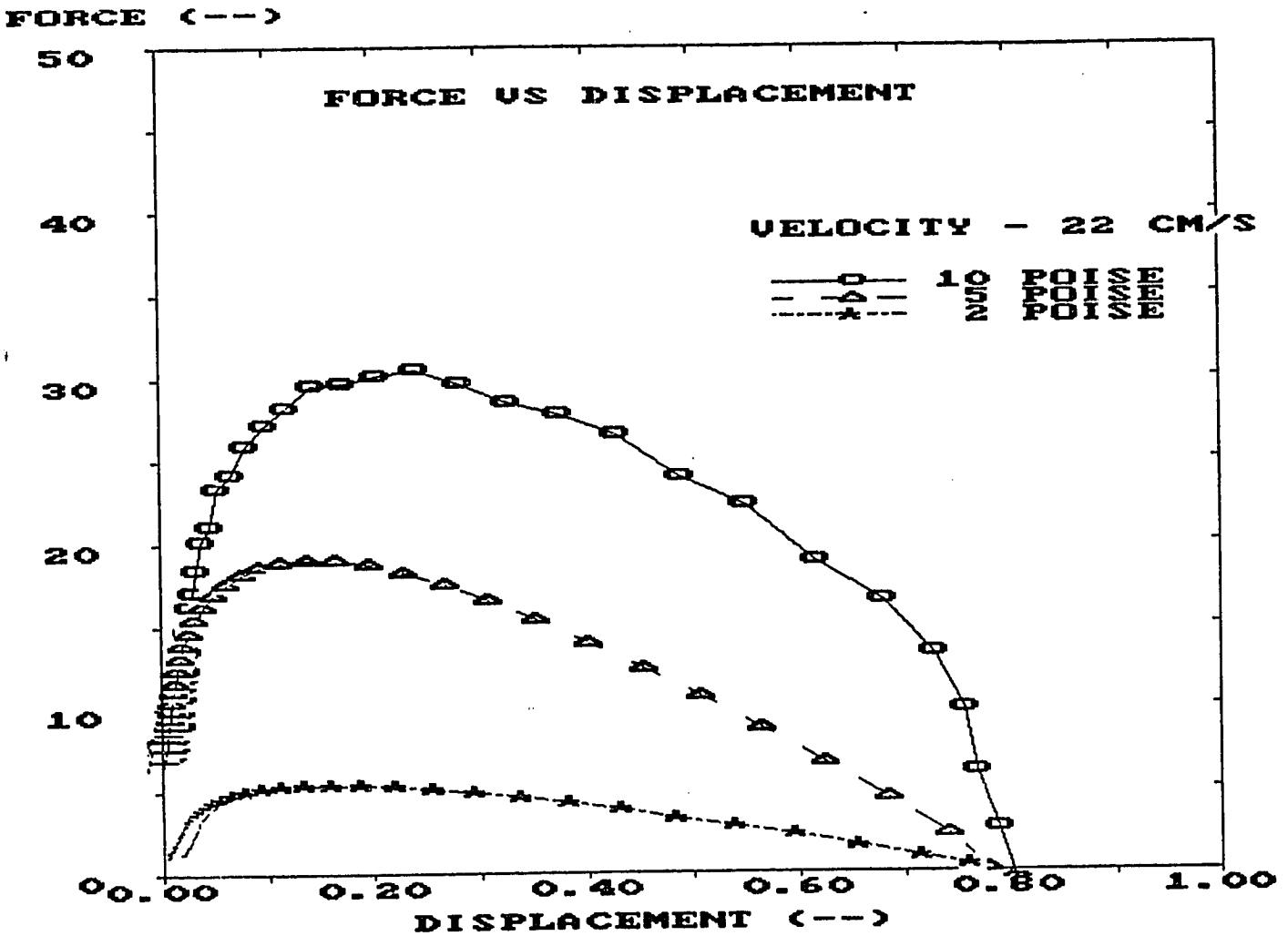

Figure 4.26. Dimensionless force vs. dimensionless displacement for various viscosity fluids with separation velocity held constant (V_b=1μL, R=0.1985 cm).

velocity is changing from zero to its steady value. It is well known that the smaller the velocity the lower is the dynamic force. Figure 4.27 shows the maximum forces as obtained from Figure 4.26 plotted as a function of viscosity. From Figure 4.27 it can be seen that for a 10 poise fluid the dynamic bridge strength is thirty times greater than the corresponding static bridge. This directly verifies the results of Section 4.3.1 where the forces were obtained indirectly.

A comparison of the experimental results with the model of squeezing flow between two spheres as developed by Adams and Perchard (1984) and presented in Section 4.3.1 was performed. This expression for the viscous force was chosen because is was considered to be the most realistic in terms of mirroring the actual experiment. The force was obtained by substituting Eq. (4.15B) into Eq. (4.14) and taking the derivative dx_s/dt to be the constant velocity term v_s:

$$F_{vis} = 3\pi\mu R v_s/\xi \qquad (4.21)$$

The comparison between experiment and model prediction is shown in Figure 4.28. The reason why Eq. (4.15C) was not used in the comparison of theory to experiment was that this expression for the viscous force would give a constant force value independent of the separation distance between the two spheres which is clearly not the case. As seen from Figure 4.28 the force goes to infinity as the spheres come in very close contact due to the ξ term in the denominator of Eq. (4.21). As the spheres separate, however, the force decays very quickly and for most of the range of sphere separation the force computed from the model predicts the actual force data within an order of magnitude. It has to be emphasized here that the force expression above is a simplified one which does not take into account the presence of the moving interface and the moving contact line nor does it account for the finite volume of the bridge. In other words the dynamic force expression above only considers viscous forces contributing to the strength of the moving bridge and neglects all other forces

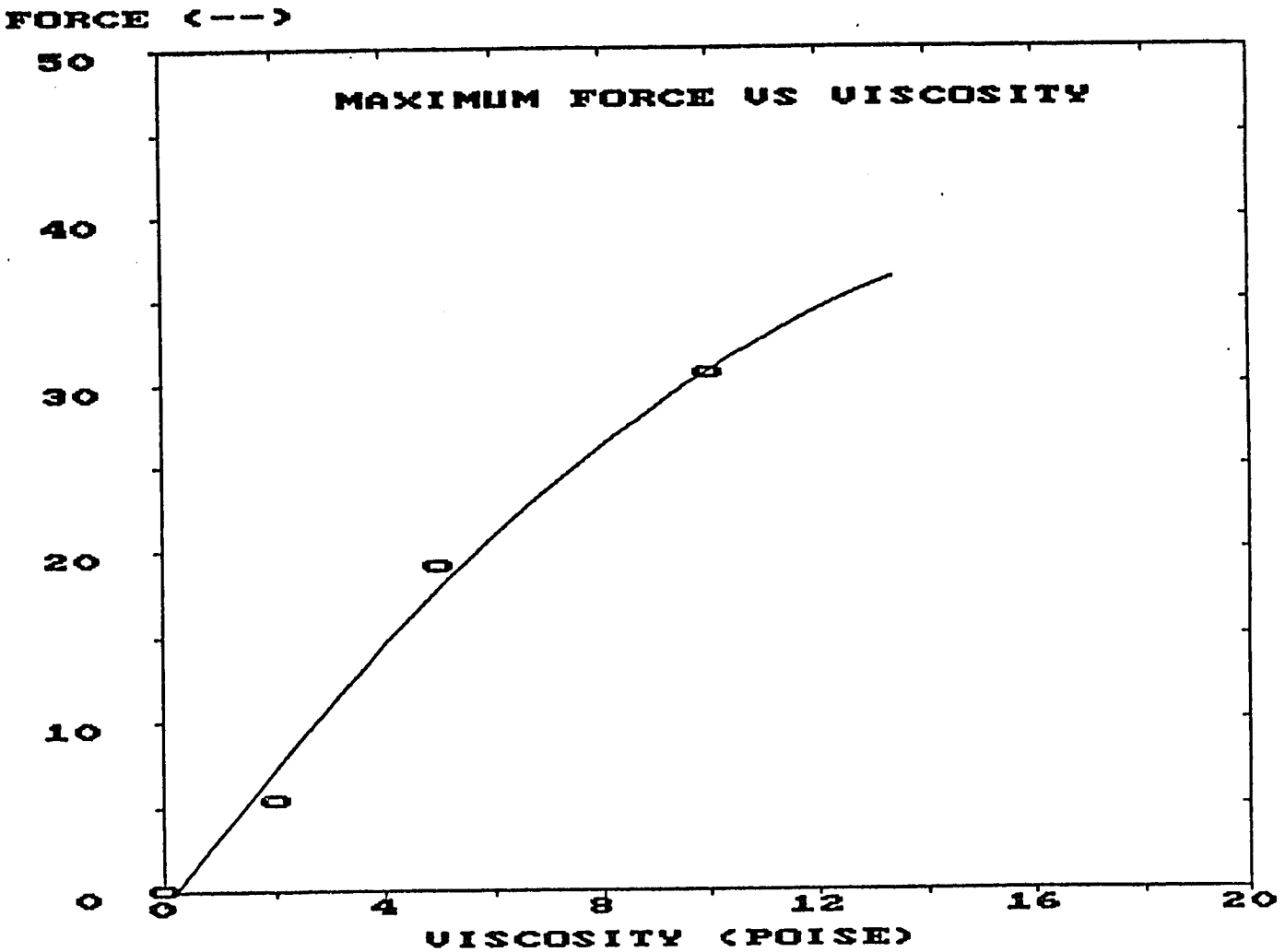

Figure 4.27.

DIMENSIONLESS MAXIMUM FORCE VS. VISCOSITY FOR A DOW CORNING SILICONE FLUID, (V_B = 1μL, R = 0.1985 cm).

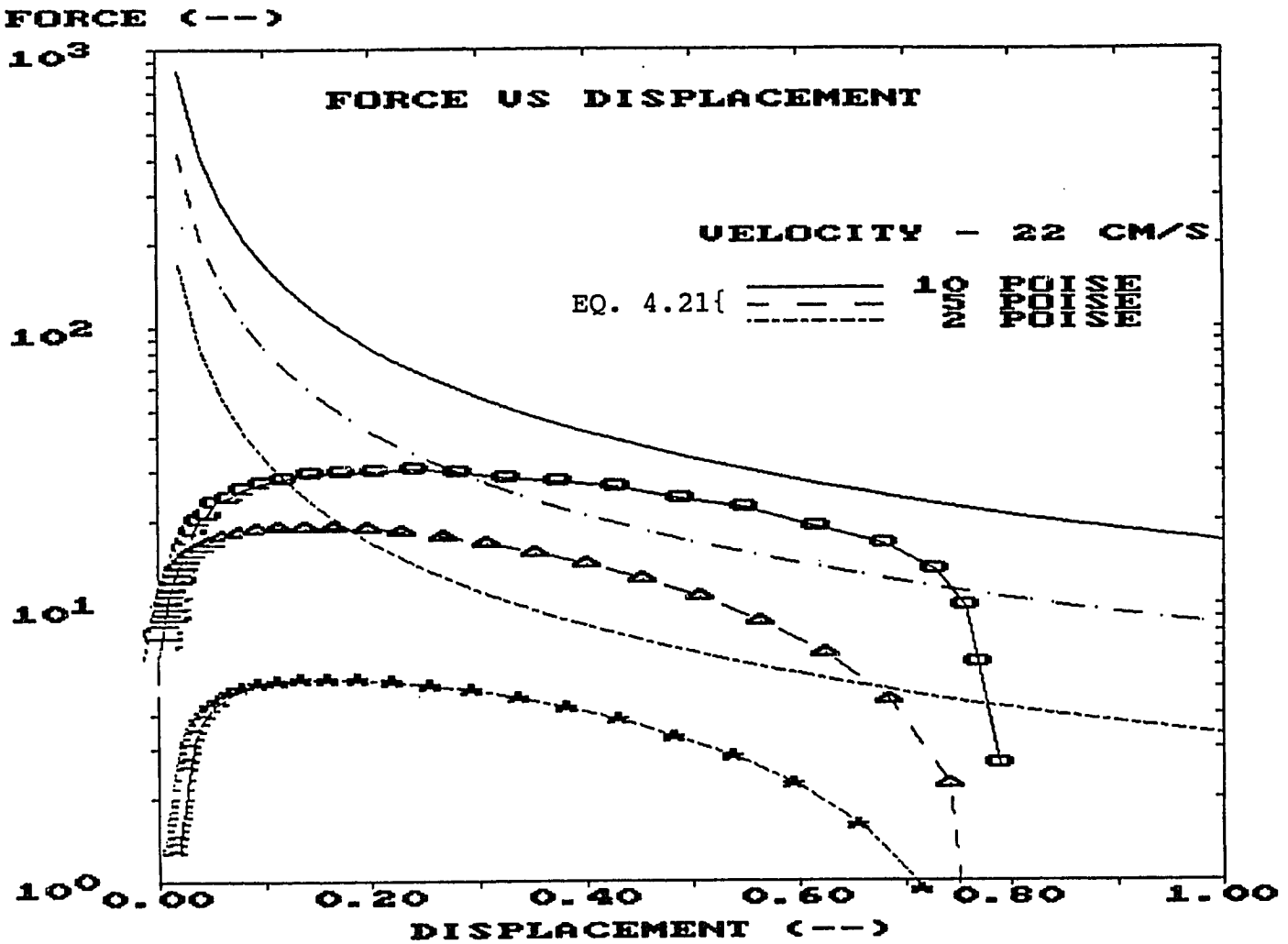

Figure 4.28. Dimensionless force vs. dimensionless displacement for various viscosity fluids with separation velocity held constant; comparison of model to experimental data (V_b=1μL, R=0.1985 cm).

such as surface tension and pressure forces. A more complicated model is necessary to predict the measured values over the entire range of separation distances. It should be stated that the Weinbaum and Caro (1976) relation (Eq. (4.15A)) would give a worse comparison to experimental data than the Adams and Perchard (1984) relation because the Weinbaum and Caro relation predicts forces four times larger than the Adams and Perchard relation.

To observe the effects of separation velocity on the strength of the bridge a set of experiments were performed and the results for a 10 poise fluid are shown in Figure 4.29. It is seen that increasing the separation velocity has the same effect as increasing the viscosity of the fluid. They both act to increase the dynamic force. The general trend of these results is embodied in Eq. (4.21) where the force is directly related to the sphere separation velocity. Figure 4.30 compares experimental results taken from Figure 4.29 with model predictions using Eq. (4.21). Once again, for a range of separation distances the model fits the experimental results reasonably well. Figure 4.31 shows similar results as Figure 4.30 but for a 5 poise fluid. The maximum forces versus separation velocity with viscosity as a parameter for a group of experiments performed is shown in Figure 4.32. Increasing viscosity at a given velocity results in an increase in the dynamic force.

Figure 4.33 shows dimensionless force versus dimensionless displacement using Ace Plastic Coating #3100. This non-Newtonian fluid is the same one used in the fluidized bed liquid coating experiments (see Section 3.3). Because of its non-Newtonian character the shapes of the curves obtained during these experiments are somewhat different from the previous ones. Similar experiments using the same binder (liquid) but with a liquid bridge volume of $V_b = 0.9\mu L$ were also performed and as a result Figure 4.34 shows the variation of force versus velocity for $V_b = 2\mu L$ and $V_b = 0.9\mu L$ bridges. As seen the dynamic bridge strength can reach as much as 500 times the value of the static bridge while the dependency on bridge volume is negligible. In fact, for the case of this very viscous fluid, as long as there is

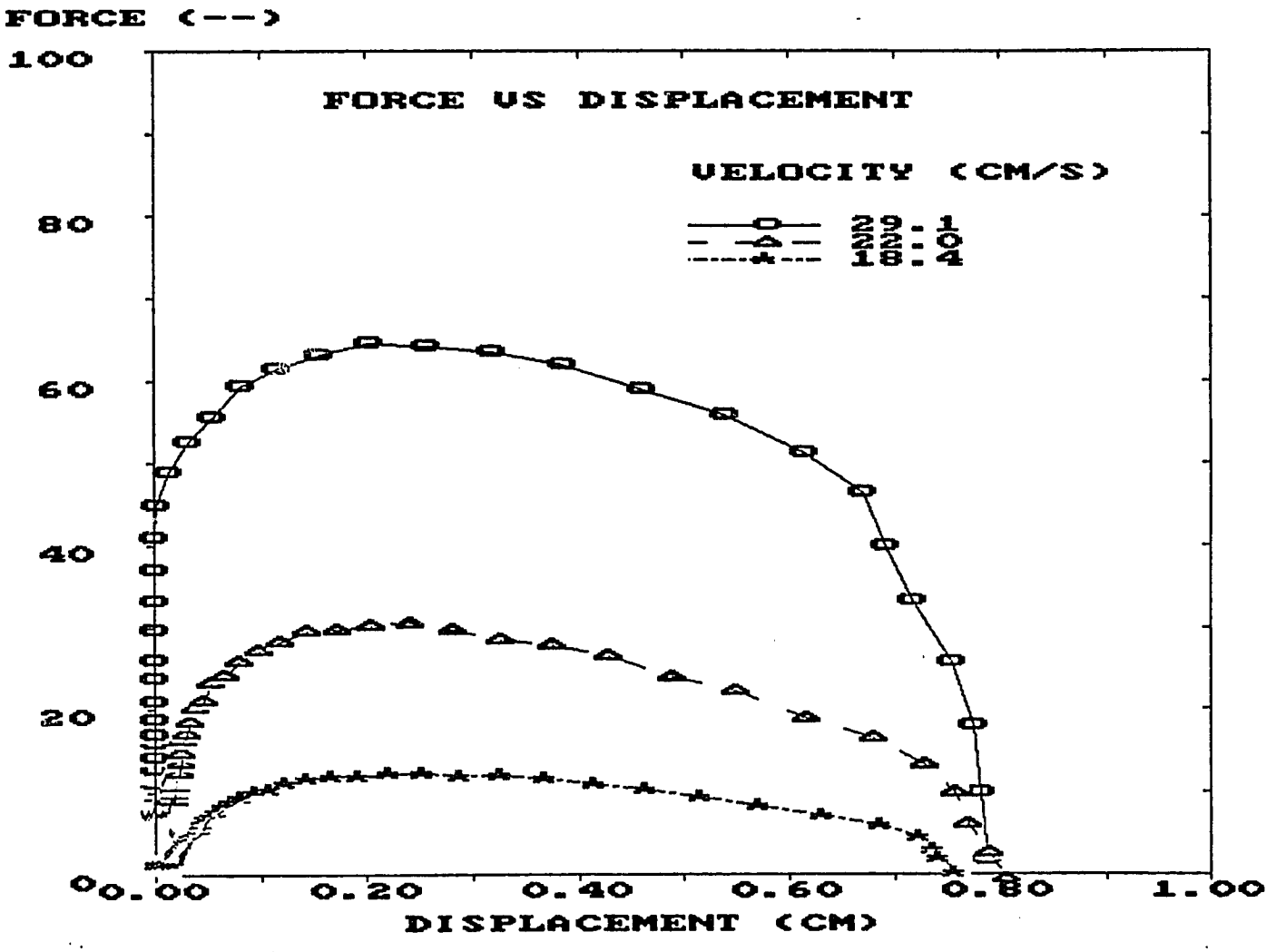

Figure 4.29. Dimensionless force vs. dimensionless displacement with separation velocity as a parameter. (Fluid - Dow Corning Silicone fluid, η=10 poise, V_b=1μL, R=0.1985 cm).

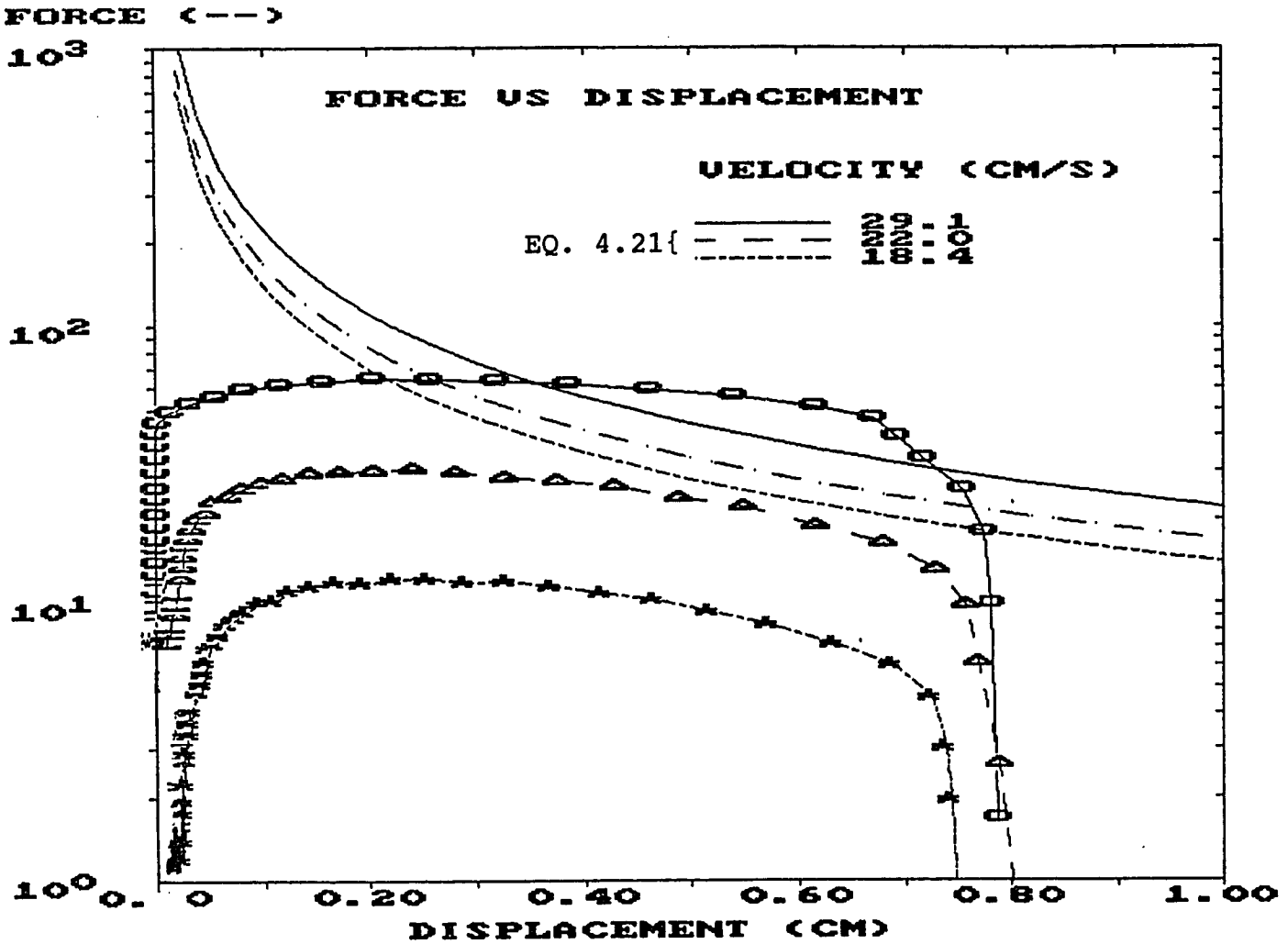

Figure 4.30. Dimensionless force vs. dimensionless displacement with separation velocity as a parameter; comparison of model to experimental data (Fluid - Dow Corning Silicone fluid, η=10 poise, V_b=1μL, R=0.1985 cm).

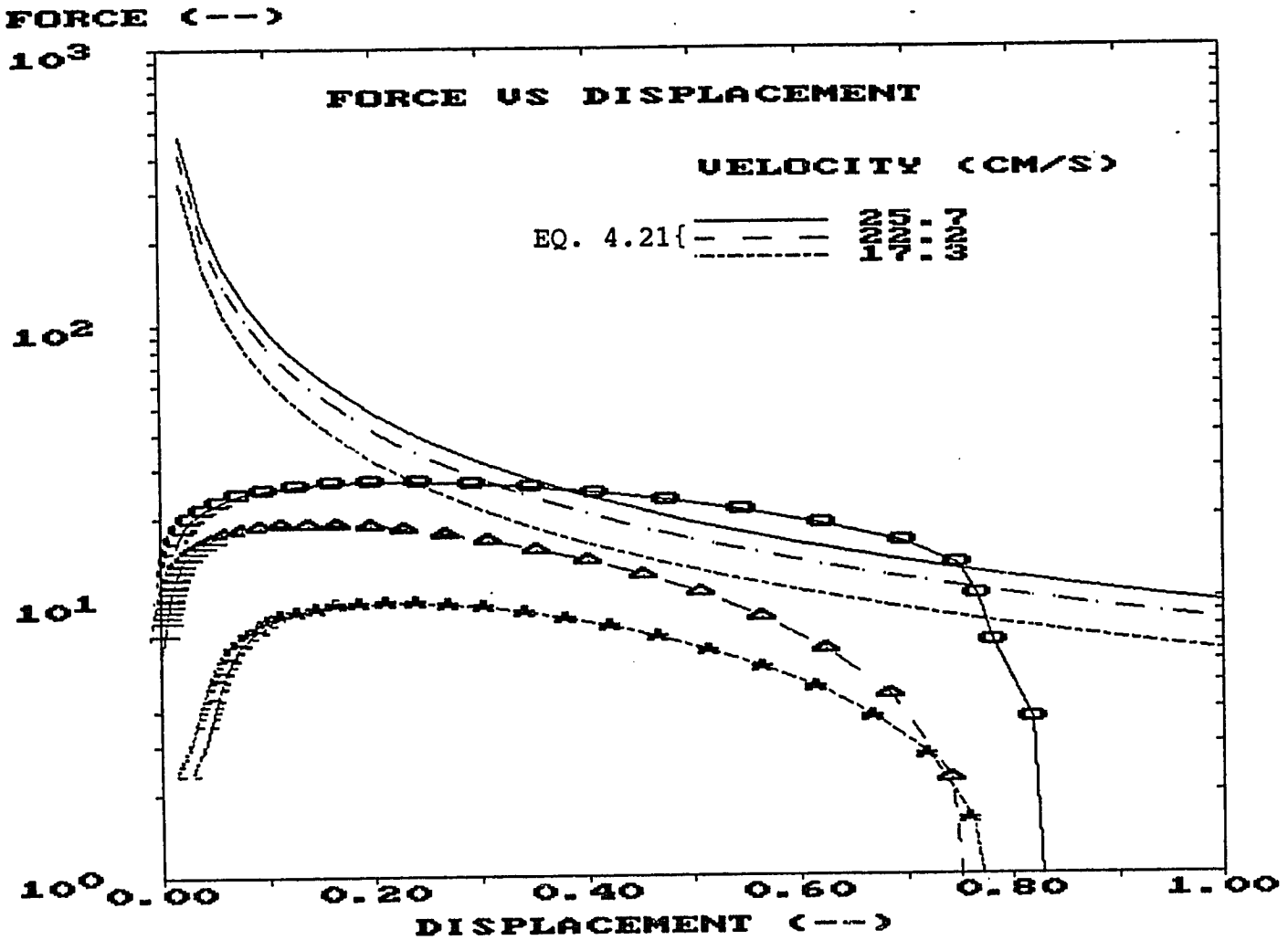

Figure 4.31. Dimensionless force vs. dimensionless displacement with separation velocity as a parameter; comparison of model to experimental data (Fluid - Dow Corning Silicone fluid, η=5 poise, V_b=1μL, R=0.1985 cm).

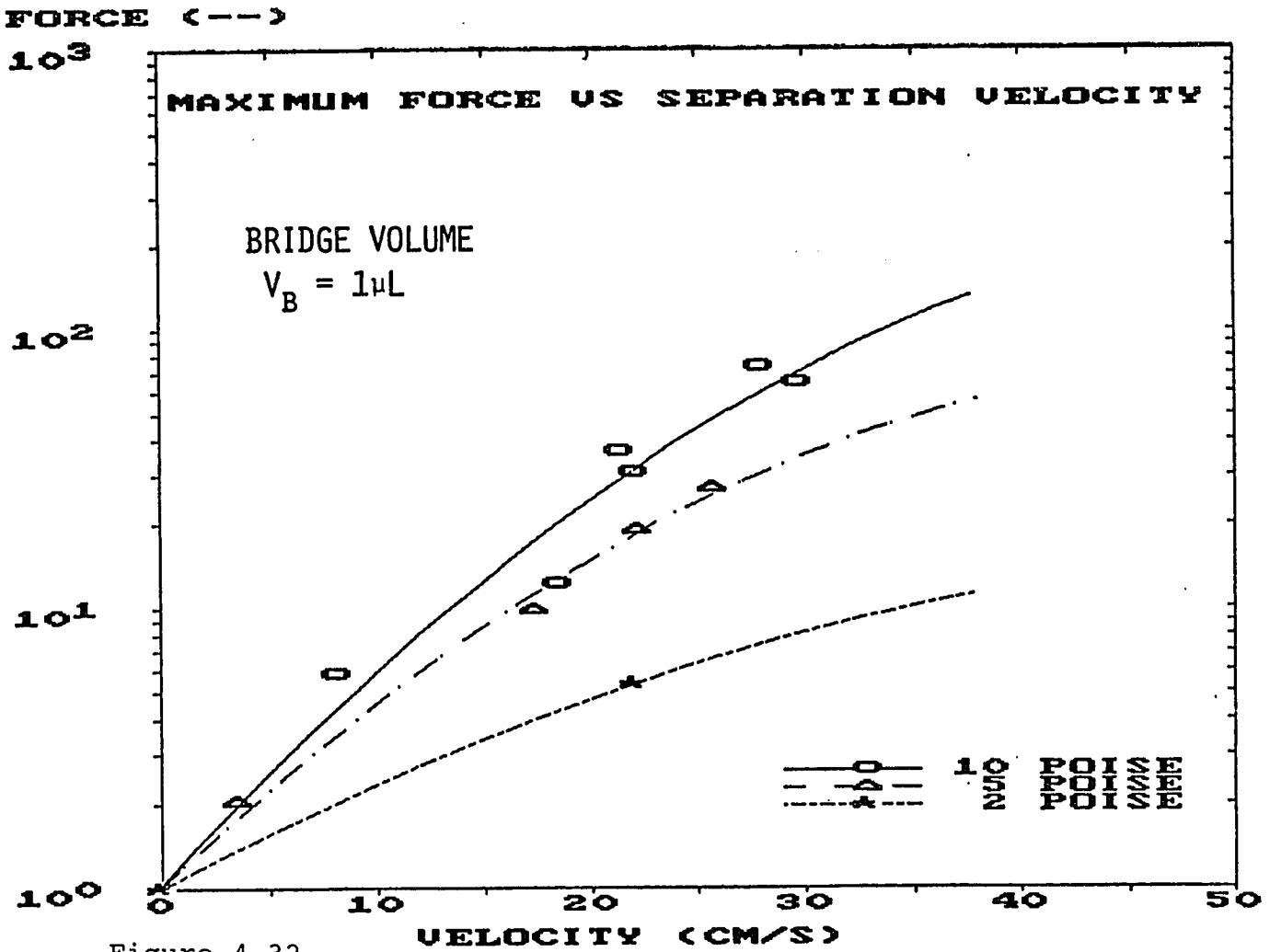

Figure 4.32

DIMENSIONLESS FORCE VS. SEPARATION VELOCITY FOR DOW CORNING SILICONE FLUIDS, (R = 0.1985 cm).

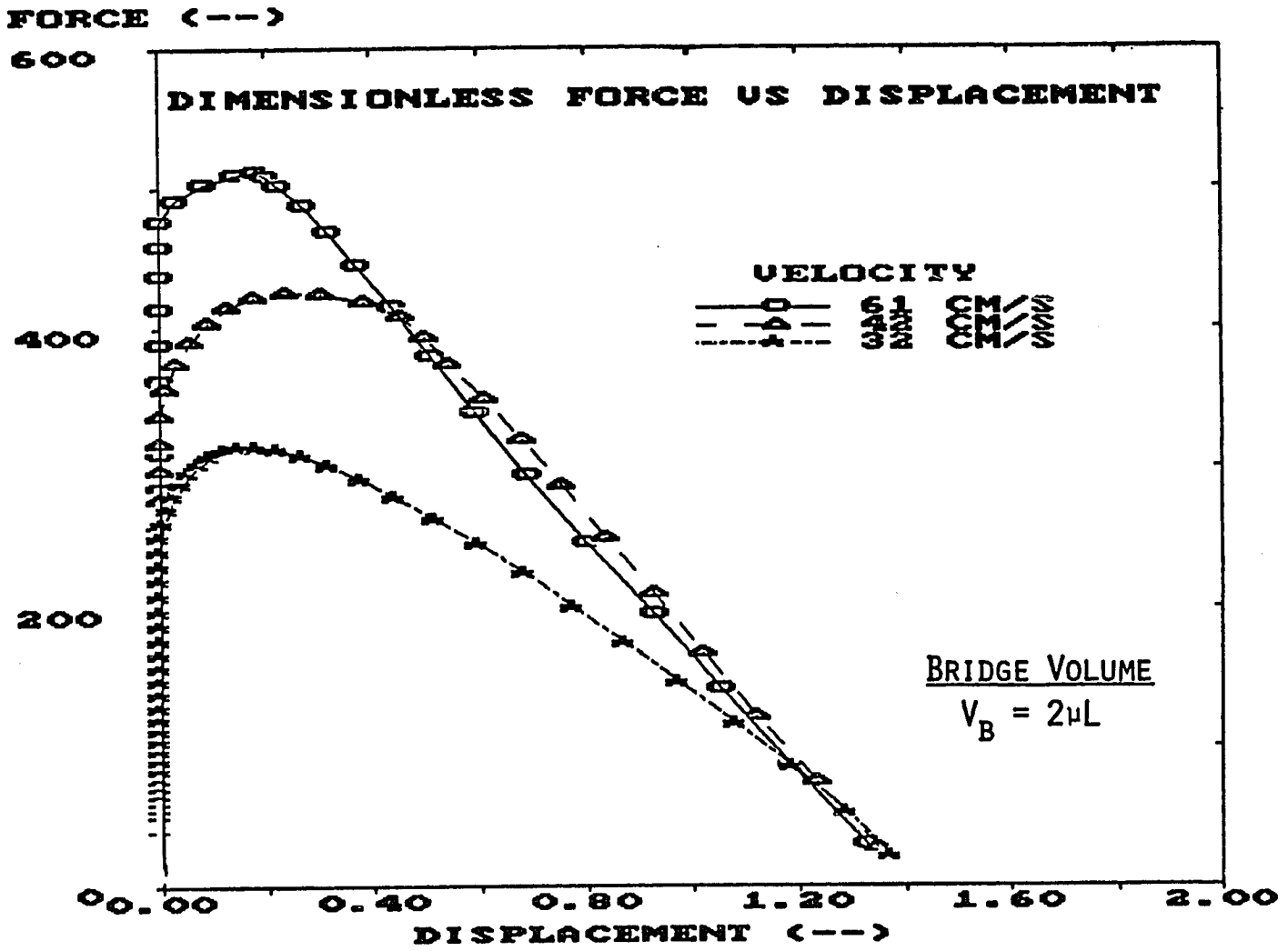

Figure 4.33. Dimensionless force vs. Dimensionless Displacement with Separation Velocity as a Parameter. (Fluid-Ace Plastic Coating #3100 η=100 poise, V_b=2μL, R=0.1985cm).

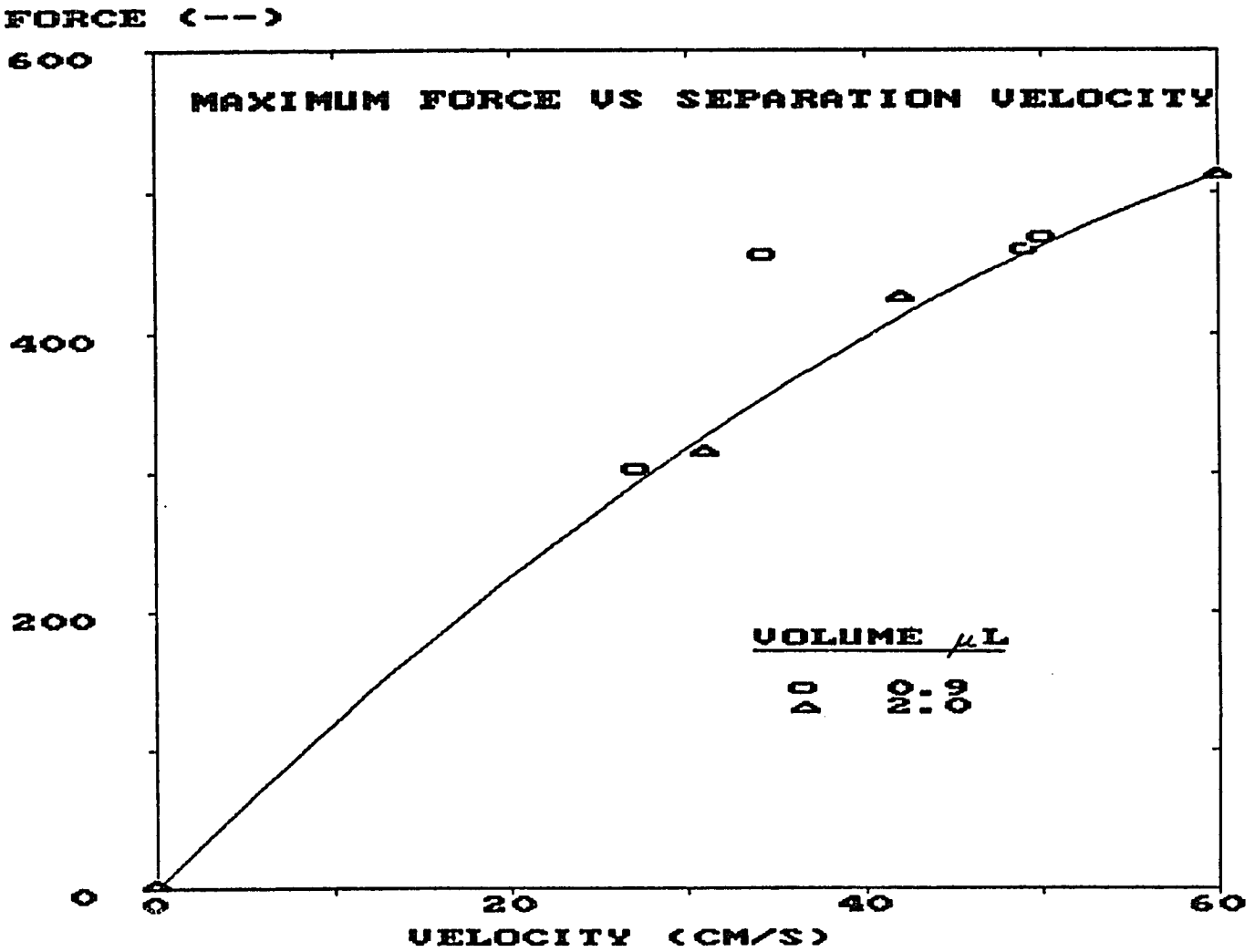

Figure 4.34

DIMENSIONLESS MAXIMUM FORCE VS. SEPARATION VELOCITY FOR ACE PLASTIC COATING #3100. (R = 0.1985 cm).

fluid in the gap between the two spheres viscous forces occur and are not very sensitive to exactly how much fluid is in this gap.

Experiments were also performed on a smaller sphere size of radius R = 0.0794 cm to see how different size spheres affect the value of the maximum force. Figure 4.35 shows the dimensionless force versus dimensionless separation distance for a Dow Corning Silicone fluid of viscosity η = 10 poise and bridge volume V_b = .06μL. Figure 4.36 compares the data from Figure 4.35 with the model prediction using Eq. (4.21). Similar trends are seen as in the case of larger spheres, except for the fact that the overall dimensionless force is smaller than for the larger spheres. Additional experiments were performed with a 125 poise Dow Corning fluid and these results are shown in Figure 4.37 as maximum force vs. separation velocity with viscosity as a parameter. This figure shows the strong dependence of the maximum force (strength) of the liquid bridge as a function of viscosity. Similar experiments using Ace Plastic Coating #3100 and smaller spheres together with the comparison to the model are shown in Figure 4.38. It is noticed that there are less data points when the smaller size spheres are separating as compared to the larger spheres because the bridge ruptures sooner and at shorter distances.

The experimental results have shown that viscous dissipation due to the liquid bridge has a very significant effect on the overall strength of a sphere-liquid-sphere system. The inability of using these results to furthur refine the model of minimum fluidization velocities of an agglomerating bed (Section 3.2) is attributable to two major difficulties. The first is that the best model for the dynamic bridge (Adams and Perchard, 1984) does a fair job of predicting the strength of the bridge only for a limited range of separation distances. Thus the Adams and Perchard model is much too crude in the present form. Secondly, the measurement of relative particle velocities in a fluidized bed which is a required known quantity in the Adams and Perchard model has not been measured.

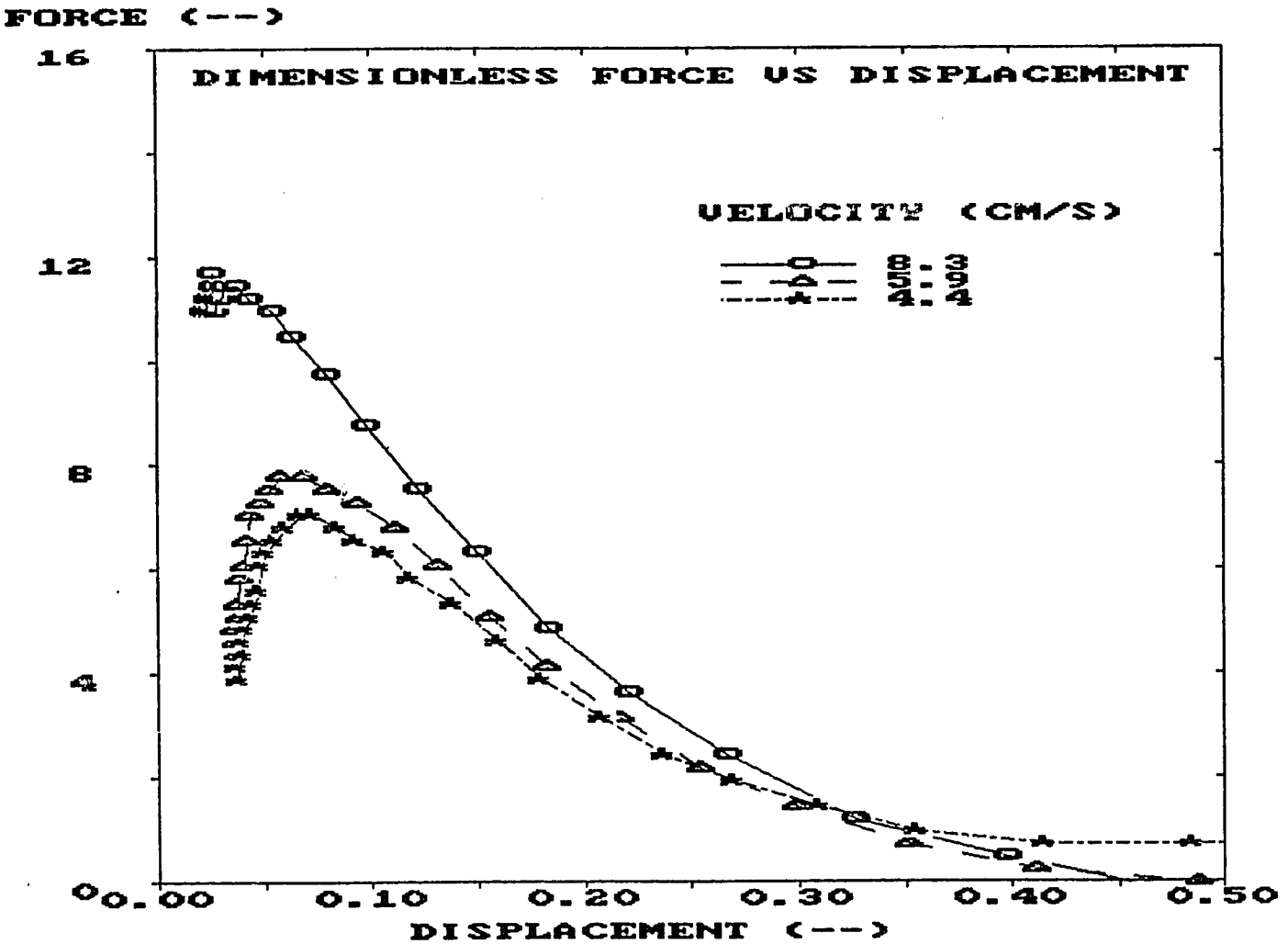

Figure 4.35 Dimensionless force vs. dimensionless displacement with separation velocity as a parameter (Fluid - Dow Corning Silicone fluid, η=10 poise, V_b=0.06μL, R=0.0794 cm).

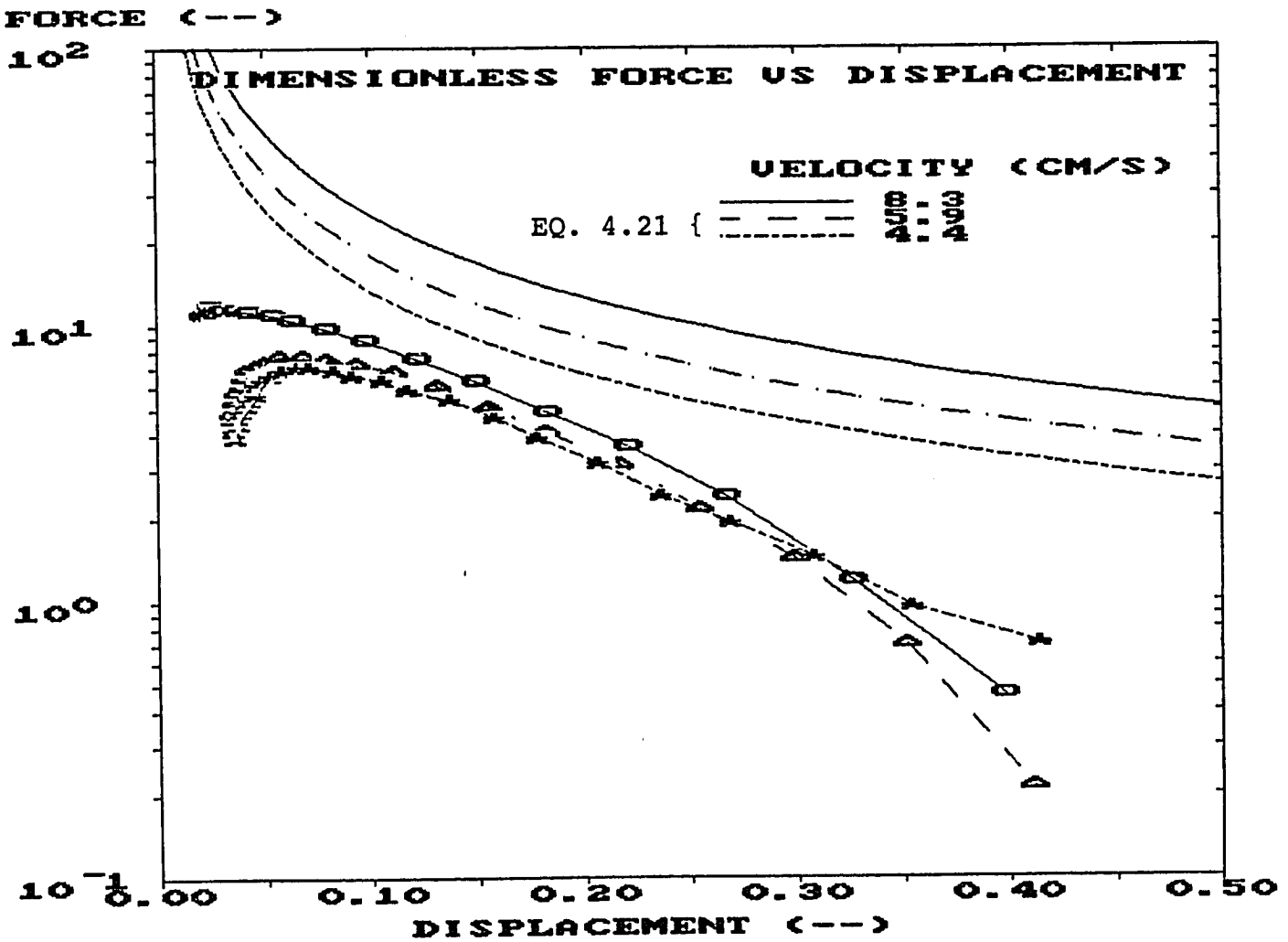

Figure 4.36 Dimensionless force vs. dimensionless displacement with separation velocity as a parameter; comparison of model to experimental data (Fluid - Dow Corning Silicone fluid, η=10 poise, V_b=0.06μL, R=0.0794 cm).

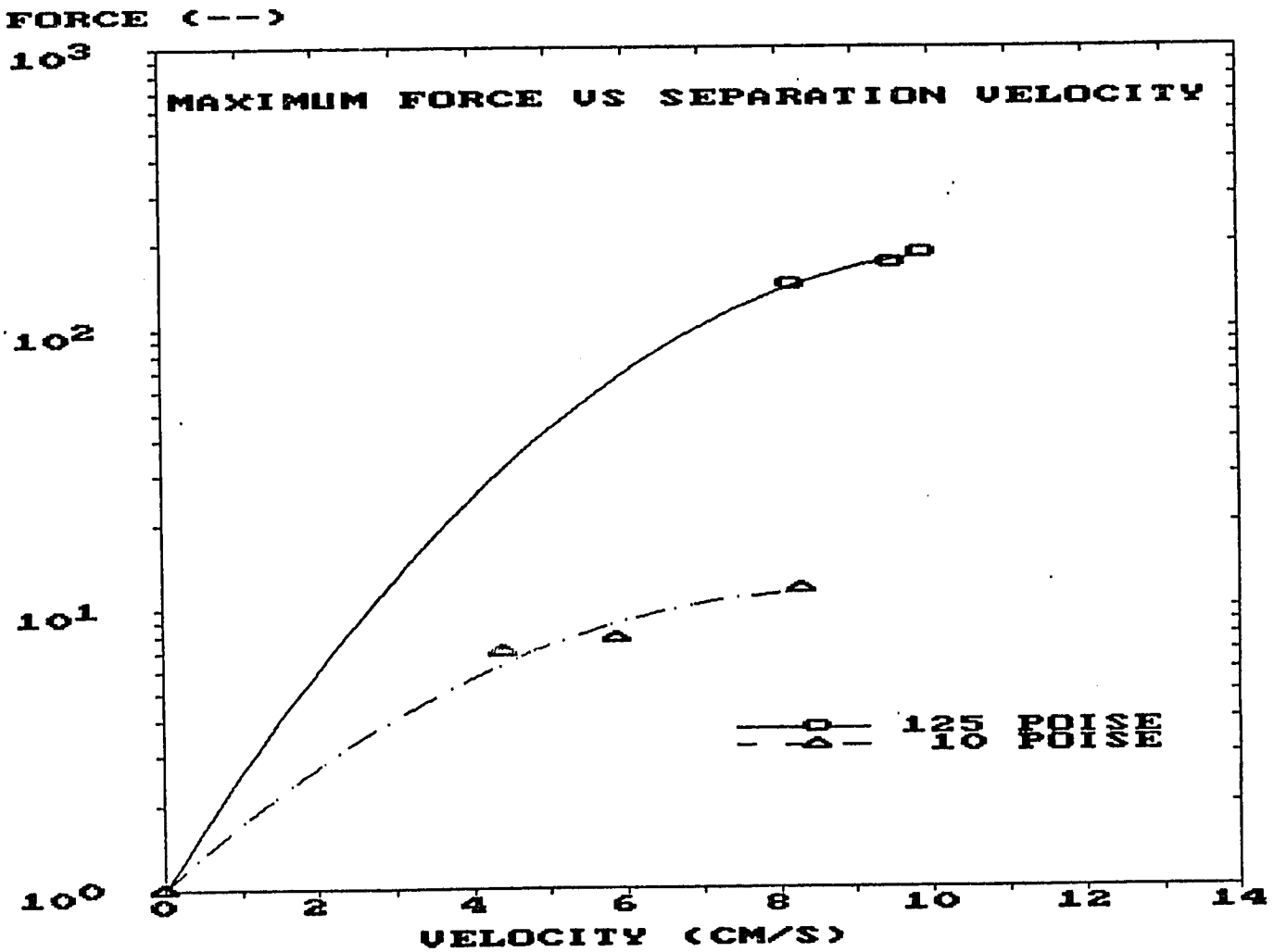

Figure 4.37 Dimensionless maximum force vs. separation velocity for Dow Corning Silicone fluids (R=0.0794 cm).

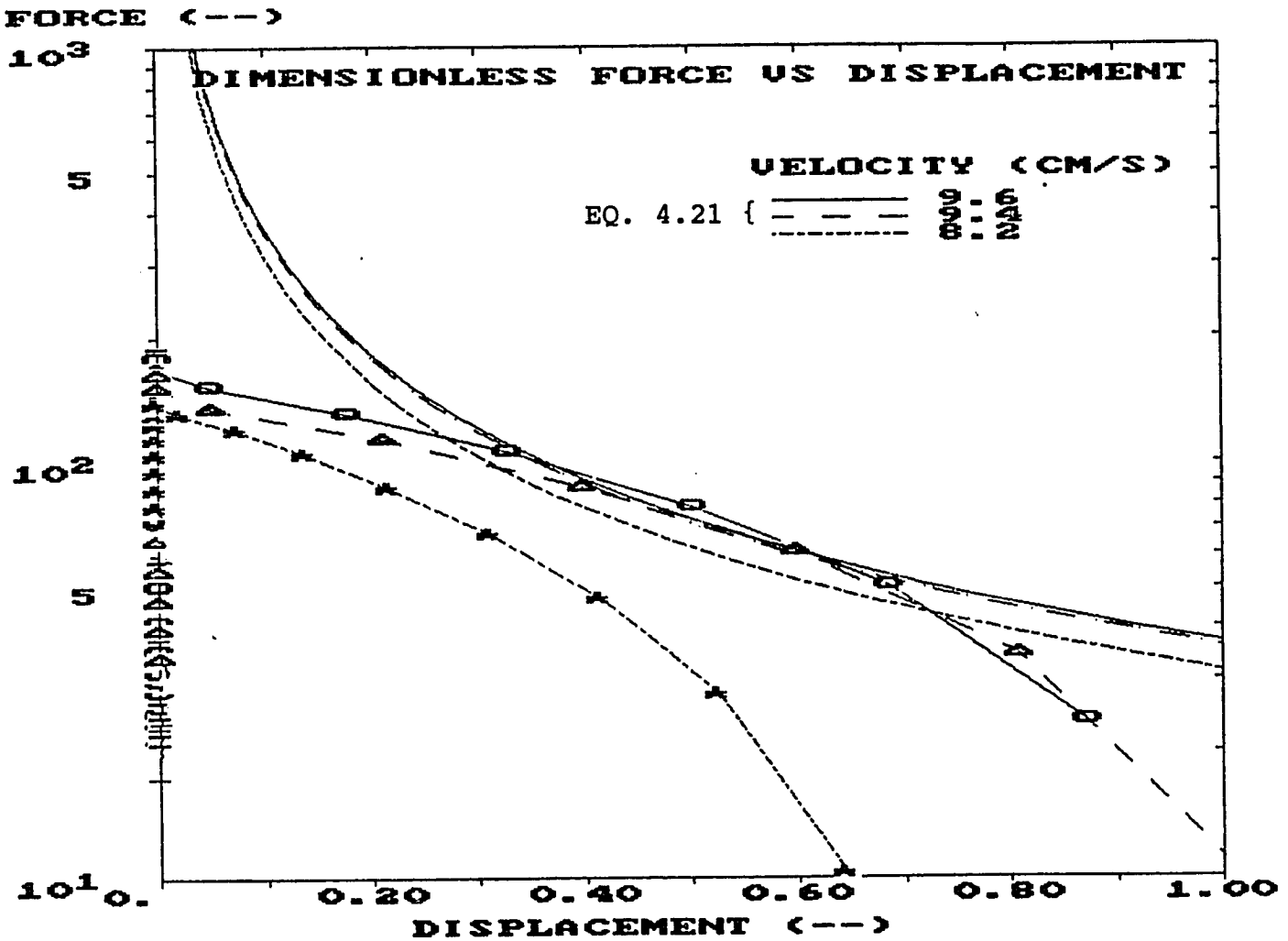

Figure 4.38 Dimensionless force vs. dimensionless displacement with separation velocity as a parameter; comparison of model to experimental data (Fluid - Ace Plastic Coating #3100, η=100 poise, V_b=0.06μL, R=0.0794 cm).

CHAPTER 5: CONCLUSIONS AND RECOMMENDATIONS

A theoretical model was developed to predict the limiting velocity, U_s, below which it is unsafe to operate a fluidized bed in which cohesive forces between particles are produced by the presence of a sticky fluid, a coating, or by softening or sintering of the granules' surface due to high temperatures. The model is based on a fail-no fail criterion of the largest aggregate formed in the bed (which in the limit can be taken equal to the size of the bed) and therefore cannot be used to predict the agglomerate size beyond the limiting condition characterized by the excess velocity, $U_s - u_{mf}$. At gas velocities higher than the limiting velocity, U_s, smaller agglomerates will obviously form since more energy is imparted to the bed from the gas; the modelling of this dynamic behavior was not attempted in this research and was left for a future effort.

For the injection of liquid material in the bed, the limiting velocity, U_s, was seen to be dependent on the dimensionless amount of liquid added as well as measurable bed and fluid properties. For agglomeration due to temperature effects, the theoretical model requires knowledge of two fundamental physical quantities, the surface viscosity, η_s, and the sinter neck yield strength, σ_s, both as functions of temperature.

Surface viscosity measurements can be performed using a dilatometer and the yield strength can either be estimated using adhesion theory or calculated from experimental data. It was demonstrated that the minimum sintering temperature T_s occurs at the temperature where the surface viscosity undergoes a significant change in magnitude over a very small temperature range. At temperatures below T_s, destabilization due to agglomeration is of no concern, but above this temperature higher gas velocities, as predicted by the model, were necessary to maintain stable fluidization.

It was shown that using a small sample of granular material and a dilatometer, surface viscosities at high temperatures approaching the melting point can be measured. The surface viscosity-temperature data can be used to determine the minimum sintering temperature of the material in question, and furthermore, the behavior of the material's surface under compression at temperatures close to and above minimum sintering can also be predicted. Surface viscosity data for a given type of fluidizable granules can be used in the developed model to predict defluidization velocities.

It was demonstrated during this study that the minimum sintering temperature is an inherent material characteristic of solid particles and determines the level at which the solid surface softens and/or partially melts and therefore creates agglomeration problems when these same particles are fluidized. It was shown that during the sintering process certain physical and thermodynamic changes occur in the solid which can be detected using a dilatometer, a differential scanning calorimeter (DSC) or a shear strength measuring device (Instron machine). For all materials studied, the minimum sintering temperature is always lower than the physical melting point, and for the majority of amorphous materials such as polymers, glass, coals, etc., this temperature is a transition or a softening point. For crystalline materials, such as chemically stable salts, the sintering behavior is complicated by the release of crystalline water at different temperatures. For these materials additional agglomeration can occur due to the formation of crystalline bridges bewteen particles after the water has been released. One has to disassociate this type of bridge formation from the actual sintering by performing succesive heating and cooling cycles on the sample until agglomeration due to water release is eliminated.

Static and dynamic liquid bridges between particles were studied. For static bridges it was shown that under certain

conditions when the Bond number, Bo, is of order unity and larger, gravity has a significant effect on the physical characteristics of the bridge, such as distorting the liquid profile, lowering the attraction force due to the bridge and also causing bridge rupture to occur at smaller separation distances as compared to the gravity free case. A criteria of rupture which predicts spreading of the liquid comprising the bridge onto the surface was developed and compared favorably to experimental data.

For the case of a dynamic bridge a simplified theoretical model to predict strengthening of the bridge between two particles due to their relative motion has been proposed. Experiments performed on such a system have shown that the strength of a dynamic bridge is on the average at least one order of magnitude greater than the corresponding static bridge and that the model fits the data well for low and medium viscosity fluids. To obtain a better model, the functional form of the viscous dissipation force, F_{vis}, needs to be theoretically more accurately determined.

A direct experimental method to measure forces of sphere-liquid-sphere systems separating at constant velocity has been developed and confirms the results that dynamic bridges are much stronger than the corresponding static bridge. The model of squeezing flow between two spheres proposed recently (Adams and Perchard, 1984) seems to fit the data approximately but only over a limited range of particle separation distances.

Possible future work

It could be agreeably argued that the refinement of the theoretical model proposed for the failure of an agglomerate which formed as a result of adding liquid in a fluidized bed is

not closed. Ideally the function F_B^* in Equation 3.4 should have two additional functional dependencies

$$\sigma_{OB} = [(1-\epsilon)\gamma_m/(\epsilon D_p)] \cdot F_B^*(\epsilon, Sa, \theta, x_s/D_p, \eta, v_s) \qquad (3.4')$$

namely the viscosity of the coating liquid, η, and the velocity of particle separation, v_s. The influence of the former parameter was studied during the present work but the latter poses particular problems. The velocity of particles relative to one another in a fluidized bed is not an easily determined quantity. There needs to be more information and research to be able to accurately determine the distribution of relative velocities of particles moving toward each other, before the functional form of F_B^* can be completely determined.

Another important problem to be solved during future work is the theoretical analysis of flow within liquid bridges between two moving particles. This is a particularly difficult problem in that it involves a continuously changing free surface (liquid-gas interface) and also a moving contact line (sphere-liquid-gas). Further complications arise if the motion cannot be regarded as "creeping flow" and/or the fluids involved are not Newtonian.

It is believed that the experimental rig to study moving bridges should be extended to allow for high temperature experiments. Solid particles can be heated above the minimum sintering temperature to generate a "soft" liquid layer on their surfaces and subsequently bridge strength and rupture distance measurements can be performed. Particle heating can be accomplished by using radiation or electric currents.

The fluidized bed agglomerator which was constructed during the present work, can reach a maximum temperature of about 600°C and can only operate with compressed air as the fluidization fluid. These limitations restrict the materials used during the experiments to relatively low temperature sintering of inert materials, such as polymers, glass, etc.. A high temperature

agglomerator (fluidized bed) which can operate with different active or inert gases should be built. Modifications and additions can be made to the present system to allow for the use of different fluidization gases other than compressed air. This can be achieved by adding a packed bed, externally heated column under the existing fluidization section of the experimental unit. This added section can have the option of using compressed air from the existing system or compressed gas from a high pressure storage tank.

Mechanistic models for agglomeration have recently been poposed. These models examine two spheres colliding and sticking or bouncing apart depending on the properties of the particles and the operating conditions (Scharff et al. 1980, Jen and Tsao, 1980). These are then incorporated into a general model based on population balances to predict agglomeration in a fluidized bed. The basic underlying assumption in these models is that the formation of agglomerates during collision of two particles depends on whether the initial kinetic energy is large enough to overcome the energy required for deformation of the surfaces and the binding energy. If the particle surface is coated with a liquid then the total energy dissipated by the particles would be the integration of the force along the spheres approach and separation trajectory. Thus an experiment can be performed whereby the piston first is extended so that the spheres approach each other and subsequently the piston retracts so that the spheres then separate. The results of this experiment would yield the total energy dissipated by the bridge which needs to be overcome to break the bridge. A preliminary experiment of this type was performed using the existing experimental setup (since the gas piston was dual motion the experiment was very easily performed). Many additional experiments should be performed and compared to the mechanistic models already proposed.

It is envisioned that the main goal of future research in this area should be to develop a general theory of agglomeration

in fluidized beds which, unlike the model already developed which only determines limiting conditions, will be able to predict agglomerate size as a function of excess gas velocity and other parameters, from a knowledge of the basic physical and geometrical properties of the particles. The groundwork for the development of such a model has been laid out in the present work by studying the strength of moving liquid bridges between particles. Future sets of experiments first should correlate the relative particle-particle velocities as a function of the geometric and hydrodynamic characteristics of the fluidized bed while another set of experiments should furthur elucidate theoretically and experimentally the strength of the liquid bridge as a function of the physical properties of the bridge itself and the particle system. The basis of the new model will be the assumption that under equilibrium conditions, at a given gas velocity, particle and/or agglomerate pairs for which their initial energy before collision is larger than the energy dissipated due to the presence of the liquid (molten) bridge will separate or break while other pairs will stick together and form larger agglomerates. Thus, the general theory will be applicable for sintering beds at high temperatures where softening of the contact point occurs as well as for low temperature beds where a liquid binder is used.

APPENDIX A

A.1 Computer programs for solution of Laplace-Young equation

For the solution of the equilibrium shape of a sphere-liquid-sphere system the solution of Eq. (4.1) was required. Eq. (4.1) was rearranged to Eqs.(4.2-4.4) which were subsequently solved by using a fourth order Runge-Kutta method.

$$d\Phi/dS = (2HoR - BoR) - (\sin\Phi/Y) \quad (4.2)$$
$$dY/dS = \cos\Phi \quad (4.3)$$
$$dX/dS = \sin\Phi \quad (4.4)$$

The programs were all written in the APL programming language. The program that does the actual Runge-Kutta routine is GILL. The subprogram CALC calculates the liquid profile for a given of the initial curvature, Ho, and filling angle, α_1. The subprogram SET contains the form of the set of three equations (4.2) to (4.4). The first of the two main programs as described in Section 4.2 is XGXS which calculates by a Newton-Raphson method the volume of the liquid bridge as a function of the filling angle for two spheres that are a specified distance apart. The second program MAIN2 calculates, again by using a Newton-Raphson method, the separation distance of the two spheres when the filling angle is given and the volume is a constraint. The two main programs and the subprogram are listed below.

```
      ∇XGXS[0]∇
[0]  HH XGXS ALPHA1
[1]   ALPHA←ALPHA1
[2]   XMIN1←2⍴0
[3]   ' NEW GUESS FOR H    |  SEPARATION DISTANCE '
[4]   '-------------------------------------------'
[5]   VOL1←HH[1]CALC ALPHA
[6]   XMIN1[1]←S4[1]-(XMIN+GXS)
[7]   17 11 ⍕(HH[1],(XMIN1[1]+GXS))
[8]   VOL2←HH[2]CALC ALPHA
[9]   XMIN1[2]←S4[1]-(XMIN+GXS)
[10]  17 11 ⍕(HH[2],(XMIN1[2]+GXS))
[11] LOOP2:HH[1]←HH[2]-((XMIN1[2])÷((XMIN1[2]-XMIN1[1])÷(HH[2]-HH[1])))
[12]  VOL←HH[1]CALC ALPHA
[13]  XMIN1[1]←S4[1]-(XMIN+GXS)
[14]  XMIN1←⊖XMIN1
[15]  HH←⊖HH
[16]  17 11 ⍕(HH[2],(XMIN1[2]+GXS))
[17]  →((|XMIN1[2])<1E¯10)/PRINT
[18]  →LOOP2
[19] PRINT:'RP= ',(⍕RP),'  HO = ',(⍕HO),' ALPHA = ',(⍕ALPHA),'   THETA= ',(⍕THETA)
[20]  'PHE = (180-(ALPHA+THETA)) IS:  ',⍕X[1;1]×180÷(○1)
[21]  ' YO = ',(⍕X[2;1]),'   XO =  ',(⍕X[3;1]),'    BO=  ',(⍕BO)
[22]  '  T = ',(⍕T)
[23]  '       S          PHE (RAD)        Y            X   SIN(PHE-THETA)-Y  PHE(DEG)'
[24]  '    ------------------------------------------------------------------------'
[25]  12 5 ⍕Z[⍳(IN+2);]
[26]  ' FORCE AT TOP =  ',(⍕FORTOP),' FORCE AT BOTTOM = ',(⍕FORBOT)
[27]  ' FT - FB =  ',(⍕FΔF),'   VOLUME FROM FORCE =  ',(⍕VOLFORC)
[28]  '  VOLUME = ',(⍕VOL),'    XMIN = ',(⍕XMIN),'   XSEP=  ',(⍕XSEP←XMIN-S4[1])
[29]  12 5 ⍕S7
```

```
     ∇MAIN2[0]∇
[0]  HH MAIN2 ALPHA1
[1]   ALPHA1←,ALPHA1
[2]   I←1
[3]   VOL1←2ρ0
[4]   VV←HHH←FF←XS←(ρALPHA1)ρ0
[5]   XY←(2,(2×ρALPHA1))ρ0
[6]  LOOP1:→(I>(ρALPHA1))/FINISHED
[7]   ' '
[8]   ' '
[9]   ' '
[10]  'NO.  | NEW GUESS FOR H   |    VOLUME      | ALPHA= ',⍕ALPHA1[I]
[11]  '-------------------------------------------------------------'
[12]  ALPHA←ALPHA1[I]
[13]  I1←1
[14]  VOL1[1]←HH[1]CALC ALPHA
[15]  VOL1[2]←HH[2]CALC ALPHA
[16]  2 0 16 6 16 6 ⍕(0,HH[1],VOL1[1])
[17]  2 0 16 6 16 6 ⍕(0,HH[2],VOL1[2])
[18] LOOP2:HH[1]←HH[2]-((VOL1[2]-VOLUME)÷((VOL1[2]-VOL1[1])÷(HH[2]-HH[1])))
[19]  I1←I1+1
[20]  →(I1>12)/END
[21]  VOL1[1]←HH[1]CALC ALPHA
[22]  HH←⌽HH
[23]  VOL1←⌽VOL1
[24]  2 0 16 6 16 6 ⍕((I1-1),HH[2],VOL1[2])
[25]  →((|(VOLUME-VOL1[2]))<1E¯6)/TEST
[26]  →LOOP2
[27] TEST:→(^/(Z[⍳IN;3]>¯1E¯6))/PRINT
[28]  'WARNING SHAPE OF PROFILE IS PHYSICALLY UNREALISTIC'
[29]  ' '
[30]  ' '
[31] PRINT:'RP= ',(⍕RP),'   HO = ',(⍕HO),' ALPHA = ',(⍕ALPHA),'   THETA= ',⍕THETA
[32]  'PHE = (180-(ALPHA+THETA)) IS:  ',⍕X[1;1]×180÷(○1)
[33]  ' YO = ',(⍕X[2;1]),'   XO =  ',(⍕X[3;1]),'     BO =  ',(⍕BO)
[34]  '  T = ',(⍕T)
[35]  '       S          PHE (RAD)        Y            X  SIN(PHE-THETA)-Y  PHE(DEG)'
[36]  '    ---------------------------------------------------------------------'
[37]  12 5 ⍕Z[(IN-2)+⍳4;]
[38]  'FORCE AT TOP =  ',(⍕FORTOP),'  FORCE AT BOTTOM = ',(⍕FORBOT)
[39]  ' FT - FB =  ',(⍕FΔF),' VOLUME FROM FORCE = ',(⍕VOLFORC)
[40]  '  VOLUME = ',(⍕VOL),'    XMIN = ',(⍕XMIN),'  XSEP= ',(⍕XSEP←(S4[1]-XMIN))
[41]  12 5 ⍕S7
[42]  HHH[I]←H
[43]  VV[I]←VOL
[44]  FF[I]←FORTOP
[45]  XS[I]←XSEP
[46]  AL←ALPHA1
[47]  XY[1;((2×I)-1),(2×I)]←X[2;1],X[3;1]
[48]  XY[2;((2×I)-1),(2×I)]←S3[1],S4[1]
[49]  I←I+1
[50]  →LOOP1
[51] FINISHED:→0
[52] END:'NO CONVERGENCE TOWARDS SOLUTION ',(⍕I1-1),' ITERATIONS TRIED'
[53]  'ALPHA = ',(⍕ALPHA),' IS PROBABLY TO SMALL'
[54]  →0
```

```
     ∇GILL[0]∇
[0]  R←T GILL X;A;B;C;D;E;F;Q;N;M;XX;Z;Y
[1]   A←1
[2]   Y←F←Q←XX←((⍴,X),1)⍴,X
[3]   B← 0.5 0.2928932188 1.707106781
[4]   C← 1 0.5857864376 3.414213562
[5]   E← 0 0.121320344 ¯4.121320344
[6]   GILLDATA←T[1],,XX
[7]   →(T[1]>T[2])/32
[8]   M←1
[9]   D←T[3]÷2
[10]  A←T[1]+0,D,D,2×D
[11]  XX←((⍴,X),1)⍴GILLDATA[⌽(1+⍴GILLDATA)-⍳⍴,X]
[12]  N←1
[13]  Q←(⍴Q)⍴0
[14]  F←A[N]SET XX
[15]  XX←XX+B[N]×2×D×F-Q
[16]  Q←(C[N]×F)+E[N]×Q
[17]  →(3≥N←N+1)/14
[18]  XX←XX+(D÷3)×((T[1]+2×D)SET XX)-2×Q
[19]  →(M= 2 3)/ 22 24
[20]  Y←XX
[21]  D←D÷2
[22]  M←M+1
[23]  →10+2×M=3
[24]  →(((⌈/|,XX-Y)<T[5]× 0.01 1),(T[3]≤T[4]))/ 27 30 30
[25]  T[3]←T[4]⌈T[3]÷2
[26]  →8
[27]  GILLDATA←GILLDATA,(T[1]←T[1]+T[3]),,XX
[28]  T[3]←T[3]×2
[29]  →7
[30]  GILLDATA←GILLDATA,(T[1]←T[1]+T[3]),,XX
[31]  →7
[32]  GILLDATA←(((⍴GILLDATA)÷1+⍴,X),1+⍴,X)⍴GILLDATA
[33]  →0


     ∇LSQR[0]∇
[0]  A←N LSQR XY
[1]   A←XY[;2]⌹XY[;1]∘.*¯1+⍳N+1


     ∇SET[0]∇
[0]  XX←T SET X;A;D;M;N;A1;A2;A3
[1]   A1←(¯1×((1∘X[1;1])÷(X[1;1]×X[2;1]))),0,-B0
[2]   A2←((2∘X[1;1])÷X[1;1]),0,0
[3]   A3←((1∘X[1;1])÷X[1;1]),0,0
[4]   A←(3 3)⍴A1,A2,A3
[5]  ⍝ D←(3 3)⍴0
[6]  ⍝ M←(3 1)⍴0
[7]   N←(3 1)⍴2×H0×RP,0,0
[8]  ⍝ XX←(A+.×X)+(D+.×M)+N
[9]   XX←(A+.×X)+N
```

```
      ∇CALC[0]∇
[0]  QQ←H1 CALC ALPHA;SS;Z1
[1]   HO←H1
[2]   X← 3 1 ρ(○(180-(ALPHA+THETA))÷180),(1○(○ALPHA÷180)),0
[3]  RET:T GILL X
[4]   TE1←(1○(GILLDATA[;2]-○THETA÷180))-GILLDATA[;3]
[5]   TE2←GILLDATA[;2]×180÷(○1)
[6]   Z←GILLDATA,⍉((2,(ρTE1))ρTE1,TE2)
[7]   P1←Z[;5]<¯1E¯6
[8]   IN←P1⍳1
[9]   →((IN+2)>(1↑ρZ))/PRINT
[10]  Z1←Z[((IN-2)+⍳4);]
[11]  S4←2 LSQR Z1[; 5 4]
[12]  S1←2 LSQR Z1[; 5 1]
[13]  S2←2 LSQR Z1[; 5 2]
[14]  S3←2 LSQR Z1[; 5 3]
[15]  S6←2 LSQR Z1[; 5 6]
[16]  Z2←GILLDATA[(⍳IN-1);⍳4],[1]S1[1],S2[1],S3[1],S4[1]
[17]  VA←(○1)×INTEGRAL1((2,(1↑ρZ2))ρZ2[;4],(Z2[;3]×Z2[;3]))
[18]  V1←(○((1-1×2○(○ALPHA÷180))*2)÷3)×((3×1)-(1-1×2○(○ALPHA÷180)))
[19]  VV2←1-1×(2○(○(S6[1]-THETA)÷180))
[20]  V2←(○(VV2*2)÷3)×((3×1)-VV2)
[21]  VOL←VA-(V1+V2)
[22]  XMIN←(2×1)-1×(2○(○ALPHA÷180))+(2○(○(S6[1]-THETA)÷180))
[23]  SS← 12 4 ⍴S7←S1[1],S2[1],S3[1],S4[1],0,S6[1]
[24]  FBO←S3[1]×S3[1]×BO×S4[1]
[25]  FORTOP←(2×S3[1]×(1○(○S6[1]÷180)))+(¯2×S3[1]×S3[1]×HO×RP)+FBO
[26]  FORTOP←FORTOP-(BO×V2÷○1)
[27]  FORBOT←(2×Z2[1;3]×(1○Z2[1;2]))-2×Z2[1;3]×Z2[1;3]×HO×RP
[28]  FORBOT←FORBOT-(BO×V1÷○1)
[29]  FΔF←FORTOP-FORBOT
[30]  →(BO=0)/TESTBO
[31]  VOLFORC←(○FΔF)÷BO
[32] RET2:QQ←VOL
[33]  →0
[34] PRINT:'NO CHANGE IN SIGN DETERMINED.  INTEGRATION HAS TO BE'
[35]  'CARRIED FURTHER, T[2] RESPECIFIED FROM ',(⍕T[2]-0.2),' TO ',(⍕T[2]←T[2]+0.2)
[36]  →RET
[37] TESTBO:VOLFORC←0
[38]  →RET2
```

```
      ∇INTEGRAL1[0]∇
[0]  R←INTEGRAL1 X;T;D
[1]   →3×⍳2=ρρX
[2]   →0,ρD←'REQUIRE MATRIX ARGUMENT'
[3]   T←X[1;]
[4]   X← 1 0 ↓X
[5]   →8×⍳(2≤ρT)^^/T=H←1↓T←1↓T-¯1⌽T
[6]   R←(0 1 ↓X+¯1⌽X)+.×T÷2
[7]   →0
[8]   R←(H÷6)×X+.×2,((¯1-D-ρT)ρ 8 4),(1+D)ρ 2 0 +3×D←2!ρT
```

A.2 Computer programs for the solution of sphere trajectory of a dynamic bridge

In order to solve for the trajectory of a moving sphere falling due to gravity which is part of a two sphere doublet surrounded by a liquid film, Eq. (4.17) was solved:

$$(1 - \frac{d^2\xi}{d\tau^2}) = \frac{1}{a^*} \{ \lambda_1(\xi) \frac{d\xi}{d\tau} + \frac{F_c^*}{Ca} \} \qquad (4.17)$$

The above equation was rearranged by letting:

$$\frac{d\xi}{d\tau} = u$$

so that two sets of first order equations were obtained:

$$\frac{du}{d\tau} = 1 - \frac{1}{a\xi} u - \frac{F_c^*}{a \cdot Ca} \qquad (A.1)$$

$$\frac{d\xi}{d\tau} = u \qquad (A.2)$$

These equations were also solved using the fourth order Runge-Kutta method using the GILL subprogram. The main program that performed the computation was DNSEP along with the subprogram SET.

```
      ∇DNSEP[□]∇
[0]  DNSEP Z;Z1;Z2;S1;S2;IN;P1
[1]  ⍝ PROGRAM TO CALCULATE THE DYNAMIC SEPARATION TIME
[2]  ⍝ FOR TWO PARTICLES CONTAINING A LIQUID BRIDGE
[3]  ⍝ THE FOLLOWING PARAMETERS ARE REQUIRED
[4]  ⍝  AA   --  DIMENSIONLESS VISCOSITY TERM
[5]  ⍝  CA   --  CAPILLARY NUMBER
[6]  ⍝  FC   --  FORCE DUE TO SURFACE TENSION AND PRESSURE
[7]  ⍝           DIFFERENCE BETWEEN PHASES
[8]  ⍝  VB   --  VOLUME OF BRIDGE
[9]  ⍝  FACT --  PROPORTION OF SEPARATION DISTANCE THAT CONTAINS
[10] ⍝           THE THREADLIKE CYLINDER
[11]  X← 2 1 ⍴0,Z
[12] ST:T GILL X
[13]  Z1←GILLDATA
[14]  L←((VB×○4)*(1÷3))×FACT
[15]  IN←(P1←Z1[;3]>L)⍳1
[16]  →((IN+3)>(1↑⍴Z1))/PRINT
[17]  '     TIME  |  DIM. VELOCITY  |  DIM. DISTANCE'
[18]  ' ---------------------------------------------'
[19]  ' '
[20]  7 4 16 6 16 6 ⍕Z1
[21]  Z2←Z1[((IN-3)+⍳6);]
[22]  S1←4 1sqr Z2[; 3 1]
[23]  S2←4 1sqr Z2[; 3 2]
[24]  ' '
[25]  '     AA = ',(⍕AA),'  CA =  ',(⍕CA),' FC = ',(⍕FC)
[26]  '     VB =  ',(⍕VB),'   L = ',(⍕L),' FACT = ',(⍕FACT)
[27]  'DIMENSIONLESS TIME OF RUPTURE IS: ',(⍕L⌊⌿S1)
[28]  'DIMENSIONLESS VELOCITY AT RUPTURE IS: ',(⍕L⌊⌿S2)
[29]  →0
[30] PRINT:'RUPTURE NOT YET REACHED.  INTEGRATION HAS TO BE CARRIED'
[31]  'FURTHER, T[2] RESPECIFIED FROM ',(⍕T[2]),' TO ',(⍕T[2]←T[2]+0.2)
[32]  →ST


      ∇SET[□]∇
[0]  XX←T SET X;A;D;M;N
[1]   A←(2 2)⍴(¯1÷AA×X[2;1]),0,1,0
[2]   D←(2 2)⍴0
[3]   M←(2 1)⍴0
[4]   FC←X[2;1]⌊⌿PC1
[5]   →(FC<0.32)/LIMIT
[6]  RET:N←(2 1)⍴(1-FC÷AA×CA),0
[7]  ⍝ XX←(A+.×X)+(D+.×M)+N
[8]   XX←(A+.×X)+N
[9]   →0
[10] LIMIT:FC←0.32
[11]  →RET
```

A.3 Computer programs for data collection

The programs for the various experiments were written by the author. The recording of dilatometer data for the contraction vs. temperature experiments described in Section 3.5 was accomplished by using a MINC 11 minicomputer and the CONTEM basic program. In order to measure surface viscosity (see Section 3.4) contraction vs. time data was obtained using the CONTIM basic program. In the fluidized bed experiments (see Section 3.2) the FBED basic program was used. The FBED programs required inputs from the keyboard as to details of the experimental run i.e. type of particles used, particle size, date etc.; its only experimental input was rotameter velocity which used pressure and temperature signals coming into the computer to correct the velocity to bed condtions. All other temperature and pressure signals were recorded automatically. The pressure drop across the bed and the pressure drop across a specified distance along the bed (to measure porosity) was also performed by the program. To measure pressures and stress fluctuations the PLATE basic program was used. This program collected 4096 sets of data points for storage into data files which were later analyzed to obtain peak information and Fourier Transform results. For the sphere-liquid-sphere experiments (see Section 4.2) an IBM-XT microcomputer was used with a Data Translation board. The static bridge strength experiment used the STRAIN basic program and the experiments with the moving piston used the PISTON basic program. The STRAIN program collected force data automatically at a given separation distance. The separation distance was measured from the Nikon 6C microscope screen and was entered from the keyboard of the computer. The PISTON program first activates a relay with a Digital Out signal that changes the air flow going to the retracting piston. Subsequently, the program collects and stores strain gauge (force) and LVDT (displacement) data into a data file.

```
10 REM Program to record Expansion/Contraction vs. Temperature
20 REM from a Dilatometer Experiment
30 PRINT 'CONTRACTION VS. TEMPERATURE EXPERIMENT'
40 PRINT 'ENTER TYPE OF PARTICLES '; \ LINPUT M$
50 PRINT 'ENTER SIZE OF PARTICLES (CM) '; \ INPUT H1
60 PRINT 'ENTER RUN NUMBER'; \ LINPUT A$
70 PRINT 'ENTER INITIAL LENGTH OF SAMPLE '; \ INPUT L0
75 PRINT 'ENTER LOWER LIMIT OF TEMPERATURE '; \ INPUT T8
80 PRINT 'ENTER UPPER LIMIT OF TEMPERATURE '; \ INPUT T9
82 PRINT 'ENTER HEATING RATE (@C/MIN): '; \ INPUT H5
84 S9=(T9-T8)/H5*60/500
85 PRINT 'FOR 500 DATA SETS TO BE STORED THE SAMPLING'
86 PRINT USING 'INTERVAL SHOULD BE ###.## SECONDS',S9
90 PRINT 'ENTER SAMPLING INTERVAL (SEC) '; \ INPUT S1
100 PRINT 'ENTER GRAMS OF WEIGHTS TO BE ADDED '; \ INPUT W
122 PRINT 'MAKE SURE EXPANSION SIGNAL IS ON CHANNEL 1'
124 PRINT 'AND THERMOCOUPLE LEADS ARE ON CHANNEL 16'
130 PRINT 'IS MEASURING HEAD ZEROED (Y/N)? '; \ INPUT C1$
140 IF C1$='N' THEN 170 \ IF C1$='n' THEN 170
150 IF C1$='Y' THEN 210 \ IF C1$='y' THEN 210
160 GO TO 130
170 GOSUB 840
180 GO TO 130
190 PRINT 'MAKE SURE EXPANSION SIGNAL IS ON CHANNEL 1'
200 PRINT 'AND THERMOCOUPLE LEADS ARE ON CHANNEL 16'
210 PRINT "ENTER AMPLIFICATION VALUE ON DILATOMETER"
215 PRINT "VALID VALUES ARE 100000 OR 10000"; \ INPUT C2
216 IF C2=100000 THEN L8=1 \ GO TO 240
217 IF C2=10000 THEN L8=10 \ GO TO 240
218 GO TO 210
220 IF C2$='Y' THEN 240 \ IF C2$='y' THEN 240
230 GO TO 190
240 PRINT 'ENTER THE FILENAME OF THE SPECIFICATION FILE ' \ LINPUT S$
250 PRINT 'ENTER THE FILENAME OF THE DATA FILE: ' \ LINPUT D$
251 S$="DY1:"+S$
252 D$="DY1:"+D$
255 L8=1
260 OPEN S$ FOR OUTPUT AS FILE #2
270 PRINT #2,A$
280 PRINT #2,W,',',S1,',',H5,',',T8,',',T9
290 PRINT #2,L0
300 PRINT #2,H1
310 PRINT #2,M$
320 PRINT #2,D$
330 CLOSE #2
340 PRINT 'START EXPERIMENT BY PRESSING START BUTTON ON'
350 PRINT 'THE DILATOMETER, ARE YOU READY? ' \ INPUT C4$
360 IF C4$='Y' THEN 380 \ IF C4$='y' THEN 380
370 GO TO 340
380 DIM Q(2000)
381 DIM #1,D(2000)
382 OPEN D$ FOR OUTPUT AS FILE #1
390 I=1
400 AIN(,Q(I+1),,,1)
```

```
410 TEMPERATURE("K,C",16,Q(I))
415 IF Q(I+1)>.9 THEN  GOSUB 1000
416 IF Q(I+1)<-.9 THEN  GOSUB 1000
420 REM Convert from volts to elongation
430 REM in units of Centimeters
440 Q(I+1)=Q(I+1)*.0254/L0*L8
445 V8$='TEMP= ###.##     ELONGATION/L0= **.***^^^^     VOLTAGE= **.**
450 PRINT USING V8$,Q(I),Q(I+1),Q(I+1)*L0/(.025*L8)
460 D(I)=Q(I)
465 D(I+1)=Q(I+1)
467 IF T>=2000 THEN 500
468 IF Q(I)>T9 THEN 495
470 I=I+2
480 PAUSE(S1)
490 GO TO 400
495 CLOSE #1
496 GO TO 531
500 DIM #3,S(2000)
510 OPEN D$ FOR OUTPUT AS FILE #3
520 BLOCK_MOVE(Q(1),S(1),2000)
530 CLOSE #3
531 OPEN S$ FOR OUTPUT AS FILE #4
532 PRINT #4,A$
533 PRINT #4,W,',',S1,',',H5,',',T8,',',T9
534 PRINT #4,L0
535 PRINT #4,H1
536 PRINT #4,M$
537 PRINT #4,D$
538 PRINT #4,(I-1)/2
539 CLOSE #4
540 GO TO 920
840 REM Subroutine to zero measuring head
850 FOR L=1 TO 20
860 PAUSE(1)
870 AIN(,V,,,1)
880 PRINT V
890 NEXT L
900 RETURN
920 GO TO 1100
1000 FOR K=1 TO 20
1010 PRINT 'RESET MAGNIFICATION ON DILATOMETER TO 10,000X '+CHR$(7)
1020 PAUSE(.25)
1030 NEXT K
1040 PRINT 'HAS MAGNIFICATION ON DILATOMETER BEEN CHANGED (Y/N) ';
1050 IF C5$='Y' THEN 1070 \ IF C5$='y' THEN 1070
1060 GO TO 1040
1070 Q(I+1)=Q(I+1)/10
1080 L8=10
1090 RETURN
1100 END
```

```
10 REM Program to record Expansion/Contracion vs. Time
20 REM from a Dilatometer Experiment
30 PRINT 'CONTRACTION VS. TIME EXPERIMENT'
40 PRINT 'ENTER TYPE OF PARTICLES '; \ LINPUT M$
50 PRINT 'ENTER SIZE OF PARTICLES (CM) '; \ INPUT H1
60 PRINT 'ENTER RUN NUMBER'; \ LINPUT A$
70 PRINT 'ENTER INITIAL LENGTH OF SAMPLE '; \ INPUT L0
75 PRINT 'ENTER TEMP. AT WHICH HEATING RATE WILL CHANGE'
76 PRINT 'ENTER ZERO (0) IF NO CHANGE IN RATE '; \ INPUT T9
77 IF T9=0 THEN T9=2000
80 PRINT 'ENTER SOAK TEMPERATURE '; \ INPUT T
90 PRINT 'ENTER GRAMS OF WEIGHTS TO BE ADDED '; \ INPUT W
100 PRINT 'ENTER SAMPLING INTERVAL BEFORE SOAK '; \ INPUT S1
110 PRINT 'ENTER SAMPLING INTERVAL AFTER SOAK  '; \ INPUT S2
120 PRINT 'ENTER NUMBER OF DATA POINTS AFTER SOAK '; \ INPUT N1
122 PRINT 'MAKE SURE EXPANSION SIGNAL IS ON CHANNEL 1'
124 PRINT 'AND THERMOCOUPLE LEADS ARE ON CHANNEL 16'
130 PRINT 'IS MEASURING HEAD ZEROED (Y/N)? '; \ INPUT C1$
140 IF C1$='N' THEN 170 \ IF C1$='n' THEN 170
150 IF C1$='Y' THEN 210 \ IF C1$='y' THEN 210
160 GO TO 130
170 GOSUB 840
180 GO TO 130
190 PRINT 'MAKE SURE EXPANSION SIGNAL IS ON CHANNEL 1'
200 PRINT 'AND THERMOCOUPLE LEADS ARE ON CHANNEL 16'
210 PRINT 'IS AMPLIFICATION ON DILATOMETER AT 100,000X ' \ INPUT C2$
220 IF C2$='Y' THEN 240 \ IF C2$='y' THEN 240
230 GO TO 190
240 PRINT 'ENTER THE FILENAME OF THE SPECIFICATION FILE ' \ LINPUT S$
250 PRINT 'ENTER THE FILENAME OF THE DATA FILE: ' \ LINPUT D$
260 OPEN S$ FOR OUTPUT AS FILE #2
270 PRINT #2,A$
280 PRINT #2,T,',',W,',',S1,',',S2,',',N1
290 PRINT #2,L0
300 PRINT #2,H1
310 PRINT #2,M$
320 PRINT #2,D$
330 CLOSE #2
340 PRINT 'START EXPERIMENT BY PRESSING START BUTTON ON'
350 PRINT 'THE DILATOMETER. ARE YOU READY? ' \ INPUT C4$
360 IF C4$='Y' THEN 380 \ IF C4$='y' THEN 380
370 GO TO 340
380 DIM T(600),E(600)
390 I=1
400 AIN(,E(I),,,1)
410 TEMPERATURE("K,C",16,T(I))
420 REM Convert from volts to elongation
430 REM in units of Centimeters
440 E(I)=E(I)*.0254
445 V8$='TEMP= ###.##     ELONGATION= ##.###^^^^     VOLTAGE= ##.#### '
450 PRINT USING V8$,T(I),E(I),E(I)/.0254
460 IF T-T(I)<2 THEN 500
461 IF T9-T(I)<2,THEN 491
470 I=I+1
```

```
480 PAUSE(S1)
490 GO TO 400
491 FOR K=1 TO 10
492 PRINT CHR$(7)
493 PAUSE(1)
494 NEXT K
495 PRINT 'RESET HEATING RATE! ARE YOU READY TO '
496 PRINT 'RESTART PROGRAM'; \ LINPUT D9$
497 IF D9$='Y' THEN 499 \ IF D9$='y' THEN 499
498 GO TO 495
499 T9=2000 \ GO TO 390
500 REM This is when the experiment begins
510 FOR K=1 TO 10
520 PRINT CHR$(7)
530 PAUSE(1)
540 NEXT K
550 PRINT 'EXPERIMENT NOW BEGINS'
560 PRINT USING 'INSERT ###.## GRAMS ',W
570 PRINT 'YOU MUST REZERO MEASURING HEAD.  READY  ' \ INPUT C5$
580 IF C5$='Y' THEN 600 \ IF C5$='y' THEN 600
590 GO TO 570
600 GOSUB 840
610 PRINT 'HAS THE MEASURING HEAD BEEN CORRECTLY REZEROED(Y/N) ? ';
620 INPUT C3$
630 IF C3$='Y' THEN 660 \ IF C3$='y' THEN 660
640 IF C3$='N' THEN 570 \ IF C3$='n' THEN 570
650 GO TO 610
660 DIM Q(200)
670 DIM #1,D(200)
680 START_TIME('LINE')
690 OPEN D$ FOR OUTPUT AS FILE #1
700 I1=1
710 AIN(,Q(I1+1),,,1)
720 TEMPERATURE("K,C",16,Q(I1+2))
730 GET_TIME(Q(I1))
740 Q(I1+1)=Q(I1+1)*.0254
750 D(I1)=Q(I1)
760 D(I1+1)=Q(I1+1)
770 D(I1+2)=Q(I1+2)
780 PRINT USING 'TIME= ####.#     CONTRACTION= ##.#####^^^^     TEMP= ###.#
790 IF Q(I1+1)>2 THEN 910
800 IF ((I1+2)/3)>=N1 THEN 910
810 I1=I1+3
820 PAUSE(S2)
830 GO TO 710
840 REM Subroutine to zero measuring head
850 FOR L=1 TO 20
860 PAUSE(1)
870 AIN(,V,,,1)
880 PRINT V,
890 NEXT L
900 RETURN
910 CLOSE #1
920 END
```

```
10 REM Program to record data from a Fluidized
20 REM Bed experiment.
25 X1$=DAT$
30 PRINT 'ENTER THE RUN NUMBER  '; \ INPUT B3
35 PRINT "ENTER BED DIAMETER IN INCHES" \ INPUT B
36 B9=32.892/(B*B)
40 PRINT 'ENTER THE TYPE OF MATERIAL '; \ LINPUT S1$
50 PRINT 'ENTER THE AVERAGE SIZE(cm) '; \ INPUT B1
60 PRINT 'ENTER WEIGHT OF BED(Kg) '; \ INPUT B2
70 PRINT 'ENTER SPECIFICATION FILENAME '; \ LINPUT S8$
75 S2$='DY1:'+S8$
80 PRINT 'ENTER DATA FILENAME '; \ LINPUT S9$
85 S3$='DY1:'+S9$
90 OPEN S2$ FOR OUTPUT AS FILE #2
100 PRINT #2,S1$
110 PRINT #2,B1;',';B2;',';B3
120 PRINT #2,S3$
121 PRINT #2,X1$
122 PRINT 'IS THE TEST SECTION THAT MEASURES BED VOIDAGE '
124 PRINT 'ATTACHED TO THE BED (Y/N)  '; \ LINPUT D1$
126 PRINT 'OK FELLA HOW MANY TEMPERATURE POINTS YOU WANNA SEE ';
140 R=0
150 PRINT 'ENTER # OF VALUES  USED TO AVERAGE PRESSURE READINGS ';
160 PRINT 'ENTER SAMPLING INTERVAL IN THE AVERAGING OF THE PRESSURE
170 INPUT S2
180 S5=2*S1
181 OPEN 'LP:' FOR OUTPUT AS FILE #7
182 PRINT #7,'**********************PRES. DROP V. VELOCITY EXPT******
183 PRINT #7,'LEGEND: QR=ROTO VEL.(SCFH)    LV=LINEAR VEL.(CM/SEC)
184 PRINT #7,'P DROP(CM H20)  DPB=P DROP IN BED  TBB=T BEFORE BED
185 PRINT #7,'
186 PRINT #7,'AGGLOMERATION EXPT. NO. '; \ PRINT #7,B3
187 PRINT #7,'TYPE OF MATERIAL='; \ PRINT #7,S1$
188 PRINT #7,'AVERAGE PARTICLE SIZE (MESH)='; \ PRINT #7,B1
189 PRINT #7,'COLUMN DIAMETER= '; \ PRINT #7,B
190 PRINT #7,'THE FILENAME IS(DAT)  '; \ PRINT #7,S3$ \ CLOSE #7
191 PRINT 'NUMBER OF DATA POINTS TAKEN SO FAR IS: ';R
192 PRINT 'STORE DATA ON FILE (F) OR JUST DISPLAY (D) '
193 PRINT 'OR STOP THE TAKING OF DATA FOR THE RUN (STOP) '; \ LINPUT B4$
194 IF B4$='STOP' THEN 1240 \ IF B4$='stop' THEN 1240
200 PRINT 'ENTER THE ROTAMETER VELOCITY (ft^3/min) '; \ INPUT Q0
205 M9=Q0 \ REM THIS IS FOR THE LP PRINT STATEMENT #1232
214 REM LINE 215 NECESSARY FOR SCFH ROTOMETERS
215 Q0=Q0/60
220 PRINT 'ENTER THE ROTAMETER TEMPERATURE (@F) '; \ INPUT R7
230 R3=(R7-32)/1.8
231 DIM Z(40)
232 AIN(,Z(1),40,.1,4)
233 S=0
234 FOR I=1 TO 40
235 S=S+Z(I)
236 NEXT I
237 R2=S/40
240 Q=Q0*SQR((273+R3)/(25281*(14.7+R2))) \ REM m3/min
```

```
250 REM Q is the corrected volumetric flow at the Rotameter
260 PRINT 'CORRECTED ROTAMETER VELOCITY IS (m3/min): ';Q
270 REM Get the Temperature of the air
280 S=0
290 DIM R1(20)
300 FOR I=1 TO 3
310 TEMPERATURE('K,C',17,T1)
320 S=S+T1
330 NEXT I
340 A1=S/3
350 S=0
360 FOR I=1 TO 3
370 TEMPERATURE('K,C',18,T2)
380 S=S+T2
390 NEXT I
400 DIM P1(200)
410 DIM E(512)
420 A2=S/3
430 AIN(,P1(1),S5,S2,2,2)
440 S3=0 \ S4=0
450 FOR I=1 TO S1 STEP 2
460 S2=P1(I)*S2+S3
470 S4=P1(I+1)*S2+S4
480 NEXT I
490 P3=S3*10/(S1*S2/2)
500 P4=S4*10/(S1*S2/2)
505 IF D1$='N' THEN P4=0 \ IF D1$='n' THEN P4=0
510 AIN(,R1(1),20,S2,4)
520 S7=0
530 FOR I=1 TO 20 \ S7=R1(I)*S2+S7 \ NEXT I
540 P5=S7*200/(20*S2)
545 IF D5$='N' THEN 660 \ IF D5$='n' THEN 660
550 AIN(,E(),513,.01,5)
560 S6=E(0)+E(512)
570 FOR I=1 TO 511 STEP 2 \ S6=S6+4*E(I) \ NEXT I
580 FOR I=2 TO 510 STEP 2 \ S6=S6+2*E(I) \ NEXT I
590 S6=S6*.01/3
600 P6=ABS(S6/(.01*512))
610 REM set the velocity of the bed using the pitot
620 REM tube values
621 S=0
622 FOR I=1 TO 3
623 TEMPERATURE('E,C',19,T3)
624 S=S+T3
625 NEXT I
626 A3=S/3
630 V3=SQR(574.549*P6*(A3+273.15)/(P5+1034))
640 REM V4 is the velocity at the bed conditions
650 V4=V3*.11615*((P5+1034)*(A1+273.15)/((P3+1034)*(A3+273.15)))
660 DIM #1,D(39,6)
665 Q3=((R2*70.37)+1034)*(A1+273.2)/((P3+1034)*(R3+273))
666 Q4=Q*B9*Q3
670 IF B4$='D' THEN 700 \ IF B4$='d' THEN 700
680 IF B4$='F' THEN 690 \ IF B4$='f' THEN 690
690 GOSUB 1140
700 PRINT
```

```
760 F1$='QUC (ft3/min)= ###.##     PROT (psig)= ##.##     TROT (@C)= ###.##
770 PRINT USING F1$,Q0,R2,R3
780 F3$=' P<>BED (cm H20)= ###.##  P<>PH (cm H20)= ###.## '
790 PRINT USING F3$,P3,P4
800 F2$='  TBBED= ######.##          TOFRED= ####.##     '
810 PRINT USING F2$,A1,A2
820 Q3=((R2*70.37)+1034)*(A1+273.2)/((P3+1034)*(R3+273))
830 Q4=Q*B9*Q3
840 PRINT USING 'LINEAR VELOCITY IN THE BED IS: **.**** (meters/sec) ',Q4
881 GOSUB 1050
882 PRINT 'CONTINUE DISPLAYING TEMPERATURE (Y/N)  ';\ LINPUT S8$
886 IF S8$='Y' THEN  GOSUB 1050 \ IF S8$='y' THEN  GOSUB 1050
887 IF S8$='N' THEN 900 \ IF S8$='n' THEN 900
888 GO TO 882
900 IF R>=40 THEN 920
910 GO TO 191
920 GO TO 980
930 AIN(,M,,,2,)
940 AIN(,N,,,3)
950 PRINT M,N
960 PAUSE(1)
970 GO TO 930
980 GO TO 1040
990 DIM #5,H(39,6)
1000 OPEN S3$ FOR INPUT AS FILE #5
1010 FOR K=0 TO 6
1020 PRINT H(R-1,K);'  ';
1030 NEXT K
1040 GO TO 1130
1050 FOR J=1 TO J5
1060 F6$=' LINEAR VELOCITY= ###.#### (m/s)   TBBED= ###.##
1070 TEMPERATURE('K,C',17,T1)
1080 TEMPERATURE('K,C',18,T2)
1090 PRINT USING F6$,Q4,T1,T2
1100 PAUSE(2)
1110 NEXT J
1120 RETURN
1130 GO TO 1240
1140 OPEN S3$ AS FILE #1
1150 D(R,0)=Q0
1160 D(R,1)=R2
1170 D(R,2)=R3
1180 D(R,3)=P3
1190 D(R,4)=A1
1200 D(R,5)=A2
1210 D(R,6)=P4
1220 CLOSE #1
1225 R=R+1
1229 OPEN 'LP:' FOR OUTPUT AS FILE #7
1230 F7$='NO.=##  QR=###  LV=###.#  DPT=##.#  DPB=##.#  TBB=###.#
1232 PRINT #7,USING F7$,R,M9,Q4*100,P3,P4,T1,T2
1233 CLOSE #7
1235 RETURN
1240 PRINT #2,R
1250 CLOSE #2
1260 GO TO 1330
1300 FOR K=1 TO 200
1310 GOSUB 1050
1320 NEXT K
1330 END
```

```
10 REM PLATE.BAS
20 REM Program to record Pressure Fluctuations in a Fluidized Bed
30 PRINT " ***********************************************"
40 PRINT " * PRESSURE FLUCTUATIONS ON AN AGGLOMERATE EXPERIMENT *"
50 PRINT " ***********************************************"
60 PRINT "ENTER RUN NUMBER  "; \ INPUT R1
70 PRINT "ENTER TYPE OF PARTICLES  "; \ LINPUT T$
80 PRINT "ENTER FREQUENCY OF SAMPLING "; \ INPUT F
90 PRINT "ENTER THE ROTAMETER VELOCITY (ft*3/min) "; \ INPUT Q0
95 Q0=Q0/60
96 PRINT " ********THIS PROGRAM IS FOR PER HOUR ROTOMETERS ********"
97 PRINT " ******* .   SEE LINE 95  ********************"
110 PRINT "ENTER THE ROTAMETER TEMPERATURE (@F) "; \ INPUT R7
111 DIM Z(40)
112 AIN(,Z(1),40,.1,4)
113 S=0
114 FOR I=1 TO 40
115 S=S+Z(I)
116 NEXT I
117 R2=S/40
120 R3=(R7-32)/1.8
130 Q=Q0*SQR((273+R3)/(25281*(14.7+R2))) \ REM m3/min
140 REM Q IS THE CORRECTED VOLUMETRIC FLOW AT THE ROTAMETER
150 REM GET THE TEMPERATURE OF THE AIR
160 S=0
170 S5=40
180 S1=S5/2
190 S2=.05
200 FOR I=1 TO 3
210 TEMPERATURE('K,C',17,T1)
220 S=S+T1
230 NEXT I
240 A1=S/3
250 S=0
260 FOR I=1 TO 3
270 TEMPERATURE('K,C',18,T2)
280 S=S+T2
290 NEXT I
300 A2=S/3
310 DIM P1(44)
320 AIN(,P1(1),S5,S2,2,2)
330 S3=0 \ S4=0
340 FOR I=1 TO S5/2 STEP 2
350 S3=P1(I)*S2+S3
360 S4=P1(I+1)*S2+S3
370 NEXT I
380 P3=S3*10/(S1*S2/2)
390 P4=S4*10/(S1*S2/2)
400 Q3=((R2*70.37)+1034)*(A1+273.2)/((P3+1034)*(R3+273.2))
405 PRINT "ENTER BED DIAMETER(3 OR 6 IN.)  " \ INPUT B
406 B1=32.892/(B*B)
410 V=Q*B1*Q3
420 PRINT USING 'LINEAR VELOCITY IN THE BED IS: **.**** (meters/sec) ',V
425 PRINT USING 'TOT P DROP OVER THE BED IS :  **.*** (CM H20) ',P3
430 DIM #1,Y(4097)
440 DIM X(2047)
450 PRINT "ENTER SPECIFICATION FILENAME "; \ LINPUT S$
```

```
460 PRINT "ENTER DATA FILENAME "; \ LINPUT D$
470 S1$="DY1:"+S$
480 D1$="DY1:"+D$
490 OPEN S1$ FOR OUTPUT AS FILE #2
500 PRINT #2,R1,',',F,',',V
510 PRINT #2,T$
520 PRINT #2,D1$
530 CLOSE #2
540 PRINT "ARE YOU READY TO START THE COLLECTION OF DATA (Y/N) ";
550 LINPUT S2$
560 IF S2$="Y" THEN  GOSUB 580 \ IF S2$="y" THEN  GOSUB 580
570 GO TO 540
580 OPEN D1$ FOR OUTPUT AS FILE #1
592 I4%=0
594 I3%=0
596 AIN('CONTINUOUS',X(),2048,F,5)
598 WAIT_FOR_DATA(X(),I1%)
599 IF I4%=4 THEN  GO TO 610
600 BLOCK_MOVE(X(I1%),Y(I3%),1024)
602 I4%=I4%+1
604 I3%=I3%+1024
607 GO TO 598
610 CLOSE #1
620 PRINT 'DO YOU WANT TO SEE PLOT (Y/N) '; \ LINPUT E5$
630 IF E5$="Y" THEN  GO TO 1105 \ IF E5$'y' THEN  GO TO 1105
640 STOP
1000 DISPLAY_CLEAR
1005 PRINT 'DO YOU WANT TO CHANGE WINDOW (Y) OR END THE PROGRAM (E)'
1007 LINPUT E6$
1008 IF E6$="Y" THEN  GO TO 1010 \ IF E6$="y" THEN  GO TO 1010
1009 GO TO 1110
1010 PRINT "INPUT WINDOW STATEMENT VALUES"
1020 PRINT "LOW X, LOW Y, HIGH X, HIGH Y  ; "; \ INPUT A,B,C,D
1030 PRINT "SHADE OR LINES "; \ LINPUT E$
1040 WINDOW("EXACT",A,B,C,D)
1050 GRAPH(E$,C-A,,X())
1060 STOP
1100 GO TO 1005
1105 GRAPH("L",,,X())
1106 GO TO 1005
1110 STOP
2000 OPEN D1$ FOR INPUT AS FILE #6
2010 DIM #6,B(4097)
2020 FOR I=4000 TO 4097
2030 PRINT I,B(I)
2040 NEXT I
2050 CLOSE #6
```

```
980 ' ******************  STRAIN  ****************************
990 ' *  Program to record the strength as a function of     *
992 ' *  separation distance for a static bridge experiment. *
994 ' ********************************************************
1000 PRINT "STATIC SEPARATION DISTANCE VS. FORCE EXPERIMENT"
1010 INPUT "Enter filename: ",FILE$
1020 INPUT "Enter radius of spheres: ",RADIUS
1030 INPUT "Enter type of liquid: ",LIQUID$
1040 INPUT "Enter volume of liquid (Micro-Liters): ",VOL
1045 GOSUB 4000
1050 NUMBER%=1
1130 DEF SEG=7936       ' This specifies where in memory to place PCTHERM.
1140 BLOAD "PCTHERM",0  ' This actually performs the PCTHERM load.
1150 '
1160 '   All variables should be given initial values
1170 '   before being used in PCTHERM calls.
1180 '
1190 DIM ANALOG.ARRAY%(512)
1200 NUMBER.OF.VALUES% = 512
1210 '
1212 ANALOG.VALUE% = 0
1214 ADC.VALUE = 3
1220 SETUP.ADC = 9              ' This is a PCTHERM entry point.
1230 ADC.SERIES = 12            ' This is a PCTHERM entry point.
1240 SET.CLOCK.DIVIDER = 45     ' This is a PCTHERM entry point.
1250 ',
1260 HIGH.V! = +10!             ' Highest voltage in range.
1270 LOW.V!  = -10!             ' Lowest voltage in range.
1280 RANGE! = HIGH.V! - LOW.V!  ' Total voltage range.
1290 '
1300 NOC! = 4096!
1310 ' For 1420 a DT2801/5716 and DT2805/5716:   NOC! = 65536!
1320 ' For DT2808: NOC! = 1024!
1330 '
1340 LSB! = RANGE!/NOC!                 ' Voltage of Least Significant Bit.
1350 '
1360 '  The following section sets up the A/D.
1370 '
1380 TIMING.SOURCE% = 0         ' Software trigger, internal clock.
1390 '
1400 ' Define channel scan.
1410 '
1420 CLS
1430 INPUT " Enter channel number that is to be scanned  ",START.CHAN%
1440 END.CHAN%=START.CHAN%
1450 '
1460 IF (START.CHAN% <= END.CHAN%) GOTO 1510
1470 PRINT "In this example program the starting channel number";
1480 PRINT "cannot be greater than the ending channel number."
1490 GOTO 1430
1500 '
1510 SCAN.LENGTH% = (END.CHAN% + 1) - START.CHAN%
1520 NUMBER.OF.SCANS% = (NUMBER.OF.VALUES% / SCAN.LENGTH%) - 1
1530 ' " This will perform ";NUMBER.OF.SCANS%;" complete scans."
```

```
1531 CLS
1532 PRINT
1533 PRINT
1536 PRINT USING "So far ### data points have been taken. " ;NUMBER%-1
1537 PRINT "Do you want to "
1538 PRINT " (1) Store separation vs. force data on file. "
1540 PRINT " (2) Just display the voltage data. "
1541 PRINT " (3) End the program. "
1542 INPUT CHK1%
1544 IF CHK1%=3 THEN END
1550 INPUT " Enter the desired Gain (1,2,4,8,10,100 or 500) ",GAIN%
1560 '
1570 CALL SETUP.ADC (TIMING.SOURCE%, START.CHAN%, END.CHAN%, GAIN%)
1580 '
1590 SCALED.LSB! = LSB! / GAIN%          ' Calculate scaled LSB.
1600 SCALED.LOW! = LOW.V! / GAIN%        ' Calculate scaled LOW voltage.
1610 '
1620 ' Next set up the internal clock.
1630 '
1635 IF CHK1%=2 THEN 6000
1638 PRINT "Enter the separation distance of the spheres: "
1639 INPUT "In grid units: ",SEPDIS
1640 '  " Enter the clock frequency ( 13. - 12000.) ",REQUESTED.FREQ
1641 SEPDIS=SEPDIS*.0049612
1644 PRINT "SEPARATION DISTANCE IS (cm):  ",SEPDIS
1645 REQUESTED.FREQ = 100
1650 CLOCK.DIVIDER% = (400000! / REQUESTED.FREQ) - .5
1660 ACTUAL.FREQ = 400000! / CLOCK.DIVIDER%
1670 ' " Actual frequency is ";ACTUAL.FREQ;" Hertz"
1680 '
1690 CALL SET.CLOCK.DIVIDER (CLOCK.DIVIDER%)
1700 '
1710 ' This performs the actual data collection.
1720 '
1730 OUT &H21,(INP(&H21) OR &H1)    ' Turn off PC's time of day clock.
1740 CALL ADC.SERIES (NUMBER.OF.VALUES%, ANALOG.ARRAY%(0))
1750 OUT &H21,(INP(&H21) AND &HFE) ' Turn on PC's time of day clock.
1760 GOSUB 3000
1770 GOTO 1532
1780 '
3000 S=0
3010 OPEN FILE$ FOR APPEND AS 1
3030 S=((ANALOG.ARRAY%(0)*SCALED.LSB!)+SCALED.LOW!)+((ANALOG.ARRAY%(512)*SCALED.LSB!)
LED.LOW!)
3040 FOR I=1 TO 511 STEP 2
3045 R=(ANALOG.ARRAY%(I)*SCALED.LSB!)+SCALED.LOW!
3050 S=S+(4*R)
3060 NEXT I
3070 FOR I=2 TO 510 STEP 2
3075 R=(ANALOG.ARRAY%(I)*SCALED.LSB!)+SCALED.LOW!
3080 S=S+(2*R)
3090 NEXT I
3100 S=(S*512)/(6*256)
3110 PRINT "Calculated integral is:  ";S
3115 AVG1=S/512
```

```
3120 PRINT "Average VOLTAGE of signal is:  ";AVG1
3122 PRINT #1,SEPDIS
3124 PRINT #1,AVG1
3126 NUMBER%=NUMBER%+1
3128 CLOSE #1
3130 RETURN
4000 OPEN FILE$ FOR OUTPUT AS #2
4010 PRINT #2,RADIUS
4020 PRINT #2,LIQUID$
4030 PRINT #2,VOL
4040 CLOSE #2
4050 RETURN
5000 INPUT "Enter data FILENAME  ",FILE$
5005 OPEN FILE$ FOR INPUT AS #3
5010 INPUT #3,RADIUS
5020 PRINT RADIUS
5030 INPUT #3,LIQUID$
5040 PRINT LIQUID$
5050 INPUT #3,VOL
5060 PRINT VOL
5070 FOR I=1 TO 40
5080 INPUT #3,TMSEP
5090 INPUT #3,TMFOR
5094 PRINT TMSEP,TMFOR
5100 NEXT I
5110 CLOSE #3
5120 STOP
6000 FOR I=1 TO 20
6008 CALL ADC.VALUE(START.CHAN%,GAIN%,ANALOG.VALUE%)
6010 VOLTAGE! = (ANALOG.VALUE% * SCALED.LSB!) +SCALED.LOW!
6020 PRINT VOLTAGE!
6030 FOR J=1 TO 400
6040 NEXT J
6050 NEXT I
6060 PRINT "Continue the display of the voltage (C) or GO back to the"
6070 INPUT "taking of data (GO) ? " ,CHK1$
6080 IF CHK1$="GO" THEN GOTO 1531
6090 IF CHK1$="go" THEN GOTO 1531
6100 GOTO 6000
```

```
1100 ' ****************  PISTON  ****************************
1110 ' *     Program to retract piston and measure voltage    *
1120 ' *     from strain gauge and from LVDT and to store     *
1130 ' *     data on a file.                                  *
1150 ' ***********************************************************
1180 DEF SEG=7936        ' This specifies where in memory to place PCTHERM.
1190 BLOAD "PCTHERM",0   ' This actually performs the PCTHERM load.
1200 ENABLE.FOR.OUTPUT = 60
1210 OUTPUT.DIGITAL.VALUE = 66
1220 OUTPUT.DIGITAL.ON.TRIGGER = 72
1230 SET.TIMEOUT = 105
1330 PORT.SELECT% = 0
1400 ' Convert bit (0-7) into Bit MASK.
1420 D.MASK% = 2 ^ DIGITAL.LINE%
1510 DIGITAL.LINE% = 0
1511 D.VALUE% = &H0
1512 CALL ENABLE.FOR.OUTPUT (PORT.SELECT%)
1514 CALL OUTPUT.DIGITAL.VALUE (PORT.SELECT%, D.MASK%,D.VALUE%)
1550 PRINT " Bit mask = &H";HEX$(D.MASK%)
1570 INPUT " Enter desired state (H = High/ L = Low) ",D.STATE$
1572 IF D.STATE$="H" OR D.STATE$="h" THEN D.VALUE% = &HFFFF : GOTO 1600
1574 IF D.STATE$="L" OR D.STATE$="l" THEN D.VALUE% = &H0 : GOTO 1600
1576 PRINT " Enter JUST H or L" : GOTO 1570
1580 '
1590 '
1600 INPUT " Enter the desired Gain (1,10,100 or 500) ",GAIN%
2300 '
2400 '   All variables should be given initial values
2500 '   before being used in PCTHERM calls.
2600 '
2610 NUMBER.OF.VALUES%=5000
2700 DIM ANALOG.VALUES%(10001)
2900 '
3000 SETUP.ADC = 9               ' This is a PCTHERM entry point.
3100 BEGIN.ADC.DMA = 15          ' This is a PCTHERM entry point.
3200 WAIT.ADC.DMA = 21           ' This is a PCTHERM entry point.
3300 SET.CLOCK.DIVIDER = 45      ' This is a PCTHERM entry point.
3400 SET.ERROR.CONTROL.WORD = 75 ' PCTHERM entry point.
3500 GET.ERROR.CODE = 78         ' This is a PCTHERM entry point.
3600 '
3700 ERROR.CONTROL.WORD% = 0
3800 ERROR.CODE% = 0
3810 '
4300 '
4400 '  The following section sets up the A/D.
4500 '
4600 TIMING.SOURCE% = 0
4700 START.CHAN% = 1 : END.CHAN% = 2
4800 NUMBER.OF.CHANNELS% = (END.CHAN% - START.CHAN%) + 1
4900 '
5200 '
5400 '
5405 ERROR.CONTROL.WORD% = 0
5410 CALL SET.ERROR.CONTROL.WORD(ERROR.CONTROL.WORD%)
5420 '
```

```
5500 CALL SETUP.ADC (TIMING.SOURCE%, START.CHAN%, END.CHAN%, GAIN%)
5501 CALL GET.ERROR.CODE(ERROR.CODE%)
5600 '
5605 ERROR.CONTROL.WORD% = 0
5610 CALL SET.ERROR.CONTROL.WORD(ERROR.CONTROL.WORD%)
5700 IF ERROR.CODE% = 0 GOTO 6300
5800 PRINT " Setup error, try again."
5900 GOTO 4700
6000 '
6100 ' Next setup the internal clock.
6200 '
6300 CLOCK.DIVIDER% = (400000! / 6000!) - .5     ' 6000 Hertz
6400 ACTUAL.FREQ = 400000! / CLOCK.DIVIDER%
6500 PRINT " Actual sampling frequency is ";ACTUAL.FREQ;" Hertz"
6600 '
6700 CALL SET.CLOCK.DIVIDER (CLOCK.DIVIDER%)
6800 CALL OUTPUT.DIGITAL.VALUE (PORT.SELECT%, D.MASK%, D.VALUE%)
7500 CALL BEGIN.ADC.DMA (NUMBER.OF.VALUES%, ANALOG.VALUES%(1))
7600 CALL WAIT.ADC.DMA
9000 INPUT "Enter filename of data file  ",DOM$
9002 D.VALUE% = &H0
9004 CALL OUTPUT.DIGITAL.VALUE (PORT.SELECT%, D.MASK%,D.VALUE%)
9005 CALL BEGIN.ADC.DMA (NUMBER.OF.VALUES%, ANALOG.VALUES%(5001))
9006 CALL WAIT.ADC.DMA
9007 FOR I=1 TO 1000 : NEXT I
9010 OPEN DOM$ AS #1 LEN=2
9020 FIELD #1, 2 AS Z$
9030 FOR I=1 TO NUMBER.OF.VALUES% * 2
9040 LSET Z$=MKI$(ANALOG.VALUES%(I))
9050 PUT #1,I
9060 NEXT I
9070 CLOSE #1
9080 END
10000 FOR I=1 TO NUMBER.OF.VALUES% * 2 STEP 2
10010 VOLTAGE1 = ((ANALOG.VALUES%(I)*20/4096)-10)/GAIN%
10015 VOLTAGE2 = ((ANALOG.VALUES%(I+1)*20/4096)-10)/GAIN%
10018 BB$="  #####    ####.######       #####    ####.######"
10020 PRINT USING BB$;I,VOLTAGE1,I+1,VOLTAGE2
10030 NEXT I
10040 END
```

APPENDIX B

Calibration of the strain gauge and LVDT

The strain gauge force measuring device which was used in both the static and dynamic bridge strength experiments described in Sections 4.2 and 4.3 was calibrated to assure that an accurate force value could be obtained from the recorded voltage. For the static bridge experiments the forces measured were very small so that a long lever arm that connected to two strain gauges was used to maximize the sensitivity. A sample calibration curve is shown in Figure B.1. As seen the force vs. voltage signal is quite linear in the range of interest for the static bridge experiments.

When performing the dynamic bridge experiments the lever arm was shortened so that the force measuring device would not be so sensitive. This was necessary because of the tremendous increase in the strength of the dynamic bridge as compared to the static bridge. Figure B.2 shows the calibration curve for this force measuring system. Once again a linear relationship is obtained.

Finally the Linear Variable Differential Transformer (LVDT) that was connected to the moving piston as described in Section 4.3 was calibrated with the voltage signal output. This distance vs. voltage calibration curve is shown in Figure B.3. The distance was accurately measured by the projection of the piston onto the Nikon 6C projection microscope which has a 20X magnification.

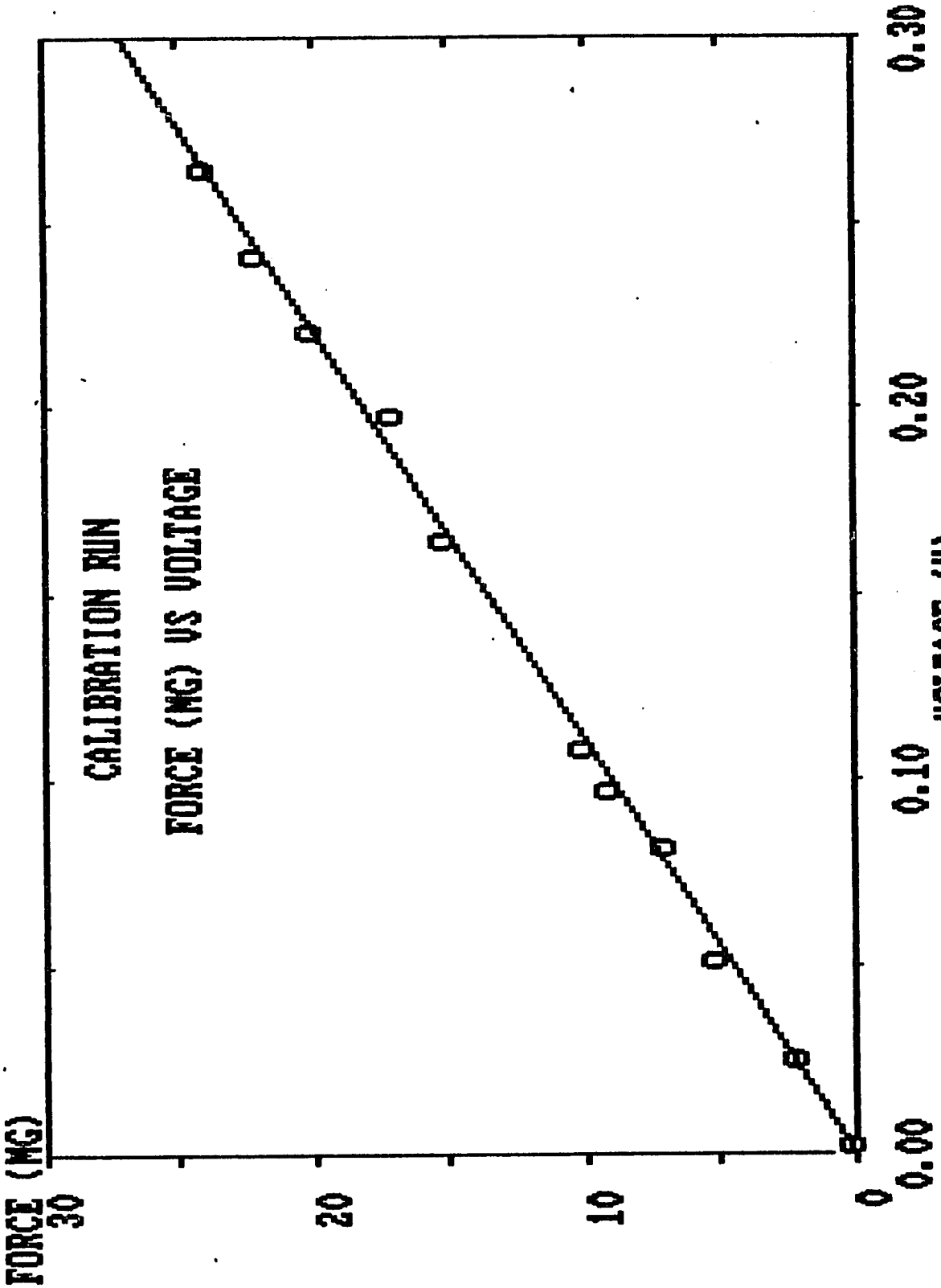

Figure B.1. Force vs voltage; calibration curve for the strain gauge used in the static bridge experiments.

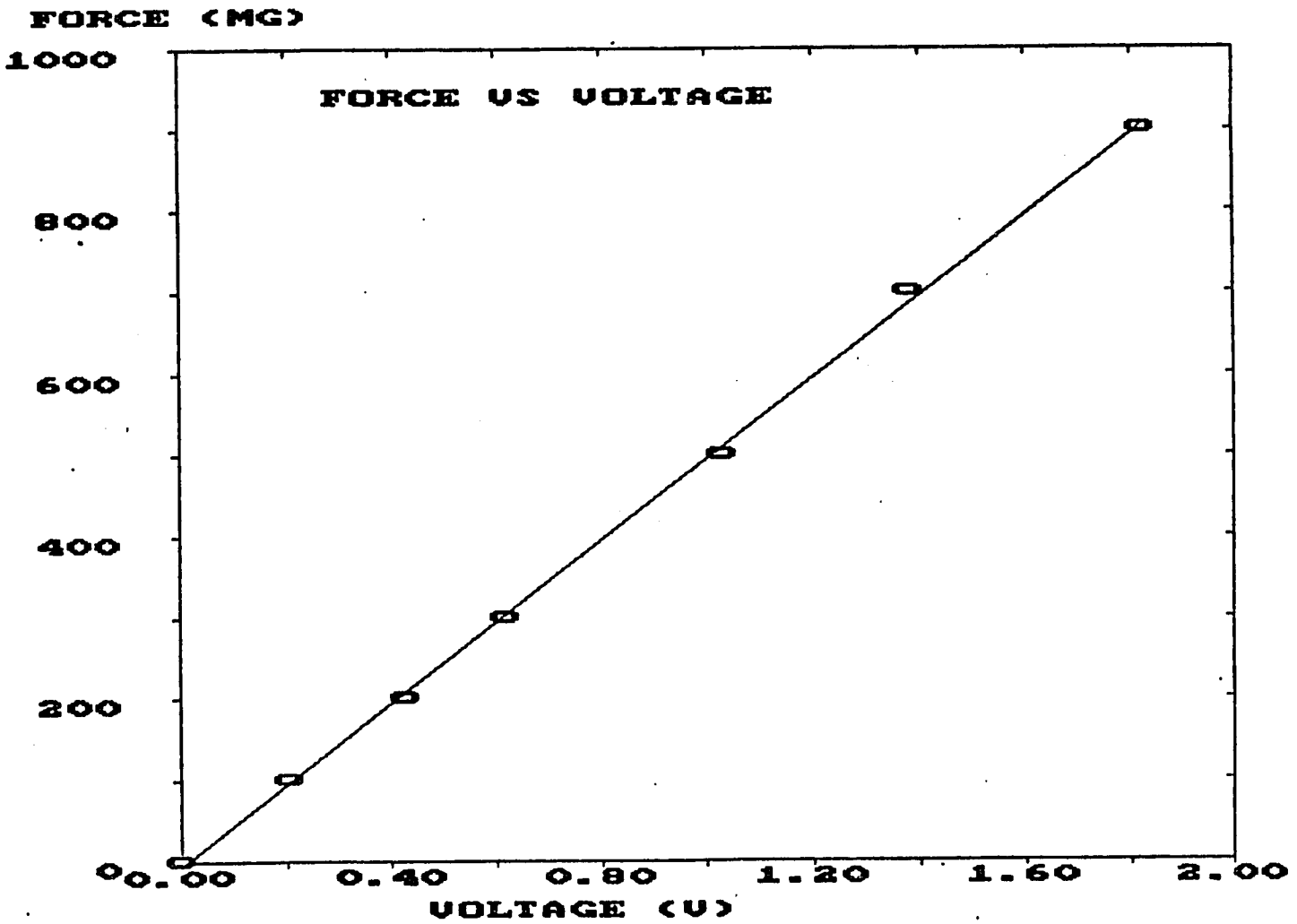

Figure B.2. Force vs. voltage; calibration curve for the strain gauge used in the dynamic bridge experiments.

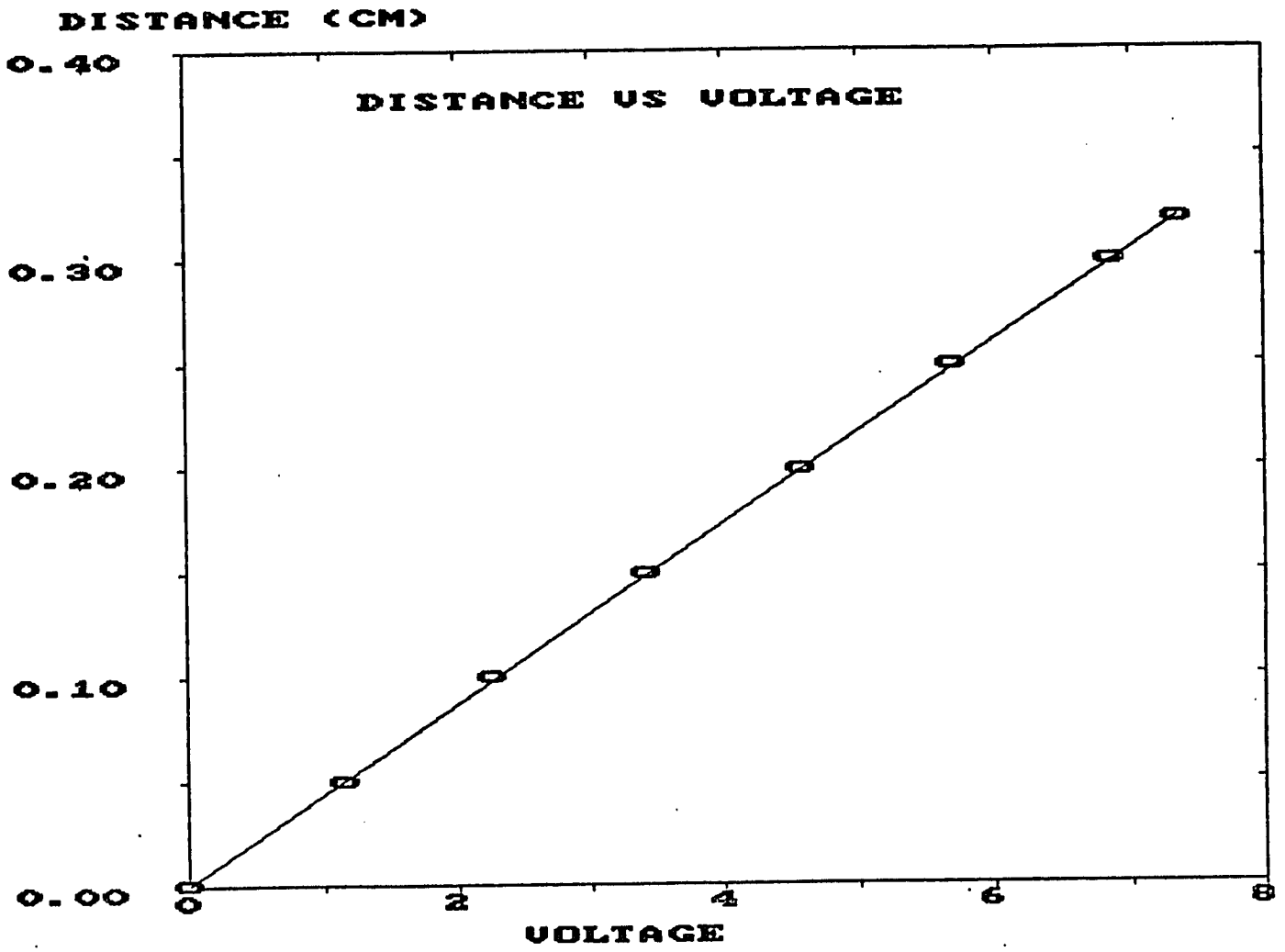

Figure B.3. Displacement vs. voltage; calibration curve for the LVDT used in the dynamic bridge experiments.

APPENDIX C

Determination of the minimum fluidization velocity in a fluidized bed

To determine the minimum fluidization velocity in the fluidized bed experiments the following procedure was performed. Temperature and pressure data for each experimental run was stored in a MINC-11 minicomputer. Subsequently, the air velocity through the rotameter was corrected to give the actual superficial air velocity at different points in the system and the pressure drop due to the particles in the fluidized bed was calculated from the total pressure drop in the bed by the use of two pressure taps that were connected to a pressure transducer. The minimum theoretical fluidization velocity u_{mf} of the bed was calculated from (Kunii and Levenspiel, 1969):

$$Ga = 150(1 - \epsilon_{mf}) \frac{Re_{mf}}{\phi^2 \epsilon_{mf}^3} + \frac{1.75}{\phi \epsilon_{mf}^3} Re_{mf}^2 \qquad (C.1)$$

where,

$$Ga = \rho_g(\rho_s - \rho_g)D_p^3 g/\mu \qquad (C.2)$$

$$Re_{mf} = \rho_g u_{mf} D_p/\mu \qquad (C.3)$$

where u_{mf} is the minimum fluidization velocity, g is the acceleration due to gravity, D_p is the diameter of the particle, ϵ_{mf} is the bed voidage at incipient fluidization, ρ_g is the density of the fluid, ρ_s is the density of the particles, μ_g is the viscosity of the fluid and ϕ is the sphericity of the solid granules. Both the pressure drop in the bed and the velocity of the gas are made dimensionless by

$$P = \frac{\Delta P_b}{W/A} \qquad (C.4)$$

$$U = u/u_{mf} \qquad (C.5)$$

where A is the cross sectional area of the bed (m^2), W is the weight of the particles (kg), ΔP_b is the pressure drop (kg/m^2), u

is the linear velocity (m/sec) and u_{mf} is the calculated minimum fluidization velocity from Eq. (C.1).

A number of experiments were performed as described in Section 3.3 for a 2 kg bed of D_p=0.2 cm polypropylene particles with the following characteristics: density, ρ_s= 0.92 g/cm^3 and sphericity ϕ=.78. These particles have a melting point of 172^{o}C and a sintering temperature T_s of 143^{o}C. Experiments were performed at air temperatures of 25, 90, 143, 160 and 164 degrees Centigrade. The dimensionless pressure drop, P, versus dimensionless velocity u_{mf} at room temperature (25^{o}C) is shown in Figure C.1. The experimental minimum fluidization velocity, u_{mf}, was obtained by the intersection of two linear least squares fitted lines of the data points. The two lines correspond to the pressure-velocity data for the fixed and for the fluidized bed region, respectively. The experiment was performed by first decreasing the velocity from the fluidized state to the packed bed state and then refluidizing the bed by increasing the gas velocity. As seen from Figure C.1 there is no noticeable hysterisis effect for the fluidized bed at room temperature. The agreement between the experimentally determined fluidization velocity and that obtained by the use of Eq. (C.1) is excellent, as can be judged from the value of the intercept, u/u_{mf} = 1.027.

Figure C.2 shows pressure drop versus velocity data for the bed at 160^{o}C a value which is near the minimum sintering temperature, T_s. In this case there is a noticeable difference in the behavior of the bed when the velocity was increased or decreased. The behavior when decreasing the velocity to the fixed bed state was similar in all respects to the run at room temperature. When the velocity was increased and the point of refluidization was approached a hole or channel was formed in the center of the bed, in this region particles were geysering due to the passage of air in the hole. The rest of the bed, apart from this "hole" was in the fixed bed mode. With slowly increasing velocity it was observed that the "hole" increased until it comprised the whole bed. This point corresponded to a fully fluidized bed. For this run the minimum fluidization velocity determined experimentally

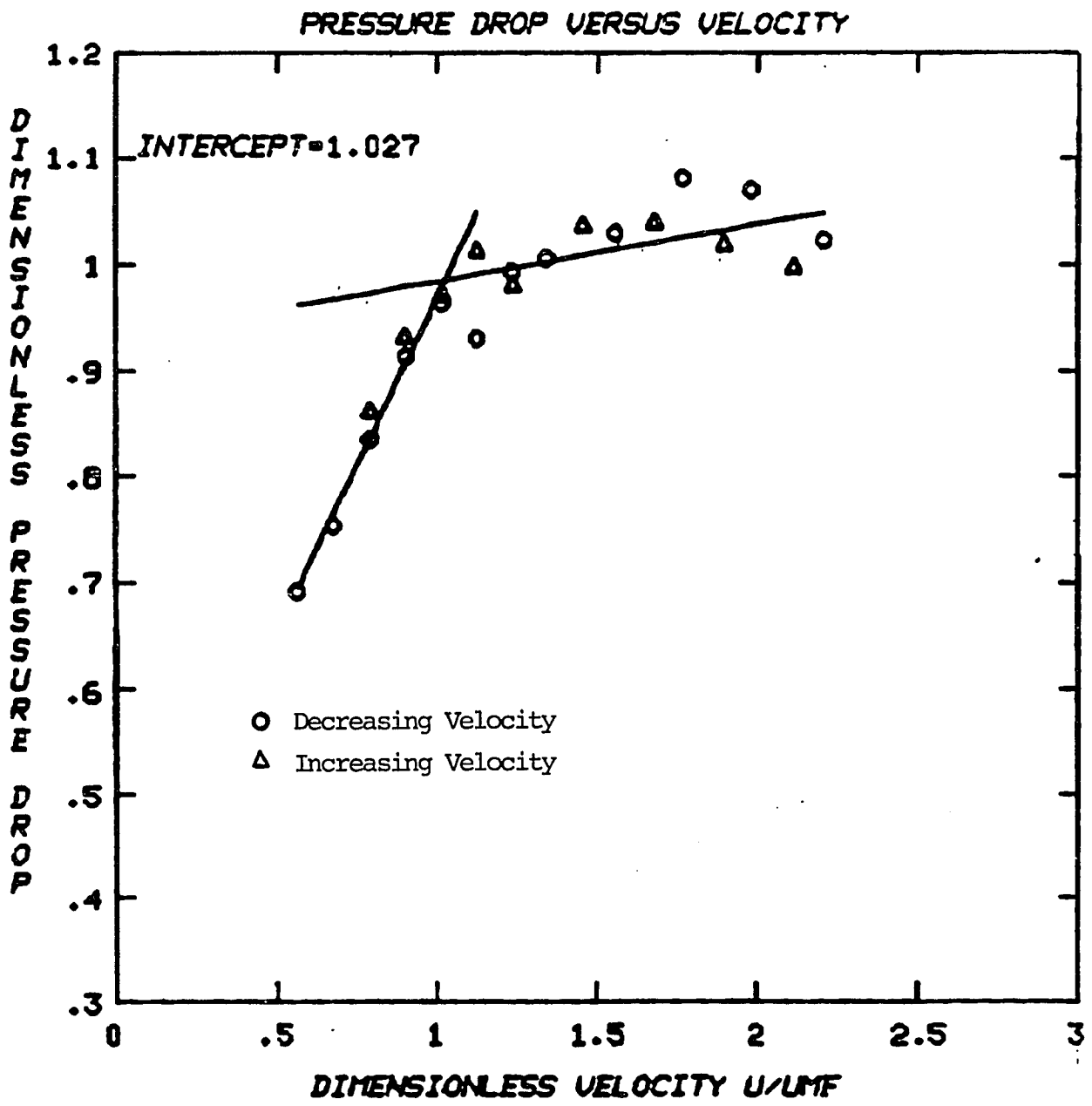

Figure C.1. Pressure drop vs. gas velocity in the bed at 25°C. (polypropylene particles).

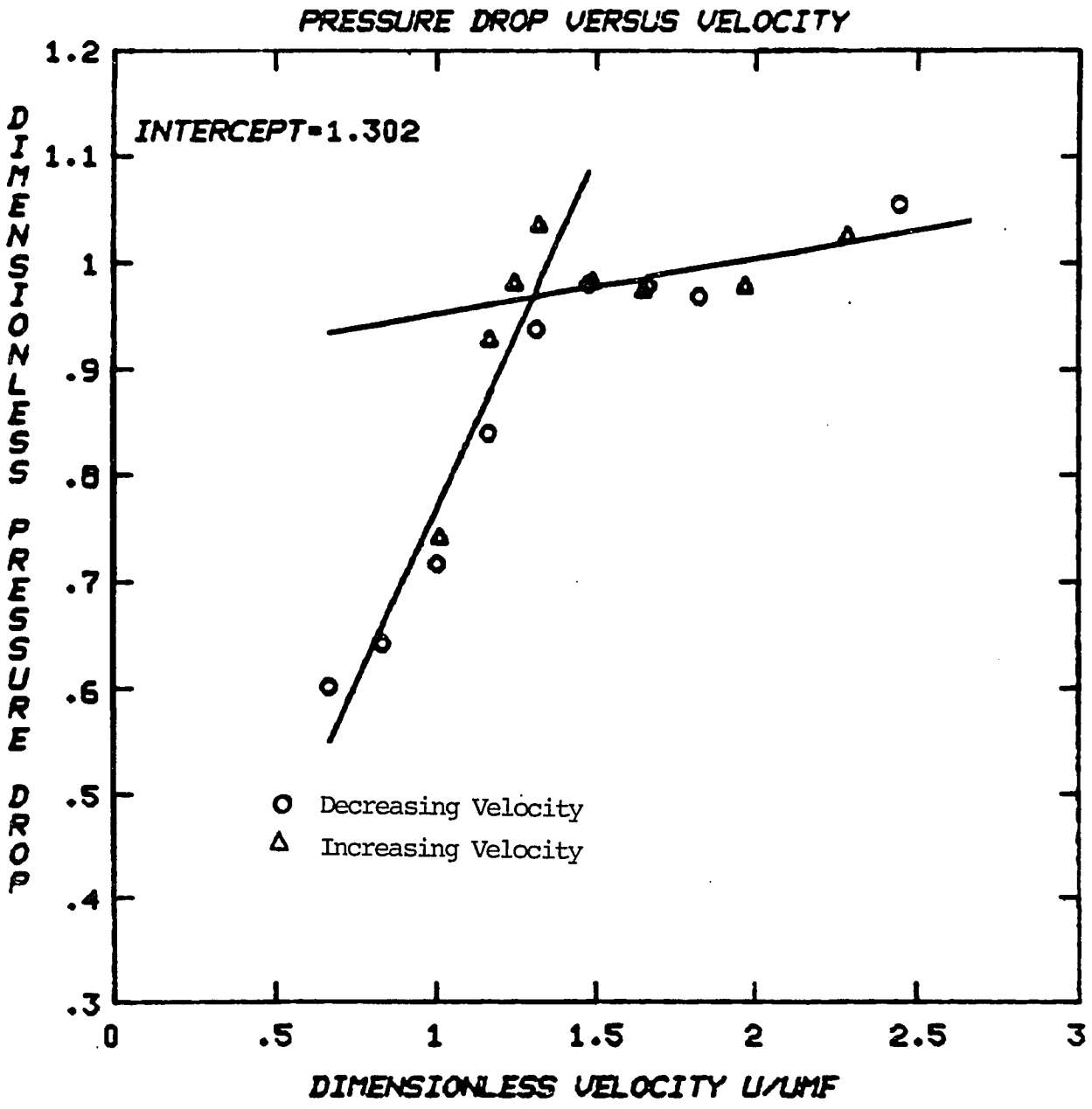

Figure C.2. Pressure drop vs. gas velocity in the bed at T=160°C. (polypropylene particles).

was 30% higher than that calculated using Eq. (C.1) (u/u_{mf} = 1.30). Even in fluidization agglomerates were observed in the bed and the bubble motion of the bed was reduced. The agglomerates were observed to be broken by the action of the bubbles as the velocity was increased. On inspection of the bed material after the run was completed, agglomerates were still present. Most of the agglomerates were 3-5 particles sintered together. There was one large agglomerate that was approximately 5 cm in diameter.

Figure C.3 shows pressure versus velocity for a run at 164°C. This bed behaved in much the same way as the run at 160°C but with some difference. Two holes were formed when the velocity was being increased from the fixed to the fluidized bed state. These holes grew somewhat as the velocity was increased but the bed remained packed even when the velocity was increased much beyond defluidization. This is shown clearly in Figure C.3 where the data points for the increasing velocity are always lower than those corresponding to the decreasing velocity points. The pressure drop of the refluidized bed was always lower than that of the originally fluidized bed throughout the range of fluidization. This is due to the channeling of the bed. The minimum fluidization velocity for this case was determined in Figure C.3 by the intersection of the linear least square fitted lines for the downward set of velocity data points only. This value u/u_{mf}=1.517, was considerably higher than the value for the run at 160°C even though the difference in temperature of the two experiments was only 4°C. The minimum fluidization velocity is seen to be that velocity in which the rate of sintering is balanced by the breakup of agglomerates due to hydrodynamic forces. Once the velocity is decreased an irreversible effect occurs and the bed is unable to refluidize to its original fluidized state if the temperature is too close to the melting point of the granules. If the fluidization velocity is kept above this experimentally determined minimum then the bed remains fluidized in the normal sense and permanent agglomerates are not formed.

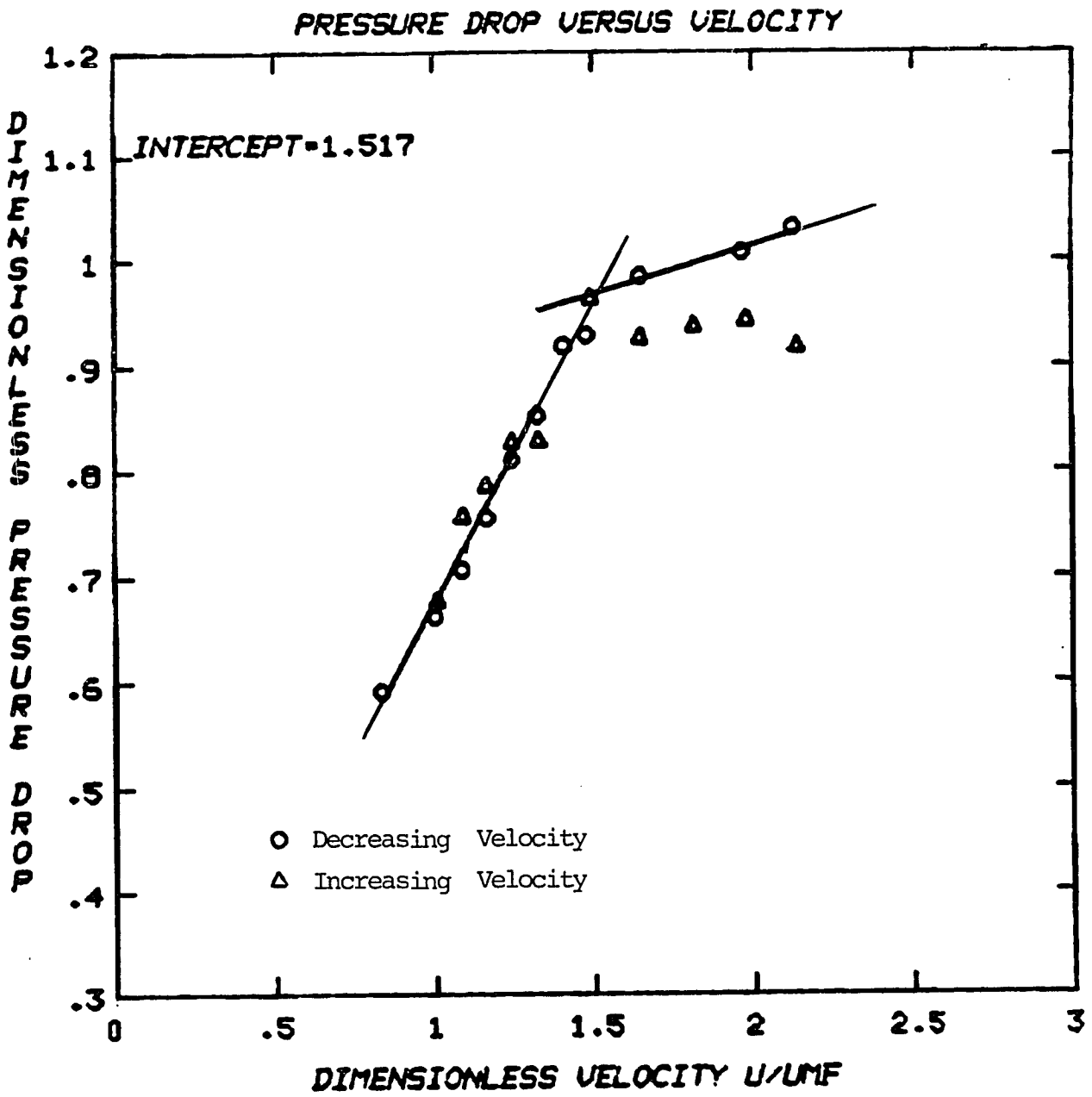

Figure C.3. Pressure drop vs. gas velocity in the bed at T=164°C. (polypropylene particles).

Similar experiments as described above were performed using polyethylene particles with the following characteristics: bed weight of 4 kg, D_p=.07 cm and D_p=.32 cm, ρ_s= .92 g/cm^3 and sphericity ϕ=.62. These results are shown in Section 3.3.

APPENDIX D

Yield criteria for a circular laterally loaded plate

(a) Elastic Regimes in Pressure Loaded Plates

In all these considerations we assume a circular plate of radius a and thickness h subjected at the surface to a constant pressure q (all over the surface) so that the total force on the plate is:

$$F = \pi a^2 q \tag{D.1}$$

where F is the total force on the plate. The geometry and the load are presented schematically in Figure D.1.

Much of the following considerations are taken from Timoshenko and Godier "The Theory of Plates and Shells". Using the deflection of the plate W and its resistance or toughness:

$$D = \frac{Eh}{12\ (1-\nu)} \tag{D.2}$$

where ν is the Poisson ratio and E is Young's modulus. The moments at any radius can be computed from:

$$M_r = -D \left\{\frac{d^2W}{dr^2}\right\} \tag{D.3A}$$

$$M_t = -D \left\{\frac{1}{r}\frac{dW}{dr} + \nu \frac{d^2W}{dr^2}\right\} \tag{D.3B}$$

The equilibrium of the plate requires the following differential equation to hold true:

$$\frac{d}{dr}\left[\frac{1}{r}\frac{d}{dr}\left(r \frac{dW}{dr}\right)\right] = \frac{qr}{2D} \tag{D.4}$$

The solution of equation (D.4) is given by:

$$W = \frac{qr^4}{64D} + C_1 \frac{r^2}{4} + C_2 \log \frac{r}{a} + C_3 \tag{D.5}$$

For the plate with clamped (built-in) edges Eq. (D.5) becomes:

$$W = \frac{q}{64D}\left(a^2 - r^2\right)^2 \tag{D.6}$$

and the moments are obtained from Eqs. (D.3A) and (D.3B) as:

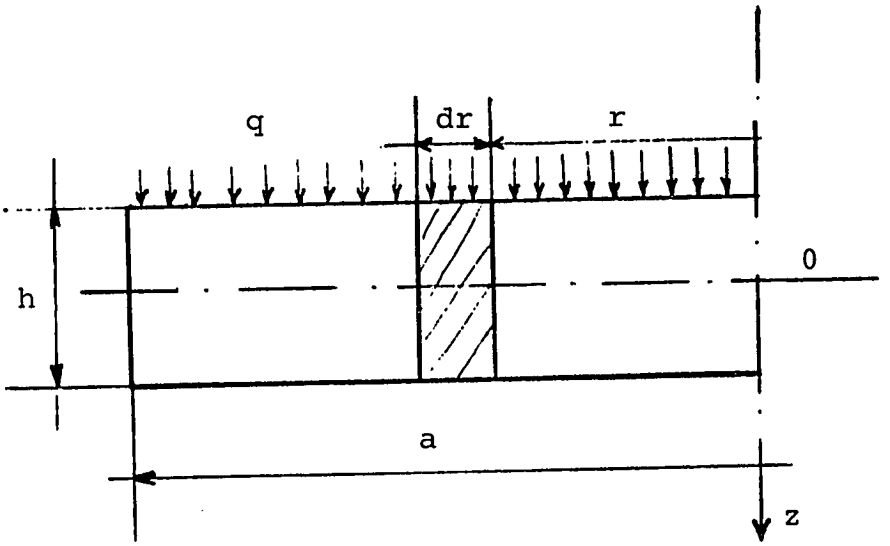

Figure D.1. Laterally loaded circular plate

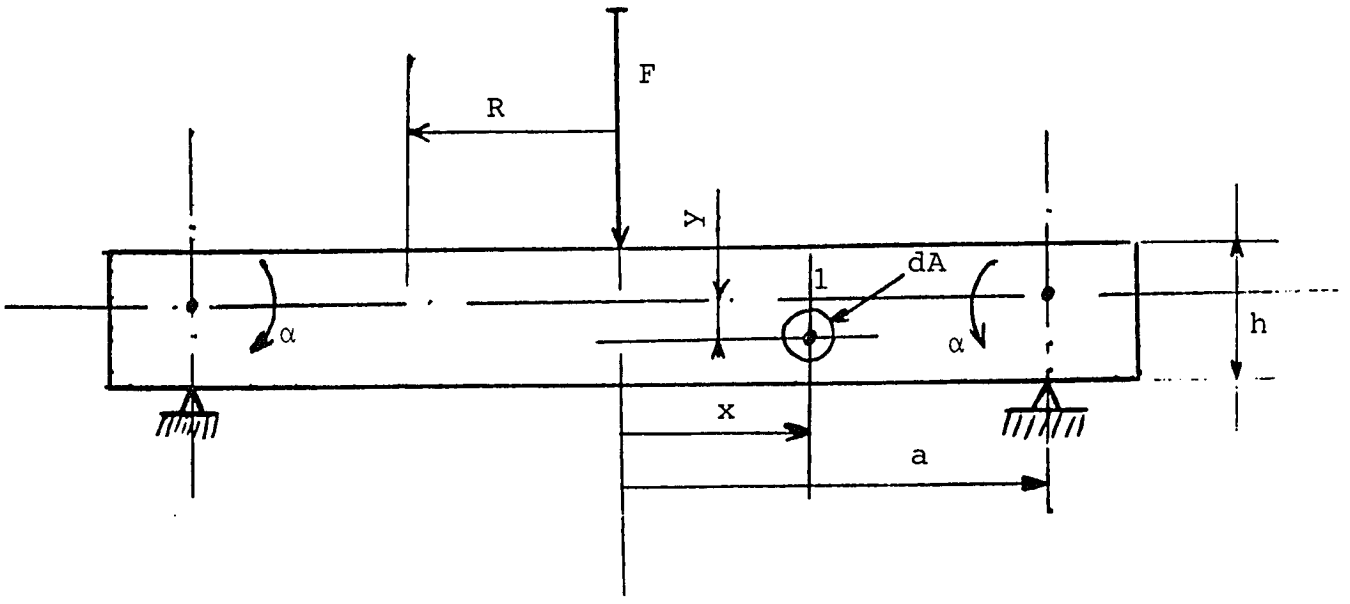

Figure D.2. Plastic deformation of a circular plate

$$M_r = \frac{q}{16} [a^2 (1+\nu) - r^2 (3+\nu)] \tag{D.7A}$$

$$M_t = \frac{q}{16} [a^2 (1+\nu) - r^2 (1+3\nu)] \tag{D.7B}$$

From Eqs. (D.7A) and (D.7B) one can compute the moments at any radius, thus at the clamped edge:

$$M_r\Big|_{r=a} = - \frac{qa^2}{8} \quad ; \quad M_t\Big|_{r=a} = - \nu \frac{qa^2}{8} \tag{D.8}$$

and at the center of the plate Eqs. (D.7A) and (D.7B) give:

$$M_r\Big|_{r=0} = M_t\Big|_{r=0} = \frac{1+\nu}{2} \frac{qa^2}{8} \tag{D.9}$$

Comparing Eqs. (D.8) and (D.9) one can see that the maximum moment appears at r = a.

Using the relationship between the stresses and the moments:

$$\sigma = - \frac{6M}{h^2} \tag{D.10}$$

and Eqs. (D.8) and (D.9) the stresses in the plate can be computed as follows:

$$\sigma_r\Big|_{r=a} = \frac{3}{4} \frac{a^2}{h^2} q \tag{D.11A}$$

$$\sigma_t\Big|_{r=a} = \frac{3}{4} \nu \frac{a^2}{h^2} q \tag{D.11B}$$

$$\sigma_r\Big|_{r=0} = - \frac{3}{4} \frac{1+\nu}{2} \frac{a^2}{h^2} q \tag{D.12A}$$

$$\sigma_t\Big|_{r=0} = - \frac{3}{4} \nu \frac{1+\nu}{2} \frac{a^2}{h^2} q \tag{D.12B}$$

For the plate with freely supported edges Eq. (D.5) becomes:

$$W = \frac{q(a^2-r^2)}{64D} [\frac{5+\nu}{1+\nu} a^2 - r^2] \tag{D.13}$$

and Eqs. (D.3A) and (D.3B) transform to:

$$M_r = \frac{q}{16} [(3+\nu) (a^2-r^2)] \tag{D.14A}$$

$$M_t = \frac{q}{16} [a^2(3+\nu) - r^2(1+3\nu)] \tag{D.14B}$$

The maximum moment appears in the center at r=0 so that:

$$M_r\Big|_{r=0} = M_t\Big|_{r=0} = \frac{3+\nu}{2}\,\frac{qa^2}{2} \tag{D.15}$$

and the stresses are:

$$\sigma_r\Big|_{r=0} = \sigma_t\Big|_{r=0} = \frac{6M_r}{h^2} = \frac{qa^2}{h^2}\,\frac{3(3+\nu)}{8} \tag{D.16}$$

Comparing Eqs. (D.11), (D.12) and Eq. (D.13) one can see that the maximum stress in the free supported plate is by a factor of

$$\lambda = \frac{3+\nu}{2} \tag{D.17}$$

greater than the maximum stress in the clamped plate. Here ν is the Poisson coefficient which is $\nu = 0.5$ for an elasto-plastic material.

(b) Yield Criteria for Elastic-Plastic Materials

If a material is loaded by stresses on a three-dimensional system there is a problem of defining the condition where the material stops behaving in the elastic regime. If there is only one stress, σ_1, the equation:

$$\sigma_1 \leq \sigma_y \tag{D.18}$$

determines this condition. However, if the stress systems are three-dimensional there are three stresses ($\sigma_1 > \sigma_2 > \sigma_3$) and by definition

$$\tau_{max} = \frac{1}{2}\,(\sigma_1 - \sigma_3)$$

is the maximum shear stress. A yield criteria is a postulate which replaces Eq. (D.18) in the case of three-dimensional stresses:

(1) The Rankine theorem states that yield will not occur if the maximum shear stress will be less than the yield stress:

$$\sigma_1 \leq \sigma_y \tag{D.19}$$

(2) The Tresca theorem states that yield will not occur if the maximum shear stress will be less than the yield shear stresses:

$$\tau_{max} \leq \sigma_y \tag{D.20}$$

or:

$$\sigma_1 - \sigma_3 = 2\tau_y \tag{D.21}$$

It can be shown that in this case one obtains for a one-dimensional stress ($\sigma_3 = 0$):

$$\sigma_y = 2\tau_y \tag{D.22}$$

and combining Eqs. (D.21) and (D.22) the yield criteria becomes:

$$\sigma_1 - \sigma_3 \leq \sigma_y \tag{D.23}$$

(3) The Von Mises theorem states that yield will not occur if:

$$(\sigma_1 - \sigma_2)^2 + (\sigma_2 \sigma_3)^2 + (\sigma_1 - \sigma_3)^2 \leq 6\tau_y^2 \tag{D.24}$$

Similarly, Eq. (D.22) in this case becomes:

$$\sigma_y = \sqrt{3}\,\tau_y \tag{D.25}$$

so that Eq. (D.24) can be written as:

$$(\sigma_1 - \sigma_2)^2 + (\sigma_2 - \sigma_3)^2 + (\sigma_1 - \sigma_3)^2 \leq 2\sigma_y^2 \tag{D.26}$$

For the case of two-dimensional stress distributions as is the case of the plate loaded with a distributed pressure the stress σ_3=0. Therefore, the yield criteria becomes:

$$(1)\quad \sigma_1 \leq \sigma_y \tag{D.27A}$$

$$(2)\quad \sigma_1 \leq \sigma_y \tag{D.27B}$$

$$(3)\quad \sigma_1^2 + \sigma_2^2 - \sigma_1\sigma_2 \leq \sigma_y^2 \tag{D.27C}$$

and it is not necessary to distinguish bewteen conditions (1) and (2).

The Rankine, Tresca and Von Mises criteria are general yield conditions applicable to metallic and non-metallic materials. For the special case of powder like or granular material a special condition is applicable namely the Coulomb criteria. This criteria was modified recently by Molerus (1978) and it reads:

$$(4)\quad \frac{\tau}{\sigma_o + \sigma} \leq \tan \delta \tag{D.28}$$

where σ_o is the maximum tensile strength and δ is the friction angle of the material, both being determined from experiment.

Criteria (2), (3) and (4) will be applied now to the case of the elastic plate loaded by a laterial uniform pressure. The maximum pressure q which will keep the plate in the elastic regime will be computed. For the plate with clamped edges Eqs. (D.11) and (D.12) yield:

$$\text{(A)} \qquad \sigma_1\Big|_{r=a} = \frac{3}{4}\frac{qa^2}{h^2}$$

$$\sigma_2\Big|_{r=a} = \frac{3}{4}\frac{qa^2}{h^2}\,\nu$$

and:

$$\text{(B)} \qquad \sigma_1\Big|_{r=0} = \sigma_2\Big|_{r=0} = \frac{3}{4}\frac{1+\nu}{2}\frac{qa^2}{h^2}$$

The Tresca condition gives for (A)

$$q \le \frac{4}{3}\,\sigma_y\,\frac{h^2}{a^2} \tag{D.29}$$

and for (B)

$$q \le \frac{4}{3}\,\sigma_y\,\frac{h^2}{a^2}\,\frac{2}{1+\nu} \tag{D.30}$$

The Von Mises condition gives for (A):

$$q \le \frac{4}{3}\,\sigma_y\,\frac{h^2}{a^2}\,\frac{1}{\left\{1+\nu^2-\nu\right\}^{1/2}} \tag{D.31}$$

and for (B):

$$q \le \frac{4}{3}\,\sigma_y\,\frac{h^2}{a^2}\,\frac{2}{1+\nu} \tag{D.32}$$

Comparing Eqs. (D.29) to (D.32) one can see that the most restrictive condition is Eq. (D.29) and therefore the maximum pressure admissible under the plate with clamped edges is:

$$q_{ce} = \frac{4}{3}\,\sigma_y\,\frac{h^2}{a^2} \tag{D.33}$$

The application of the modified Coulomb criteria to case (A) is not straightforward. However, in case (B), since $\sigma_1=\sigma_2$, the shear stress at $\sigma=0$ will be $\tau=\sigma_1$ and including this condition into Eq. (D.28) one obtains:

$$\sigma_1 = \sigma_o \frac{\tan\delta}{1-\tan\delta} \tag{D.35}$$

Assuming that the yield stress in the granular material is $\sigma_o=\sigma_y$, and corresponds to the maximum tensile stress, and using the value for σ_1 from condition (B) one gets

$$q \leq \frac{4}{3} \sigma_y \frac{h^2}{a^2} \frac{2}{1+\nu} \frac{\tan\delta}{1-\tan\delta} \tag{D.35}$$

Condition (D.35) for the admissible pressure is more restrictive than the value given by Eq. (D.33) only if the friction angle of the material δ is less than about $\delta \approx 23^o$.

For the case of the plate with free edges the criteria (2)-(3) and Eq. (D.16) yield:

$$\frac{3}{4} \frac{qa^2}{h^2} \frac{3+\nu}{2} \leq \sigma_y \tag{D.36}$$

or the maximum pressure will be:

$$q_{fe} = \frac{4}{3} \sigma_y \frac{h^2}{a^2} \frac{2}{3+\nu} \tag{D.37}$$

The equivalent of Eq. (D.35) for the plate with free edges is:

$$q \leq \frac{4}{3} \sigma_y \frac{h^2}{a^2} \frac{2}{3+\nu} \frac{\tan\delta}{1-\tan\delta} \tag{D.38}$$

(c) Plastic Regimes in Pressure Loaded Plates

The relations developed in the previous section give the maximum pressure which can be carried by the plate before the plastic stress σ_y appears at the most stressed point.

In this section a relationship for the maximum pressure which generates a uniform stress in the plate of σ_y is developed.

Referring to Figure D.2, the strain of point 1 due to plastic deformation is:

$$\epsilon_\theta = \frac{\alpha y}{x} \tag{D.39}$$

The plastic work done on 1 and its surroundings is:

$$dW_p = \sigma_y \epsilon_\theta dV = 2\pi\sigma_y \alpha y dA \tag{D.40}$$

which must be equal to the total work done by the force F:

$$Fa\alpha = \int_A dW_p = 2\pi\sigma_y \alpha \int_A y\, dA \tag{D.41}$$

which when carried out gives:

$$F = \pi\sigma_y \frac{h^2}{2} = 2\pi M_o \tag{D.42}$$

where M_o is the plastic moment and is given by:

$$M_o = \sigma_y \frac{h^2}{4} \tag{D.43}$$

A more general form of Eq. (D.42) for a load distributed within a radius R is given by Hopkins and Prager (1953):

$$F = \frac{6\pi M_o}{3-2R/a} \tag{D.44}$$

which naturally reduces to Eq. (D.42) when R=0. When the load is uniformly distributed then R=a and Eq. (D.44) becomes:

$$F = 6\pi M_o \tag{D.45}$$

For the case of the plate with built-in (clamped) edges Eq. (D.45) must be replaced by:

$$F = 12\pi M_o \tag{D.46}$$

Exact mathematical considerations and not energy considerations as used above give a slightly different value of the numerical constant (Hopkins and Prager, 1953) in Eq. (D.46):

$$F = 11.26\pi M_o \tag{D.47}$$

when the Tresca condition is used and the expression:

$$F = 12.5\pi M_o \tag{D.48}$$

when the Von Mises condition is used. Due to their simplicity Eqs. (D.45) and (D.46) are used to compute maximum plastic stress in the plate. Using Eq. (D.1) and Eq. (D.43) and relations (D.45) and (D.46) one obtains:

$$\pi a^2 q = 6\pi\sigma_y \frac{h^2}{4} \tag{D.49A}$$

$$\pi a^2 q = 12\pi\sigma_y \frac{h^2}{4} \tag{D.49B}$$

and from Eqs. (D.49A) and (D.49B) one gets the maximum admissible pressures:

$$q_{fp} = \frac{3}{2}\sigma_y \frac{h^2}{a^2} \tag{D.50A}$$

$$q_{cp} = 3\,\sigma_y \frac{h^2}{a^2} \qquad \text{(D.50B)}$$

The coefficient A_1 in equation (3.3) was taken to be approximately $A_1=2$, a value intermediate between $A_{1fp}=1.5$ and $A_{1cp}=3$.

APPENDIX E

Derivation of equations used to solve for the equilibrium shape and force of a liquid bridge

The Laplace-Young equation can be derived from purely mechanical equilibrium considerations (Boucher and Evans, 1975) or by a minimization of the free energy of a sphere-liquid-sphere system to be:

$$2HoR - BoX = \left\{ \frac{1}{R_1} + \frac{1}{R_2} \right\} \qquad (E.1)$$

where R_1 and R_2 are the radii of curvature of the liquid profile and are related to Y and to the angle Φ between the tangent at (Y,X) to the profile and the horizontal (see Figure 4.1). R_1 and R_2 are given by:

$$R_1 = \left\{1 + (dX/dY)^2\right\}^{3/2}/(d^2X/dY^2) \qquad (E.2)$$

$$R_2 = Y \left\{1 + (dX/dY)^2\right\}^{1/2}/(dX/dY) \qquad (E.3)$$

From geometrical considerations it directly follows that:

$$R_1 = dY/d(\sin \Phi) \qquad (E.4)$$

$$R_2 = Y/\sin \Phi \qquad (E.5)$$

Equation (E.1) can be rearranged by taking the arc length S as a dependent variable. From simple geometric considerations:

$$\cos \Phi = dY/dS \qquad (E.6)$$

$$\sin \Phi = dX/dS \qquad (E.7)$$

Substituting Eqs. (E.4) and (E.5) into Eq. (E.1) and using the relations given by Eqs. (E.6) and (E.8)

$$d(\sin \Phi) = \cos \Phi \, d\Phi \qquad (E.8)$$

equation (E.9) is obtained:

$$d\Phi/dS = (2HoR - BoX) - (\sin \Phi)/Y \qquad (E.9)$$

This equation along with the ancillary equations

$$dY/dS = \cos \Phi \qquad (E.6)$$

$$dX/dS = \sin \Phi \tag{E.7}$$

are the set of first order equations that were solved for the meriodonal profile.

A force balance around the plane at point (1) in Figure 4.1 yields:

$$f_1 = -\iint_{\bar{A}} p^o \, \underline{n} dA \; -\iint_{\underline{A}} p^f \, \underline{n} dA + 2\pi y_1 \gamma \sin \Phi_1 \tag{E.10}$$

where Φ_1 is the filling angle at point (1), γ is the surface tension, p^o is the pressure of the outer fluid (usually air), p^f is the pressure of the liquid bridge, $\underline{A}$ is the area of the spherical cap that is wet by the inner fluid and $\bar{A}$ is the area of the sphere that is in contact with the outer fluid. From hydrostatic considerations:

$$p^o = - \rho^o g x + c_1 \tag{E.11}$$

$$p^f = - \rho^f g x + c_2 \tag{E.12}$$

thus Eq. (E.10) becomes:

$$f_1 = - \iint_{\bar{A}} c_1 dA - \iint_{\underline{A}} c_2 dA + \rho^o g \iint_{\bar{A}} \underline{n} \, x dA + \rho^f g \iint_{\underline{A}} \underline{n} \, x dA$$

$$+ 2\pi y_1 \sin \Phi_1 \tag{E.13}$$

to convert these area integrals into volume integrals the following integral theorem is used:

$$\iint_A \underline{n} \, \psi \, dA = \iiint_V \nabla \psi \, dV \tag{E.14}$$

where A is the area enclosing the closed volume V. The following integrals are added and subtracted to the right hand side of Eq. (E.12) in order to close the areas and apply (E.14):

$$\iint_{\tilde{A}} c_1 \underline{\delta}_x dA + \iint_{\tilde{A}} c_2 \underline{\delta}_x dA + \rho^o g \iint_{\tilde{A}} \underline{\delta}_x \, x dA + \rho^f g \iint_{\tilde{A}} \underline{\delta}_x \, x dA$$

where $\tilde{A}$ is the area of the circular disk at point (1) and $\underline{\delta}_x$ is the unit vector in the vertical x direction. By adding and subtracting the above expression to Eq. (E.13) one arrives at:

$$f_1 = (c_1 - c_2)\pi y_1^2 + \rho^o g V_r + \rho^f g V_{sc} + 2\pi y_1 \gamma \sin \Phi_1 \qquad (E.15)$$

where V_{sc} is the volume of the spherical cap above the plane at x=0 and V_r is the remaining volume of the sphere (if V_T is the total sphere volume, then $V_r = V_T - V_{sc}$). At x=0 the following expression is true:

$$c_1 - c_2 = -(p^f - p^o) = -\Delta P_o \qquad (E.16)$$

substituting for V_r in terms of V_T and V_{sc}, and $c_1 - c_2$ in Eq. (E.15) yields:

$$f_1 = -\Delta P_o \pi y_1^2 + (\rho^f - \rho^o) g V_{sc} + 2\pi y_1 \sin\Phi_1 + V_T \rho^o g \qquad (E.17)$$

The coordinates can be made dimensionless with respect to the radius R, the volume with respect to R^3. The dimensionless force is then given by $F_1 = f_1/\pi R\gamma$ and since $Bo = \Delta\rho g R^2/\gamma$ and $Ho = \Delta P_0/2\gamma$ Eq. (E.14) becomes (the last term in Eq. (E.17) can be neglected when the outer fluid is a gas):

$$F_1 = -2Y_1^2 HoR + \frac{Bo}{\pi} V_{sc}^* + 2Y_1 \sin \Phi_1 \qquad (E.18)$$

Eq. (E.19) follows from geometrical considerations:

$$V_{sc}^* = \frac{\pi}{3} (1 - \cos \alpha_1)^2 \{3 - (1 - \cos \alpha_1)\} \qquad (E.19)$$

it can now be seen that the second term on the right hand side of Eq. (E.18) is identically the expression F_{B1} in Eq. (4.7)

$$F_{B1} = \frac{Bo}{3} V_{sc}^{*} = \frac{Bo}{3} (1 - \cos \alpha_1)^2 \{3 - (1 - \cos \alpha_1)\} \qquad (E.20)$$

a similar force balance at point (2) of Figure 4.1 would yield the force expression given by Eq. (4.6).

REFERENCES

Adams, M.J. and V. Perchard, "The Cohesive Forces Between Particles with Interstitial Liquid", I. Chem. Eng. Symp. Series No. 91., (1984).

Adorjan, L.A., "Theoretical Prediction of Strength of Moist Particulate Materials", "Agglomeration 77", K.V.S. Sastry (Ed.), AIME, 130 (1977).

Baker, C.G.J. and M.A. Bergougnou, "Precipitation of Sparingly Soluble Salts: A Model of Agglomeration Controlled Grwoth", Can. J. of Chem Eng., 52, 246 (1974).

Basu, P., "A Study of Agglomeration of Coal-Ash in Fluidized Beds", Can. J. of Chem Eng., 60, 791 (1982).

Basu, P. and Sarka, "Agglomeration of Coal Ash in Fluidized Beds", Fuel, 62, 924 (1983).

Boucher, E.A. and M.J.B. Evans, "Pendent Drop Profiles and Related Capillary Phenomena", Proc. R. Soc. Lond. A., 346, 349 (1975).

Boucher, E.A., M.J.B. Evans and S. McGarry, "Capillary Phenomena: XX. Fluid Bridges Between Horizontal Solid Plates in a Gravitational Field", J. Coll. Interf. Sci., 89, 154 (1982).

Capes, C.E. "Particle Size Enlargement," Elsevier Scientific Publishing Company, Amsterdam (1980).

Clark, W.C., J.M. Haynes and S. Mason, "Liquid Bridges Between a Sphere and a Plane", Chem Eng. Sci., 23, 810 (1968).

Compo, P., G.I. Tardos, D. Mazzone, and R. Pfeffer, "Minimum Sintering Temperatures of Fluidizable Particles", Particle Characterization, 1, 171 (1984).

Corriell, S.R., S.C. Hardy and M.R. Cordes, "Stability of Liquid Zones", J. Coll. Interf. Sci., 60, 126 (1977).

Cross, N.L. and R.G. Picknett, "International Conference on Mechanics of Corrosion by Fuel Impurities", Marchwood Eng. Lab., England (1963).

De Bisschop, F.R.E. and J.L. Rigole, "A Physical Model for Liquid Capillary Bridges Between Adsorptive Solid Spheres: The Nodoid of Plateau", J. Coll. Interf. Sci., 88, 117 (1982).

Dencs, B. and Z. Ormos, "Particle Formation from Solutions in Gas Fluidized Beds IV", Hung. J. Ind. Chem., 6, 343 (1978).

Dullien, F.A.L., "Porous Media - Fluid Transport and Pore Structure", Academic Press, New York (1979).

Erle, M.A., D.C. Dyson and N.R. Morrow, "Liquid Bridges Between Cylinders in a Torus, and Between Spheres", AIChE J., 17, 115 (1971).

Fisher, R.A., "On the Capillary Forces in an Ideal Soil: Correction of Formulae Given by W.B. Haines", J. Agric Sci., 16, 492 (1926).

Fortes, M.A., "Axisymmetric Liquid Bridge Between Parallel Plates", J. Coll. Interf. Sci., 88, 338 (1982).

Gluckman, M.J., J. Yerushalmi and A.M. Squires, "Defluidization Characteristics of Sticky or Agglomerating Beds", in "Fluidization Technology", Vol. II, D.L. Keairns (Ed.), Hemisphere Publishing, New York, 395 (1975).

Godel, A. and P. Cosar, "The Scale-up of Fluidized Bed Combustion Systems to Utility Boilers", AIChE Symp. Series, 67, 210 (1967).

Harada, K., "Granulation with Simultaneous Coating and Agglomeration in a Fluidized Bed: Particle Size Distribution and Growth Rate in the Steady State", Kagoku Kogaku, 36, 79 (1972).

Hopkins, H.G. and W. Prager, "The Load Carrying Capacities of Circular Plates", J. Mech. Phys. Solids, 2, 1 (1953).

Hosny, H. And J.R. Grace, Fluidization Conference held in Japan, May 28-31 (1983).

Hotta, K., K. Takeda and K. Iinoya, "The Capillary Binding Force of a Liquid Bridge", Powder Tech., 10, 231 (1974).

Hovmand, S., "Agglomeration in Fluidized Beds", 75th AIChE Meeting, Miami, (November 1978).

Hulburt, H. and S. Katz, "Some Problems in Particle Technology - A Statistical Mechanical Formulation", Chem. Eng. Sci., 19, 555 (1964).

Jen, C.O. and K.C. Tsao, "Coal-Ash Agglomeration Mechanism and its Application in High Temperature Cyclones", Separation Science and Technology, 15 (3), 263 (1980).

Kapur, P.C., "Balling and Granulation", "Advances in Chemical Engineering", T.B. Drew (Ed.), 10, Academic Press, New York, 55 (1978).

Kennedy, T.C., J.E. Donovan and A. Trigas, AIChE J., 27, 2 (1981).

Kousaki, Y., K. Okuyama, A. Shimizu, and T. Yoshida, "Dispersion Mechanism of Aggregate Particles in Air", J. Chem. Eng. Japan, 12, 151 (1979).

Krupp, H., "Particle Adhesion, Theory and Experiment", Adv. Coll. Interf. Sci., 1, 111 (1967).

Kunii, D. and O. Levenspiel, "Fluidization Engineering", John Wiley and Sons Inc., New York (1969).

Langston, B.G. and F.M. Stephens, Jr., "Self Agglomerating Fluidized Bed Reduction", J. of Metals, 12, 312 (April 1960).

Levenspiel, O., D. Kunii, and T.Fitzgerald, "The Processing of Solids of Changing Size in Bubbling Fluidized Beds", Powder Tech., 2, 87 (1969).

Lau. I.T., "Defluidization Characteristics in Sticky Beds of Caking Coals", paper presented at the Second World Congress of Chemical Engineers, Montreal, Canada, October (1981).

Liss, B., T.R. Blake, A.M. Squires, and R. Bryson, "Incipient Defluidization of Sinterable Solids", Fourth International Conference on Fluidization, Japan, June (1983).

Livshits, Y.Y., A.I. Tamarin, and S.S. Zabrodsky, "Maximum Forces Acting on a Body Immersed in a Fluidized Bed", Fluid Mech.-Sov. Res., 7, 30 (1978).

MacMullen, R.J. and C.A. Johnson, "Direct Reduction by the H-Iron Process", Min. Congr. J., 48, 47 (1962).

Mason, G. and W.C. Clark, "Liquid Bridges Between Spheres", Chem. Eng. Sci., 20, 859 (1965).

Mehrotta, V.P. and K.V.S. Sastry, "Pendular Bond Strength Between Unequal-Sized Particles", Powder Tech., 25, 203 (1980).

Molerus, O., "Effect of Interparticle Cohesive Forces on the Flow Behaviour of Powders", Powder Tech, 20, 161 (1978).

Newitt, D.M. and J.M. Conway-Jones, "A Contribution to the Theory and Practice of Granulation", Trans. Inst. Chem. Engrs., 36, 422 (1958).

Nguyen, T.H. and J.R. Grace, "Forces on Objects Immersed in Fluidized Beds", Powder Tech., 19, 255 (1978).

Ormos, Z. and K. Pataki, "Studies on Granulation in a Fluidized Bed VIII", Hung. J. Ind. Chem., 7, 105 (1979).

Orr, F.M., L.E. Scriven and A.P. Rivas, "Pendular Rings Between Solids: Meniscus Properties and Capillary Force", J. Fluid Mech., 67 , 723 (1975).

Pietsch, W.B., E. Hoffman, and H. Rumpf, "Tensile Strength of Moist Agglomerates", I&EC Prod. Res. Devel., 8, 58 (1969).

Pulvermacher, B. and E. Ruckenstein, "Two Kinds of Self-Preserving Size Spectra of a Cloud of Particles", AIChE J., 21, 128 (1975).

Randolph, A.D. and C.R. Youngquist, "Secondary Nucleation in a Class II System: Ammonium Sulfate-Water", AIChE J., 18, 421 (1972).

Robinson, T. and B. Waldie, "Dependency of Growth on Granule Size in a Spouted Bed Granulator", Trans. Inst. Chem. Eng., 57, 121 (1979).

Rumpf, H., "The Strength of Granules and Agglomerates", in "Agglomeration", W.A. Knepper (Ed.), John Wiley and Sons, New York, 379 (1962).

Rumpf, H., "Particle Adhesion", in "Agglomeration 77", K.V.S. Sastry (Ed.), AIME, 97 (1977).

Rumpf, H., K. Sommer, and K. Steier, "Mechanism der Haftkraftverstarkung bei der Partikelhaftung durch Plastisches Verformen, Sintern und Viskoelastisches Fliessen", Chem. Ing. Techn., 48, 300 (1976).

Scharff, M.F. et al., "Computer Modeling of Mixing and Agglomeration in Coal Conversion Reactors", First Annual Report, U.S. DOE, FE-3195-5, February (1980).

Schubert, H., "Tensile Strength and Capillary Pressure of Moist Agglomerates", in "Agglomeration 77", K.V.S. Sastry (Ed.), AIME 144 (1977).

Sekiguchi, I. and T. Tohata, "Effect of Temperature on the Agglomerate Strength of Polymeric Particles: Part 2", 1982 annual IFPRI Report, Chuo University, Japan (1982).

Sherwin, M.B., R. Shinner, and S. Katz, "Dynamic Behavior of the Well-Mixed Isothermal Crystallizer", AIChE J., 13,1141 (1967).

Siegell, J.H., "Defluidization Phenomena in Fluidized Beds of Sticky Particles at High Temperatures", Ph.D. Dissertation, The City University of New York (1976).

Siegell, J.H., "High-Temperature Defluidization", Powder Tech., 38, 13 (1984).

Smith, P.G. and A.W. Nienow, "Growth Mechanism in Fluidized Bed Granulation", I. Chem. E. Symp. Series No. 63, D2/k/1 (1981).

Squires, A.M., "Iron and Steel with Hydrogen", Atomic Energy Comm. Symp. Series, 14, 181 (1969).

Squires, A.M., "Clean Power from Dirty Fuels", Scientific American, 227, 26 (1972).

Stefan, J., Sitzber Math. - Nature kl. Bayer Akad. Wiss Munchen, 69, 713 (1874).

Tardos, G.I., D. Mazzone, and R. Pfeffer, "Agglomeration of Particulate Systems in Fluidized Beds - A Review",paper presented at the First Annual IFPRI Meeting, Loughborough, England, May (1980).

Tardos, G.I., D. Mazzone, and R. Pfeffer, "Agglomeration of Particulate Systems in Fluidized Beds - Phase II", paper presented at the Second Annual IFPRI Meeting, Houston, Texas, June (1981).

Tardos, G.I., D. Mazzone, and R. Pfeffer, "Agglomeration of Particulate Systems in Fluidized Beds - Phase III", paper presented at the Third Annual IFPRI Meeting, Clausthal, Germany, June (1982).

Tardos, G.I., D. Mazzone, R. Pfeffer and P. Compo, "Agglomeration of Particulate Systems in Fluidized Beds - Phase IV", paper presented at the Fourth Annual IFPRI Meeting, Tarrytown, New York, June (1984).

Tardos, G.I., D. Mazzone, P. Compo and R. Pfeffer, "Agglomeration of Particulate Systems in Fluidized Beds - Phase V", Annual Report to IFPRI (1984).

Tardos, G.I., D. Mazzone and R. Pfeffer, "Destabilization of Fluidized Beds Due to Agglomeration Part I: Theoretical Model", Can. J. Chem. Eng., 63, 377 (1985).

Tardos, G.I., D. Mazzone and R. Pfeffer, "Destabilization of Fluidized Beds Due to Agglomeration Part II: Experimental Verification", Can. J. Chem. Eng., 63, 384 (1985).

Tardos, G.I., D. Mazzone and R. Pfeffer, "Measurement of Surface Viscosities Using a Dilatometer", Can. J. Chem. Eng., 62, 884 (1984).

Timishenko, S. and L.T. Godier, "Theory of Plates and Shells", John Wiley and Sons, New York (1960).

Tomasicchio, G., "Magnetic Reduction of Iron Ores by the Fluosolids System", Proceedings of Int'l. Symp. on Fluidization, Netherlands Univ. Press, Amsterdam, 725 (1967).

Tsubaki, J. and G. Jimbo, "Mechanism of the Failure of Aggregates in Flow Field", J. Chem. Eng. Japan, 12, 250 (1978).

Visser, J. "On Hamaker Constants: A Comparison Between Hamaker Constants and Lifshitz-Van der Waals Constants", Adv. Coll. Interf. Sci., 3, 331 (1972).

Weinbaum, S. and C. Caro, J. of Fluid Mech., 74, 611 (1976).

Wolfram, E. and J. Pinter, "Mechanical Stability of Liquid Bridges Immersed in a Second Liquid", Acta Chem. Acad. Sci. Hung., 100, 433 (1979).

Yerushalmi, J., M. Kolodney, R.A. Graff, A.M. Squires, and R.D. Harvey, "Agglomeration of Ash in Fluidized Bed Gasifying Coal: The Godel Phenomena", Science, 187, 646 (1975).